ELECTRON TRANSPORT AND SPIN PHENOMENA IN HYBRID ORGANIC/INORGANIC SYSTEMS

PROEFSCHRIFT

ter verkrijging van
de graad van doctor aan de Universiteit Twente,
op gezag van de rector magnificus,
prof.dr. H. Brinksma,
volgens besluit van het College voor Promoties,
in het openbaar te verdedigen
op vrijdag 26 februari 2010 om 15.00 uur

door

Wouter Johannes Marinus Naber

geboren op 30 juni 1981
te Leiderdorp

Dit proefschrift is goedgekeurd door de promotoren:
Prof. dr. ir. D.N. Reinhoudt
Prof. dr. ir. W.G. van der Wiel

ELECTRON TRANSPORT AND SPIN PHENOMENA IN HYBRID ORGANIC/INORGANIC SYSTEMS

Samenstelling van de promotiecommissie:

Prof. dr. ir. A.J. Mouthaan,	Universiteit Twente, voorzitter & secretaris
Prof. dr. ir. D.N. Reinhoudt,	Universiteit Twente, promotor
Prof. dr. ir. W.G. van der Wiel,	Universiteit Twente, promotor
Prof. dr. A.F. Morpurgo,	Université de Genève, Zwitserland
Prof. dr. ir. J. Huskens,	Universiteit Twente
Prof. dr. ir. H.J.W. Zandvliet,	Universiteit Twente
Dr. P.A. Bobbert,	Technische Universiteit Eindhoven
Prof. dr. J.M.D. Coey,	Trinity College, Ireland

The work in this thesis is part of the MESA$^+$ Strategic Research Orientation NanoElectronics, and is financially supported by the MESA$^+$ Institute for Nanotechnology, Netherlands Organization for Scientific Research (NWO), the Technology Foundation STW and NanoNed.

Cover design: Wouter J.M. Naber

Front: Photograph of rubrene single-crystal (partly) overlapping with Co/Al_2O_3 electrodes and the molecule structure of rubrene (top), and the schematic picture of a monolayer of the molecules $[Co(tpy)(tpy\text{-}SH)]^{2+}$ and $[Zn(tpy)(tpy\text{-}SH)]^{2+}$ on gold (bottom).

Back: Photograph of Co/Al_2O_3 structures, representing two electrons and their spin. The height of the structures is approximately 750 μm.

Printed by: Wöhrmann Print Service, Zutphen

Copyright © 2010 by Wouter J.M. Naber

ISBN 978-90-365-2988-4

voor mijn ouders en mijn vriendin

Preface

If we knew what it was we were doing,
it would not be called research, would it?
- Albert Einstein

While I am writing this preface of my thesis, I realize that more than four years of research at the University of Twente has almost come to an end. Research is not always easy, but I had the luck of benefitting from the help and support of numerous people, who made it a little bit easier. When you start thanking people, there is always the danger of forgetting someone. So I would like to say that I am very grateful to everybody who helped and supported me in any way during the research that I will describe in this thesis, and during projects that did not make it to this thesis.

The opportunity for this research position was offered to me by my PhD advisor, Wilfred van der Wiel. I am very thankful for this offer, since I very much enjoy doing research. I think our history dates back to an encounter in a lovely hospital at the foot of mount Fuji, and after that we met again in Atsugi and Twente. I enjoyed being your first 'real' PhD student in the SRO NanoElectronics, which later became the NanoElectronics Group with you as a full professor, just in time to be my promotor. I learned a lot from your stimulating enthusiasm for research and your creativity in solving (difficult) problems. Thank you for everything!

It was also refreshing to hear the chemical point of view from my other promotor, David Reinhoudt. I am thankful that I could benefit from your huge experience as a promotor and as a scientist.

Tian, you were the second 'real' PhD student in the SRO. It was good to have another PhD student during our weekly meetings, and I also learned a lot from your chemical background. Besides the research, it was always good to have a little small talk in between the experiments. Thanks for being my paranimf!

During these four years, I was in different rooms, with different room mates, and I want to thank them all for the nice atmosphere. My first room mate, Regina

Luttge, my room mates of my second room, Yunjae Lee, Rajesh Ramanetti, and Lan Ahn Tran for a short while and my last room mate, Ivan Vera Marún. Ivan, it was good to have a fellow writer in the room with a tight schedule. I hope your thesis will follow soon!

I would also thank the rest of the SMI/NE group. Cock Lodder and Ron Jansen for sharing their knowledge, Byoung-Chul Min for helping me with my first devices and measurements, Tamalika Banerjee (the "grandmother" of our group) for help and keeping the lab ordered, and Michel de Jong, Saroj Prasad Dash, Ram Shanker, Sandeep Sharma and Monica Graciun for all their help. No group can function without technicians, so many thanks to Johnny Sanderink, Thijs Bolhuis and Martin Siekman, for all their technical help inside and outside the cleanroom. Besides that, also thanks to all group members for all the good times besides the research, like the yearly group outing (NEvent) and several drinks.

Good luck to the persons who are just starting as I am about to leave: Ina Rianasari, Jean-Christophe le Breton, Johnny Wong, Serkan Büyükköse.

I would also like to thank all the other SRO NanoElectronic members, for feedback on my project and letting me learn from your own projects.

Although not directly related to my research, also thanks to all the other people walking around at floor 6 for the good atmosphere and useful (or not so useful, but still enjoyable) discussions, some of them belonging to the former SMI group: Leon Abelman, Wabe Koelmans, Johan Engelen, Mink Hoexum, Alexander le Febre, Michael Delalande and Hans Groenland.

I also learned a lot from supervising several students, and I hope they also learned something from me: Abhishek Kumar, Jasper Lemmens (I profited a lot from the successful photolithography devices), Koert Vergeer and Peter Tijssen (sorry I am stopping half-way, I hope for a good continuation of my projects with good results), Sven Krabbenborg (although not really 'my' student), and our visiting students Varada Bal and Murat Eskin. Good luck to all other students still in the group: Mostafa Shawrav, Bernardus Zijlstra, Maarten Groen and Michel Zoontjes. Pim Voorthuijzen, it was interesting to do some measurements on your doped substrates.

Thanks to all the secretaries, Thelma, Carolien, Joyce, Carla, Annerie, Karen, from both the NE/SMI group and from MESA$^+$, for all their help with the administrative work.

Alberto Morpurgo, without you my project would not have been possible. Thanks for all the advice and knowledge about the organic single-crystal devices. A lot of organic-single crystals grown in your group are used in this thesis, and it was great that I could come and take crystals whenever I needed. It was nice

to make a short visit to your new group in Geneva. Anna Molinari and Ignacio Gutiérrez Lezama, thanks for growing the crystals. They were always ready when I came and I really appreciated that. Anne Arkenbout, thanks for mastering rubrene single-crystal growth and sending me crystals whenever I asked. Hennie Valkenier, as I am writing this preface, I still have to measure your organic single-crystals. Also thanks to Thom Palstra, for letting me benefit of his facilities and advice for our paper.

I also learned a lot from several chemists, and I am very thankful for all their help. Christian Nijhuis (thanks for the coffee breaks at Langezijds, they shouldn't have replaced the fresh coffee for machines), Kim Wimbush (sorry for the smelly stuff we used) and Sachin Kinge. Jurriaan Huskens, Aldrik Velders and Deniz, thanks for the help with the spins-on-surfaces experiments. Deniz, I, being a physicist, still find it amazing how you can almost make every molecule we think of. Thanks for all the synthesis and sample preparation.

A lot of the fabrication work (almost all), happens inside the cleanroom, so I want to thank the whole cleanroom staff, Hans Mertens, Rene Wolf, Huib van Vossen, Ite-Jan Hoolsema, Peter Linders, Marion Nijhuis, Samantha Ooijman, Eddy Ruiter, Ton Jenneboer, Dominique Altpeter, Robert Wijn, Gerard Roelofs, Sharron Koch, Anita Kooij, for all their help with the equipment, maintaining the cleanroom and looking out for the safety of the cleanroom users.

I would also like to thank Veronica Mugnaini for the EPR measurements, Chuang Du and Anja van Langen for fabricating the e-beam devices, of which I always wanted as much as possible as soon as possible, Ruud van Damme for the discussions about the magnetic and temperature dependence in our 2D spin systems (I hope this will be fully explained in the end), Gerard Kip for XPS measurements, Rico Keim and Patrick Grunder for the TEM preparation and measurements, even when the preparation was not used for TEM, Mark Huijben for the introduction to and help with the PPMS system, and for growing LSMO electrodes, which in the end seemed to work in combination with our single-crystals, Meint de Boer for help with the fabrication of the shadow masks, Peter Bobbert and Sander Kersten for the discussion about the spin relaxation time in our organic single-crystals , and Harold Zandvliet and Rien Wesselink for some preliminary STM measurements on our paramagnetic molecules.

I want to thank all my committee members, of which I have not mentioned Michael Coey yet, for reading my thesis and their useful comments.

I am also very lucky to have great friends outside the lab. Jurre (discussing physics, waterpolo rules or K-1 with a beer is always enjoyable, thanks for being my paranimf!), Nathalie (I guess that explaining this whole thesis will take more than one trip by train), Annemijn (you can always ask if I invented something

and I am lucky I did not have to break the tradition of visiting all your working places all over the world), Victor (good to have someone to talk about the Tour de France, Giro, and Grand Slams), Marlies(je) (who I have to thank when I win the Nobel Prize), and all other people with whom I enjoyed several drinks, concerts, festivals, waterpolo tournaments and other event, thanks for all the fun besides the physics, but also for being interested in what I am doing.

It was also a good thing that I could relax (at least, stop thinking about physics) during sporting at SG/WS Twente. Thanks to all my teammates, trainers, coaches, and other people (too much to mention here) who contributed in any way to the great 4 years, with a lot of great achievements, prizes, and most important of all, a lot of fun!

Also thanks to my brothers ('what a day!') and their girlfriends, Chris and Wilma (thanks for the laptop when mine broke down and for all your support), and the rest of my family and 'family-in-law', for all the support and interest in me.

Especially I would like to thank my parents. Lieve pappa en mamma, dankjulliewel voor jullie onvoorwaardelijke steun en interesse bij alles wat ik doe. Ik vond het fijn dat jullie begrepen dat ik niet altijd regelmatig langs kon komen, maar dat ik altijd welkom was als ik wel richting het westen kwam. Bedankt voor alles gedurende mijn promoveren en ik ben blij dat jullie Bad Boekelo zo leuk vonden!

Finally, the last part of this preface is reserved for my girlfriend. Li(e)ve Becca, dankjewel voor je begrip toen ik in het verre Enschede ging promoveren. En dankjewel voor al je steun en vertrouwen in mij tijdens deze vier jaar. Gelukkig was er tenminste altijd één iemand die zeker wist dat het allemaal ging lukken. En het is ook gelukt, maar zonder jou was het allemaal veel moeilijker geweest. Ik hoop dat ik hetzelfde terug kan doen!

Wouter Naber
Enschede, January 2010

Contents

1 Introduction **1**

1.1 Electron spin . . . 2
1.2 Electron transport and spin phenomena in hybrid organic/inorganic systems . . . 2
1.3 Organic spintronics . . . 3
1.4 Kondo effect and RKKY interaction . . . 6
1.5 Crystal field theory . . . 9
1.6 Fabrication and measurement setups . . . 11
1.6.1 Electron beam evaporator . . . 12
1.6.2 Magnetic transport measurement setup . . . 13
1.6.3 Vibrating sample magnetometer . . . 14
1.6.4 Physical property measurement system . . . 15
1.6.5 Cryogenically cooled transport measurement system . . . 15
1.7 Outline of this thesis . . . 17
References . . . 18

2 Concepts of organic spintronics **23**

2.1 Organic electronics . . . 24
2.1.1 Organic materials . . . 26
2.1.2 Charge transport in organic devices . . . 28
2.2 Spin-polarized current models . . . 31
2.2.1 Tunnel magnetoresistance . . . 31
2.2.2 Giant magnetoresistance . . . 33
2.2.3 Conductivity mismatch . . . 35
2.2.4 Spurious effects . . . 37
2.2.5 Spin relaxation . . . 38
2.3 Spin injection in organic materials . . . 42
2.3.1 Spin injection in organic thin films . . . 42
2.3.2 Spin injection in single-molecule devices and SAMs . . . 46
2.3.3 OMAR . . . 47

2.3.4 Spin injection in carbon nanotubes . . . 48
2.3.5 Spin injection in C_{60} . . . 51
2.3.6 Spin injection in graphene . . . 51
2.3.7 Two-photon photoemission and low-energy muon spin rotation . . . 52
2.4 Discussion of organic spin valves . . . 53
2.5 Organic single-crystals for spintronics . . . 57
References . . . 59

3 Fabrication of organic single-crystal field-effect transistors with ferromagnetic electrodes 73
3.1 Device layout . . . 74
3.2 Organic single-crystal growth . . . 75
3.3 Electrode fabrication . . . 78
3.3.1 Shadow-mask evaporation . . . 78
3.3.2 Photo- and e-beam lithography . . . 86
References . . . 89

4 Interfaces between ferromagnetic electrodes and organic materials 93
4.1 Introduction . . . 94
4.2 Photoemission of organic semiconductors and Co or Co/Al_2O_3 . . . 95
4.2.1 Ultraviolet photoemission spectroscopy and X-ray photoelectron spectroscopy . . . 95
4.2.2 Sample fabrication . . . 99
4.2.3 Core level spectroscopy . . . 100
4.2.4 Valence level spectroscopy . . . 102
4.2.5 Energy level alignment . . . 104
4.3 Cleaning of interfaces by plasma oxidation . . . 106
4.3.1 Contaminated interfaces . . . 107
4.3.2 Cleaned interfaces . . . 108
4.4 Ferromagnetic electrodes . . . 110
4.5 Conclusions . . . 112
References . . . 112

5 Controlled tunnel-coupled ferromagnetic electrodes for spin injection in organic single-crystal transistors 115
5.1 Introduction . . . 116
5.2 Device characterization . . . 117

5.3 Field-effect transistor measurements . . . 119
5.4 Ferromagnetic electrodes fabricated using e-beam lithography . . 122
5.5 $LaSrMnO_3$ electrodes . . . 123
5.6 Conclusion . . . 125
References . . . 125

6 Metal transfer printing of electrodes on organic single-crystal 129
6.1 Introduction . . . 130
6.2 Conditions for Au transfer to organic single-crystals . . . 131
6.3 Transferred Au electrodes on organic single-crystals . . . 134
6.4 Electrical characterization . . . 136
6.5 Conclusions . . . 139
6.5.1 Metal transfer printing with FM materials . . . 139
References . . . 140

7 Low-temperature solution synthesis of chemically functional ferromagnetic FePtAu nanoparticles 143
7.1 Introduction . . . 144
7.2 FePtAu nanoparticle synthesis . . . 145
7.3 Chemical characterization of FePtAu nanoparticles . . . 146
7.4 Magnetic characterization of FePtAu nanoparticles . . . 150
7.5 Patterning of FePtAu nanoparticles . . . 151
7.6 Conclusions . . . 152
References . . . 152

8 Two-dimensional organic spin systems and their interaction with electrons 155
8.1 Introduction . . . 156
8.2 Monolayer fabrication and characterization . . . 157
8.3 Temperature dependent resistivity measurements . . . 160
8.4 Magnetic field dependent resistivity measurements . . . 163
8.5 Conclusions and outlook . . . 166
References . . . 169

A Fabrication recipes 171
A.1 Shadow mask fabrication . . . 171
A.2 Electrode fabrication with shadow mask . . . 173
A.3 Electrode fabrication with photoresist . . . 173
A.4 Electrode fabrication with e-beam resist . . . 173
A.5 Lift-off . . . 174

A.6 Contact pad fabrication with photoresist 174
A.7 Plasma oxidation times 174

Summary **177**

Samenvatting **181**

Curriculum Vitae **185**

List of publications **187**

Chapter 1

Introduction

1.1 Electron spin

The ancient Greek may well have been the first electrical engineers. They noticed that amber attracted small objects, after it had been rubbed with fur. This phenomenon is still reflected in the term 'electricity', which comes from the Greek word $\eta\lambda\epsilon\kappa\tau\rho o\nu$ (elektron) for amber. Later, in the 19th century, the electron was identified as the fundamental carrier of electrical current. Still, the electron is considered to be a fundamental particle, i.e. an elementary building block of matter.

The concept of the intrinsic angular momentum of an electron, later referred to as its *spin*, was introduced by the Dutch physicists George Uhlenbeck and Samuel Goudsmit in 1925. In retrospect, the electron's spin was first observed in 1922 by the Stern-Gerlach experiment [1]. The original aim of this experiment was to test the Bohr-Sommerfeld hypothesis that the orbital angular momentum of electrons in atoms is quantized. Stern and Gerlach found that a bundle of neutral silver particles is split in two beams due to the interaction with an inhomogeneous magnetic field and explained this by two quantized states of the angular momentum. However, the net orbital angular momentum of silver atoms is zero, so a splitting of the bundle is not expected based on the Bohr-Sommerfeld theory. The correct theoretical explanation of the Stern-Gerlach experiment was given in 1927 by Wolfgang Pauli [2], by taking into account the intrinsic angular momentum of electrons, their spin. The spin of an electron is a pure quantum mechanical property, which cannot be described by classical mechanics. It is represented by the spin quantum number, which can take the values $\frac{1}{2}$ or $-\frac{1}{2}$ in the case of an electron. These two eigenstates are usually referred to as *spin-down* and *spin-up*.

1.2 Electron transport and spin phenomena in hybrid organic/inorganic systems

Electrons and their spin manifest themselves in different physical phenomena, some of which are investigated in this thesis. All devices studied in this thesis are hybrid organic/inorganic systems. The combination of these two classes of materials provides systems that are both interesting from a fundamental point of view as well as of technological relevance, since these systems offer the possibility of exploiting the potential of organic chemistry. It allows for engineering structures at the atomic level, with a large choice of building blocks, bottom-up fabrication and self-assembly, thereby opening up ways to experimentally study and

understand key problems in solid-state physics, like quantum coherence, magnetic interactions and the control of individual nanosystems. It has also been argued that hybrid organic/inorganic systems may be the only way to downscale electronics below 10 nm [3].

The experiments described in this thesis all try to exploit the advantages of inorganic/organic systems to study electron transport and spin phenomena in solid-state devices. The investigated phenomena are introduced in the following sections.

1.3 Organic spintronics

Organic spintronics [4–6] is a relatively new and promising research field where organic materials are applied to mediate or control a spin-polarized signal. It is hence a fusion of organic electronics [7–9] and spin electronics (or *spintronics*) [10–15].

Organic materials[‡] were for long time only associated with electrical insulators. In 1963, however, high conductivity was reported in iodine-doped and oxidized polypyrrole [16]. Research on organic conductors was further boosted by the discovery of high conductivity in oxidized, iodine-doped polyacetylene [17, 18], for which Heeger, MacDiarmid and Shirakawa received the Nobel Prize in Chemistry in 2000. Driven by the technological potential of organic materials, interest arose in organic electronics. Since then, many organic conductors have been studied, including organic thin films [19–26], ultra-pure organic single-crystals [27–31], single-molecules [32, 33], carbon nanotubes [34–40] and graphene [41–43]. Organic materials have been successfully applied in organic light-emitting diodes (OLEDs) [20, 21], photovoltaic cells [22, 23], and field-effect transistors (FETs) [44, 45]. The advantages of organic materials include chemical tuning of electronic functionality, easy structural modification, possibility for self-assembly and mechanical flexibility. These characteristics are exploited for low-weight, large-area and low-cost electronic applications [24–27, 46] (see Fig. 1.1 for some applications of organic electronics).

The field of spintronics studies the spin of the electron in solid-state devices and the application of the electron's spin, instead of or in addition to its charge,

[‡] The word 'organic' stems from the 19th-century belief that certain compounds, termed organic materials, could only be formed in living organisms. This belief turned out to be incorrect, but the definition is still somewhat ambiguous. Organic materials are now often defined as those materials which contain carbon-hydrogen bonds. This definition would exclude fullerenes like carbon nanotubes, as they consist of C only. Fullerenes are however mostly considered organic materials.

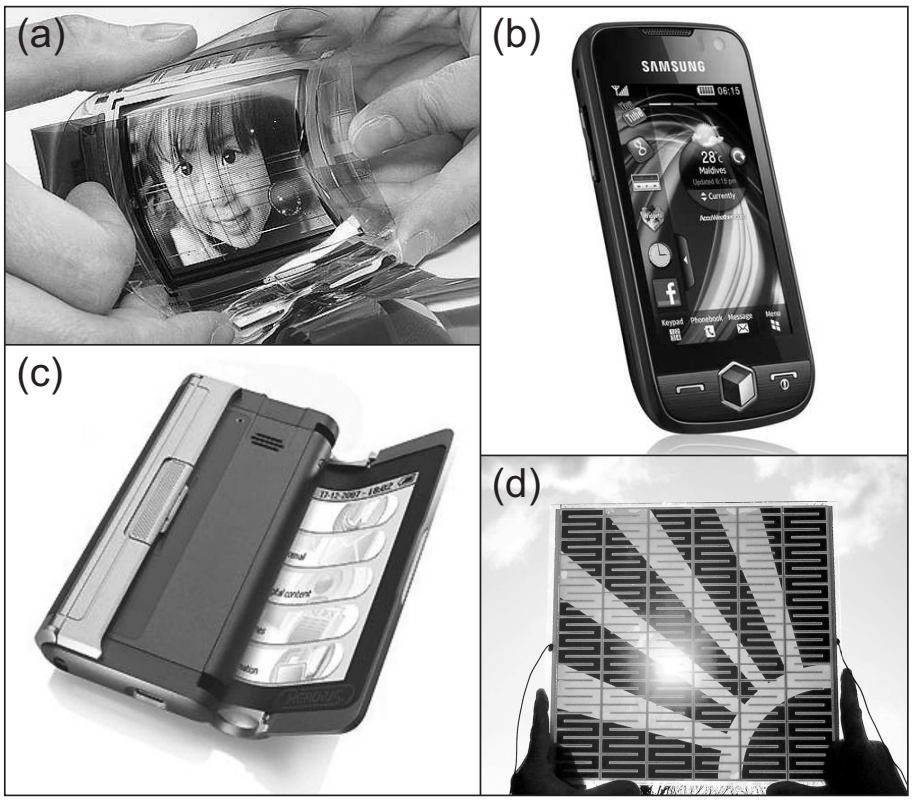

Figure 1.1: Applications of organic electronics. (a) Flexible organic light-emitting diode (OLED) display (Sony). (b) Mobile phone with active matrix OLED (AMOLED) touch display (Samsung). (c) Pocket eReader with rollable display (Polymer Vision). (d) Organic-dye solar cells (Fraunhofer Institute).

for a new class of electronic devices. Figure 1.2 schematically shows the canonical example of a spintronic device, the *spin valve*. Two ferromagnetic (FM) electrodes with different coercive fields (H_c), applied as spin injector and spin detector, respectively, are separated by a non-magnetic (NM) spacer. The role of the spacer is to decouple the FM electrodes, while allowing spin transport from one electrode to the other. The electrical resistance depends on the relative orientation of the magnetization of the two FM electrodes. The relative orientation can be tuned by an external magnetic field between the anti-parallel (AP), as in Fig. 1.2a, and parallel configuration (P), as in Fig. 1.2b. The resistance is usually higher for the AP configuration, an effect referred to as giant magnetoresistance (GMR)[†]. The

[†] The qualification 'giant' is used to distinguish the effect from anisotropic magnetoresistance (AMR). AMR refers to the dependence of the electrical resistance on the angle between the direction of the electrical current and the orientation of the magnetic field [47]. The observed

spacer consists of a NM (semi)conductor, or a thin insulating layer [in the case of a magnetic tunnel junction (MTJ)]. The magnetoresistance (MR) effect in the latter case is referred to as tunnel magnetoresistance (TMR).

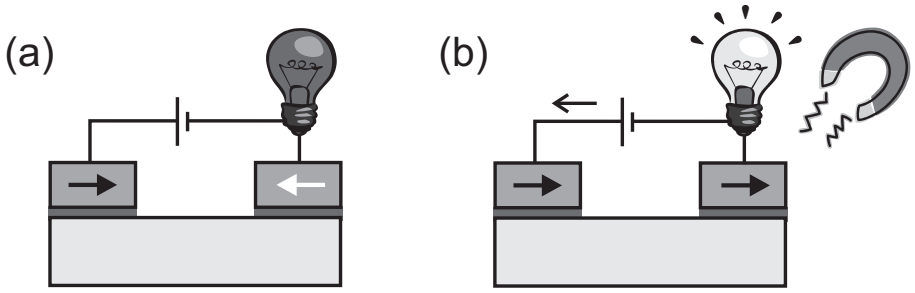

Figure 1.2: Schematic representation of a spin valve. Two ferromagnetic (FM) electrodes (magnetization denoted by arrows) are separated by a non-magnetic (NM) spacer (bottom). One of the electrodes is used as spin injector, the other one as spin detector. A tunnel barrier in between the FM electrode and the NM spacer can enhance the spin signal. The light bulb schematically indicates (a) low conductance in the case of anti-parallel magnetization, and (b) large conductance for parallel magnetization.

The application of the electron's spin was triggered in 1973, when Tedrow and Meservey determined for the first time experimentally the spin polarization of the conduction band in an FM material, using an FM/tunnel barrier/superconductor junction [48]. This work led to the discovery of TMR in FM/tunnel barrier/FM junctions by Jullière in 1975 [49]. As the relative orientation of the electrodes in a TMR device, and hence its resistance, depends on the magnetic history, a TMR structure can be used as a memory element [50, 51]. With the discovery of GMR in 1988, for the first time spin-polarized *transport* through a NM metal was demonstrated. GMR was discovered independently by Fert *et al.* [52] and Grünberg *et al.* [53], and triggered a tremendous amount of research on spintronic devices. For their discovery they jointly received the 2007 Nobel Prize in Physics. The field of spintronics was very much stimulated by the commercial success of GMR devices. IBM already produced the first GMR-based hard disk read head in 1997 [54].

Spintronics allows for non-volatile devices, in which logic operations, storage and communication can be combined. Spintronic devices are also potentially faster and consume less electrical power [55], since the relevant energy scale for spin dynamics is considerably smaller than that for manipulating charges.

GMR effects are about an order of magnitude larger.

The field of organic spintronics not only combines the aforementioned advantages of organic electronics and spintronics, it has particularly attracted attention because of the potentially very long spin relaxation times in organic materials [56]. Using different resonance techniques, room-temperature spin relaxation times larger than 10 μs have been found [57, 58] (as compared to $\sim 10^{-10}$ s in metals [59]). These large spin relaxation times are due to the small spin-orbit coupling in organic materials, being composed mainly of the light atoms carbon and hydrogen.

It is also argued that the hyperfine interaction in organic materials is low, since ^{12}C (98.9 prevalency) has no nuclear spin and the wavefunctions of the π-electrons mainly consist of p_z orbitals, whose nodal plane coincides with the molecular plane [56]. However, the influence of ^{1}H with nuclear spin $\frac{1}{2}$ might be far from negligible [60].

These advantages make organic spintronics a very interesting field with the potential for commercially attractive devices. The field is relatively young, but rapidly expanding. Research in this area is likely to ultimately lead to new spin-based, versatile devices and possibly even to robust quantum bits for quantum information and computation.

1.4 Kondo effect and RKKY interaction

The Kondo effect is a many-body phenomenon, which arises from the interaction between a localized spin and the electrons in a surrounding Fermi sea. The history of the Kondo effect started in 1934, when de Haas *et al.* [61] observed an anomalous electrical resistivity minimum in gold samples. The origin of the anomaly remained unknown, until the Japanese physicist Jun Kondo provided an explanation for this phenomenon in 1964 [62, 63]. He attributed the observed temperature dependence of the resistivity to the presence of diluted magnetic impurities. Conduction electrons with spin $\overrightarrow{s}$ tend to screen the spin of the magnetic impurity $\overrightarrow{S}$ due to an antiferromagnetic coupling $\lambda \overrightarrow{S} \cdot \overrightarrow{s}$, where λ is the exchange constant. Using perturbation theory, Kondo showed that taking into account terms to the third order in λ, leads to a contribution to the resistivity that depends logarithmically on temperature T and diverges at low temperatures. Combining this logarithmic dependence with the phonon contribution, which is proportional to T^5, he provided an explanation for the observed resistivity minimum (see also Fig. 1.3b).

The internal quantum degree of freedom, provided by the spin of the magnetic impurity, makes it impossible to treat the scattering off this magnetic impurity as

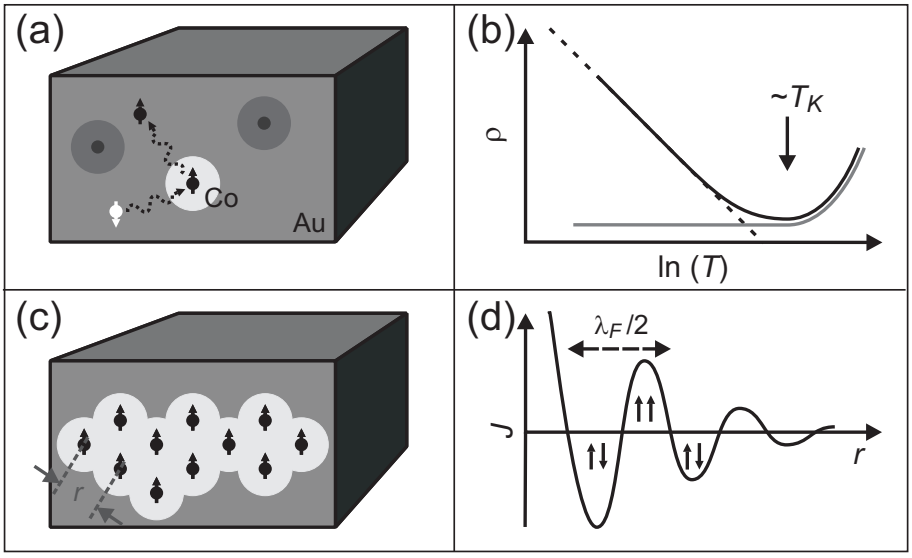

Figure 1.3: Characteristics of the Kondo effect and RKKY interaction. (a) Magnetic impurities (Co) in a non-magnetic metal (Au) cause the electrons to scatter which can result in an effective spin-flip event. (b) Resistivity ρ vs. temperature T for a pure metal (grey line) and a metal with magnetic impurities (black line), resulting in a resistance minimum and a logarithmic upturn (denoted by the dashed line) below the Kondo temperature T_K. (c) Schematic picture of (ferromagnetic) coupling between impurity spins separated by a distance r. (d) RKKY interaction J_{RKKY} vs. distance r. The arrows denote ferromagnetic ($\uparrow\uparrow$) and anti-ferromagnetic ($\uparrow\downarrow$) coupling.

a single-particle problem. When the spin on the impurity is pointing upward, the Pauli exclusion principe allows only spin-down electrons to hop on the impurity. This situation is reversed when an electron going out of the impurity has a different spin as the ingoing one, i.e. when this scattering event has effectively flipped the impurity spin (see also Fig. 1.3a). As a result, the Pauli principle establishes a correlation between the scattering events. This implies higher-order scattering terms have to be taken into account to evaluate the resistivity. Many of such spin-flip events added coherently, generate a many-body singlet state, the Kondo resonance, which is found to emerge as a peak in the local density of states with a width of $\sim k_B T_K$. Here, k_B is the Boltzmann constant and T_K, referred to as the Kondo temperature, is the characteristic energy scale for the Kondo effect. For the pure Kondo effect, where the localized spins are not coupled to each other,

$$T_K \propto E_F \times e^{1/(N|\lambda|)}, \tag{1.1}$$

where N is the density of states at the Fermi energy E_F. The logarithmic diver-

gence found by Kondo is ultimately determined by the energy sharpness of the Fermi surface ($\sim k_B T$).

A wide interest in the Kondo effect exists, since the theory behind this many-body problem can help to describe other complex systems, like heavy-fermion systems and high-T_c superconductors. However, not all characteristics of the Kondo effect are known. The extent over which the conduction electrons interact with the magnetic impurity, for example, denoted as the Kondo cloud [64, 65], has never been determined experimentally. Besides from a fundamental point of view, the details about the spin interaction might also be interesting for quantum technologies in which the spin of an electron is controlled in structures with sizes down to the atomic level. The spatial extension of the Kondo cloud is predicted to be in the order of the Kondo length [65]

$$\xi_K = \frac{\hbar v_F}{k_B T_K}, \tag{1.2}$$

where $\hbar$ is the reduced Planck constant and v_F the Fermi velocity. A theoretical study [66] shows that in 3D the size of the Kondo cloud is limited to a distance of the order of the Fermi wavelength, while in lower dimensions it is again determined by ξ_K. The extent of the Kondo cloud is however still under debate, and dubbed the "holy grail" of research on the Kondo effect [67].

If the concentration of magnetic impurities gets so large, that they start to magnetically couple, spin-flip processes get harder, and the Kondo effect is suppressed (Fig. 1.3c). One possible spin-spin coupling mechanism is an indirect interaction via the conduction electrons, also known as the Ruderman-Kittel-Kasuya-Yosida (RKKY) interaction [68–70]. The interaction $-J_{RKKY}\overrightarrow{S_i} \cdot \overrightarrow{S_j}$, where J_{RKKY} is the RKKY interaction between the spins of two magnetic impurities on site i and j, is a result of the antiferromagnetic coupling between the impurity spin and the conduction electrons (which is also responsible for the Kondo effect). As a result, oscillatory spin density rings are induced around the impurity (RKKY oscillations, akin to the Friedel oscillations of charge). When a second impurity is nearby, the localized spins interact via the Friedel oscillations, resulting in either a ferromagnetic or anti-ferromagnetic interaction, depending on the separation between the localized spins (Fig. 1.3d). For 2D systems, this interaction is given by [71]

$$J_{RKKY} \propto \lambda^2 N \cos(2k_F r_{ij})/r_{ij}^2, \tag{1.3}$$

where k_F is the Fermi wave vector and r_{ij} is the distance between site i and j.

Whereas the Kondo effect only involves the coupling between a localized spin and the conduction electrons, the RKKY interaction describes the coupling between localized spins through their coupling to the conduction electrons. For

a given metal and magnetic impurities, all parameters determining the Kondo effect and the strength of the RKKY interaction are set, except for the distance between the localized spins. By varying this distance, the relative weight of the Kondo effect and the RKKY interaction can be varied, which can be used to study the competition between these two phenomena. This can for example be done by using a system in which molecules with an unpaired spin act as the localized spin, as will be discussed in chapter 8. Crystal field theory can be used to describe the spin-state inside these molecules.

1.5 Crystal field theory

Crystal field theory (CFT) [72] describes the electronic structure of metal complexes. A metal complex is a molecule consisting of a central metal atom or ion, bonded to a surrounding array of molecules. In case of a metal ion, CFT can be used to determine the existence of an unpaired spin inside the metal complex. CFT takes into account the charge of the metal ion and the electronic interaction with the surrounding ligands.

As an example the metal complex $[Co(tpy\text{-}SH)_2]^{2+}$ is taken, where (tpy-SH) is the thiol-modified terpyridine ligand 4'-(5-mercaptopentyl)-2,2':6',2"-terpyridinyl, which is investigated in chapter 8. The $[Co(tpy\text{-}SH)_2]^{2+}$-molecule is a metal complex with one Co^{2+} ion in an approximate octahedral environment of ligands (carbon rings with a nitrogen atom, see Fig. 1.4a). The electron configuration of Co is [Ar] $3d^7$ $4s^2$, which means Co^{2+} has 7 valence electrons in the d-orbital.

If the different unperturbed orbitals of the metal ion are considered, the unperturbed s-orbital is spherically symmetric (see Fig. 1.5) and therefore has an equal interaction with all ligands. The result is an increase in energy of the s-orbital as compared to a free ion (i.e. not enclosed by ligands).

The unperturbed p-orbital of the metal consists of the p_x, p_y and p_z orbitals (see Fig. 1.5). The resulting p-orbital can be thought of as six lobes pointing in the direction of the ligands. A completely filled p-orbital is therefore spherically symmetric, which will result in an equal interaction with the ligands and the degenerate p-orbital shifts up in energy.

The unperturbed d-orbitals (see Fig. 1.5) are no longer symmetric with respect to the ligands. Some of the d-orbitals (d_{x2-y2} and d_{z2}), being in the e_g symmetry group, point toward the ligands, while the other d-orbitals (d_{xy}, d_{xz} and d_{yz}), which are in the t_{2g} symmetry group, have lobs in between the ligands. This results in different electrostatic interaction between the ligands and these two groups of d-orbitals, and consequently in different energy shifts. The energy

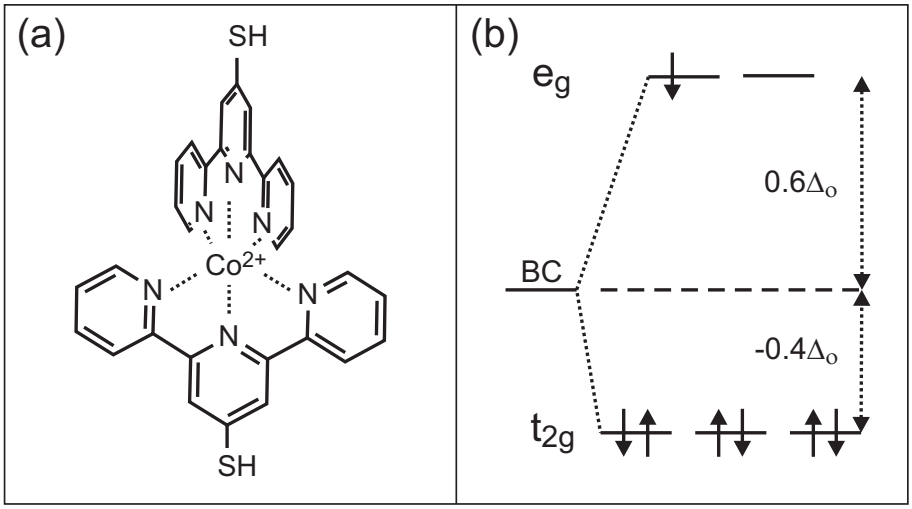

Figure 1.4: (a) Molecular structure of the Co-complex. (b) Energy diagram of the complex in (a). Splitting Δ_o of the e_g and t_{2g} orbitals relative to the barycenter (BC), and filling of the energy levels by spin-up and spin-down electrons, represented by the arrows. The seven arrows correspond to the seven valence electrons in the d-orbitals of Co^{2+} in a low-spin state.

difference Δ_o between these two groups in an octahedral structure is referred to as the crystal field splitting parameter. Its value depends on the specific ligands, the metal ion, the oxidation state of the metal ion and the distance between the ligands and the metal ion.

In an octahedral structure the t_{2g} orbitals have an energy shift of $-0.4\Delta_o$, while the e_g orbitals move to $0.6\Delta_o$ with respect to the barycenter (see Fig. 1.4b), which is the hypothetical value of the energy of the metal ion in a spherical field. The first three electrons will be in the three lowest energy levels. If there are more than three electrons in the d-orbital, different electron configurations exist. The first three electrons are in the threefold degenerate lower energy t_{2g} level, but the fourth electron can be in either one of these three lower energy levels or the higher energy e_g level. The electron configuration is governed by the stabilization energy

$$E_s = (-0.4n + 0.6m)\,\Delta_o + pE_p, \tag{1.4}$$

where n is the number of electrons in the t_{2g} orbitals, m the number of electrons in the e_g orbitals, p the number of pairs of electrons in the same energy level and E_p the pairing energy, the exchange energy for two electrons in the same energy level. The values of n, m and p are such, that E_s is minimized. When E_p is so

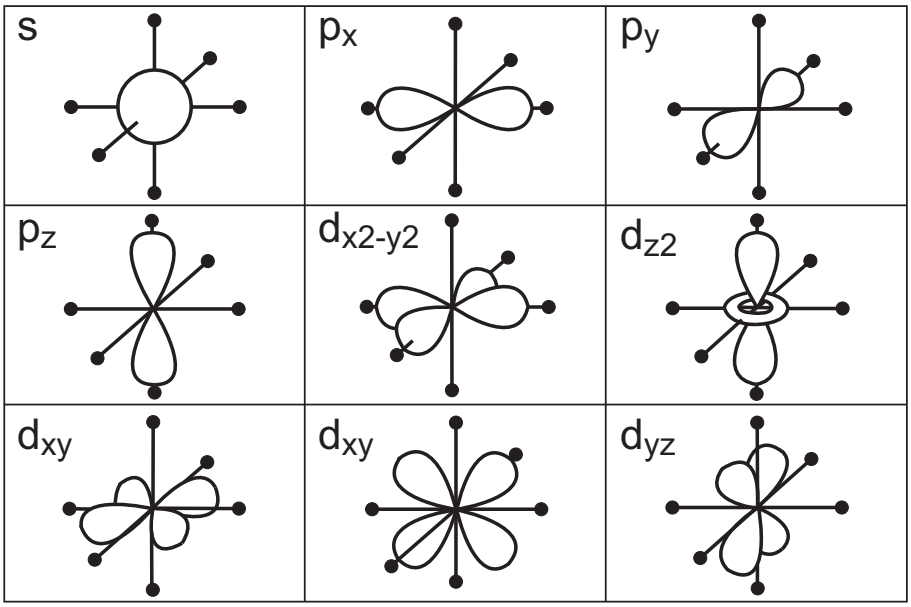

Figure 1.5: Schematic representation of the unperturbed s-, p- and d-orbitals of the metal ion in the Co-complex. The names of the orbitals are given in the panels. The black dots represent the ligands positions in case of the metal complex.

large compared to Δ_o that first the e_g orbitals are completely filled when there are more than three electrons in the d-orbital, the system is in the weak-field limit and has more unpaired spins as compared to the high-field limit, where first the t_{2g} orbitals are filled. These two states are therefore referred to as the high-spin and low-spin state, respectively. According to the literature [73], the $[Co(tpy\text{-}SH)_2]^{2+}$ complex is mostly in the low-spin state (depending on the distortion of the molecule by the Jahn-Teller effect), as drawn in Fig. 1.4b.

1.6 Fabrication and measurement setups

The devices discussed in this thesis have been fabricated using a range of equipment and measured in several experimental setups. In the following sections the equipment to fabricate metal FM electrodes for organic FET devices and the setups to characterize these devices by measuring the magnetization of the electrodes and the transport properties of the FET structure are described. Setups which are able to measure transport properties at low temperatures, needed to investigate localized spins and their interaction with the environment, are also discussed.

1.6.1 Electron beam evaporator

High-quality metal and oxide films were deposited using a Metal-600 molecular beam epitaxy (MBE) system from DCA Instruments. Substrates are mounted on a sample holder and introduced into the loadlock of the setup. After pumping down the loadlock to $\sim 1 \cdot 10^{-7}$ Torr ($\sim 1 \cdot 10^{-5}$ Pa), the sample holder is transferred to the evaporation chamber, which is in ultra high vacuum (UHV) with a base pressure $p_b \leq 1 \cdot 10^{-10}$ Torr ($\leq 1 \cdot 10^{-8}$ Pa). This pressure is achieved by a helium cryo-pump and a nitrogen-filled jacket.

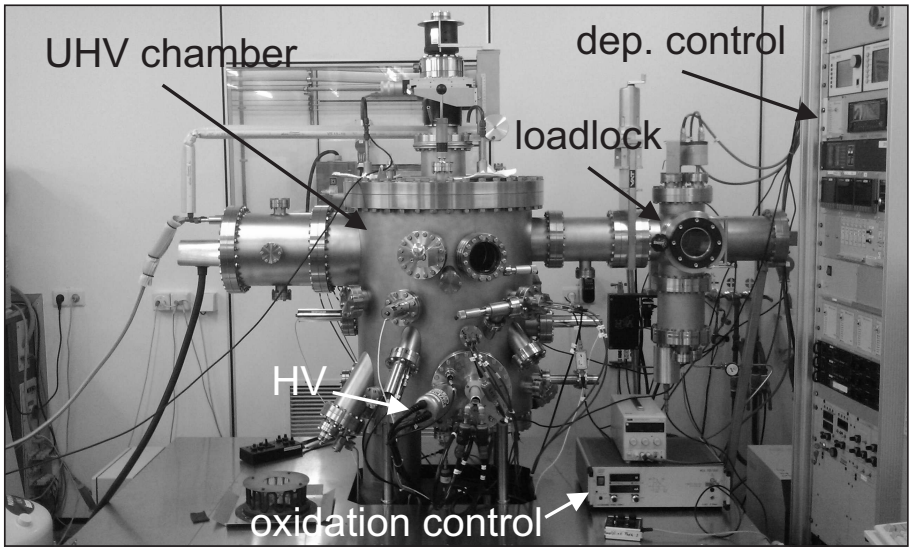

Figure 1.6: Photograph of the DCA Metal-600 MBE system, showing the ultra-high vacuum (UHV) chamber, loadlock, deposition (dep.) control monitors, high-voltage (HV) source and voltage control for the oxidation.

Different metals can be evaporated by an electron beam, coming from the high-voltage (HV) source. The layer thickness is monitored by the eigenfrequency change of a crystal inside the vacuum chamber. This allows growing films as thin as 1 nm in a controlled fashion. Oxidation of Al, used to obtain high-quality Al_2O_3 layers used in this thesis, is done in the loadlock by plasma oxidation. O_2 is introduced into the loadlock, and a voltage of 800 V is applied over two electrodes to generate the plasma. A photograph of the DCA Metal-600 MBE system is given in Fig. 1.6.

Metal electrodes for some of the devices presented in this thesis are fabricated using photo- or e-beam lithoghraphy. These processes are schematically shown

in Fig. 1.7. First, an organic resist is spin-coated on a substrate. A pattern is defined in this resist with UV light and a mask (in the case of photolithography), or a focused electron beam (in the case of e-beam lithography). The photon- or electron-sensitive resist is washed away after this step by a developer. Depending on the tone of the resist, which can be positive or negative, the exposed or unexposed parts of the resist are washed away, respectively. A metal is then evaporated on the substrate. This metal is only in contact with the substrate on the places where the resist is exposed and developed. In the last step (the "lift-off" step), the resist is removed by acetone, leaving only the metal which is deposited directly on the substrate. For a detailed overview of the fabrication process the reader is referred to chapter 3 and appendix A.

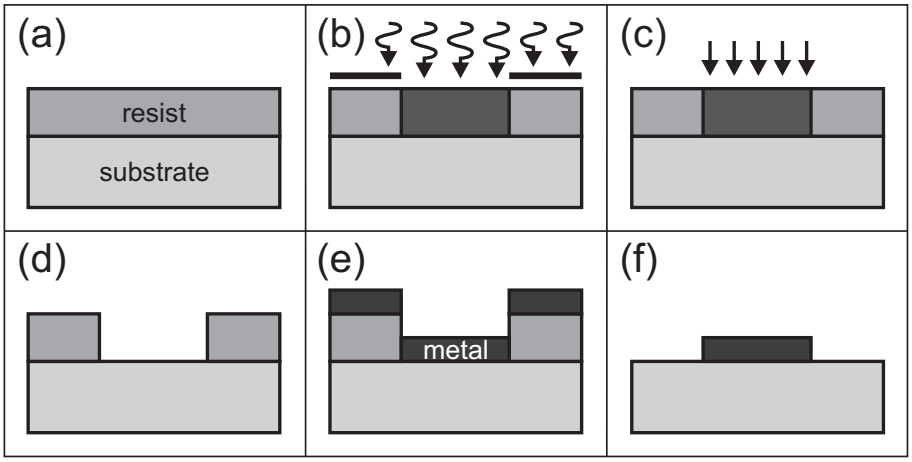

Figure 1.7: Different steps of the lithography process. (a) Resist is spin-coated on a substrate. Resist is developed by (b) UV light and a mask (in the case of photolithography), or (c) a focused electron beam (in the case of electron-beam lithography). (d) Resist is developed. (e) Metal is evaporated. (f) Resist is removed (lift-off).

1.6.2 Magnetic transport measurement setup

Electrical transport measurements as a function of magnetic field and temperature can be performed in a measurement setup including an electromagnet from Bruker Corporation. A sample with a maximum size of 11 x 11 mm^2 can be fitted in a sample holder and introduced into a flow cryostat. Via a measurement computer, a current can be applied with a Keithley 6221 DC and AC current source, or a voltage by a Keithley 2400 source meter or a Keithley 236 source measure unit. The voltage can be measured by a Keithley 2182 nanovolt meter, or the

current by the Keithley 2400 and Keithley 236. The lowest voltage noise is 5 μV in a 1 kΩ device, using the Keithley 6221 and Keithley 2182. The sample is in the center of the Bruker electromagnet, which can generate magnetic fields up to 2 T. The sample can be measured in vacuum and in a He environment. Cooling can be achieved by a flow of liquid He along the sample chamber which is filled with He gas, which allows for temperatures as low as 5 K. Higher temperatures, up to ∼350 K, can be achieved by heaters. A photograph of the setup is given in Fig. 1.8.

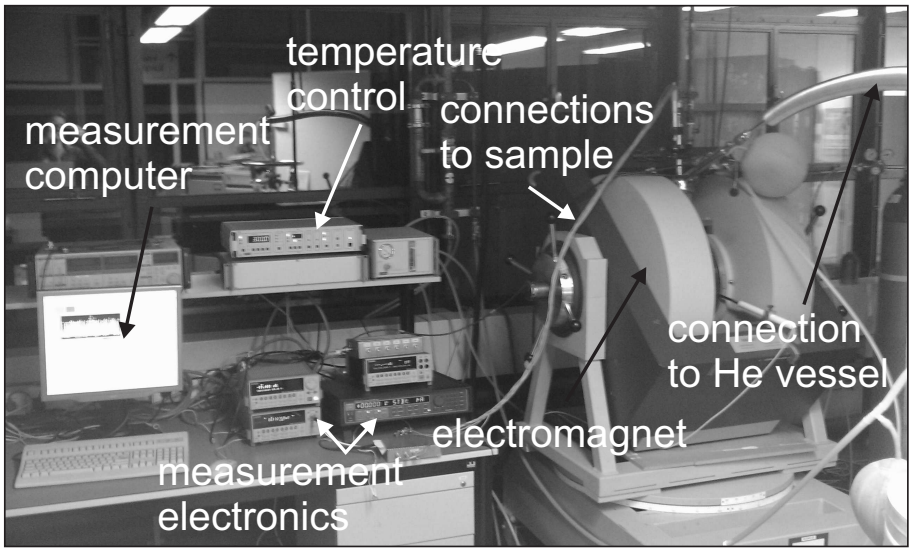

Figure 1.8: Photograph of the flow cryostat with a 2 T Bruker electromagnet, showing the measurement computer, the temperature controller, the measurement electronics, the cable with the connections to the sample, the electromagnet and the connection to a He vessel, used to cool the sample.

1.6.3 Vibrating sample magnetometer

To measure the magnetization of a sample, a model 10 vibrating sample magnetometer (VSM) from Digital Measurement Systems Division of ADE Technologies is available. Samples up to 8 x 8 mm^2 can be loaded in this measurement setup. Using an electromagnet, magnetic fields from -2 to 2 T can be applied with a resolution of 10 mT and magnetic moments as low as 10^{-9} Am^2 can be measured. The sample can be perpendicular or parallel to the magnetic field and can be rotated 540°. Cooling the sample is achieved by a flow of nitrogen along the sample, allowing for temperatures down to 120 K. Heaters can be used to heat

the sample to high temperatures up to 700 K. A photograph of the VSM is given in Fig. 1.9.

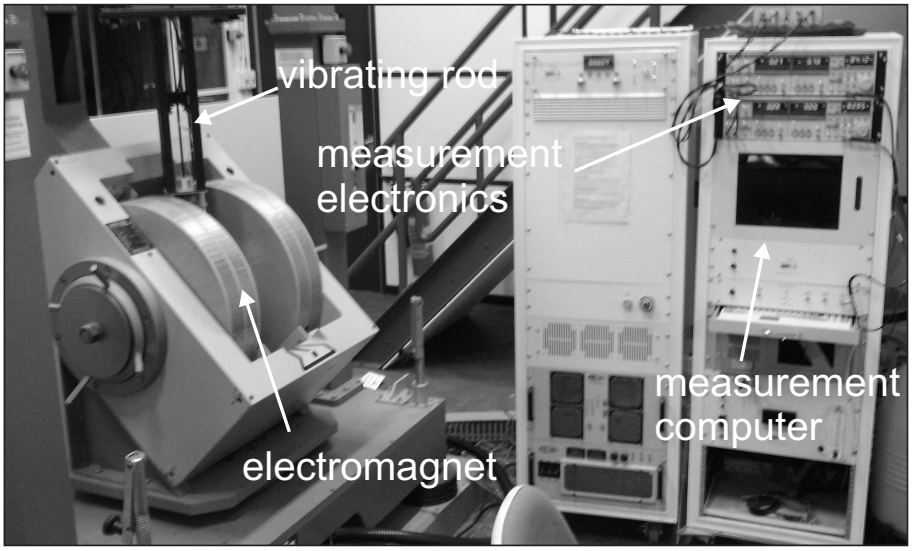

Figure 1.9: Photograph of the DSM 10 VSM, showing the electromagnet, the vibrating rod on which the sample is mounted, the measurement electronics and the measurement computer.

1.6.4 Physical property measurement system

A physical property measurement system (PPMS) from Quantum Design is used to measure the sample resistivity at various temperatures between 1.9 and 400 K and magnetic fields up to 9 T. Data acquisition electronics and analysis software are integrated in the system.

Several inserts are available, which allow measuring the sample at different angles with respect to the magnetic field. A VSM option is also available for this system, to measure the magnetization as a function of the magnetic field. The sensitivity is 10^{-8} Am^2. A photograph of the PPMS is given in Fig. 1.10.

1.6.5 Cryogenically cooled transport measurement system

To perform electrical transport measurements at temperatures below 1 K, a Heliox VL from Oxford Instruments is available with a 10 T superconducting magnet. The sample is mounted in an insert which contains the electrical wiring and

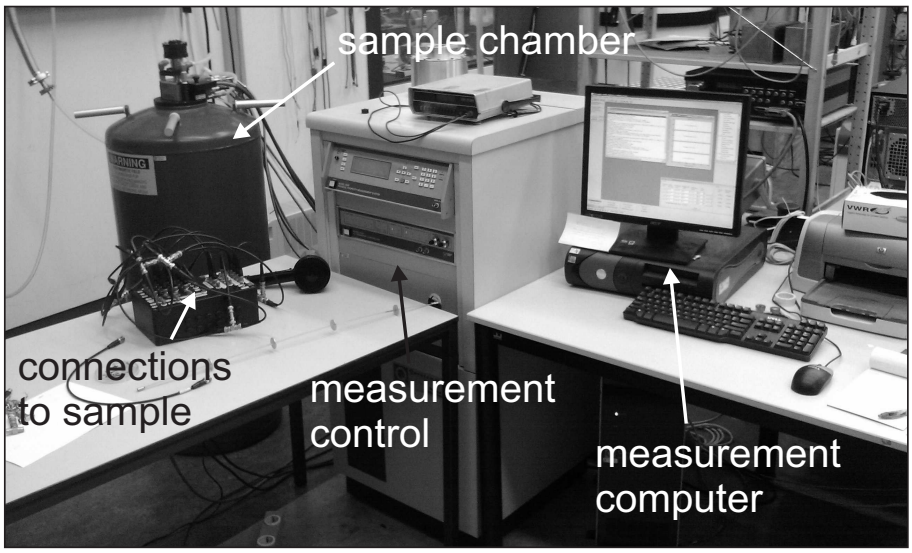

Figure 1.10: Photograph of the PPMS system, showing the sample chamber, the connections to the sample inside the system, the measurement control unit and the measurement computer.

is isolated by an inner vacuum chamber (IVC). The sample is further isolated by an outer vacuum chamber and a ^{4}He filled dewar, when it is inserted in the system. To cool down to base temperature, first ^{3}He, which is in a closed system, is collected in the ^{3}He pot. By pumping ^{4}He, the temperature of a so-called 1K plate is decreased to 1.2 K. At this temperature, ^{3}He condenses and flows in the ^{3}He pot. Temperatures lower than 1.2 K are reached by pumping on the ^{3}He pot. A built-in ^{3}He sorption pump decreases the vapor pressure of the ^{3}He. Evaporation of the liquid ^{3}He cools the ^{3}He pot to its base temperature of 240 mK. The sample is cooled by putting it in thermal contact with a ^{3}He pot. Heaters can be used to measure at higher temperatures up to 80 K.

The battery-driven measurement electronics are custom-made at Delft University of Technology and designed by Ing. R.N. Schouten. An optical fiber connecting the electronics and the measurement computer, and isolation amplifiers galvanically isolate the measurement electronics from the outside world, allowing for very low-noise measurements. A photograph of the Heliox VL is given in Fig. 1.11.

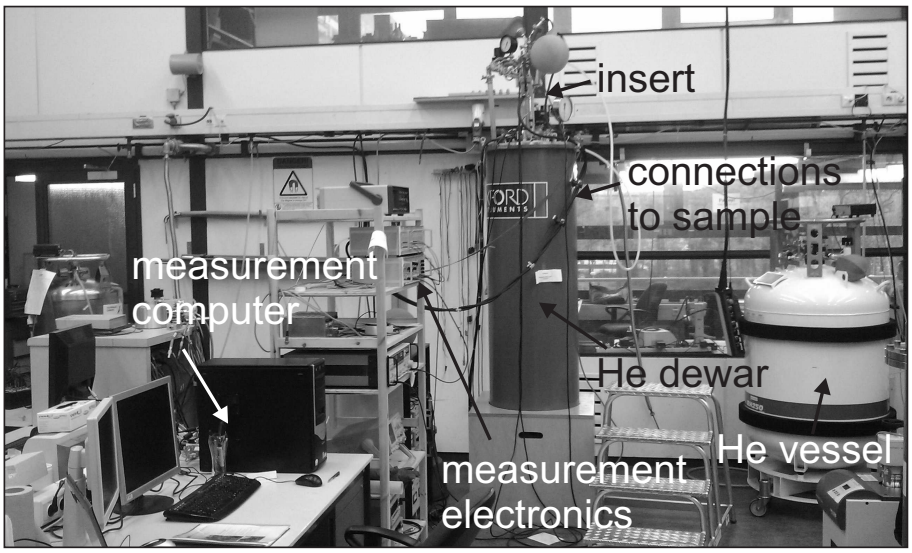

Figure 1.11: Photograph of the Heliox VL system, showing the measurement computer, the measurement electronics, the He dewar, the insert, the cable which connects the measurement electronics to the sample inside the system and a He vessel, used to fill the He bath.

1.7 Outline of this thesis

This thesis describes several experiments in hybrid organic/inorganic systems, in which electron transport and/or spin behavior is studied.

Chapter 2 starts with giving the basic concepts of organic electronics and spintronics, needed to understand the spin-valve experiments described in this thesis. The problems and obstacles for injecting a spin-polarized current into organic materials and the potential of using organic single-crystals in spintronic devices are discussed.

Different methods for fabricating organic single-crystal FET devices with FM electrodes are explained in chapter 3. First, the growth of organic single-crystals is discussed. Then, the fabrication of FM electrodes with shadow masks, photo- and e-beam lithography is explained.

Chapter 4 deals with the interface of fabricated FM electrodes and organic materials. UV photoemission spectroscopy and X-ray photoelectron spectroscopy are performed to study the energy level alignment in FM/organic thin film samples. The effect of the lithography processes on the spin injection properties of the FM electrode are investigated and a cleaning step applied to the interfaces is investigated.

In chapter 5, measurements on rubrene single-crystal FETs with FM/tunnel barrier electrodes are discussed. The critical spin-valve properties of these devices are investigated and it is shown that this FET has the potential of being used as a spin valve. The current flowing through the device can be fitted to a back-to-back Schottky model, which show that electrons are injected via a well-defined tunnel barrier fabricated on top of our FM electrodes.

A different fabrication method is discussed in chapter 6. Here, transferring Au electrodes to organic single-crystals by soft elastomeric stamps, with and without the facilitation of organic molecules, is investigated. Measurements in the space-charged-limited-current regime and on FET devices are presented and discussed.

FM nanoparticles (NPs), capped with organic ligands, are discussed in chapter 7. These NPs have the potential of being used for high-density data storage. A systematic study of the annealing of these NPs in solution at relative low temperatures is described. The annealing is needed to obtain high magnetocrystalline anisotropy. The low-temperature annealing leaves the organic ligands intact, which can be used for patterning.

In chapter 8 experiments performed on a two-dimensional organic spin system to study the interaction of the spins with their environment are discussed. The system consists of a thin Au film covered with a monolayer of molecules containing an unpaired spin. The signature of the Kondo effect, a local resistance minimum as a function of temperature, is observed under certain conditions. The behavior of this effect in the presence of a magnetic field is also investigated.

References

[1] W. Gerlach and O. Stern, Zeitschrift für Physik **9**, 353 (1922).

[2] W. Pauli, Z. Physik **43**, 601 (1927).

[3] K. K. Likharev, "Electronics below 10 nm" in *Nano and Giga Challenges in Microelectronics*, 27, Elsevier, Amsterdam (2003).

[4] W.J.M. Naber, S. Faez and W.G. van der Wiel, Journal of Physics D: Applied Physics **40**, R205 (2007).

[5] G. Szulczewski, S. Sanvito and M. Coey, Nature Mater. **8**, 693 (2009).

[6] V.A. Dediu, L.E. Hueso, I. Bergenti and C. Taliani, Nature Mater. **8**, 707 (2009).

[7] R. Farchioni and G. Grosso, *Organic Electronic Materials*, Springer-Verlag, Berlin (2001).

[8] G. Cuniberti, G. Fagas and K. Richter (eds.), *Introducing Molecular Electronics*, Springer-Verlag, Berlin Heidelberg (2005).

[9] H. Klauk (ed), *Organic Electronics: Materials, Manufacturing and Applications*, Wiley-VCH, Weinheim (2006).

[10] G.A. Prinz, Physics Today **48**, 58 (1995).

[11] G.A. Prinz, Science **282**, 1660 (1998).

[12] S.A. Wolf, D.D. Awschalom, R.A. Buhrman, J.M. Daughton, S. von Molnár, M.L. Roukes, A.Y. Chtchelkanova and D.M. Treger, Science **294**, 1488 (2001).

[13] S. Das Sarma, Am. Sci. **89**, 516 (2001).

[14] J.F. Gregg, J. Petej, E. Jouguelet and C. Dennis, J. Phys. D: Appl. Phys. **35**, R121 (2002).

[15] I. Zutič, J. Fabian and S. Das Sarma, Rev. Mod. Phys. **76**, 323 (2004).

[16] B.A. Bolto, R. McNeill and D.E. Weiss, Australian Journal of Chemistry **16**, 1090 (1963).

[17] C.K. Chiang, C.R. Fincher Jr, Y.W. Park and A.J. Heeger, Phys. Rev. Lett. **39**, 1098 (1977).

[18] H. Shirakawa, E.J. Louis, A.G. MacDiarmid, C.K. Chiang and A.J. Heeger, J. Chem. Soc. Chem. Commun. **16**, 578 (1977).

[19] A. Facchetti, Materials Today **10**, 28 (2007).

[20] C.W. Tang and S.A. van Slyke, Appl. Phys. Lett. **51**, 913 (1987).

[21] R.H. Friend, R.W. Gymer, A.B. Holmes, J.H. Burroughes, R.N. Marks, C. Taliani, D.D.C. Bradley, D.A. Dos Santos, J.L. Brédas, M. Lögdlund and W.R. Salaneck, Nature **397**, 121 (1999).

[22] C.J. Brabec, N.S. Sariciftci and J.C. Hummelen, Adv. Funct. Mat. **11**, 15 (2001).

[23] P. Peumans, S. Uchida and S.R. Forrest, Nature **425**, 158 (2003).

[24] D. Voss, Nature **407**, 442 (2000).

[25] C. Reese, M. Roberts, M.M. Ling and Z. Bao, Materials Today **7**, 20 (2004).

[26] S.R. Forrest, Nature **428**, 911 (2004).

[27] R.W.I. de Boer, M.E. Gershenson, A.F. Morpurgo and V. Podzorov, Phys. Stat. Sol. (a) **201**, 1302 (2004).

[28] V.C. Sundar, J. Zaumseil, V. Podzorov, E. Menard, R.L. Willett, T. Someya, M.E. Gershenson, and J.A. Rogers, Science **303**, 1644 (2004).

[29] C. Reese and Z. Bao, Materials Today **10**, 20 (2007).

[30] O.D. Jurchescu, J. Baas and T.T.M. Palstra, Appl. Phys. Lett. **84**, 3061 (2004).

[31] V. Podzorov, E. Menard, A. Borissov, V. Kiryukhin, J.A. Rogers and M.E. Gershenson, Phys. Rev. Lett. **93**, 086602 (2004).

[32] A. Aviram and M.A. Ratner, Chem. Phys. Lett. **29**, 277 (1974).

[33] M.A. Reed, C. Zhou, C.J. Muller, T.P. Burgin and J.M. Tour, Science **278**, 252 (1997).

[34] C. Dekker, Physics Today **52**, 22 (1998).

[35] T. Rueckes, K. Kim, E. Joselevich, G.Y. Tseng, C. Cheung and C.M. Leiber, Science **289**, 94 (2000).

[36] P. Avouris, Acc. Chem. Res **35**, 1026 (2002).

[37] C. Joachim, J.K. Gimzewski and A. Aviram, Nature **408**, 541 (2000).

[38] M. Menon and D. Srivastava, J. Mat. Res. **13**, 2357 (1998).

[39] M. Dresselhaus, G. Dresselhaus and P. Avouris (eds.), *Carbon Nanotubes: Synthesis, Structure, Properties, and Applications*, Springer, Berlin (2001).

[40] R.H. Baughman, A.A. Zakhidov and W.A. de Heer, Science **297**, 787 (2002).

[41] A.K. Geim and K.S. Novoselov, Nature Mater. **6**, 183 (2007).

[42] A.K. Geim, Science **324**, 1530 (2009).

[43] K.S. Novoselov, A.K. Geim, S.V. Morozov, D. Jiang, Y. Zhang, S.V. Dubonos, I.V. Grigorieva and A.A. Firsov, Science **306**, 666 (2004).

[44] H. Sirringhaus, P.J. Brown, R.H. Friend, M.M. Nielsen, K. Bechgaard, B.M.W. Langeveld-Voss, A.J.H. Spiering, R.A.J. Janssen, E.W. Meijer, P. Herwig and D.M. de Leeuw, Nature **401**, 685 (1999).

[45] C.D. Dimitrakopoulos and P.R.L. Malenfant, Adv. Mater. **14** 99 (2002).

[46] *see e.g.* http://www.polymervision.com

[47] W. Thomson, Proc. R. Soc. London **8**, 546 (1857).

[48] P.M. Tedrow and R. Meservey, Phys. Rev. B **7**, 318 (1973).

[49] M. Jullière, Phys. Lett. **54**, 225 (1975).

[50] J.S. Moodera, L.R. Kinder, T.M. Wong and R. Meservey, Phys. Rev. Lett. **74**, 3273 (1996).

[51] A.T. Filip, *Ph.D. Thesis*, Rozenberg, Groningen (2002).

[52] M.N. Baibich, J.M. Broto, A. Fert, F. Nguyen Van Dau, F. Petroff, P. Eitenne, G. Creuzet, A. Friederich and J. Chazelas, Phys. Rev. Lett. **61**, 2472 (1988).

[53] G. Binasch, P. Grünberg, F. Saurenbach and W. Zinn, Phys. Rev. B **39**, 4828 (1989).

[54] *Wall Street Journal* 10 november 1997, B8.

[55] D.D. Awschalom and M.E. Flatté, Nature Phys. **3**, 153 (2007).

[56] S. Sanvito and A.R. Rocha, J. Comput. Theor. Nanosci. **3**, 624 (2006).

[57] C.B. Harris, R.L. Schlupp and H. Schuch, Phys. Rev. Lett. **30**, 1019 (1973).

[58] V.I. Krinichnyi, Synth. Met. **108**, 173 (2000).

[59] F.J. Jedema, A.T. Filip and B.J. van Wees, Nature **410**, 345 (2001).

[60] P.A. Bobbert, W. Wagemans, F.W.A. van Oost, B. Koopmans and M. Wohlgennant, Phys. Rev. Lett. **102**, 156604 (2009).

[61] W.J. de Haas, J.H. de Boer and G.J. van den Berg, Physica **1**, 1115 (1934).

[62] J. Kondo, Prog. Theor. Phys. **32**, 37 (1964).

[63] A.C. Hewson, *The Kondo problem to Heavy Fermions*, Cambridge University Press, Cambridge (1997).

[64] I. Affleck and P. Simon, Phys. Rev. Lett. **86**, 2854 (20011).

[65] G. Bergmann, Phys. Rev. B **77**, 104401 (2008).

[66] J. Simonin, http://arxiv.org/pdf/0708.3604v1.pdf

[67] L.P. Kouwenhoven and L.I. Glazman, Physics World **14**, 33 (2001).

[68] M.A. Ruderman and C. Kittel, Phys. Rev. **96**, 99 (1954).

[69] T. Kasuya, Prog. Theor. Phys. **16**, 45 (1956).

[70] K. Yosida, Phys. Rev. **106**, 893 (1957).

[71] M. Ternes, A.J. Heinrich and W.D. Schneider, J. Phys.: Condens. Matter **21**, 053001 (2009).

[72] J.H. van Vleck, Phys. Rev. **41**, 208 (1932).

[73] S. Kremer, W. Henke and D. Reinen, Inorg. Chem. **21**, 3013 (1982).

Chapter 2

Concepts of organic spintronics

In this chapter, the properties and the relevant theoretical background of organic electronics and spintronics are discussed, introducing the key elements of these fields. To illustrate the concepts of these fields, and to present the state-of-art in the field of organic spintronics, several experiments showing spin-polarized transport in organic materials using electrical injection and detection are reviewed. Thin films, self-assembled monolayers, single-molecules, carbon nanotubes, C_{60} and graphene have been exploited to transport a spin-polarized signal. Other methods to show spin injection in organic materials, low-energy muon spin rotation and two-photon photoemission, are briefly discussed. The magnetic effect observed in organic materials without using ferromagnetic electrodes, named organic magnetoresistance (OMAR), is also mentioned. The problems and obstacles for spin injection in organic materials as encountered in the reviewed experiments will be discussed. It is argued that organic single-crystals are potentially suitable materials for spintronic applications.

Parts of this chapter have been published as W.J.M. Naber, S. Faez and W.G. van der Wiel, Journal of Physics D: Applied Physics **40**, R205 (2007).

2.1 Organic electronics

As already mentioned in chapter 1, organic materials open the way to cheap, light-weight, mechanically flexible, chemically interactive, and bottom-up fabricated electronics. Present-day electronics, however, is dominated by the Si/SiO_2 metal-oxide semiconductor field-effect transistor (MOSFET), where a gate voltage forms an inversion layer in between the source and drain electrodes of the transistor [1]. The ability to drastically change the carrier density in semiconductors by electrical gating is essential in electronics. Control of the carrier density by doping, usual in inorganic (extrinsic) semiconductors, is not straightforward for most organic semiconductors. The effect of doping only manifests itself at high doping levels, mainly because the purity of these materials is still too low as compared to electronic grade silicon [2]. As a consequence the behavior is more metallic than semiconducting. Therefore, in organic transistors the thin-film-transistor (TFT) geometry (see Fig. 2.1a) is used rather than that of the MOSFET. In an organic TFT, a conducting channel is capacitively induced at the interface between the dielectric and the organic material. The charge does thus not originate from dopants as in MOSFETs. Carriers are instead side-injected into the gate-induced conduction channel from the metallic electrodes. Electrical conduction in (disordered) thin films normally results from carrier hopping between localized states (see section 2.1.2), and not from band-like transport through delocalized states, as typical for inorganic semiconductors.

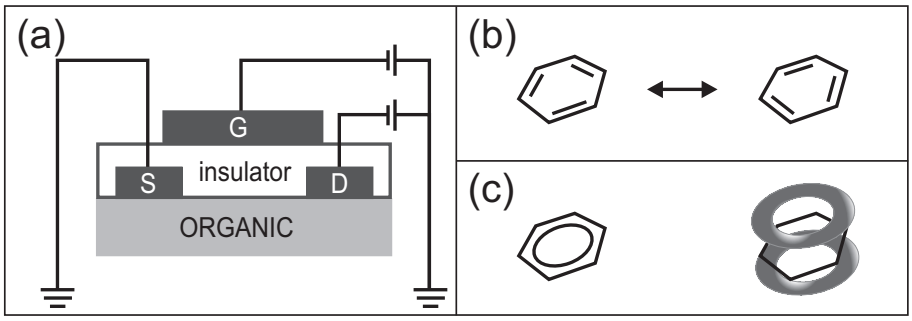

Figure 2.1: (a) Schematic layout of an organic thin-film transistor. The gate (G) electrode, which induces a conducting channel, is separated from the organic film by an insulator. The current through the organic material is injected and collected by source (S) and drain (D) electrodes. (b) Two equivalent configurations of benzene, showing the alternating single and double bonds. (c) Representation of benzene, showing the delocalized bonds (left) and the resulting electron π-clouds above and below the carbon ring.

Present-day organic semiconductors are mainly π-conjugated materials. These materials have a sequence of alternating single and double bonds in their molecules. As illustrated in Fig. 2.1b for benzene, different, but equivalent configurations exist for these alternating bonds. This effectively means that the wave function of one of the four valence electrons of carbon, which forms a π-bond with its neighboring electrons, is delocalized along the molecule, forming a π-cloud (see Fig. 2.1c). In this case, the mobility along one molecule can be rather high [3]. Next to the conduction within one molecule, also the interaction of a π-system with the π-system of a neighboring molecule determines the conductivity of the organic film [4]. The Peierls instability [5] causes that in practice all conjugated materials act as semiconductors, since the rearrangement of atoms leads to the formation of a band gap.

The transport through organic TFTs (OTFTs) is usually described using theory developed for MOSFETs [1]. According to this theory, the source-drain current I_{SD} through the OTFTs in the linear regime, when $V_G - V_{th} \gg V_{SD}$, where V_G is the gate voltage, V_{th} the threshold voltage and V_{SD} the source-drain voltage, is given by

$$I_{SD,lin} = \frac{W}{L}\mu C_i(V_G - V_{th})V_{SD}, \tag{2.1}$$

where W and L are the width and length of the conducting channel, respectively, μ the charge carrier mobility and C_i the capacitance of the gate dielectric. The current in the saturation regime ($V_G - V_{th} \ll V_{SD}$) becomes independent of V_{SD} and is given by

$$I_{SD,sat} = \frac{W}{2L}\mu C_i(V_G - V_{th})^2. \tag{2.2}$$

Although this gives a good description of some of the features of FETs made with high-purity organic single-crystals (see section 2.1.1) [6], it is not exactly known to what extent the MOSFET theory can be used for organic devices.

Besides electronic transport through organic thin films, also the idea was put forward to use single molecules as electrical components, such as switches and diodes. The latter field is often referred to as *single-molecule electronics* or *molecular electronics* [7]. Single molecules may eventually be the ultimately miniaturized electronic components, although still important issues remain to be solved [8].

2.1.1 Organic materials

Thin films

Organic thin films are usually divided in *polymers* and *small molecules*, with ∼1.5–3.5 eV band gaps [9]. The structure of polymer films is rather irregular (more or less 'spaghetti-like'), strongly limiting the carrier mobility. The maximum mobilities of polymer films are typically 0.1 $cm^2(Vs)^{-1}$ [2], although there are some reports of polymers with large crystalline regions and a relatively high mobility of 0.6 $cm^2(Vs)^{-1}$ [10, 11]. Despite the low mobility, the big advantage of polymer films is that there are well-developed deposition techniques available to process them.

More ordered films can be realized with small molecules, resulting in higher mobilities (∼1 $cm^2(Vs)^{-1}$) [12, 13]. One of the materials most commonly used for (p-type) OTFTs is pentacene with highest reported mobility of 6 $cm^2(Vs)^{-1}$ [14]. Most thin films of small molecules are grown by vapor deposition. The film-dielectric interface turns out to be of great importance for the performance of the OTFT and a lot of effort has been put in improving this interface, e.g. by introducing self-assembled monolayers [15].

Organic single-crystals

Ultra-pure organic single-crystals (OSCs) [16] of some materials can be grown nowadays, and their electronic properties are well-reproducible [17]. In OSCs grain boundaries are eliminated and the concentration of charge traps is minimized [18], making them suitable for studying the intrinsic electronic properties of organic materials and the physical limitations of organic FETs [19]. In contrast, thin films of polymers or small molecules are often strongly affected by imperfections of the film structure and by insufficient purity of the materials [20]. Recently, the electric mobilities increased substantially, reaching room-temperature values of 35 $cm^2(Vs)^{-1}$ in pentacene [21] and 40 $cm^2(Vs)^{-1}$ in rubrene [22].

Hall measurements in a rubrene single-crystal [23–25], probing the intrinsic mobility, even suggest diffusive bandlike transport at room temperature, with electronic states having a significant wave function overlap. This has to be stated with care, since the mean free path in these studies is comparable to the intermolecular distance. It has also been shown that models developed for inorganic devices show remarkable good results when used to describe the behavior of OSC devices [26].

OSCs can be deposited from solution [27], but the physical vapor transport (PVT) method [2, 28] gives much better results so far. The techniques for fab-

ricating OTFTs with as-grown OSCs have been reviewed in Ref. [17]. Recently, selective growth of OSCs on domains of octadecyltriethoxysilane was reported [29].

Carbon nanotubes

Transport in carbon nanotubes (CNTs) has attracted a lot of interest because of their exceptional electronic and mechanical properties [30]. They have been been proposed for many organic electronics applications [31–34]. CNTs are carbon cylinders of a few nanometers in diameter and up to several millimeters in length [30, 35, 36]. They were discovered by Sumio Iijima in 1991 [37]. The electronic behavior of CNTs can be metallic or semiconducting, depending on the chiral vector [30]. Single-walled carbon CNTs (SWCNTs) consist of a single carbon cylinder, whereas multi-walled CNTs (MWCNTs) are made up of multiple concentric cylinders. SWCNTs have been put forward as ideal 1D electronic systems in which Tomonaga-Luttinger-liquid (TLL) [38, 39] behavior should be observable. The small dimensions of CNTs also allows for the definition of a quantum dot (QD) inside the CNT [40].

Graphene

Graphene, a two-dimensional sheet of carbon atoms in a hexagonal lattice, is very interesting for electronic applications, because of its very high mobility (>10,000 $cm^2(Vs)^{-1}$ at room temperature and up to 250,000 $cm^2(Vs)^{-1}$ at 5 K) and other unique properties [41, 42]. Experimental research on graphene took off in 2004, when a single layer of graphene was isolated [43]. Graphene is a semi-metal (or zero-gap semiconductor), which can show both electron and hole conduction, depending on the position of its Fermi level. Because of the distinct electronic spectrum, charge carriers behave like mass-less particles, described by a Dirac-like equation. They can travel over large (submicron) distances without scattering. Due to the mass-less particles and low scattering, quantum effects in graphene can survive even at room temperature. The fact that the sheet is only one atom thick, makes it measurable by scanning probes, and easy to influence by nearby dielectrics and metals.

Single molecules

In a 1974 paper, Aviram and Ratner [44] introduced the concept of a molecular rectifier, based on the idea of 'donor-acceptor' systems already put forward in the 1940s by Mulliken and Szent-Györgi [45]. The first experimental study of

single-molecule conductance was reported by Reed *et al.* in 1997 [46]. One of the most important issues in single-molecule electronics is the contact of the molecule with (metal) electrodes [47]. Obviously the electrode spacing needs to be very small, typically in the order of 1 nm. The nature of the molecule-metal interface is of crucial importance to the transport properties [48]. Good mechanical contact does not automatically imply good electrical contact. End-group engineering offers the possibility to chemically anchor the molecules to metal electrodes. Apart from hooking up a single molecule to source and drain electrodes, effective gating of the molecule is rather difficult due to screening of the nearby metallic electrodes. Many different nano-contacting schemes have been developed over the last decade. Examples include mechanical break junctions [46], nanopores [49], electromigration [50] and conducting-probe atomic force microscopy [51].

2.1.2 Charge transport in organic devices

Hopping versus band transport

Charge injection and transport in organic materials are still not understood in full detail. In general, one can distinguish two main charge transport mechanisms: *hopping* and *band transport*. The hopping mechanism is typical for disordered materials such as organic thin films. Transport occurs via hopping between localized molecular states [52] and strongly depends on parameters like temperature, electric field, traps present in the material and the carrier concentration [17, 53–56]. This leads to a much smaller mobility than via delocalized band states, as in crystalline inorganic semiconductors [55]. Band-like conduction in organic materials is only expected at low temperature for highly ordered systems [57, 58], such as the OSCs mentioned before, when the carrier mean free path exceeds the intermolecular distance [16]. The valence band generally originates from the overlap of the HOMO levels, and the conduction band from the overlap of the LUMO levels of the molecules [59].

p-type and n-type conduction

It should be noted that the terms 'n-type' and 'p-type' in organic semiconductors do not have the same meaning as for inorganic semiconductors. In the inorganic case, 'n-type' ('p-type') refers to doping with electron donors (acceptors). In the organic case however, an 'n-type' ('p-type') material is a material in which electrons (holes) are more easily injected than holes (electrons) [2]. In organic semiconductors, p-type conduction is much more common than n-type

conduction, i.e. in most organic materials hole transport is favored. This has been explained by the fact that electrons are much more easily trapped at the organic-dielectric interface than holes [60, 61]. There are a few reports on n-type organic semiconductors [62–65], and also *ambipolar* organic materials (showing both p-type and n-type behavior, dependent on the gate voltage) [61, 66] have been identified. However, the electron mobility is generally considerably lower than the hole mobility. For electronic logic it would be favorable to combine n- and p-type organic materials to realize complementary circuitry (as in CMOS technology [1]).

Polarons

As the intermolecular (van der Waals) forces in organic materials are much weaker than the covalent and ionic bonds of inorganic crystals, organic materials are less rigid than inorganic substances [67]. A propagating charge carrier is therefore able to locally distort its host material. The charge carrier combined with the accompanying deformation can be treated as a quasi-particle called a *polaron* [68]. A polaron carries spin half, whereas two nearby polarons (referred to as a *bipolaron*) are spinless [69]. Polaron formation generally reduces the carrier mobility [57, 70–75]. It is more and more realized that electronic transport in organic materials is not only determined by the characteristics of the organic conductor itself, but also by the interplay with the adjacent dielectric layer [76–78]. It is therefore important to find a suitable conductor-dielectric combination [61].

Contacting

Apart from the conduction mechanism, also the charge injection into the organic material is of crucial importance for the performance of the device. The charge injection mechanism strongly depends on the interface between the electrode and organic material. This can involve impurities, structural defects, charging, dangling bonds, dipoles, chemical moieties and other effects, in which also the fabrication method of the device plays a significant role.

Carrier injection across the metal-organic interface is determined by the energy barrier height and the density of states (DOS) at the Fermi level (E_F) of the metal electrode [79, 80]. Contact resistance can be the result of a mismatch of the HOMO (for p-type semiconductors) or LUMO (for n-type semiconductors) with respect to the work function of the electrode metal. The resulting Schottky barrier gives rise to non-linear (diode-like) behavior. The interface resistance depends exponentially on the barrier height, and linearly on the DOS of the metal

electrode at E_F.

The Schottky barrier at the interface between a metal and organic semiconductor usually directly scales with the metal work function, as opposed to the case of inorganic semiconductors, where the Schottky barrier only weakly depends on the metal work function [9, 81]. Hence, low-work-function metals such as Ca are used to inject electrons, and high-work-function metals such as Au or InSnO (ITO) are used to inject holes into an organic semiconductor.

Since organic materials in general are rather fragile, conventional contacting methods can easily damage the material, causing a bad interface between the material and the electrode. A number of techniques have been developed for non-destructively contacting, including soft lithography (e.g. micro transfer printing) [82–84], ink-jet printing [85], solution-based methods [86, 87] and vapor phase deposition [88, 89]. The interface properties are especially important for spin injection, as is discussed in more detail in section 2.2.3.

Single-molecule transport

Transport through a single molecule is very different from bulk transport. At sufficiently low temperatures transport can be dominated by Coulomb blockade and quantum confinement effects [90–93]. In the simplest model only transport through one molecular level is considered. When this level is between the Fermi levels of the two leads, current will flow [94]. A more accurate method which is by far most used is the non-equilibrium Green's function (NEGF) method [95].

A number of methods has been developed for calculating transport [96–102]. Some of these [96–98, 100], are also applicable for spin-polarized transport, e.g. in molecular spin valves, consisting of a molecule sandwiched between two nanoscale ferromagnetic (FM) electrodes [103]. Rocha *et al.* [104] showed that it is possible to obtain a very high spin-dependent signal. They used the code SMEAGOL [96] (spin and molecular electronics in an atomically generated orbital landscape). This code combines the NEGF method with the density-functional-theory code SIESTA (Spanish initiative for electronic simulations with thousands of atoms) [105]. The code SMEAGOL is especially designed for spin-polarized transport.

Emberly and Kirczenow [106] have theoretically reproduced experiments on a gold break junction bridged with benzenedithiol molecules with a semi-empirical model. They extended this model to break junctions formed by nickel, and systems with a nickel STM tip scanning a nickel substrate covered with a bezenethiol monolayer. In both cases they find spin-valve behavior with this model.

2.2 Spin-polarized current models

In this section, the concepts of tunnel magnetoresistance (TMR) and giant magnetoresistance (GMR), as already shortly mentioned in chapter 1, are discussed. These models are widely used to describe transport in organic spintronic devices. Some problems in (organic) spintronics, the conductivity mismatch problem, spurious effects and spin relaxation, are also reviewed here.

2.2.1 Tunnel magnetoresistance

TMR (see chapter 1) originates from the difference between the Fermi surfaces of spin-up $N_\uparrow(E_F)$ and spin-down $N_\downarrow(E_F)$ electrons. Given the conservation of spin orientation during tunneling, electrons can only tunnel from a given spin subband in the first FM electrode to the *same* spin subband in the second FM electrode, as schematically depicted in Fig. 2.2. The tunnel rate is proportional to the product of the corresponding spin subband DOS at E_F, and hence on the relative magnetization orientation of the electrodes. Consequently, the resistance in the parallel (P) configuration (Fig. 2.2a and c) is usually lower than in the anti-parallel (AP) configuration (Fig. 2.2b and d).

Based on the work of Tedrow and Meservey [107], assuming spin and energy conservation, Jullière [108] derived a compact expression for the difference in resistance between the P and AP configurations, the TMR ratio¶

$$TMR \equiv \frac{R_{AP} - R_P}{R_P} = \frac{G_P - G_{AP}}{G_{AP}} = \frac{2P_1P_2}{1 - P_1P_2}, \tag{2.3}$$

where $R_{P(AP)}$ is the resistance in the P (AP) configuration, $G_{P(AP)}$ the conductance in the P (AP) configuration, and $P_{1(2)}$ the polarization of the first (second) FM electrode with

$$P_i = \frac{N_{i\uparrow}(E_F) - N_{i\downarrow}(E_F)}{N_{i\uparrow}(E_F) + N_{i\downarrow}(E_F)}, \qquad i = 1, 2. \tag{2.4}$$

Although the Jullière model gives a good basic insight, it cannot explain a number of experimental observations like the dependence on temperature, bias voltage, tunnel barrier material, and the height and width of the barrier [109]. A model incorporating all these effects is still lacking.

The Jullière model treats the FM electrodes as independent, and is only valid for a square barrier. In real devices, the carrier wave functions from both FM

¶ Note that the following, alternative, definitions of the TMR ratio are also frequently used: $TMR' \equiv \frac{R_{AP}-R_P}{R_{AP}} = \frac{2P_1P_2}{1+P_1P_2}$, and $TMR'' \equiv 2\frac{R_{AP}-R_P}{R_{AP}+R_P} = 2P_1P_2$.

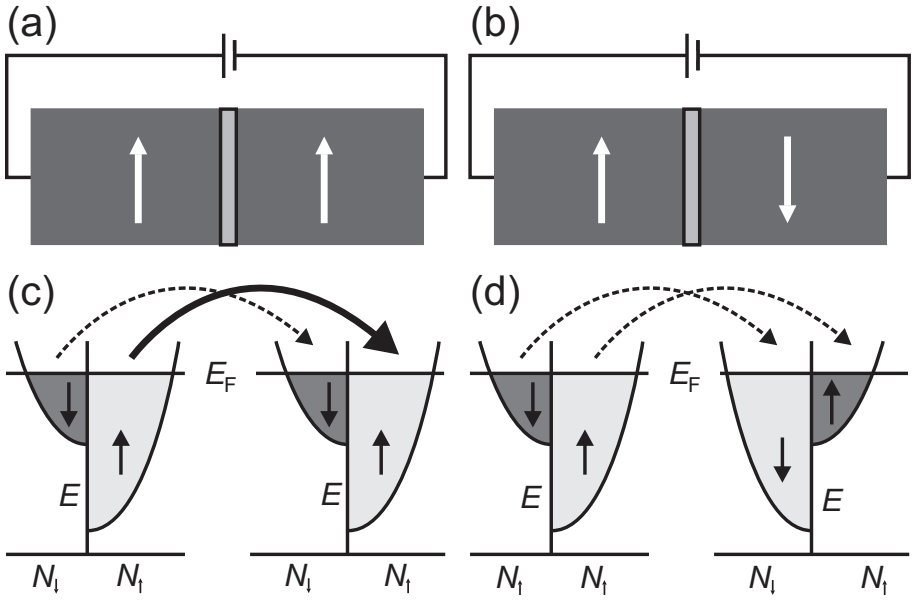

Figure 2.2: (a) Schematic representation of a TMR device, consisting of two FM materials (dark gray) separated by a tunnel barrier (light gray). The magnetization can be parallel (a) or anti-parallel (b), denoted by the arrows. Spin subbands of the FM materials are given for the parallel (c) and anti-parallel magnetization (d). The dashed (solid) arrow represents low (high) spin current.

electrodes overlap, and a finite bias voltage gives a non-square barrier shape. Slonczewski [110] altered the Jullière model, taking into account the permeability of both barriers, resulting in an overlap of the wave functions inside the barrier. Although Slonczweski's model is more realistic, it does not account for either the temperature and voltage dependence of the TMR ratio. Vacuum tunnel barriers give MR with very little V-dependence [111]. Based on this result, two-step tunneling through localized states in the tunnel barrier has been put forward as a possible explanation for the V- and T-dependence, as well as for negative TMR values [112–114].

Room-temperature TMR ratios up to 600% have been realized [115], sufficiently large to make TMR hard disk read heads [116] and 16 MB Magnetic Random Access Memory (MRAM) [117] commercially attractive. Since TMR relies on tunneling through the non-magnetic (NM) layer, and not on transport as in GMR (see next section), one can apply insulating organic layers as spacer. A self-assembled monolayer (SAM) of alkanethiols has for example been used for this purpose [118] (see also section 2.3.1).

2.2.2 Giant magnetoresistance

The basic layout of a GMR device has already been presented in Fig. 1.2. Analogous to the MTJ discussed above, an external magnetic field is used to switch the relative magnetic orientations of the FM layers from P to AP, or vice versa. The P configuration usually, but not necessarily, has a lower resistance. Although the working of the device seems relatively simple, the GMR effect was not predicted and its underlying principles are not straightforward. Before it was explained that TMR is *directly* related to the DOS asymmetry between the FM electrodes on both sides of the tunnel barrier. GMR is also related to a different DOS for both spin subbands, but in a more indirect fashion. As in the case of TMR, spin-flip scattering (i.e. the change of spin-up to spin-down, or vice versa) is assumed to be negligible. This turns out to be a very good approximation on the timescale of the dissipative processes that give rise to electrical resistivity [119]. The lack of interchange between both spin species makes it possible to treat their transport in terms of two independent transport channels, a model referred to as the *two-channel model* introduced by Mott [120–122]. All conductors are assumed to be in the diffusive limit, i.e. the electron mean free path is much shorter than the typical dimensions of the conductors. This assumption normally holds for organic conductors. However, in the case of carbon nanotubes (CNTs) transport can be ballistic.

When a FM electrode is connected to a NM material and a current is driven through the system, the spin-up current is different from the spin-down current, due to the current polarization in the FM (see also Fig. 2.3). A finite magnetization builds up in the NM material, which is known as *spin accumulation* [123]. The spin accumulation is defined as the difference between the electrochemical potential for spin-up electrons, $\mu_\uparrow$, and that for spin-down electrons, $\mu_\downarrow$. The magnitude of the spin accumulation depends on the spin injection rate into the normal material and the spin relaxation time, and it decays exponentially away from the injecting electrode on a length scale set by the spin relaxation length l_s

$$\mu_\uparrow - \mu_\downarrow \propto \exp(-l/l_s), \tag{2.5}$$

where l is the distance from the injecting electrode. The net spin density resulting from the spin accumulation is typically orders of magnitude smaller than the charge density in the NM. However, the spin accumulation in the NM can be probed by a second FM electrode, the spin detector, if it is placed at a distance smaller or comparable to the spin relaxation length l_s from the spin injector.

A finite spin accumulation implies different densities of spin-up and spin-down carriers at the site of the detector interface. The transmission is now

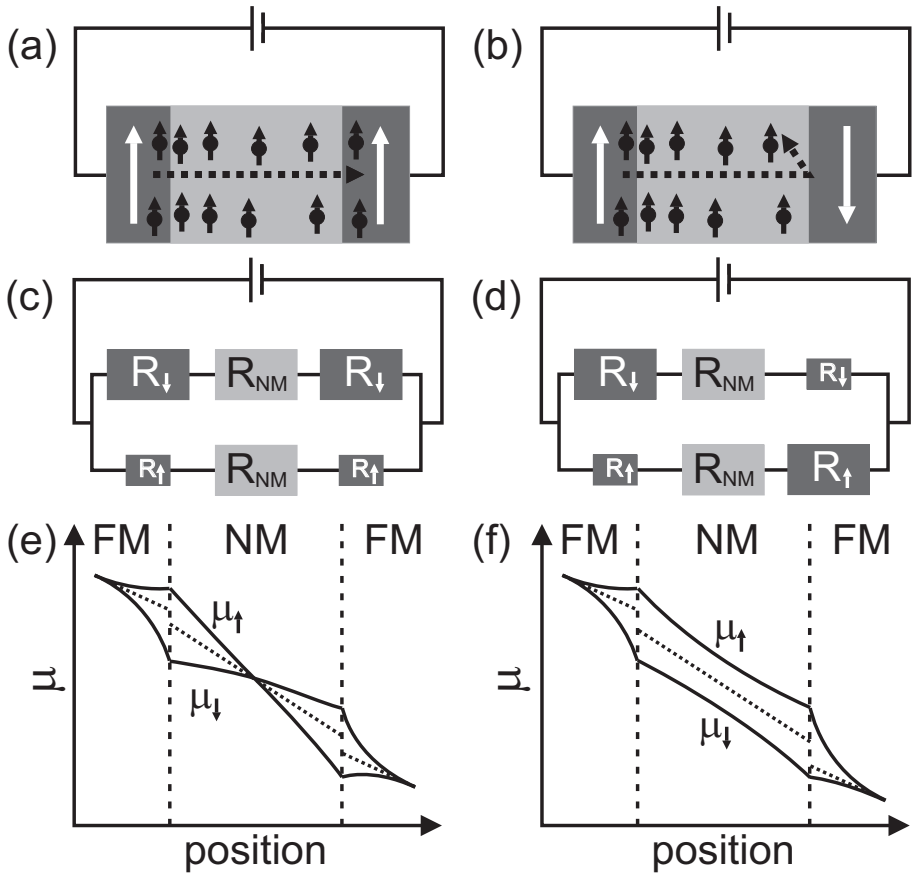

Figure 2.3: Schematic representation of a GMR device consisting of two FM electrodes (dark grey) separated by a spacer (light grey) for the P (a) and AP configuration (b). The magnetization of the FM electrodes is denoted by the white arrows. The dotted arrows represent the spin current. The corresponding resistor model is given for the P (c) and AP configuration (d). The colors correspond to the layers in (a) and (b), and bigger resistors represent a larger resistance for the denoted spin species. The electrochemical potentials μ for the two spin species are given for the P (e) and AP configuration (f). The dotted lines are the asymptotes of the electrochemical potentials to which they would collapse at large distances. The dashed lines correspond to the interfaces in (a) and (b).

largest when the magnetization of the detector electrode is parallel to the net spin accumulated at its interface. GMR can also be described in terms of a parallel resistor model, as shown in Fig. 2.3c and d. A more thorough theoretical description of GMR based on the Boltzmann equation, has been provided by Valet and Fert [124]. With their model, the electrochemical potentials of the two spin species can be calculated, as illustrated in Fig. 2.3e and f. It reveals the splitting of the electrochemical potentials at the interfaces of the FM electrodes and NM material. It also shows the different voltage drop (represented by the discontinuity of the asymptote) at the interfaces for the P and AP configuration, which leads to the difference in resistance between these two cases. As the spin accumulation decays exponentially from the injector, the GMR ratio depends exponentially on the distance between injector and detector. This feature is very useful for determining the spin relaxation length l_s in (organic) materials.

2.2.3 Conductivity mismatch

A fundamental obstacle for spin injection from a FM metal into a semiconductor is the so-called *conductivity mismatch problem* [125–131]. The conductivity of a semiconductor is usually much lower than that of a metal. In a spin valve, one likes to detect the resistance change due to the different magnetization orientations in the FM layers. If the resistance of the whole device is dominated by the resistance of the semiconductor spacer, the overall resistance change is negligible. This can also be seen from the resistor model in Fig. 2.3. When the resistance of the NM material, R_{NM}, is much larger than the other resistances, this dominates the overall resistance and no change is observed. This is particularly relevant for organic spintronics, since most organic materials are much less conductive than the FM electrodes.

There are two possible solutions to this problem. The first one is to use a fully spin-polarized FM material, i.e. a *half-metal* such as $LaSrMnO_3$ (LSMO) [132, 133]. In a half-metal, only one spin subband is occupied at the Fermi level and the spin polarization P therefore approaches 100% at low temperatures. In the case of LSMO ($T_C \sim 370$ K), there is a fully polarized conduction band of 3d character at E_F, and no s band. Even if the bulk properties of a material indicate half-metallic behavior, it is not *a priori* clear, however, whether the spin polarization can efficiently be transferred across the interface with a NM material. The maximum electrode spin polarization value observed in magnetic tunnel junctions (MTJs) with LSMO is 0.95 [133]. LSMO electrodes have been applied in spin-valve devices with CNTs and organic thin films.

Another possible solution for the conductivity mismatch problem, is the intro-

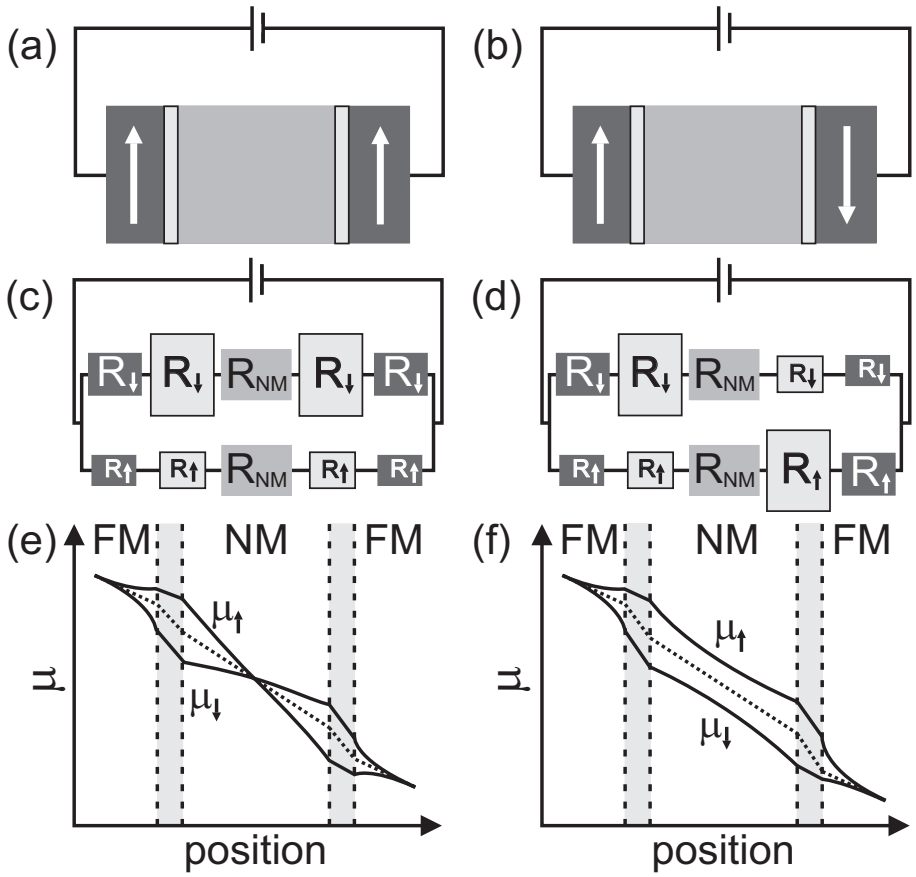

Figure 2.4: Schematic representation of a GMR device consisting of two FM electrodes (dark grey) separated by a spacer (light grey) and tunnel barriers (light grey with black outline) for the P (a) and AP configuration (b). The corresponding resistor model is given for the P (c) and AP configuration (d). Colors correspond to the different parts in (a) and (b). The electrochemical potentials μ for the different spin species are given for the P (e) and AP configuration (f). The dotted lines are the asymptotes of the electrochemical potentials to which they would collapse at large distances. The dashed lines correspond to the interfaces in (a) and (b).

duction of a large spin-dependent resistance [125, 129–131]. This spin-dependent resistance could be a tunnel barrier in between the FM electrode and semiconductor spacer. This spin-dependent resistance gives a larger change in resistance between the P and AP configuration, as can be visualized by the resistor models in Fig. 2.4c and d. In the model by Valet and Fert this will lead to a larger spin splitting at the interface and a larger difference in the voltage drop over the whole device for the two configurations (see also Fig. 2.4e and f).

2.2.4 Spurious effects

Injecting and detecting spins in a NM material is not trivial, as is apparent from the discussion of the conductivity mismatch problem above. In this section, a number of phenomena (or 'spurious effects') are discussed that can give rise to MR effects, but are not related to (but are easily mistaken for) the TMR and GMR effects described above. For the correct interpretation of organic spintronic experiments, it is crucial to take these effects into account.

The Lorentz force curves the electron trajectories and has a (positive) MR effect on the order of $(l_e/l_B)^4$, where $l_B = \sqrt{h/(eB)}$ is the magnetic length [134]. *Lorentz magnetoresistance* (LMR) is relevant for systems with a relatively large mean free path, such that $\omega_c\tau > 1$, where ω_c is the cyclotron frequency and τ the elastic scattering time [135]. In systems where transport takes place by hopping, a magnetic field can enhance the localization of the carriers on the hopping sites, thereby also increasing the resistance [136].

In the coherent, diffusive transport regime, conductance can be affected by a magnetic field via electron interference phenomena such as *weak localisation* (WL) and *universal conductance fluctuations* (UCF) [137]. WL is interpreted as coherent backscattering and gives rise to an enhanced resistance around $B = 0$, where the width of the resistance maximum is determined by the (charge) coherence length, l_ϕ. UCF are of the order e^2/h, regardless of the sample size and the degree of disorder (hence the name 'universal'). UCF result from the microscopic change in electron interference paths due to a change in E_F, impurity configuration or enclosed magnetic flux.

Another MR effect that is not caused by spin accumulation in the NM material is the *local Hall effect*. Stray fields coming from the FM electrodes can penetrate the NM spacer and induce local Hall voltages. When the magnetization of the FM electrodes changes, so do the Hall voltages [138, 139]. In this way, these voltages can obscure the true spin-valve signal.

In small systems, such as CNTs, where Coulomb charging effects are relevant, the *magneto Coulomb effect* (MCE) can play a role [140]. Due to this effect, the conductance in a system connected to two FM leads, changes as a function of magnetic field, but not due to spin accumulation. In a FM electrode, the spin subbands are shifted by the Zeeman energy in opposite direction under the influence of an external magnetic field. As the DOS at E_F in a ferromagnet is in general different for both spin species, repopulation of the electrons takes place through spin-flip scattering. This gives a shift in the chemical potential [141]. When the FM electrodes are connected to large NM leads, the change in chemical potential in the FM electrodes causes electrons to flow across the

FM/NM interface. This leads to a change in the dipole layer at the interface. The voltage change can couple to the conductor in between the two FM leads via the capacitance and therefore effectively acts like a gate. As the magnetization of the FM material switches its direction at the coercive field, the conductance changes discontinuously at this field due to the MCE. The MCE can therefore easily be mistaken for the spin-valve effect in small structures [140].

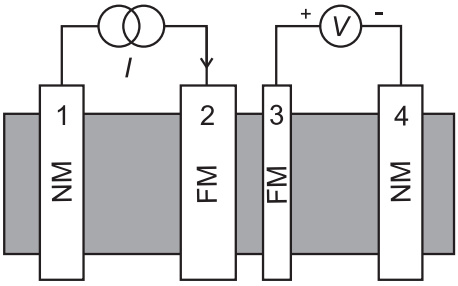

Figure 2.5: Non-local geometry for measuring spin accumulation. A current is driven between electrodes 1 and 2, while the voltage is measured between electrodes 3 and 4. When electrode 2 is FM, a spin-polarized current is injected. The spins diffuse in both directions and can therefore be probed by electrode 3, which is also FM. Therefore a voltage difference is observed between the parallel and antiparallel state of the two FM electrodes. As the measured voltage is not influenced by the charge current, the signal is purely due to spin accumulation.

In principle, it is possible to calculate the magnitude of the above spurious effects or measure them in control devices [142]. However, a more elegant and rigorous way to rule out the discussed effects is to measure spin accumulation using the so-called *non-local geometry* of Fig. 2.5 [123, 143]. A current is injected by two electrodes, while the voltage is measured by two other electrodes. When at least two electrodes are FM, the spin accumulation can be probed in such a way that the measured spin diffusion is isolated from the current path. In this way, the measured signal is only due to pure spin accumulation.

2.2.5 Spin relaxation

The spin relaxation time, τ_s, or spin lifetime, is given by

$$\frac{1}{\tau_s} = \frac{1}{\tau_{\uparrow\downarrow}} + \frac{1}{\tau_{\downarrow\uparrow}}, \tag{2.6}$$

with the spin flip time $\tau_{\uparrow\downarrow}$ indicating the average time for an up-spin to flip to a down-spin, and $\tau_{\downarrow\uparrow}$ for the reverse process. The spin relaxation time is a key

parameter in spintronic devices, as it sets the timescale – and hence the length scale – for loss of spin polarization. The spin relaxation length, l_s, is related to the spin relaxation time as

$$l_s = \sqrt{\frac{\tau_s}{4e^2 N(E_F)\rho_N}}, \tag{2.7}$$

in the case of a NM metal or a degenerate Fermi gas semiconductor [125, 144]. Here e is the electron charge, $N(E_F)$ the DOS at the Fermi level E_F, and ρ_N the resistivity of NM spacer material. For a semiconductor in the non-degenerate regime, l_s is given by [125, 144]

$$l_s = \sqrt{\frac{k_B T \tau_s}{2ne^2\rho_N}}, \tag{2.8}$$

where k_B is the Boltzmann constant, T the temperature, and n the total number of carriers.

In general, one can distinguish two classes of spin relaxation. The first one describes the decay of a net spin component along the axis of spin quantization, which is defined as the z-axis. The z-component (or *longitudinal* component) of the total spin, S_z, decays exponentially to equilibrium due to individual spin flips on a timescale T_1. This T_1 is equal to the spin relaxation time τ_s, defined in Eq. 2.6. As this process requires energy exchange with the environment, it is a rather slow process. There is a second process, however, that does not require energy exchange and affects the spin component perpendicular to the quantization axis, i.e. the *transverse* component $S_\perp$. This process affects the quantum-mechanical phase of individual spins and leads to loss of *coherence* on a timescale T_2. For different spins within an ensemble the phases are in general affected unequally, which results in the spins getting out of phase. The timescale related to this process of ensemble dephasing is often denoted as T_2^* [145–147]. Usually $T_2^* < T_2$, an effect referred to as *inhomogenous broadening*. The time evolution of a spin ensemble with total spin $\mathbf{S}$[§] in an external magnetic field $\mathbf{B}$ along the z-axis can then be described by the Bloch equations

$$\frac{dS_z}{dt} = \gamma(\mathbf{B}\times\mathbf{S})_z - (S - S_z)/T_1 \tag{2.9}$$

$$\frac{dS_\perp}{dt} = \gamma(\mathbf{B}\times\mathbf{S})_\perp - (S - S_\perp)/T_2^*, \tag{2.10}$$

where γ is the gyromagnetic ratio.

§ The symbol $\mathbf{S}$ is used for the resultant spin vector of a spin ensemble, whereas $\overrightarrow{S}$ is used for denoting an individual spin vector.

In the next sections, the underlying mechanisms for spin relaxation in solids will be discussed, divided in mechanisms related to spin-orbit coupling and to hyperfine interaction. Spin-orbit coupling is expected to be small, but not completely negligible for most organic materials. Hyperfine interaction might not be negligible [148], although it is sometimes argues to be small [149]. The dominant relaxation mechanisms in organic materials are still rather unclear. There are a few reports where the spin relaxation length is determined from fitting to Jullière's formula (see section 2.2.1), but it is hard to distinguish between spin relaxation at the interfaces and within the organic material itself. Also, the simple Jullière formula is not always very appropriate for the applied device configurations.

Spin-orbit coupling

Spin-orbit coupling is a relativistic effect, describing the interaction between the electron's spin and its orbital motion around an atomic nucleus. More generally, spin-orbit coupling occurs whenever a particle with non-zero spin moves in a region with a finite electric field. In the rest frame of a particle moving at a relativistic velocity, a static electric field Lorentz-transforms in a field with a finite magnetic component. Thus, although the spin degree of freedom only couples to a magnetic field, it is indirectly affected by an electric field via spin-orbit coupling. The electrical field can have various physical origins, such as the electric field of an atomic nucleus or the band structure of a solid [150].

As spin-orbit coupling generally grows with atomic number Z (it scales as Z^4 in the case of an hydrogen-like atom [149]), and organic materials consist mainly of low-Z materials (in particular C), spin-orbit coupling is usually small in organic materials. Sulphur atoms could provide a considerable spin-orbit coupling, but these atoms normally play a marginal role in carrier transport in organic materials [151]. Depending on the exact band structure of the organic material, spin-orbit coupling is actually not always negligible [152].

In (inorganic) solids one can distinguish two main contributions to spin-orbit coupling. The first one, termed the *Dresselhaus contribution*, occurs in crystals that exhibit bulk inversion asymmetry, which implies that there is a net electric field for certain crystal directions [153, 154]. The second one, referred to as the *Rashba contribution*, occurs in systems with net electric fields due to structural inversion asymmetry [129, 155]. Three different spin-orbit-coupling-related spin relaxation mechanisms can be distinguished in non-magnetic solids: Elliot-Yafet (EY), D'yakonov-Perel (DP), and Bir-Aronov-Pikus (BAP).

The EY mechanism [156] is due to the fact that under the influence of spin-orbit coupling momentum eigenstates are no spin eigenstates anymore. Any

momentum scattering event has hence a finite probability to flip the spin. The EY mechanism leads to a spin relaxation time τ_s that is proportional to the momentum scattering time. Momentum scattering is mainly caused by impurities at low temperature and phonons at high temperature [157]. Usually EY is the dominant mechanism in metals, and it has been recently claimed to be dominant in organic semiconductors as well [158, 159].

The DP [154] mechanism arises when the solid lacks a center of symmetry, and is therefore directly related to the Dresselhaus contribution. As the internal magnetic field is $\overrightarrow{k}$-dependent, the axis around which the spin precesses is randomized upon electron (momentum) scattering. This results in a loss of memory of the initial spin direction. Heavy scattering slows down the spin relaxation, because the spin cannot follow the internal magnetic field when it changes too rapidly. Therefore, the spin relaxation time is inversely proportional to the scattering time.

The BAP [160] mechanism is caused by electron-hole exchange interaction, and therefore only plays a role in systems where there is a large overlap between the electron and hole wave functions.

The spin-orbit-coupling-related relaxation mechanisms directly affect T_1, and indirectly T_2.

Hyperfine interaction

Another source for spin relaxation is the hyperfine interaction. It originates from the interaction of the electron spin with the nuclear spins of the host material. In general, the electron spin interacts with many, say N, nuclear spins. The electron-nuclear coupling Hamiltonian is then given by

$$H_{hyp} = \sum_{i}^{N} A_i \overrightarrow{I_i} \cdot \overrightarrow{S}, \tag{2.11}$$

where $\overrightarrow{I_i}$ and $\overrightarrow{S}$ are the spin operator for nucleus i and the electron spin, respectively, and A_i the coupling strength between them.

The nuclear spins affect the spin relaxation time T_1 by means of so-called electron-nuclear flip-flops. In addition, fluctuating nuclear spins also result in dephasing, thus affecting T_2. For an electron spin interacting with N nuclear spins, the statistical fluctuation scales with $1/\sqrt{N}$ [146, 161]. Hence the more delocalized the electron wave function is, the less is the influence of the nuclei.

The nuclear spins in organic materials are mainly originating from the isotopes ^{1}H ($I = 1/2$), ^{13}C ($I = 1/2$), and ^{14}N ($I = 2$). The isotope ^{13}C has a 1.1% abundancy, while the isotope ^{12}C has nuclear spin zero.

2.3 Spin injection in organic materials

In this section, experiments on organic spin valves are discussed where the spacer between the FM electrodes is formed by organic thin films, self-assembled monolayers (SAMs) or single molecules. Although this thesis is not focused on fullerenes, spin injection in carbon nanotubes (CNTs), C_{60} and graphene will also be discussed in this section since they are important from a historical viewpoint. Fullerenes combine a high carrier velocity ($\sim 10^6$ m/s) with a potentially very long τ_s. It is therefore no surprise that the field of organic spintronics took off with work on CNTs. The fabrication of fullerenes devices is still challenging however, whereas easy fabrication methods exists for thin films.

2.3.1 Spin injection in organic thin films

Giant magnetoresistance

The first report of spin injection in an organic semiconducting film are the experiments by Dediu *et al.* [162], in which two LSMO electrodes in a lateral geometry were used to inject a spin-polarized current in sexithienyl (T_6) (see Fig. 2.6a and b for the device layout). As the coercive fields of the LSMO electrodes are the same, they do not succeed in switching the magnetization of each FM electrode independently but find a negative *MR* of ∼30% by changing the electrode orientation from random, at low field, to parallel at higher field. A rough estimate of $l_s = 200$ nm is made, which leads to a spin relaxation time $\tau_s \sim 1$ μs, when a mobility of 10^{-4} cm^2(Vs)$^{-1}$ [163, 164] is used.

To obtain P and AP magnetization, Xiong *et al.* [165, 166] fabricated a vertical device with different electrode materials. The organic material 8-hydroxyquinoline aluminium (Alq_3) was sandwiched between LSMO (bottom electrode) and Co (top electrode) (see the left inset of Fig. 2.6c). The evaporation of the top Co electrode causes pinholes and Co inclusions in the Alq_3 layer over a distance of ∼100 nm. Although the Co/Alq_3 interface is therefore poorly defined, they found an *MR* of -40% at 11 K (right inset of Fig. 2.6c), and made an estimate for the spin relaxation length l_s of ∼45 nm, using an adjusted Jullière model. The negative MR is ascribed to the negative spin-polarization of the Co d-band. The temperature dependence (Fig. 2.6c) is dominated by spin relaxation in Alq_3 (and not by the temperature dependence of the magnetization of the LSMO), as confirmed in spin-valve devices where LSMO is replaced by Fe [167] and by photoluminescence measurements.

Room-temperature spin-valve behavior was claimed in similar devices consisting of LSMO/P3HT/Co [168] and LSMO/P3OT/LSMO [169]. P3HT is poly(3-

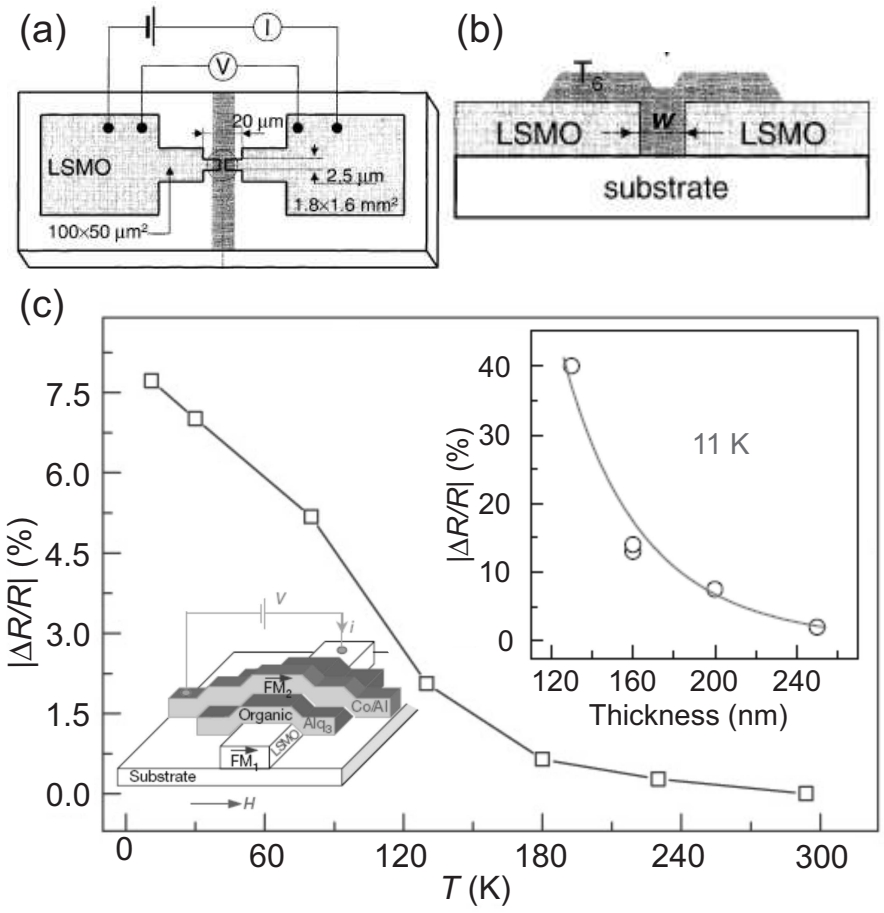

Figure 2.6: Schematic top view (a) and cross section (b) of a hybrid LSMO/T_6/LSMO junction. Typical dimensions are given in the figure. (c) *MR* as a function of temperature for a vertical LSMO/T_6/Co device measured at a voltage of 2.5 mV for an Alq_3 thickness of 160 nm. Left inset: schematic picture of an organic spin-valve device. Right inset: *MR* as a function of thickness at a temperature of 11 K. The line through the data points is a three parameter fit to an adjusted Jullière model. Reprinted from [162] and [165].

hexyl thiophene) and P3OT is poly(3-octylthiophene), both semiconducting π-conjugated polymers. For FeCo/P3HT/NiFe spin valves, a small MR value at room temperature was reported [170]. The MR value decreased with increasing layer thickness, as is expected when the MR depends on the spin relaxation length l_s in the organic semiconductor.

The Co/organic interface was optimized by Dediu *et al.* [171]. This experiment included a tunnel barrier between the Co electrode and Alq_3 in a vertical

LSMO/Alq_3/Co device, to obtain a well-defined interface without Co inclusions. They used Al_2O_3 and LiF as a tunnel barrier in their devices. The influence of the fabrication of the top electrode in vertical devices was further emphasized by Shimada *et al.* [172]. In a vertical Fe/pentacene/Co:TiO_2 spin valve they deposited the top Fe electrode by different methods, and found very different behavior of the MR, which they ascribed to the difference in kinetic energy of the Fe particles.

Wang *et al.* [173] argued that LSMO can not be used for spin injection at room temperature. In vertical devices with different organic materials sandwiched between LSMO and Co, they found a negative *MR* of 10–18% at 14 K, which vanishes at 220 K. They conclude that this is due to the vanishing interface polarization of LSMO. However, by optimizing the LSMO interface, Dediu *et al.* [171] achieved room temperature *MR* of -0.15%. The MR follows the magnetization of LSMO, which vanishes at 325 K. Dediu *et al.* also provided an alternative explanation for the negative MR observed in this kind of devices. They argued that transport of spin-polarized electrons occurs via the LUMO level in Alq_3 which is aligned with the spin-down bands in LSMO and Co, while spin-up electrons are injected when a voltage is applied.

Positive MR has also been measured in Alq_3 devices [174]. In this paper, Liu *et al.* report MR values of 9% and 1% at 80 K and 290 K, respectively, in a Fe/Alq_3/Co device with an organic layer of 46 nm. The MR value decreases with thicker organic layers, though the large variability makes it hard to estimate the spin relaxation length l_s. Using the Jullière model they find a spin relaxation length of l_s of $\sim$43 nm at 80 K. By measuring the interface properties by X-ray reflectivity and polarized neutron reflectometry, they find that a larger MR value corresponds to a sharper Co/Alq_3 interface and a magnetically dead layer at the Fe/Alq_3 interface. They thereby relate the microstructure of the interface to the observed MR. The magnetically dead layer could act as a tunnel barrier to overcome the conductivity mismatch.

Spin injection in rubrene thin film has been demonstrated by Shim *et al.* [175]. With a Co/Al_2O_3/rubrene/Fe spin-valve device they claimed to measure tunnel currents, although the thickness of the rubrene is 4-16 nm, larger than the typical tunnel thickness. This could indicate spin injection into the rubrene layer. Shim *et al.* found a spin relaxation length l_s of $\sim$13 nm in this amorphous organic material, which leads to their prediction that it could be in the order of mm in rubrene single-crystal.

Spin injection in *nanowire* devices has been demonstrated by Pramanik *et al.* [158]. They measured ensembles of Co/Alq_3/Ni nanowires and observed a MR effect of about 1% at low temperature. From their estimate of the spin relaxation

length l_s by the Jullière model they calculated the spin relaxation time, which turns out to be extremely long. Values between a few milliseconds and a second are obtained, depending on what value is taken for mobility in the Alq_3, which is not exactly known.

The experiment by Pramanik *et al.* [158] is the only experimental work so far that addresses the question which spin relaxation mechanism is dominant in organic semiconductors. It is argued that the D'yakonov-Perel (DP) [154] mechanism is proportional to the carrier mobility, whereas the Elliot-Yafet (EY) [156] mechanism has an inverse dependence. Since it is more likely that the mobility has decreased in the nanowires as compared to bulk Alq_3, due to more Coulomb scattering at surface states, comparison between their results and that of Xiong *et al.* [165] gives an indication that the EY mechanism is dominant. However, the comparison is made between to completely different experiments and the mobility is not explicitly measured. Therefore, more studies, also in different organic systems, will be necessary to tell whether this conclusion is generally valid.

Tunnel magnetoresistance

Santos *et al.* [176] demonstrated spin-polarized *tunneling* through a thin Alq_3 barrier sandwiched between a Co (bottom) and $Ni_{80}Fe_{20}$ (permalloy, Py) electrode (top) at *room temperature*. *I-V*- and polarization measurements indicate the good quality of the Alq_3 barrier without any Co inclusions. The TMR value was improved by an Al_2O_3 layer in between the Co and the Alq_3 tunnel barrier, which reduced the formation of interfacial charge states. The highest *TMR* they found at room temperature is 6%. They argued that the negative *TMR* observed in other devices was not because of the negative polarization of the Co d-band, as proposed by Xiong *et al.*, but might originate from the opposite spin asymmetry coefficients of Co and LSMO.

TMR has also been claimed by Xu *et al.* [177] in Alq_3 and tetraphenyl porphyrin (TPP) sandwiched between LSMO and Co electrodes. Although they deposited relatively thick films of ∼20 nm, the film is not uniform and tunneling probably occured at spots with a thin film layer in the order of a few nm. For both materials they found an MR value of -15% at 80 K, which decreases to 0 at 300 K. Szulczewski *et al.* [178] observed TMR in CoFeB/MgO/Alq_3/Co devices with values around 12% at room temperature for different thicknesses (2–8 nm) of Alq_3. They estimated the spin relaxation in the hopping regime, for thicknesses larger than 4 nm, to be much larger than 10 nm. Recently, very large MR values in the order of 300% have been detected in LSMO/Alq_3/Co nanosized tunnel

junctions [179].

Wen *et al.* [180] have shown MR in a granular system of Co nanoparticles in a P3HT matrix. They found an MR value of 3% for 17 vol % Co at 10 K.

2.3.2 Spin injection in single-molecule devices and SAMs

In the search for miniaturization of electronic functional devices, molecular monolayers, and eventually single molecules are the ultimate limit. The spintronic properties of such systems are not explored extensively yet, but a few interesting studies are discussed below.

Using time-resolved Faraday rotation spectroscopy, Ouyang and Awschalom demonstrated coherent spin transfer of photo-excited carriers between semiconductor quantum dots through conjugated molecules at room temperature [181]. Their devices consisted of multilayer CdSe QDs solids that were bridged by 1,4-benzene-dimethanethiol, and they showed that the spin transfer efficiency is ∼20%.

Pasupathy *et al.* [182] have observed the Kondo effect [183, 184] in single C_{60} molecules connected to two Ni electrodes. Different shapes of the electrodes allowed for independent switching of their magnetization. The Kondo behavior was confirmed by the dependence of the conductance on the temperature and the magnetic field. TMR values of -38% and -80% are found, much larger than the predicted value of 21% by the Jullière model, which is explained by the fact that for AP magnetization, the Kondo resonance occurs closer to the Fermi energy, thereby enhancing its conductance.

The first transport measurements on a spin valve involving a single molecular layer were reported by Petta *et al.* [118]. The device was a nanometer-scale magnetic tunnel junction in the nanopore geometry [185, 186], consisting of a SAM of octanedithiol (100–400 molecules) sandwiched in between Ni electrodes. The majority of the octanedithiol devices had resistances larger than h/e^2, implying tunneling transport. Both positive and negative *MR* up to 16% was reported for low bias voltage at 4.2K, rapidly decreasing with bias voltage and temperature. The largest MR was measured for the most resistive devices. Using $P_1 = P_2 = 0.31$ for Ni, one found a *TMR* of 21%, somewhat larger than the experimentally observed MR values. Several test devices were done in order to rule out artifacts of the fabrication process. Localized states in the SAM tunnel barrier could possibly explain the anomalous behavior. Also the observed telegraph noise may be due to imperfections in the molecular barrier.

2.3.3 OMAR

There have been a number of studies – mainly by Mermer, Wohlgenannt and coworkers – reporting a considerable MR effect in organic semiconductor devices *without* FM electrodes, referred to as "organic magnetoresistance" (OMAR) [134, 136, 169, 187–189]. Although this is not a pure spin injection phenomenon, this effect is briefly discussed here, as it is a magnetic effect in organic materials and, besides being interesting on its own, might be important for spin injection experiments, since it can be superimposed on the MR resulting from spin injection. In experiments on the polymer polyfluorene (PFO) [187], the small molecule Alq_3 [188] and several more π-conjugated polymers and small molecules [136], it was shown that this OMAR [defined as $\Delta R/R = [R(B) - R(0)]/R(0)$] is quite universal in nature, can be either positive or negative, and reaches values up to 10% for $B \sim 10$ mT at room temperature. OMAR is shown to be related to the bulk resistance of the organic film [187, 188]. Depending on the organic material, OMAR obeys the empirical law $\Delta R(B)/R \propto B^2/(B^2 + B_0^2)$ or $\Delta R(B)/R \propto B^2/(|B|+B_0)^2$, where $B_0 \approx 5$ mT in most materials [136], increasing with spin-orbit coupling. The effect is only weakly dependent on temperature, is independent of magnetic field direction and impurities, and it typically decreases with increasing voltage and carrier density [187, 188]. The OMAR effect has also been observed in pentacene single-crystals by Nishioka *et al.* [190]. Between 150 and 300 K, they observed a small OMAR effect of 0.57% at 9 T.

Several models have been put forward to explain the physics underlying the OMAR effect. Prigodin *et al.* [134] proposed a model to explain OMAR based on the assumption that charge transport in organic semiconductors is electron-hole recombination limited. It is argued that in the space-charge-limited transport regime, both electrons and holes are injected (possibly with very different mobilities). The electron and holes can form electron-hole (e-h) pairs, that are either in the singlet (S) or triplet (T) state. It was shown that the space-charge-limited current density increases with decreasing e-h recombination rate. As the recombination rate depends on the degree of mixing between S and T states, the recombination rate – and hence the current density – becomes B-dependent. However, the experimental fact that OMAR is weakly dependent on the minority carrier density and also occurs in heavily p-doped devices and devices with only unipolar transport is not in agreement with this model. Therefore, exciton models are not believed to give a full explanation for the OMAR effect.

Hyperfine interaction as the cause of OMAR has been put forward by Sheng *et al.* [189, 191]. A model based on the hyperfine interaction has been developed by Bobbert *et al.* [192, 193]. In these papers, OMAR was explained by hopping,

which is restricted by Pauli blockade. Hopping from a single occupied (SO) state to another SO state, forming a double occupied (DO) state, is not allowed when the spins are parallel, due to the Pauli principle. The chance of a hopping event is therefore proportional to the singlet probability of two SO states. Applying an external magnetic field sets a global quantization axis for the spins of the carriers. Without this magnetic field, the spins are quantized along a local axis, set by the local hyperfine field. In absence of the magnetic field, hops are allowed between all SO sites with a certain probability. Due the global quantization axis in the presence of a magnetic field, Pauli blockade decreases the number of hopping events. Monte Carlo simulations based on this theory show good agreement with measured data.

The bipolaron model by Bobbert *et al.* is supported by several experimental papers by the group of Koopmans. They relate the voltage induced sign change of OMAR to the existence of two different OMAR channels [194], one giving a positive and the other one giving a negative contribution. These two channels might be the electrons and holes, which have a different response to the magnetic field. The sign change that occurs at the onset of bipolar charge transport [195], also supports the bipolaron model and it is shown that the bipolaron model can qualitatively explain the observed sign change of the OMAR effect with temperature [196].

More research is needed to give a theory describing all the phenomena associated with OMAR.

2.3.4 Spin injection in carbon nanotubes

Spin injection in multi-wall carbon nanotubes

The first organic spintronic devices ever were multi-wall CNT (MWCNT) contacted by Co electrodes on top using e-beam evaporation, made by Tsukagoshi *et al.* [197] (see Fig. 2.7a and b). A large resistance spread in these devices could be attributed to CoO or resist remnants at the Co/CNT interface. The two electrodes are nominally the same, but the authors argue that AP alignment is possible due to local magnetization fluctuations on the scale of the MWCNT diameter (30 nm). An *MR* of 9% is observed at 4.2 K (Fig. 2.7c – e), which disappears at 20 K, ascribed to the poor interface quality. In other devices [198, 199] a negative MR is observed above 20 K, which could be due to CoO [199] or the negative spin-polarization of the Co d-band. Based on one electrode separation, they found a spin relaxation length of 130 nm, estimated from the Jullière model and neglecting the interfaces. For comparison, no MR is observed in devices with

only one FM electrode [200]. Similar devices had been tested by other groups [201–204]. Although MR behavior has been repeatedly reported, there is a lack of consistency both qualitatively and quantitatively.

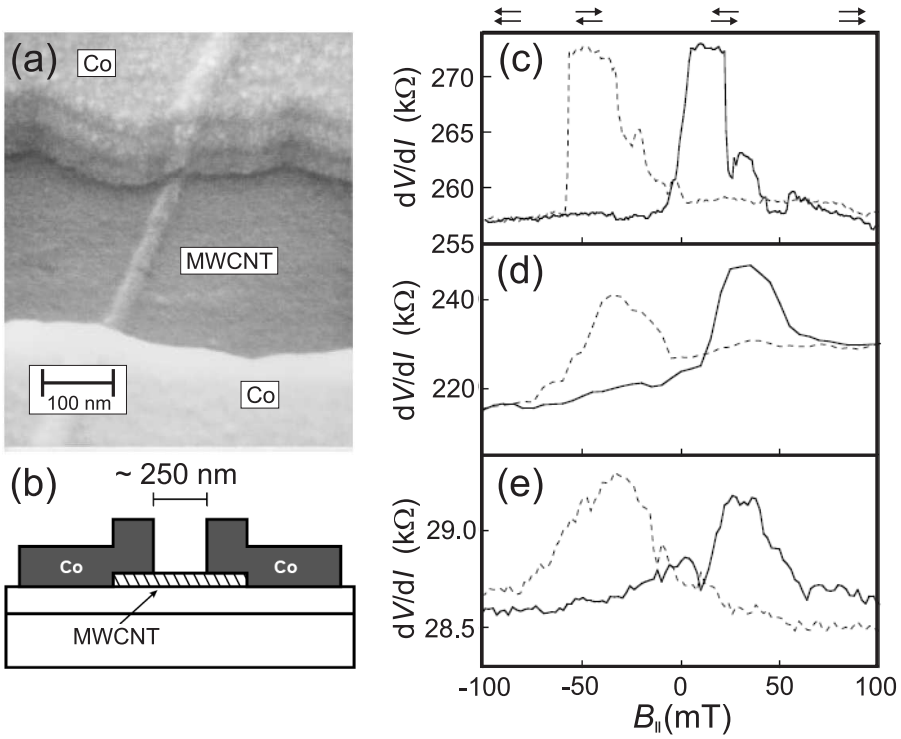

Figure 2.7: (a) Scanning electron microscope picture and (b) schematic diagram of a device, consisting of a MWCNT connected by two Co electrodes, fabricated by EB lithography and thermal evaporation. The two-terminal differential resistances of three different MWCNT devices at 4.2 K are given in (c), (d) and (e). The magnetic field is parallel to the substrate and the obtained MR values are (c) 6%, (d) 9% and (e) 2%. The arrows at the top of the graph denote the magnetization of the left and right electrode. Reprinted from [197].

Devices with electrodes of different materials were measured by Orgassa *et al.* [201]. Co and NiFe was evaporated on top of SMCNTs, resulting in a maximum 2.2% negative and 0.6% positive *MR* below 30 K for 2 out of 10 devices. Using the Jullière model they found a spin relaxation length of 380 nm, based on one electrode spacing. It is likely that also in this experiment the growth conditions of the electrodes dominated the device performance. A very large *MR* was reported by Zhao *et al.*, claiming 30% and -36% [202] *MR* in Co/MWCNT/Co devices at 4.2 K. Their fabrication method is very much like Tsukagoshi's and a wide

range of device resistances is reported as well. The *MR* disappears above 10K. At low temperature non-linear transport is observed, possibly caused by Coulomb blockade in the ∼200 nm long devices.

More reliable, low-ohmic $Pd_{0.3}Ni_{0.7}$ electrodes have been fabricated by Sahoo *et al.* [205, 206]. The low contact resistance avoids charging effects and hence the magneto-Coulomb effect. The *MR* varies between -5% and 6% at 1.85 K, depending on the gate voltage. This behavior is consistent with quantum interference [207], which is substantiated in the discussion of their SWCNT experiment in the next section.

A very large *MR* of 61% at 5 K was observed in devices with MWCNT dispersed onto pre-fabricated LSMO electrodes by Hueso *et al.* [208, 209]. The *MR* vanished at 120 K, which is a higher temperature than measured in CNT devices by other groups. A spin relaxation time of 30 ns and length of 50 μm was found. In their devices, the MWCNT/LSMO interface behaved like a tunnel barrier .

Spin injection in single-wall carbon nanotubes

The first SWCNT spin valve was reported by Kim *et al.* [210]. Evaporated and annealed Co electrodes were weakly coupled to the SWCNT, leading to a possible tunnel barrier at the interface and quantum-dot behavior in the CNT. No *MR* was observed for low-ohmic contact, which might be due to the conductivity mismatch. A maximum *MR* of 3.4% was measured at 0.2 K. Based on one electrode separation, they found a spin relaxation length of 1.4 μm at 4.2 K. This is however not very reliable, since devices with smaller electrode spacing showed a higher MR value.

Jensen *et al.* [211] fabricated SWCNT contacted by Fe electrodes. The contact resistance in these devices is large when compared to devices with pure Au electrodes. They report an *MR* of 100% at 300 mK and of 60% at 4.2 K.

The same group also fabricated a fully semiconducting device, with SWCNT fully encapsulated in epitaxially grown (Ga,Mn)As, having a Curie temperature of 70 K [212, 213]. At 0.3 K, a reproducible MR sign alternation was found as function of the gate voltage. High MR ratios of the order of 100% have been reported. Somewhat troublesome, hysteretic MR was also found for devices with only one FM electrode. Jensen *et al.* cannot provide an explanation for the large MR, the sign change and the fact that MR also shows up with one FM electrode.

Sahoo *et al.* [206] measured quantum-dot behavior at 1.85 K in a SWCNT contacted by PdNi electrodes. They found that the sign of *MR* changes on each conductance resonance and varied between -7% and 17%, which is an order of magnitude lower than observed for SWCNT contacted by non-magnetic materi-

als. The oscillatory behavior could be explained by combining the spin-dependent Breit-Wigner formula for resonant tunneling through a QD coupled to FM electrodes [214–216] with the Jullière TMR expression [108].

As opposed to the Coulomb blockade regime described above, Man *et al.* [217] have investigated a SWCNT connected to *highly transparent* PdNi electrodes. In this regime, the SWCNT device acted like a Fabry-Pérot (quantum) interferometer. The observed *MR* with a maximum of 4% at 4.2 K oscillated with gate voltage in phase with the resistance, which excluded magneto-Coulomb effects and could be fitted with a model based on the Landauer-Büttiker picture. Oscillations as a function of the bias voltage were also seen, and could be understood in terms of the model.

In order to eliminate spurious MR effects Tombros *et al.* used a 4-terminal, non-local geometry to measure spin accumulation in SWCNTs [218]. The non-local geometry allows to separate the spin and charge currents and this was successfully applied to inorganic (metallic) systems before [123, 143, 219] (see also Fig. 2.5). Co electrodes were evaporated on top of the SWCNT and resulted in low-ohmic contact. Importantly, Tombros *et al.* conclude that in their only working device the MR in conventional, two-terminal measurements (also applied in all experiments discussed so far) is dominated by spurious effects. It is concluded that 90% of the MR in the two-terminal measurement cannot be attributed to spin accumulation. Spin accumulation hence seems to be easily overshadowed by spurious effects.

2.3.5 Spin injection in C_{60}

In addition to CNTs, also spin transport through C_{60} films has been studied. Zare-Kolsaraki and Micklitz [220–224] studied MR in granular films of Co clusters mixed with C_{60} molecules. MR is observed in films with a Co fraction between 0.23 and 0.32. The highest MR they measured is around 30% at 4K and drops to a few percent at 60K. Miwa *et al.* [225] studied the same system, but performed ex-situ measurements (i.e. not under vacuum conditions as in the case of Zare-Kolsaraki and Micklitz), allowing for better characterization of their device. Good-quality devices give a MR of 8% at 4.2K and around 0.1% at room temperature.

2.3.6 Spin injection in graphene

Spin injection in graphene has also been reported. Hill *et al.* [226] measured a MR signal of 10% in a device consisting of a graphene sheet in between two

large NiFe electrodes. They relied on imperfections in the electrodes to have different switching fields. A more elaborate study of spin injection in graphene has been reported by the group of van Wees [227–229]. In a non-local geometry, they observed spin injection from Co/Al_2O_3 electrodes. The spin signals were relatively independent of temperature in a range from 4 K to room temperature. By performing Hanle spin precession experiments and fitting this to the one-dimensional Bloch equations, they extracted a spin relaxation length l_s between 1.5 and 2 μm. By improving their fabrication techniques, they predicted to get a higher mobility (2000 $cm^2(Vs)^{-1}$ in the device used) and thereby a larger spin relaxation length l_s.

Spin injection in graphene using a non-local geometry has also been reported by Ohishi *et al.* [230]. Using Co electrodes, they observed a non-local spin signal at room temperature. Permalloy electrodes were used for spin injection in at most two layers of graphene in a non-local measurement by Cho *et al.* [231]. At 20 K and 300 K, they observed a non-local spin signal. At the lower temperature, they observed changes in the magnitude and the sign of the spin-valve signal, which they attributed to quantum interference effects.

2.3.7 Two-photon photoemission and low-energy muon spin rotation

Direct observation of spin injection (i.e. not relying on electrical detection) is not straightforward. Common time-resolved techniques, in which spins are created and detected by short pulses of polarized light, rely on strong spin-orbit interaction, which is usually low in organic materials. However, two different techniques, which do not rely on electrical detection, have been developed to observe spin injection in organic materials.

Cinchetti *et al.* [232] investigated the spin injection efficiency from Co thin films into copper phthalocyanine (CuPc) and the spin relaxation length l_s in this organic semiconductor using spin-resolved two-photon photoemission. A photon generates a spin-polarized electron in the Co film, which has a chance to cross the Co/CuPc interface and reach the CuPc surface. Here, photoemission can occur when a second photon is absorbed. The energy and spin of these photoemitted electrons were measured and by comparing with the values for the bare Co film, information about the spin injection efficiency can be extracted. At room temperature, a spin injection efficiency of 85% and a spin relaxation length l_s of $\sim$13 nm are found. Improvement can be achieved by reducing the energy of the photoemission, since electrons are excited far above the LUMO energy, giving higher scattering rates than electrons in transport measurements [233].

The spin relaxation in an electrically functional spin valve, consisting of FeCo/LiF/Alq_3/TPD/NiFe (TPD: N-N'-diphenyl-N-N'-bis(3-methylphenyl)-1,1'-bi-phenyl-4,4'-diamine), was measured by Drew *et al.* [234]. Spin-polarized muons were implanted in the Alq_3 to study the spin polarization of the charge carriers. A spin relaxation length l_s of ∼35 nm was found for a temperature of ∼10 K. The low value can be explained by the imperfect injection efficiency of the measured device [233].

2.4 Discussion of organic spin valves

Spin relaxation length

MR has been reported in a few organic thin films at different temperatures. Although the mobilities in these materials are rather low, reasonably large spin relaxation lengths (100–200 nm) and accompanying large spin relaxation times (1 μs) have been reported. These values are however still rough estimates.

For CNTs, MR is only observed at low temperatures with a maximum of 120 K [209]. Reasonably long spin relaxation times (up to 30 ns) and lengths (1.4–50 μm) have been derived. The spin relaxation length in graphene is 1.5–2 μm at room temperature.

A few experimental studies exist on spin transport through a SAM or single molecule. These experiments are very interesting from a fundamental point of view and could provide more information about tunneling and transport mechanisms in organic spintronic devices.

Most spin relaxation lengths reported so far for organic devices are comparable to metals and inorganic semiconductors. The largest relaxation length [209] is however an order of magnitude larger than electrically detected in GaAs (6 μm) [235] and almost two others of magnitude larger than that measured electrically for metals (around 1 μm at 4.2 K and several hundreds of nm at room temperature [143]). However, these values have to be considered with care. Most of the time, the relaxation length is obtained with a modified Jullière model for only one electrode spacing and does therefore not account for spin relaxation at the interface. Moreover, the non-local measurement scheme has only been used to determine the spin relaxation length in CNTs and graphene.

The general trend of the spin relaxation time and length for different materials is shown in Fig. 2.8. As can be seen in the figure, the organic materials cluster in the top-left corner, having a large spin relaxation time τ_s, but a small relaxation length l_s. Improving the mobility in organic materials and the properties of the FM/organic interface (see below) could lead to larger spin relaxation lengths.

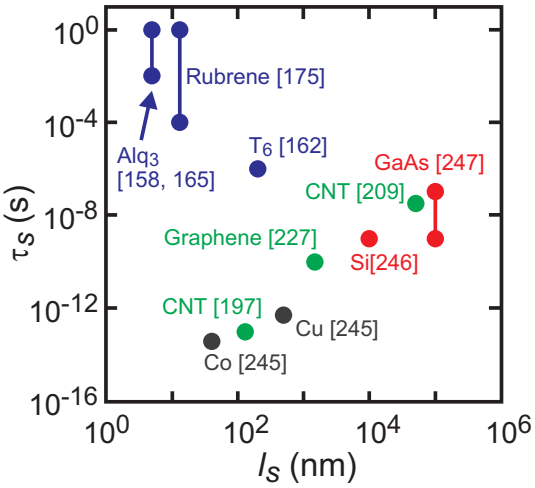

Figure 2.8: Spin relaxation length l_s vs. spin relaxation time τ_s for various materials. References are given in the figure. Reprinted from [237].

Spin injection and relaxation models

Spin injection and transport

Obtaining any definite conclusions about the spin injection efficiency and the spin relaxation length in organic spin valves is hard since widely used spintronic theories are developed for purely inorganic devices. The transport in these inorganic devices can be described by band transport and the spin relaxation is dominated by the spin-orbit coupling. Hybrid inorganic/organic devices are however completely different. Due to the difference between the metal FM electrode and the organic material, no clear model about spin injection has been developed yet. The transition from a delocalized band structure in the metal to strongly localized states in the organic material leads to a symmetry breaking and the failure of commonly used models for spin injection in fully inorganic devices. It has to be noted that besides (theoretical) research on spin injection in organic materials, charge injection in organic materials is also not fully understood yet. Progress has been made over the recent years [236], but open questions remain and further research on the transport properties will also help to describe spin transport.

Transport in organic conductors is in general described by hopping between strongly localized state. Only very pure and ordered organic materials show signs of band transport at low temperatures. Spin polarized currents through hybrid organic/inorganic devices are usually described by tunneling across the inorganic/organic interface, followed by hopping through strongly localized states

in two different conducting channels, the HOMO and/or LUMO levels of the organic material (see also section 2.1.2). Besides this, also interface states and interface dipoles [237] and defects in the organic material have to be taken into account. Moreover, due to the strong electron-phonon interaction, also transport by polarons has to be considered. This is also important for spin injection, since the formation of bipolarons (two nearby polarons) can occur. Singlet bipolarons have no spin and the spin-polarized current is only carried by polarons.

For the conduction via bipolarons Ren *et al.* [238] theoretically found, like in the case of inorganic semiconductors, an increase of the spin polarization when the conductivity of the organic material approaches or surpasses the conductivity of the FM material, or when a spin-dependent interface resistance is introduced. The influence of the bipolarons in their calculations is not drastic. When there are only bipolarons the spin polarization is of course zero, but when the fraction of polarons is only 20%, the spin polarization is 90% of the value attainable with only polarons and no bipolarons. However, Xie *et al.* [239] showed the importance of the electron-phonon coupling by using a Su-Schrieffer-Heeger model. They showed that spin injection into organic polymers could be absent, depending on the applied voltage and the FM material.

For spin transport through single molecules, a number of methods has been developed [96–100], as already explained in section 2.1.2. The code SMEAGOL [96] is especially designed for spin-polarized transport.

Spin relaxation

As already mentioned, spin relaxation in inorganic materials is dominated by spin-orbit coupling. This effect is however small in organic materials, due to the low weight of the atoms involved, carbon and hydrogen. It has been proposed that the relaxation occurs due to the hyperfine interaction with the hydrogen nuclei, as is described by Bobbert *et al.* [240] and fitted to experiments by Schoonus *et al.* [241]. They described the relaxation of the spin by a precession of the spin around an effective local magnetic field. This field is set by the external magnetic field and the effective field originating from the hyperfine field, which can be in the order of 5 mT. During hopping, the hyperfine field is a random field at each hopping site, leading to different precession directions and a depolarization of the spins.

In summary, the study of spin injection, transport, and relaxation in organic materials is still in its infancy. There is still a lot to learn about the role of the transport mechanism (band or hopping conduction, polaronic transport) on spin

transport. Also for finding the relevant spin relaxation mechanisms in organic materials, more theoretical and experimental work is needed.

Interfaces

Interfaces are very important in spintronic devices [237]. Following the different results in similar organic spin-valve devices, which might originate from the irreproducability of the interfaces, this is especially true for hybrid organic/inorganic spintronic devices. Evaporated materials could damage the organic material at the interface and possible reactions of the organic molecules with the metal can occur, as illustrated by the metal inclusions and pinholes found in the organic material by Xiong *et al.* [165] and the very different results obtained by Shimada *et al.* [172] when using different fabrication methods. Possible reactions with metal electrodes might explain the popularity of LSMO in organic devices (besides the fact that is a half-metal), since it is chemical very stable.

Krompiewski [242] has shown that the GMR in a CNT depends on the detailed properties of the interface. Especially the introduction of an oxide layer in between the metal and the CNT, of which the coupling is assumed to be antiferromagnetic (as in the case of CoO, but also for NiO and FeO), can drastically influence the GMR ratio. The influence of the detailed structure of the interface on GMR in thin film devices has been discussed by Liu *et al.* [174].

Progress has been made by introducing a tunnel barrier between the organic layer and FM electrode [171], but the fabrication of a top electrode could still damage the soft organic materials. This damaging has even been proposed to account for a non-volatile electric memory effect in a vertical organic spin-valve structure [243].

The concept of conductivity mismatch is also a widely accepted theory, when injecting a spin-polarized current from metal FM electrodes into a semiconducting channel. As a solution, introducing a tunnel barrier in between the two materials has been proposed. However, organic devices with a direct contact between the metal electrode and organic material have also shown spin-valve behavior. The explanation of this can lie in the fact that a tunnel or Schottky barrier is formed between the metal and organic material, which is for example measured by Liu *et al.* [174].

In conclusion, the interface properties of the FM/organic interface are not (yet) fully under control. More research, and maybe different fabrication methods are needed to obtain very clean and sharp interfaces, without damaging the soft organic materials.

Device layout and measurements

The most popular geometry for organic thin films spin valves is by far the vertical device structure. The reason is probably the ease of fabrication by evaporating thin layers on top of each other. Different materials for the top and bottom electrode (ensuring different switching field) can easily be deposited and thin organic channels can easily be fabricated. Only one lateral device has been reported for organic thin film spin valves [162], but the data of this device are hard to interpret, since there is no way of comparing parallel and anti-parallel magnetization of the FM electrodes. The OMAR effect has been suggested as the origin of the observed effect in this study [165].

The vertical devices have also a few drawbacks. Length dependence is hard to study, since it is not straightforward to compare completely different devices which have to be made to obtain different organic layer thicknesses. Especially the variation of the MR value for different devices, which might by due to the irreproducibility of the organic/inorganic interface, seems to be a big problem in this case.

Besides this, the vertical 2-terminal devices also exclude the possibility of non-local measurements. These measurements would be a good way to show spin injection without any MR signal that comes from spurious effects. However, non-local MR has only been measured in lateral graphene and carbon nanotubes devices. Another way of confirming spin injection would be to perform a Hanle-type experiment. However, thus far this has only been demonstrated in (lateral) graphene spin valves.

2.5 Organic single-crystals for spintronics

Given the problems described above, in this section it is argued that lateral devices made of Co/Al_2O_3 electrodes and a OSC spacer are possible candidates for electrical spin injection and detection in organic materials.

A first problem in organic materials is the relatively low mobility (usually $\ll 1$ $cm^2(Vs)^{-1}$) as compared to their inorganic counterparts. Despite the long spin relaxation time, this will still give a short spin relaxation length. The highest mobility in organic materials (if the fullerenes are excluded) is achieved in OSCs. Values of 35 $cm^2(Vs)^{-1}$ and 40 $cm^2(Vs)^{-1}$ have been reported for pentacene and rubrene single-crystals, respectively (see section 2.1.1). The high mobility and the low impurity density, which can act as spin scatterers, make them candidates for spin injection. In one paper, the spin relaxation has been predicted to be in the order of mm [175]. Because of the low defect density, the OSCs are excellent

candidates to study the *intrinsic* spin properties and the physical limitations of spin injection and transport in organic materials.

Co/Al_2O_3 electrodes for spin injection and detection are proposed for several reasons. Metals are easy to deposit with e-beam evaporation and Co has the highest spin polarization among metals ($\sim$45%). The Al_2O_3 tunnel barrier protects the Co from oxidation in between electrode fabrication and OSC placement, and can help to overcome the conductivity mismatch problem. The combination of Co and Al_2O_3 is proven to have good spin injection and detection properties and has been used in several other spin-valve devices [176, 227]. Besides this, the workfunction of Co (5 eV) is approximately the same as that of the HOMO level of rubrene single-crystal. Although these are bulk values and the exact values for the interfaces in this particular device are not a priori known, it is anticipated that the alignment of the workfunction of Co and the HOMO level of rubrene single-crystal will give good hole injection properties without a large Schottky barrier.

Using lateral devices, the spin-valve structures are suitable for both local and non-local measurements, as will be explained in chapter 5. Non-local measurements would give a definite proof of spin injection into the OSC. Hanle spin precession experiments are also possible with this device geometry to confirm the spin injection. The lateral devices also allow fabricating all the electrodes before the organic spacer is placed. Using this procedure, very clean electrodes which can be made by using different techniques, as will be discussed in chapter 3 and 4. It also prevents damaging of the OSCs, since the electrode fabrication and OSC placement is separated.

OSC are usually fabricated in a field-effect transistor layout. This gives another very interesting property of an OSC spin valve. In this structure, a FET is combined with a spin-valve device. In this way, logic and memory elements are combined in the same device. The combination of a FET and a spin valve has, to the best of our knowledge, not been realized yet. Interestingly, rubrene single-crystals have also been fabricated in a FET layout on flexible substrates [244]. Even after bending, the devices exhibit good performance. OSC could therefore also be used in flexible electronics. To ease the fabrication of OSC devices, selective growth of OSC on domains of octadcyltriethoxysilane has been reported [29].

References

[1] S.M. Sze and K.K. Ng, *Physics of Semiconductor Devices*, Wiley, New Jersey (2007).

[2] H. Klauk (ed), *Organic Electronics: Materials, Manufacturing and Applications*, Wiley-VCH, Weinheim (2006).

[3] R.W.I. de Boer, *PhD Thesis*, Ponsen & Looijen, Delft (2005).

[4] A. Salleo, Materials Today **10**, 38 (2007).

[5] R.E. Peierls, *Quantum Theory of Solids*, Oxford University Press, London, (1955).

[6] A.S. Molinari, G. Lezama, P. Parisse, T. Takenobu and A.F. Morpurgo, Appl. Phys. Lett. **92**, 133303 (2008).

[7] M.C. Petty, M.R. Bryce and D. Bloor (eds.), *An Introduction to Molecular Electronics*, Oxford University Press, New York (1995).

[8] G. Cuniberti, G. Fagas and K. Richter (eds.), *Introducing Molecular Electronics*, Springer-Verlag, Berlin Heidelberg (2005).

[9] P.P. Ruden and D.L. Smith, J. Appl. Phys. **95**, 4898 (2004).

[10] I. McCulloch, M. Heeney, C. Bailey, K. Genevicius, I. MacDonald, M. Shkunov, D. Sparrowe, S. Tierney, R. Wagner, W. Zhang, M.L. Chabinyc, R.J. Kline, M.D. McGehee and M.F. Toney, Nature Mat. **5**, 328 (2006).

[11] A.S. Dhoot, J.D. Yuen, M. Heeney, I. McCulloch, D. Moses, A.J. Heeger, PNAS **103**, 11834 (2006).

[12] S.K. Park, T.N. Jackson, J.E. Anthony and D.A. Mourey, Appl. Phys. Lett. **91**, 063514 (2007).

[13] Y. Liu, S.M. Watson, T. Lee, J.M. Gorham, H.E. Katz, J.A. Borchers, H.D. Fairbrother and D.H. Reich, Phys. Rev. B **79**, 075312 (2009).

[14] G.M. Wang, J. Swensen, D. Moses and A.J. Heeger, J. App. Phys. **93**, 6137 (2003).

[15] I.H. Campbell, J.D. Kress, R.L. Martin, D.L. Smith, N.N. Barashkov and J.P. Ferraris, Appl. Phys. Lett. **71**, 24 (1997).

[16] E.A. Silinsh and V. Čapek, *Organic Molecular Crystals: Interaction, Localization, and Transport Phenomena*, AIP Press, New York (1994).

[17] R.W.I. de Boer, M.E. Gershenson, A.F. Morpurgo and V. Podzorov, Phys. Stat. Sol. (a) **201**, 1302 (2004).

[18] V.C. Sundar, J. Zaumseil, V. Podzorov, E. Menard, R.L. Willett, T. Someya, M.E. Gershenson and J.A. Rogers, Science **303**, 1644 (2004).

[19] C. Reese and Z. Bao, Materials Today **10**, 20 (2007).

[20] G. Brocks, J. van den Brink and A.F. Morpurgo, Phys. Rev. Lett. **93**, 146405 (2004).

[21] O.D. Jurchescu, J. Baas and T.T.M. Palstra, Appl. Phys. Lett. **84**, 3061 (2004).

[22] J. Takeya, M. Yamagishi, Y. Tominari, R. Hirahara, Y. Nakazawa, T. Nishikawa, T. Kawase, T. Shimoda and S. Ogawa, Appl. Phys. Lett. **90**, 102120 (2007).

[23] V. Podzorov, E. Menard, J.A. Rogers and M.E. Gershenson, Phys. Rev. Lett. **95** (2005).

[24] J. Takeya, K. Tsukagoshi, Y. Aoyagi, T. Takenobu and Y. Iwasa, Jpn. J. Appl. Phys. **44**, L1393 (2005).

[25] J. Takeya, J. Kato, K. Hara, M. Yamagishi, R. Hirahara, K. Yamada, Y. Nakazawa, S. Ikehata, K. Tsukagoshi, Y. Aoyagi, T. Takenobu and Y. Iwasa, Phys. Rev. Lett. **98**, 196804 (2007).

[26] A.S. Molinari, G. Lezama, P. Parisse, T. Takenobu and A.F. Morpurgo, Appl. Phys. Lett. **92**, 133303 (2008).

[27] M. Mas-Torrent and C. Rovira, J. Mater. Chem. **16**, 433 (2006).

[28] R.A. Laudise, C. Kloc, P.G. Simpkins and T. Siegrist, J. Cryst. Growth **187**, 449 (1998).

[29] A.L. Briseno, S.C.B. Mannsfeld, M.M. Ling, S. Liu, R.J. Tseng, C. Reese, M.E. Roberts, Y. Yang, F. Wudl and Z. Bao, Nature **444**, 913 (2006).

[30] C. Dekker, Physics Today **52**, 22 (1998).

[31] T. Rueckes, K. Kim, E. Joselevich, G.Y. Tseng, C. Cheung and C.M. Leiber, Science **289**, 94 (2000).

[32] P. Avouris, Acc. Chem. Res **35**, 1026 (2002).

[33] C. Joachim, J.K. Gimzewski and A. Aviram, Nature **408**, 541 (2000).

[34] M. Menon and D. Srivastava, J. Mat. Res. **13**, 2357 (1998).

[35] M. Dresselhaus, G. Dresselhaus and P. Avouris (eds.), *Carbon Nanotubes: Synthesis, Structure, Properties, and Applications*, Springer, Berlin (2001).

[36] R.H. Baughman, A.A. Zakhidov and W.A. de Heer, Science **297**, 787 (2002).

[37] S. Iijima, Nature **354**, 56 (1991).

[38] S. Tomonaga, Prog. Theor. Phys. **5**, 544 (1950).

[39] J.M. Luttinger, J. Math. Phys. **4**, 1154 (1963).

[40] S. J. Tans, M. H. Devoret, H. Dai, A. Thess, R. E. Smalley, L. J. Geerligs, C. Dekker, Nature **386**, 474 (1997).

[41] A.K. Geim and K.S. Novoselov, Nature Mater. **6**, 183 (2007).

[42] A.K. Geim, Science **324**, 1530 (2009).

[43] K.S. Novoselov, A.K. Geim, S.V. Morozov, D. Jiang, Y. Zhang, S.V. Dubonos, I.V. Grigorieva and A.A. Firsov, Science **306**, 666 (2004).

[44] A. Aviram and M.A. Ratner, Chem. Phys. Lett. **29**, 277 (1974).

[45] A. Szent-Györgi, Nature **148**, 157 (1941).

[46] M.A. Reed, C. Zhou, C.J. Muller, T.P. Burgin and J.M. Tour, Science **278**, 252 (1997).

[47] T. Dadosh, Y. Gordin, R. Krahne, I. Khivrich, D. Mahalu, V. Frydman, J. Sperling, A. Yacoby and I. Bar-Joseph, Nature **436**, 677 (2005).

[48] K.W. Hipps, Science **294**, 536 (2001).

[49] J. Chen, M.A. Reed, A.M. Rawlett and J.M. Tour, Science **286**, 1550 (1999).

[50] H. Park, A.K.L. Lim, A.P. Alivisatos, J. Park and P.L. McEuen, Appl. Phys. Lett. **75**, 301 (1999).

[51] X.D. Cui, A. Primak, X. Zarate, J. Tomfohr, O.F. Sankey, A.L. Moore, T.A. Moore, D. Gust, G. Harris and S.M. Lindsay, Science **294**, 571 (2001).

[52] L. Zuppiroli, M.N. Bussac, S. Paschen, O. Chauvet and L. Forro, Phys. Rev. B **50**, 5196 (1994).

[53] M.C.J.M. Vissenberg and M. Matters, Phys. Rev. B **57**, 12964 (1998).

[54] S.F. Nelson, Y.-Y. Lin, D.J. Gundlach and N. Jackson, Appl. Phys. Lett. **72**, 1854 (1998).

[55] R. Coehoorn, Phys. Rev. B **72**, 155206 (2005).

[56] W.F. Pasveer, J. Cottaar, C. Tanase, R. Coehoorn, P.A. Bobbert, P.W.M. Blom, D.M. de Leeuw and M.A.J. Michels, Phys. Rev. Lett. **94**, 206601 (2005).

[57] K. Hannewald, V.M. Stojanović, J.M.T. Schellekens and P.A. Bobbert, Phys. Rev. B **69**, 075211 (2004).

[58] G. Horowitz, Adv. Funct. Mater. **1**, 13 (2003).

[59] R. Farchioni and G. Grosso, *Organic Electronic Materials*, Springer-Verlag, Berlin (2001).

[60] D. Dimitrakopoulos and P.R.L. Malenfant, Adv. Mater. **14** 99 (2002).

[61] L.-L. Chua, J. Zaumseil, J.-F. Chang, E.C.-W. Ou, P.K.-H. Ho, H. Sirringhaus and R.H. Friend, Nature **434**, 194 (2005).

[62] C.P. Jarrett, K. Pichler, R. Newbould and R.H. Friend *Synth. Met.* **77** 35 (1996).

[63] S. Kobayashi, T. Takenobu, S. Mori, A. Fujiwara and Y. Iwasa, Appl. Phys. Lett. **82**, 4581 (2003).

[64] H.E. Katz, A.J. Lovinger, J. Johnson, C. Kloc, T. Siegrist, W. Li, Y.Y. Lin and A. Dodabalapur, Nature **404**, 478 (2000).

[65] P.R.L. Malenfant, C.D. Dimitrakopoulos, J.D. Gelorme, L.L. Kosbar, T.O. Graham, A. Curioni and W. Andreoni, Appl. Phys. Lett. **80**, 2517 (2002).

[66] R.W.I. de Boer, N.N. Iosad, A.F. Stassen, T.M. Klapwijk and A.F. Morpurgo, Appl. Phys. Lett. **86**, 032103 (2005).

[67] M. Pope and C.E. Swenberg, *Electronic Processes in Organic Crystals and Polymers*, Oxford University Press, New York (1999).

[68] S.A. Brazovskii and N.N. Kirova, Sov. Phys. JETP **33**, 4 (1981).

[69] R.R. Chance, J.L. Brédas and R. Silbey, Phys. Rev. B **8**, 4491 (1984).

[70] Å. Johansson and S. Stafström, Phys. Rev. Lett. **16**, 3602 (2001).

[71] J.-Y. Fu, J.-F. Ren, X.-J. Liu, D.-S. Liu and S.-J. Xie, Phys. Rev. B **73**, 195401 (2006).

[72] J.H. Wei, S.J. Xie, L.M. Mei, J. Berakdar and Y.-J. Yan, New Journal of Physics **8**, 82 (2006).

[73] J.H. Wei, S.J. Xie, L.M. Mei and Y.-J. Yan, Org. Electron. **8**, 487 (2007).

[74] A.M. Stoneham, M.M.D. Ramos, A.M. Almeida, H.M.G. Correira, R.M. Ribeiro, H. Ness and A.J. Fischer, J. Phys.: Condens. Matter **14**, 9877 (2002).

[75] M.N. Bussac, J.D. Picon and L. Zuppiroli, Europhys. Lett. **66**, 392 (2004).

[76] A.F. Stassen, R.W.I. de Boer, N.N. Iosad and A.F. Morpurgo, Appl. Phys. Lett. **85**, 3899 (2004).

[77] I.N. Hulea, S. Fratini, H. Xie, C.L. Mulder, N.N. Iosad, G. Rastelli, S. Giuchi and A.F. Morpurgo, Nature Mat. **5**, 982 (2006).

[78] Y.D. Park, J.A. Lim, H.S. Lee and K. Cho, Materials Today **10**, 46 (2007).

[79] P.S. Davids, I.H. Campbell and D.L. Smith, J. Appl. Phys. **82**, 6319 (1997).

[80] J. Campbell Scott, J. Vac. Sci. Technol. A **21**, 521 (2003).

[81] I.H. Campbell and D.L. Smith, Solid State Physics **55**, H. Ehrenreich and F. Spaepen (eds.), Academic, New York (2001).

[82] Y. Xia and G.M. Whitesides, Soft Lithography. In Angew. Chem. Int. Ed. Engl. **37**, 551 (1998).

[83] S.-H. Hur, D.-Y. Khang, C. Kocabas and J.A. Rogers, Appl. Phys. Lett. **85**, 5730 (2004).

[84] J.W.P. Hsu, Materials Today **8**, 42 (2005).

[85] H. Sirringhaus, T. Kawase, R.H. Friend, T. Shimoda, M. Inbasekaran, W. Wu and E.P. Woo, Science **290**, 2123 (2000).

[86] H. Sirringhaus, N. Tessler and R.H. Friend, Science **280**, 1741 (1998).

[87] B.S. Ong, Y. Wu, P. Liu and S. Gardner, J. Am. Chem. Soc. **126**, 3378 (2004).

[88] C. Reese, M. Roberts, M.M. Ling and Z. Bao, Materials Today **7**, 20 (2004).

[89] S.R. Forrest, Nature **428**, 911 (2004).

[90] L.P. Kouwenhoven, C.M. Marcus, P.L. McEuen, S. Tarucha, R.M. Westervelt and N.S. Wingreen, *Electron transport in quantum dots (Mesoscopic Electron Transport, Kluwer Series E **345**)*, L.L. Sohn, L.P. Kouwenhoven *et al.* (eds.), 105 (1997).

[91] W.G. van der Wiel, S. De Franceschi, J.M. Elzerman, T. Fujisawa, S. Tarucha and L.P. Kouwenhoven, Rev. Mod. Phys. **75**, 1 (2003).

[92] T. Fujisawa, W.G. van der Wiel and L.P. Kouwenhoven, Physica E **7**, 413(2000).

[93] W.J.M. Naber, T. Fujisawa, H.W. Liu and W.G. van der Wiel, Phys. Rev. Lett. **96**, 136807 (2006).

[94] S. Datta, Nanotechnology **15**, S433 (2004).

[95] H. Haug and A.P. Jauho, *Quantum Kinetics in Transport and Optics of Semiconductors*, Springer, Berlin (1996).

[96] A.R. Rocha, V.M. García-Suárez, S. Bailey, C. Lambert, J. Ferrer and S. Sanvito, Phys. Rev. B **73**, 085414 (2006).

[97] J. Taylor, H. Guo and J. Wang, Phys. Rev. B **63**, 245407 (2001).

[98] Y. Xue, S. Datta and M.A. Ratner, Chem. Phys. **281**, 151 (2001).

[99] M. Brandbyge, J.-L. Mozos, P. Ordejón, J. Taylor and K. Stokbro, Phys. Rev. B **65**, 165401 (2002).

[100] J.J. Palacios, A.J. Pérez-Jiménez, E. Louis, E. SanFabián and J.A. Vergés, Phys. Rev. B **66**, 035322 (2002).

[101] A. Pecchia and A. Di Carlo, Rep. Prog. Phys. **67**, 1497 (2004).

[102] A.M. Bratkovsky, *Molecular Nanowires and Other Quantum Objects, Proceedings of the NATO Advanced Research Workshop, Bled, Slovenia from 7 to 9 September 2003 Series (NATO Science Series II: Mathematics, Physics and Chemistry, Vol.* **148***)* A.S. Alexandrov, J. Demsar (eds.), 428 (2004).

[103] C. Strunk, Science **306**, 63 (2004).

[104] A.R. Rocha, Nature Mater. **4**, 335 (2005).

[105] J.M. Soler, E. Artacho, J.D. Gale, A. García, J. Junquera, P. Ordejón and D. Sánchez-Portal, J. Phys. Condens. Matter **14**, 2745 (2002).

[106] E.G. Emberly and G. Kirczenow, Chem. Phys. **281** 311 (2002).

[107] P.M. Tedrow and R. Meservey, Phys. Rev. B **7**, 318 (1973).

[108] M. Jullière, Phys. Lett. **54**, 225 (1975).

[109] J.S. Moodera, L.R. Kinder, T.M. Wong and R. Meservey, Phys. Rev. Lett. **74**, 3273 (1996).

[110] J.C. Slonczewski, Phys. Rev. B **39**, 6995 (1989).

[111] W. Wulfhekel, H.F. Ding and J. Kirschner, J. Magn. Magn. Mater. **242**, 47 (2002).

[112] E.Y. Tsymbal, O.N. Mryasov and P.R. LeClair, J. Phys. Condens. Mater. **15**, R109 (2003).

[113] J. Zhang J and R.M. White, J. Appl. Phys. **83**, 6512 (1998).

[114] E.Y. Tsymbal, A. Sokolov, I.F. Sabirianov and B. Doudin, Phys. Rev. Lett. **90**, 186602 (2003).

[115] S. Ikeda, J. Hayakawa, Y. Ashizawa, Y.M. Lee, K. Miura, H. Hasegawa, M. Tsunoda, F. Matsukura and H. Ohno, Appl. Phys. Lett. **93**, 082508 (2008).

[116] *see* http://en.wikipedia.org/wiki/Disk_read-and-write_head

[117] *see* http://www.everspin.com/products16-16Mb.html

[118] J.R. Petta, S.K. Slater and D.C. Ralph, Phys. Rev. Lett. **93**, 136601 (2004).

[119] J.F. Gregg, J. Petej, E. Jouguelet and C. Dennis, J. Phys. D: Appl. Phys. **35**, R121 (2002).

[120] N.F. Mott, Proc. Roy. Soc. **153**, 699 (1936).

[121] N.F. Mott, Proc. Roy. Soc. **156**, 368 (1936).

[122] N.F. Mott, Adv. Phys. **13**, 325 (1964).

[123] M. Johnson and R.H. Silsbee, Phys. Rev. Lett. **55**, 1790 (1985).

[124] T. Valet and A. Fert, Phys. Rev. B **48**, 7099 (1993).

[125] A. Fert and H. Jaffrés, Phys. Rev. B **64**, 184420 (2002).

[126] A.T. Filip, B.H. Hoving, F.J. Jedema and B.J. van Wees, Phys. Rev. B **62**, 9996 (2000).

[127] G. Schmidt, D. Ferrand, L.W. Molenkamp, A.T. Filip and B.J. van Wees, Phys. Rev. B **62**, R4790 (2000).

[128] G. Schmidt, J. Phys. D: Appl. Phys. **38**, R107 (2005).

[129] E.I. Rashba, Sov. Phys. Solid State **2**, 1109 (1960).

[130] D.L. Smith and R.N. Silver, Phys. Rev. B **64**, 045323 (2001).

[131] Z.G. Yu, and M. Flatté, Phys. Rev. B **66**, R201202 (2002).

[132] J.-H. Park, E. Vescovo, H.-J. Kim, C. Kwon, R. Ramesh, T. Venkatesan, Nature **392**, 794 (1998).

[133] M. Bowen, M. Bibes, A. Barthèlèmy, J.-P. Contour, A. Anane, Y. Lemaître and A. Fert, Appl. Phys. Lett. **82**, 233 (2003).

[134] V.N. Prigodin, J.D. Bergeson, D.M. Lincoln and A.J. Epstein, Synth. Met. **156**, 757 (2006).

[135] F.Y. Yang, K. Liu, C.L. Chien and P.C. Searson, Phys. Rev. Lett. **82**, 3328 (1999).

[136] Ö. Mermer, G. Veeraraghavan, T.L. Francis, Y. Sheng, D.T. Nguyen, M. Wohlgennant, A. Köhler, M.K. Al-Suti and M.S. Khan, Phys. Rev. B **72**, 205202 (2005).

[137] C.W.J. Beenakker and H. van Houten, Solid State Physics **44**, 1 (1991).

[138] F.G. Monzon and M.L. Roukes, J. Magn. Magn. Mat. **198-199**, 632 (1999).

[139] F.G. Monzon, D.S. Patterson and M.L. Roukes, J. Magn. Magn. Mat. **195**, 19 (1999).

[140] S.J. van der Molen, N. Tombros and B.J. van Wees, Phys. Rev. B **73**, 220406(R) (2006).

[141] H. Shimada, K. Ono and Y. Ootuka, J. Phys. Soc. Jap. **67**, 1359 (1998).

[142] J.P. Bird (ed.), "*Carbon Nanotubes for Nanoscale Spin-Electronics (Electron Transport in Quantum Dots)*, Kluwer Academic Publishers, Boston/ Dordrecht/London (2003).

[143] F.J. Jedema, A.T. Filip and B.J. van Wees, Nature **410**, 345 (2001).

[144] A. Fert, J.-M. George, H. Jaffrés and R. Mattana, IEEE Trans. Electron. Devices. **54**, 921 (2007).

[145] J.M. Kikkawa, J.A. Gupta, I. Malajovich and D.D. Awschalom, Physica E **9**, 194 (2000).

[146] A.V. Khaetskii, D. Loss and L. Glazman, Phys. Rev. Lett. **88**, 186802-1 (2002).

[147] V.N. Golovach, A.V. Khaetskii and D. Loss, Phys. Rev. Lett. **93**, 016601-1 (2004).

[148] P.A. Bobbert, W. Wagemans, F.W.A. van Oost, B. Koopmans and M. Wohlgennant, Phys. Rev. Lett. **102**, 156604 (2009).

[149] S. Sanvito and A.R. Rocha, J. Comput. Theor. Nanosci. **3**, 624 (2006).

[150] A.T. Filip, *Ph.D. Thesis*, Rozenberg, Groningen (2002).

[151] M. Bennati, K. Nemeth, P.R. Surján and M. Mehring, J. Chem. Phys. **105** 4441 (1996).

[152] R. Coehoorn, *private communication*

[153] G. Dresselhaus, Phys. Rev. **100**, 580 (1955).

[154] M.I. D'yakonov and V.I. Perel, Sov. Phys. JETP **33**, 1053 (1971).

[155] Yu.A. Bychkov and E.I. Rashba, JETP Lett. **39**, 78 (1984).

[156] R.J. Elliot, Phys. Rev. **96**, 266 (1954).

[157] I. Zutič, J. Fabian and S. Das Sarma, Rev. Mod. Phys. **76**, 323 (2004).

[158] S. Pramanik, C.-G. Stefanita, S. Patibandla, S. Bandyopadhyay, K. Garre, N. Harth and M. Cahay, Nature Nanotech. **2**, 216 (2007)

[159] S. Pramanik, S. Bandyopadhyay, K. Garre and M. Cahay, Phys. Rev. B **74**, 235329 (2006).

[160] G.L. Bir, A.G. Aronov and G.E. Pikus, Sov. Phys. JETP **42**, 705 (1976).

[161] I.A. Merkulov, A.L. Efros and J. Rosen, Phys. Rev. B **65**, 205309 (2002).

[162] V. Dediu, M. Murgia, F.C. Matacotta, C. Taliani and S. Barbanera, Solid State Commun. **122**, 181 (2002).

[163] L. Torsi, A. Dodapalapur, L.J. Rothberg, A.W.P. Fung and H.E. Katz, Phys. Rev. B **57**, 2271 (1998).

[164] P. Ostoja, S. Guerri, M. Impronta, P. Zabberoni, R. Danieli, S. Rossini, C. Taliani and R. Zamboni, Adv. Mater. Opt. Electron. **1**, 127 (1992).

[165] Z.H. Xiong, D. Wu, Z. Valy Vardeny and J. Shi, Nature **427**, 821 (2004).

[166] M. Wohlgenannt, Z. Valy Vardeny, J. Shi, T.L. Francis, X.M. Jiang, Ö. Mermer, G. Veeraraghavan, D. Wu and Z.H. Xiong, IEE Proc.-Circuits Devices Syst. **152**, 385 (2005).

[167] F.J. Wang, Z.H. Xiong, D. Vu, J. Shi and Z. Valy Vardeny, Synth. Met. **155**, 172 (2005).

[168] S. Majumdar, R. Laiho, P. Laukkanen, I.J. Väyrynrn, H.R. Majumdar and R. Österbacka, Appl. Phys. Lett. **89**, 122114 (2006).

[169] J. Kumar, R.V. Singh, P.K. Siwach, H.K. Singh, R. Singh, R.C. Rastogi and O.N. Srivastava, Solid State Commun. **138**, 422 (2006).

[170] N.A. Morley, A. Rao, D. Dhandapani, M.R.J. Gibbs, M. Grell and T. Richardson, J. Appl. Phys. **103**, 07F306 (2008).

[171] V.A. Dediu, L.E. Hueso, I. Bergenti, A. Riminucci, F. Borgatti, P. Graziosi, C. Newby, F. Casoli, M.P. de Jong, C. Taliani and Y. Zhan, Phys. Rev. B **78**, 115203 (2008).

[172] T. Shimada, H. Nogawa, T. Noguchi, Y. Furubayashi, Y. Yamamoto, Y. Hirose, T. Hitosugi and T. Hasegawa, Jpn. J. Appl. Phys. **47**, 1184 (2008).

[173] F.J. Wang, C.G. Yang, Z. Valy Vardeny, Phys. Rev. B **75**, 245324 (2007).

[174] H.-W. Liu, H.-J. Chang, G.-P. Li and M. Bachman, IEEE Electron Dev. Lett. **30**, 346 (2009).

[175] J.H. Shim, K.V. Raman, Y.J. Park, T.S. Santos, G.X. Miao, B. Satpati and J.S. Moodera, Phys. Rev. Lett. **100**, 226603 (2008).

[176] T.S. Santos, J.S. Lee, P. Migdal, I.C. Lekshmi, B. Satpati and J.S. Moodera, Phys. Rev. Lett. **98**, 016601 (2007).

[177] W. Xu, G.J. Szulczewski, P. LeClair, I. Navarette, R. Schad, G. Miao, H. Guo and A. Gupta, Appl. Phys. Lett. **90**, 072506 (2007).

[178] G. Szulczewski, H. Tokuc, K. Oguz and J.M.D. Coey, Appl. Phys. Lett. **95**, 202506 (2009).

[179] C. Barraud *et al.*, *unpublished results*

[180] T. Wen, D. liu, C.K. Luscombe and K.M. Krishnan, Appl. Phys. Lett **95**, 082509 (2009).

[181] M. Ouyang and D.D. Awschalom, Science **301**, 1074 (2003).

[182] A.N. Pasupathy, R.C. Bialczak, J. Martinek, J.E. Grose, L.A.K. Donev, P.L. McEuen and D.C. Ralph, Science **306**, 86 (2004).

[183] D. Goldhaber-Gordon, H. Shtrikman, D. Mahalu, D. Abush-Magder, U. Meirav and M.A. Kastner, Nature **391**, 156 (1998).

[184] W.G. van der Wiel, S. De Franceschi, T. Fujisawa, J.M. Elzerman, S. Tarucha and L.P. Kouwenhoven, Science **289**, 2105 (2000).

[185] J. Chen, M.A. Reed, A.M. Rawlett and J.M. Tour, Science **286**, 1550 (1999).

[186] K.S. Ralls, R.A. Buhrmann and R.C. Tiberio, Appl. Phys. Lett. **55** 2459 (1989).

[187] T.L. Francis, Ö. Mermer, G. Veeraraghavan and M. Wohlgenannt, New Journal of Physics **6**, 185 (2004).

[188] Ö. Mermer, G. Veeraraghavan, T.L. Francis and M. Wohlgenannt, Solid State Commun. **134**, 631 (2005).

[189] Y. Sheng, T. Nguyen, G. Veeraraghavan, Ö. Mermer, M. Wohlgenannt, S. Qiu and U. Scherf, Phys. Rev.B **74**, 045213 (2006).

[190] M. Nishioka, Y.-B. Lee, A.M. Goldman, Y. Xia and C.D. Frisbie, Appl. Phys. Lett. **91**, 092117 (2007).

[191] Y. Sheng, T.D. Nguyen, G. Veeraraghavan, Ö. Mermer, and M. Wohlgennant, Phys. Rev. B **75**, 035202 (2007).

[192] P.A. Bobbert, T.D. Nguyen, F.W.A. van Oost, B. Koopmans and W. Wohlgennant, Phys. Rev. Lett. **99**, 216801 (2007).

[193] W. Wagemans, F.L. Bloom, P.A. Bobbert, M. Wohlgennant and B. Koopmans, J. Appl. Phys. **103**, 07F303 (2008).

[194] F.L. Bloom, W. Wagemans, M. Kemerink and B. Koopmans, Phys. Rev. Lett. **99**, 257201 (2007).

[195] F.L. Bloom, W. Wagemans and B. Koopmans, Appl. Phys. Lett. **93**, 263302 (2008).

[196] F.L. Bloom, W. Wagemans and B. Koopmans, J. Appl. Phys. **103**, 07F320 (2008).

[197] K. Tsukagoshi, B.W. Alphenaar and H. Ago, Nature **401**, 572 (1999).

[198] K. Tsukagoshi and B.W. Alphenaar, Superlattices and Microstructures **27**, 565 (2000).

[199] S. Chakraborty, K.M. Walsh, B.W. Alphenaar, L. Lei and K. Tsukagoshi, Appl. Phys. Lett. **83**, 1008 (2003).

[200] B.W. Alphenaar, K. Tsukagoshi and M. Wagner, J. Appl. Phys. **89**, 6863 (2001).

[201] D. Orgassa, G.J. Mankey and H. Fujiwara, Nanotechnology **12**, 281 (2001).

[202] B. Zhao, I. Monch, H. Vinselberg, T. Muhl and C.M. Schneider, Appl. Phys. Lett. **80**, 3144 (2002).

[203] B. Zhao, I. Monch, T. Muhl, H. Vinselberg and C.M. Schneider, J. Appl. Phys. **91**, 7026 (2002).

[204] Y. Ishiwata, H. Maki, D. Tsuya, M. Suzuki and K. Ishibashi, Phys. Stat. Sol. (c) **2**, 3137 (2005).

[205] S. Sahoo, T. Kontos, C. Schonenberger and C. Surger, Appl. Phys. Lett. **86**, 112109 (2005).

[206] S. Sahoo, T. Kontos, J. Furer, C. Hoffmann, M. Graber, A. Cotter and C. Schönenberger, Nature Phys. **1**, 99 (2005).

[207] Th. Schäpers, J. Nitta, H.B. Heersche and H. Takayanagi, Phys. Rev. B **64**, 125314 (2000).

[208] L.E. Hueso, G. Burnell, J.L. Prieto, L. Granja, C. Bell, D.J. Kang, M. Chhowalla, S.N. Cha, J.E. Jang, G.A.J. Amaratunga and N.D. Mathur, Appl. Phys. Lett. **88**, 083120 (2006).

[209] L.E. Hueso, J.M. Pruneda, V. Ferrari, G. Burnell, J.P. Valdés-Herrera, B.D. Simons, P.B. Littlewood, E. Artacho, A. Fert and N.D. Mathur, Nature **445**, 410 (2007).

[210] J.R. Kim, H.M. So, J.J. Kim and J. Kim, Phys. Rev. B **66**, 233401 (2002).

[211] A. Jensen, J. Nygård and J. Borggreen, Proceedings of International Symposium on Mesoscopic Superconductivity and Spintronics, 33, World Scientific, Singapore (2003).

[212] A. Jensen, J.R. Hauptmann, J. Nygård, J. Sadowski and P.E. Lindelof, Nano Letters **4**, 349 (2004).

[213] A. Jensen, J.R. Hauptmann, J. Nygård and P.E. Lindelof, Phys. Rev. B **72**, 035419 (2005).

[214] A. Brataas, Yu. V. Nazarov and G.E.W. Bauer, Phys. Rev. Lett. **84**, 2481 (2000).

[215] X. Waintal, E.B. Myers, P.W. Brouwer and D.C. Ralph, Phys. Rev. B **62**, 12317 (2000).

[216] M. Braun, J. König and J. Martinek, Phys. Rev. B **70**, 195345 (2004).

[217] H.T. Man, I.J.W. Wever and A.F. Morpurgo, Phys. Rev. B **73**, 241401(R) (2006).

[218] N. Tombros, S.J. van der Molen and B.J. van Wees, Phys. Rev. B **73**, 233403 (2006).

[219] F.J. Jedema, H.B. Heersche, A.T. Filip, J.J.A. Baselmans and B.J. van Wees, Nature **416**, 713 (2002).

[220] H. Zare-Kolsaraki and H. Micklitz, Phys. Rev. B **67**, 224427 (2003).

[221] H. Zare-Kolsaraki and H. Micklitz, Eur. Phys. J. B **40**, 103-109 (2004).

[222] H. Zare-Kolsaraki and H. Micklitz, J. Magn. Magn. Mat. **280**, 311 (2004).

[223] H. Zare-Kolsaraki and H. Micklitz, Phys. Rev. B **67**, 094433 (2004).

[224] H. Zare-Kolsaraki and H. Micklitz, J. Magn. Magn. Mat. **296**, 9 (2006).

[225] S. Miwa, M. Shiraishi, M. Mizuguchi, T. Shinjo and Y. Suzuki, Jap. J. Appl. Phys. **45** L717 (2006).

[226] E.W. Hill, K. Novoselov, F. Schedin and P. Blake, IEEE Transactions on Magnetics **42**, 2694 (2006).

[227] N. Tombros, C. Jozsa, M. Popinciuc, H.T. Jonkman and B.J. van Wees, Nature **448**, 571 (2007).

[228] N. Tombros, S. Tanabe, A. Veligura, C. Josza, M. Popinciuc, H.T. Jonkman and B.J. van Wees, Phys. Rev. Lett. **101**, 046601 (2008).

[229] C. Josza, M. Popinciuc, N. Tombros, H.T. Jonkman and B.J. van Wees, Phys. Rev. Lett. **100**, 236603 (2008).

[230] M. Ohishi, M. Shiraishi, R. Nouchi, T. Nozaki, T. Shinjo and Y. Suzuki, Jpn. J. Appl. Phys. **46**, L605 (2007).

[231] S. Cho, Y.-F. Chen, M.S. Fuhrer, Appl. Phys. Lett. **91**, 123105 (2007).

[232] M. Cinchetti, K. Heimer, J.-P. Wüstenberg, O. Andreyev, M. Bauer, S. Lach, C. Ziegler, Y. Gao and M. Aeschlimann, Nature Mater. **8**, 115 (2009).

[233] V.A. Dediu, L.E. Hueso, I. Bergenti and C. Taliani, Nature Mater. **8**, 707 (2009).

[234] A.J. Drew, J. Hoppler, L. Schulz, F.L. Pratt, P. Desai, P. Shakya, T. Kreouzis, W.P. Gillin, A. Suter, N.A. Morley, V.K. Malik, A. Dubroka, K.W. Kim, H. Bouyanfif, F. Bourqui, C. Bernhard, R. Scheuermann, G.J. Nieuwenhuys, T. Prokscha and E. Morenzoni, Nature Mater. **8**, 109 (2009).

[235] X. Lou, C. Adelmann, S.A. Crooker, E.S. Garlid, J. Zhang, S.M. Reddy, S.D. Flexner, C.J. Palmstrøm and P.A. Crowell, Nature Phys. **3**, 197 (2007).

[236] V. Coropceanu, J. Comil, D.A. da Silva Filho, Y. Olivier, R. Silbey and J.-L. Brédas, Chem. Rev. **107**, 926 (2007).

[237] G. Szulczewski, S. Sanvito and M. Coey, Nature Mater. **8**, 693 (2009).

[238] J.F. Ren, J.Y. Fu, S.D. Liu, L.M. Mei and S.J. Xie, Journ. Appl. Phys. **98**, 074503 (2005).

[239] S.J. Xie, K.H. Ahn, D.L. Smith, A.R. Bishop and A. Saxena, Phys. Rev. B **67**, 125202 (2003).

[240] P.A. Bobbert, W. Wagemans, F.W.A. van Oost, B. Koopmans and M. Wohlgennant, Phys. Rev. Lett. **102**, 156604 (2009).

[241] J.J.H.M. Schoonus, P.G.E. Lumens, W. Wagemans, J.T. Kohlhepp, P.A. Bobbert, H.J.M. Swagten and B. Koopmans, Phys. Rev. Lett. **103**, 146601 (2009).

[242] S. Krompiewski, J. Phys.: Condens. Matter **16**, 2981 (2004).

[243] L.E. Hueso, I. Bergenti, A. Riminucci, Y. Zhan and V.A. Dediu, Adv. Mat. **19**, 2639 (2007).

[244] A.L. Briseno, R.J. Tseng, M.-M. Ling, E.H.L. Falcao, Y. Yang, F. Wudl and Z. Bao, Adv. Mat. **18**, 2320 (2006).

[245] J. Bass and W.P. Pratt Jr., J. Phys. Condens. Matter **19**, 183201 (2007).

[246] I. Appelbaum, B. Huang and D. Monsma, Nature **447**, 295 (2007).

[247] J. Kikkawa and D.D. Awschalom, Nature **397**, 139 (1999).

Chapter 3

Fabrication of organic single-crystal field-effect transistors with ferromagnetic electrodes

In this chapter, several methods for fabricating organic single-crystal (OSC) field-effect transistors (FETs) with ferromagnetic (FM)/tunnel barrier electrodes will be discussed. First, the device layout is presented. Subsequently, the high-purity OSC growth and lamination process are described. Several fabrication techniques for realizing FM electrodes are discussed. Shadow masks, photo- and e-beam lithography are used to fabricate Co/Al_2O_3 electrodes. Using these fabrication techniques, electrodes are fabricated prior to the OSC lamination, in order to prevent any damage to the OSCs. On several FETs obtained by the different fabrication methods, electrical transport measurements have been performed.

3.1 Device layout

The general layout of an organic single-crystal field-effect transistor (OSC FET) is shown in Fig. 3.1. Two electrodes are used to inject charge into a conductive layer, which is formed at the organic/dielectric interface by applying a voltage on a gate electrode. The gate electrode and OSC are acting as a parallel plate capacitor, inducing charge in a thin layer in the OSC. In principle, ambipolar transport is possible using this device layout [1], but hole transport is mostly observed (see chapter 2). This layout has been used before in FETs using different OSCs [1–6], electrode materials [7, 8] and dielectrics [9], driven by the desire to study the intrinsic effects of organic materials in FET structures. These devices give reproducible results [5, 7, 8] with charge carrier mobilities as high as 35 $cm^2(Vs)^{-1}$ for pentacene [4] and 40 $cm^2(Vs)^{-1}$ for rubrene [10].

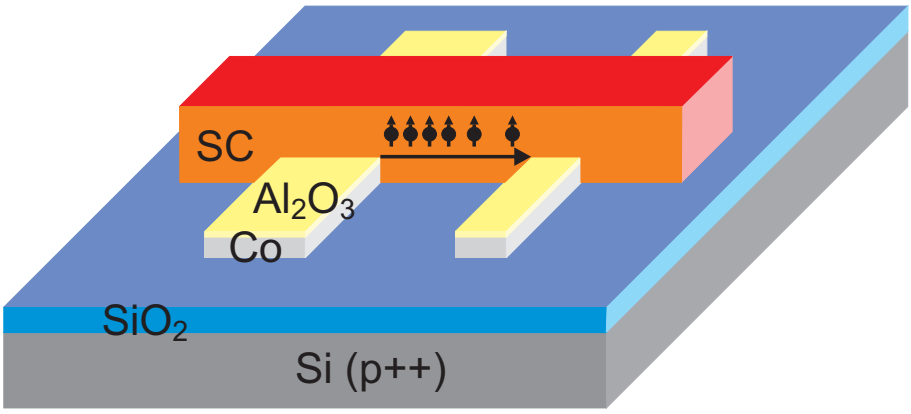

Figure 3.1: Device layout of an organic single-crystal (OSC) spin-valve FET. A highly-doped (p++) Si substrate covered with a SiO_2 layer is used as a gate electrode and dielectric, respectively. Two Co electrodes, covered with an Al_2O_3 layer, are bridged by an OSC. Spin diffusion is schematically depicted by electrons carrying a spin moving in the direction of the arrow. Not to scale.

The layout of a spin valve requires two FM electrodes which can be switched between parallel and anti-parallel magnetization [11] (see also chapter 2). To obtain different switching fields, the shape anisotropy of electrodes with different widths is used in the layout, as shown in Fig. 3.1. As will be shown in chapter 5, the width should be smaller than 10 μm, to obtain distuingishable switching fields (see chapter 1).

The electrode separation should be smaller than the spin relaxation length in the OSC. For OSCs, the spin relaxation length has not been determined experi-

mentally yet, but is predicted to be in the order of μm (see chapter 5), or even mm [12] for rubrene single-crystals (SC).

For the devices investigated in this thesis, Co electrodes were fabricated on a highly doped silicon wafer covered with a 300 nm SiO_2 layer, which are used as the gate electrode and the gate dielectric, respectively. An Al_2O_3 tunnel barrier ($\sim$1–2.5 nm) protects the Co against oxidation and can be used to overcome the conductivity mismatch [13, 14]. The thickness of the electrodes is typically 10–20 nm, to allow for smooth bending of the OSC over the electrodes without breaking. In this way, an OSC spacer is obtained in contact with both electrodes, needed for good charge injection, and the gate dielectric, to obtain a conductive layer in the OSC.

After the electrode fabrication the OSC is laminated on the SiO_2 and electrode surface. This lamination method, which relies on bonding by electrostatic forces, works best for very thin OSCs ($<$1 μm) which adhere spontaneously to the surface after placing them by hand on the pre-fabricated electrodes [15]. The advantage of this fabrication is the fact that no materials are deposited on the very vulnerable OSC surface and the electrodes can be fabricated using different techniques, as described in the following sections, without the danger of damaging or contaminating the OSC. This method has been used before for other electrode materials, and has shown to give good I-V characteristics [7, 8, 16].

3.2 Organic single-crystal growth

In this thesis, mostly 5,6,11,12-tetraphenylnaphthacene (rubrene, $C_{42}H_{28}$) SC is used as organic material, since it is known to have a very high mobility [10]). Furthermore, its HOMO level aligns with the workfunction of Co, so good charge injection properties without a large Schottky barrier are expected. Co was chosen because it is a metal with a high spin polarization ($P = 45\%$) [17].

The molecular structure of rubrene is shown in Fig. 3.2a. Rubrene consists of a tetracene backbone, with four benzene rings as substituents. Electrons from the p-orbitals are strongly delocalized inside the molecule in π-clouds on both sides of the tetracene backbone. Due to the substituents, the crystal structure of rubrene consist of layers of molecules ordered in a herringbone structure as shown in Fig. 3.2b. Due to this stacking, rubrene SC has three different crystalline directions, denoted by crystal axes a, b and c. The lattice parameters along the a, b and c axes are 14.4 Å, 7.2 Å and 27.0 Å, respectively. The difference in the overlap of the π-clouds cause a difference in the mobility along the different crystal axes. The overlap is the lowest between the different layers along the c-axis and the

highest along the *b*-axis. Consequently, the mobility is the largest along the *b*-axis [2].

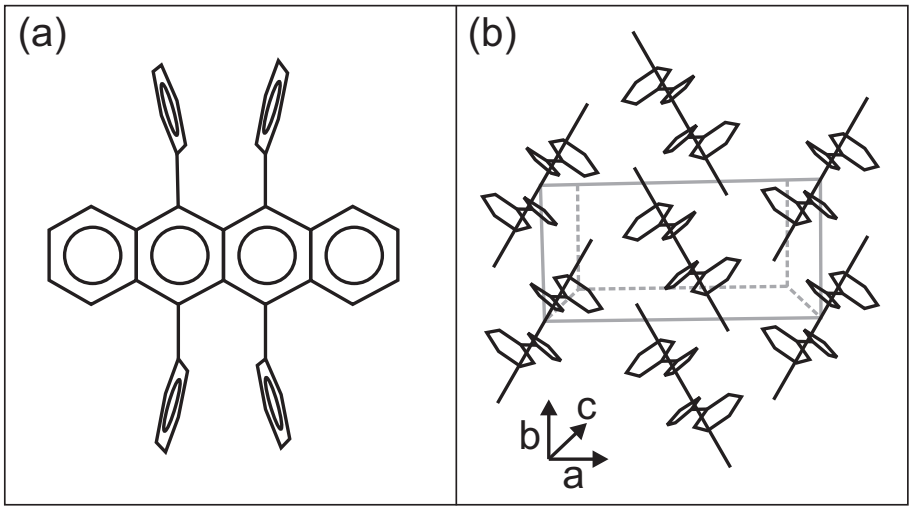

Figure 3.2: (a) Molecular structure of rubrene. The phenyl substituents are rotated due to steric hindrance of the phenyl groups. (b) Crystal structure of rubrene. The crystal axes *a*, *b* and *c* are denoted in the figure. Adapted from [2].

OSCs with a very high purity are grown using the physical vapor transport (PVT) method [5, 18], as schematically shown in Fig. 3.3a. The growth takes place in a horizontal quartz tube oven in which a temperature gradient is applied using a heating wire wrapped around the tube. The tube has a typical length of ∼50 cm. The starting organic material (purchased from Sigma-Aldrich with a purity of ∼98%) is positioned at the hottest place (around 300 °C for rubrene) at the beginning of the tube and starts to sublimate. A pure, inert gas (argon for the OSCs studied in this thesis) flows through the tube, transporting the organic material to the colder regions. The crystal growth occurs in a narrow temperature region at the end of the tube. Impurities in the starting material with different condensation temperature are deposited in other temperature regions and thus the organic material is purified. For a good separation of rubrene and impurities, a small temperature gradient (2–5 °C/cm) should be applied. Using multiple growth cycles, very pure OSCs can be obtained. Crystal growth is performed in the dark to minimize any photo-induced oxidation. A photograph of a PVT setup with two tube ovens is given in Fig. 3.3b.

OSCs grow in needle-like shapes or thin platelets. The in-plane dimensions are in the order of a few mm, while the thickness varies between ∼100 nm and ∼1

mm, depending on the growth time. Very thin OSCs (<1 μm), which are suitable for lamination, are grown in several hours. Examples of rubrene SCs grown with the PVT method are shown in Fig. 3.3c. The direction of the fastest growth depends on the anisotropy of the intermolecular interactions and corresponds to the axis of highest mobility (the *b*-axis).

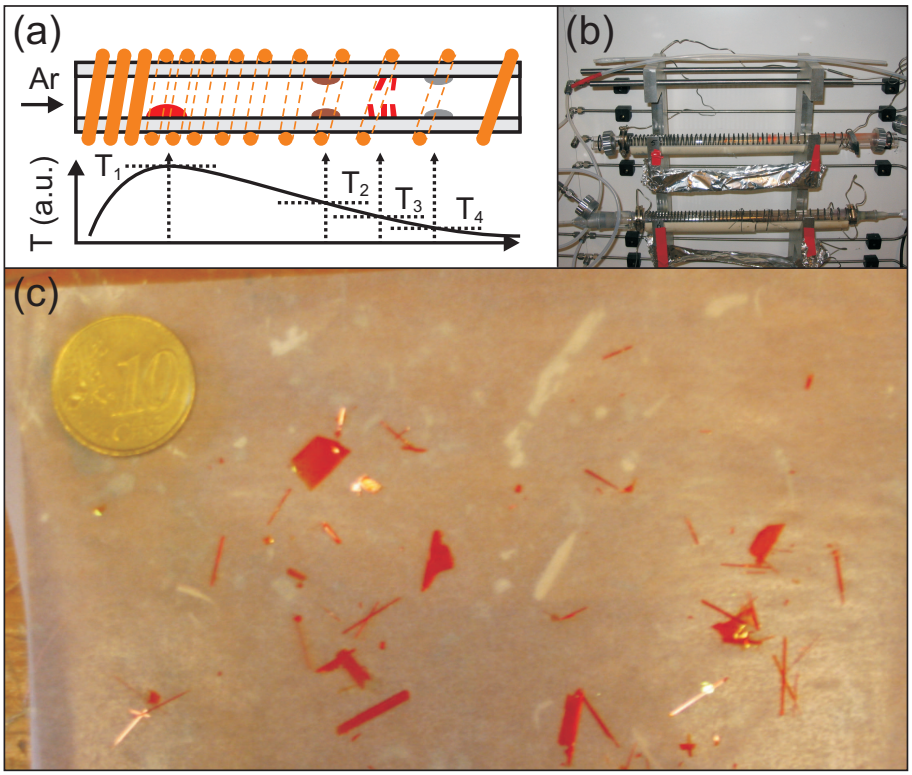

Figure 3.3: Organic single-crystal growth. (a) Schematic drawing of the setup. A metal heating wire is wrapped around a quartz tube with variable density to create a temperature gradient as depicted at the bottom. The starting material is placed at the highest temperature T_1 where it sublimates. A flow of argon transports the material along the tube where it deposits at the crystallization temperature T_3. Impurities are deposited at other temperatures T_2 and T_4. (b) Photograph of a PVT setup, showing two quartz tube ovens with heating wires and gas connections on both sides. (c) Grown rubrene single-crystals in different sizes and shapes. Photographs taken at the Delft University of Technology, group Prof. A.F. Morpurgo.

3.3 Electrode fabrication

Contacting organic materials for spin injection is not straightforward. First of all, the weak bonding between the molecules, as they are hold together by weak van der Waals forces, makes them easy to damage [19]. Metal evaporation on top of the organic material, is therefore not suited for this purpose. Another requirement for spin injection is that the interface between the ferromagnetic electrode and organic material has to be clean. Impurities can scatter the electron spin, thereby lowering the spin polarized signal [20]. As a solution to these problems, different fabrication techniques for FM electrodes are investigated. The electrodes are fabricated prior to the lamination of OSCs to prevent any damage to the organic material. The advantages and disadvantages of the different fabrication methods will be discussed.

All FM/tunnel barrier electrodes used in this thesis are deposited in a UHV chamber with a base pressure $\leq 10^{-10}$ Torr (see chapter 1), using different deposition techniques, as discussed below. First, a layer of Co or NiFe (typical thickness 8–15 nm) is deposited on a 1 x 1 cm^2 highly doped (p++) Si/SiO_2 substrate. The FM metal is covered with a layer of Al, which is oxidized by plasma oxidation in 100 mTorr O_2 and by applying 800 V to generate the plasma. The oxidation time depends on the Al layer thickness, ranging from 8 min. for 1 nm to 30 min. for 3 nm (see Appendix A).

3.3.1 Shadow-mask evaporation

Shadow masks used for the fabrication of FM electrodes were made from Si wafers using a sequence of etching techniques. A detailed process flow is presented in Appendix A. Starting with a 4-inch double-side polished Si wafer, the desired electrode features were etched in the front side of the wafer using photolithography and a dry etching technique. With this method, small etched features (down to $\sim$10 μm) with very straight walls could be obtained. The etch depth of these features is 10–15 μm. The etched features become holes by etching large areas from the backside of the wafer by a wet etching technique. This step also etched breaking lines into the wafer, making it possible to obtain shadow masks of 11 by 11 mm, as shown in Fig. 3.4. The resulting shadow masks were thin ($\sim$10 μm) Si membranes with holes in the shape of the desired electrode design, supported by thick ($\sim$500 μm) Si edges.

During deposition, the shadow masks were clamped in a holder above the substrates, which is shown in Fig. 3.5. Using three stainless steel plates with openings of different sizes, the masks could be positioned above nine positions

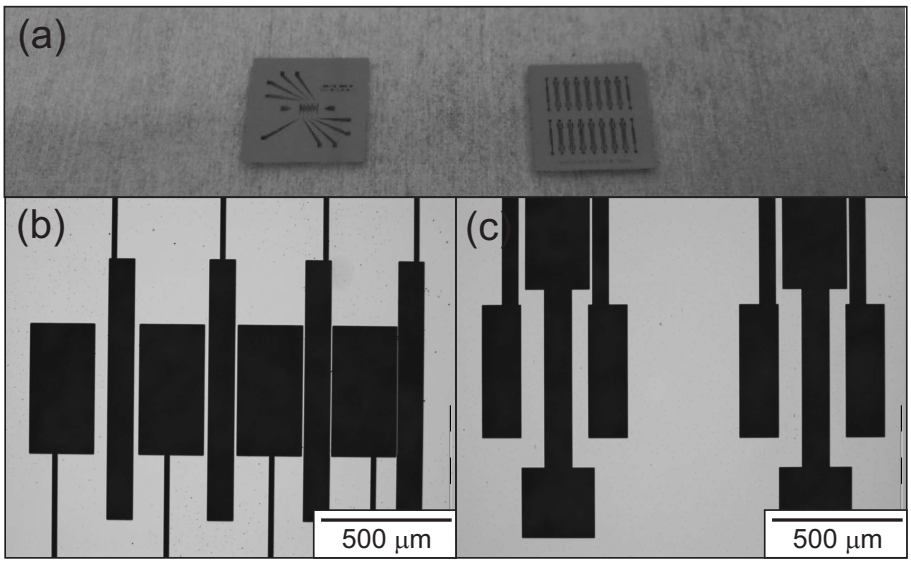

Figure 3.4: Photographs of (a) two 11 x 11 mm^2 Si shadow masks with different features and a zoom-in of the left (b) and right (c) shadow masks showing some features of the electrode design. The black areas are the openings through which metals can be evaporated.

of a round sample holder (see Fig. 3.5c). Substrates could be placed on these nine positions. To evaporate different metal structures through different shadow masks on the same substrate, the base of the sample holder could rotate in order to move the substrates to all nine positions. Evaporation could also be done over the whole substrate, when no shadow mask is placed above a certain position.

For the samples fabricated with these shadow masks, Co was evaporated through a shadow mask with the desired electrode layout. After rotating the substrate to a position without a shadow mask, Al was evaporated, resulting in an Al_2O_3 layer covering the whole substrate after oxidation. Examples of electrodes with and without laminated OSCs are shown in Fig. 3.6.

The combination of Co/Al_2O_3 has proven to give good spin injection and detection properties in magnetic tunnel junctions (MTJs) [21] and other spin-valve structures [22, 23]. These devices have all been made without exposing the interface of the spin-polarized electrodes to air. Since the Co/Al_2O_3 electrodes are exposed to air after deposition, test were performed to see if the spin injection and detection properties are still maintained.

For this purpose, MTJs were fabricated with the bottom electrode consisting of the same materials as used in the lateral OSC devices, 8 nm Co and ∼3 nm

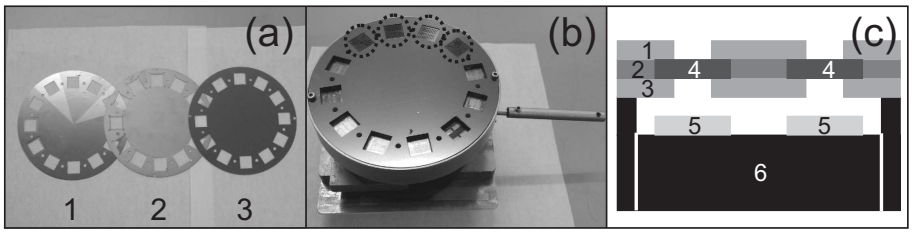

Figure 3.5: Shadow mask holder. (a) Photograph of the stainless steel plates (numbered 1–3, corresponding to numbers in (c)) which are used to clamp the shadow masks. (b) Shadow mask holder with the plates in (a) and four shadow masks at the top of the picture, denoted by the dotted circles. (c) Schematic picture of a cross section of the shadow mask holder, showing (1) the upper (2) middle and (3) lower stainless steel clamps which hold the shadow masks (4), (5) the substrates and (6) the substrate holder which can rotate 360°.

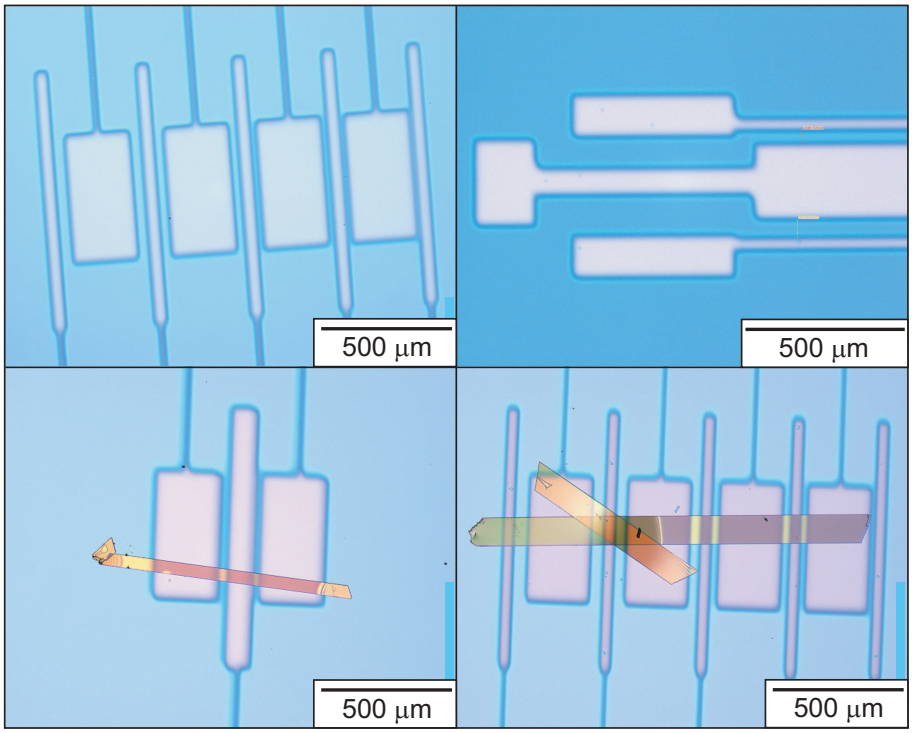

Figure 3.6: Photographs of Co/Al_2O_3 electrodes (light rectangular areas) fabricated with shadow masks as described in the text. In the two lower pictures, rubrene single-crystals are partly covering the electrodes.

Al_2O_3, using exactly the same fabrication method as described above. After that, this electrode was exposed to air for approximately one hour. A top electrode, consisting of 15 nm $Ni_{80}Fe_{20}$ (permalloy, Py) was evaporated on top to complete the MTJ. A similar MTJ of the same materials was made without breaking the vacuum. This MTJ is used as a reference sample. The *MR* measurements of these two MTJs are shown in Fig. 3.7. A voltage of V = -10 mV was applied over the MTJs and the resistance is measured as a function of the magnetic field H, from which the MR values were calculated. For both MTJs, a hysteretic curve was observed, typical for spintronic devices. The similar MR values in both devices showed that the exposure to air was not destructive for the spin injection and detection properties of the bottom electrode. These measurements therefore show that Co/Al_2O_3 electrodes can be used for rubrene SC spin-valve devices, even if the electrodes are exposed to air in between electrode fabrication and OSC lamination.

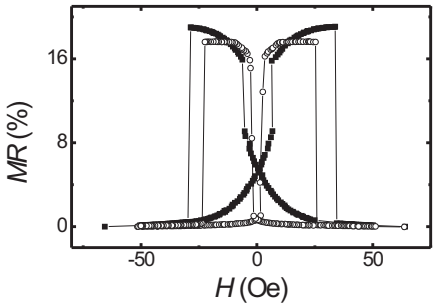

Figure 3.7: Magnetoresistance *MR* vs. magnetic field H for Co(8 nm)/Al_2O_3(3 nm)/NiFe(15 nm) MTJs. The open circles are for the MTJ exposed to air, the black squares for the MTJ fabricated without breaking the vacuum. The coercive fields are slightly different due to a small difference in the thickness of the metal layers.

Typical electrical measurements on an OSC FET with FM electrodes, fabricated using shadow-mask evaporation are shown in Fig. 3.8. Two Co(8 nm)/Al_2O_3 (3 nm) electrodes were bridged by a piece of rubrene SC. This sample was measured at room temperature in vacuum. These results have been reproduced in a large number of devices. Clear FET behavior was observed in these samples.

In Fig. 3.8a, the source-drain current I_{SD} is independent of the gate voltage V_G around source-drain voltage $V_{SD} = 0$ V, showing the current is contact dominated, instead of channel dominated, because in the latter case it should be possible to tune the current with the gate voltage, which increases or decreases the amount of charge carriers in the conducting channel. The contact-dominated behavior

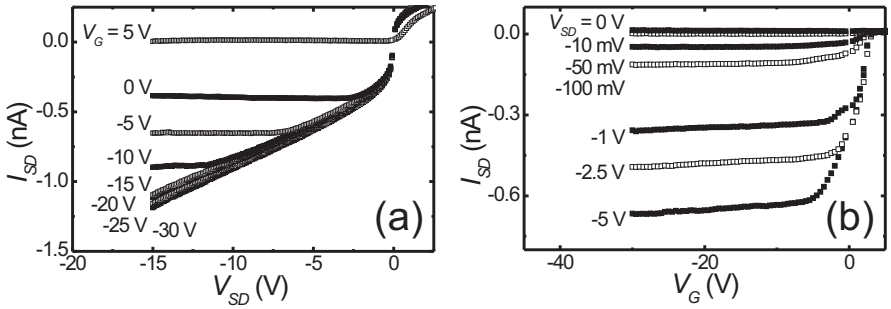

Figure 3.8: FET measurements on a rubrene single-crystal device with Co(8 nm)/Al_2O_3(3 nm) electrodes, fabricated using shadow mask evaporation. Channel length $L = 300$ μm and channel width $W = 50$ μm (set by the width of the crystal). (a) Source-drain current I_{SD} vs. source-drain voltage V_{SD} for different values of the gate voltage V_G and (b) I_{SD} vs. V_{SD} for different values of V_G.

is expected, since an Al_2O_3 tunnel barrier on the Co electrodes is introduced on purpose. The currents for different gate voltages start to deviate from each other only when $V_{SD} > (V_G - V_{th})$, where $V_{th} \sim 2.5$ V is the threshold voltage, because there is a crossover from the linear to the saturation regime and I_{SD} becomes independent of V_{SD} [24].

By rewriting Eq. 2.1 in chapter 2 an estimate for the mobility in this device can be made

$$\mu = \frac{L}{WC_iV_{SD}} \frac{\partial I_{SD}}{\partial V_G}, \tag{3.1}$$

where L is the channel length, W the channel width and C_i the capacitance of the gate dielectric. The mobility obtained for this device $\mu = 0.08$ cm^2(Vs)$^{-1}$. This is probably an underestimate of the mobility, since the (large) voltage drop over the high-resistive tunnel barriers is not taken into account and a Schottky barrier can be present at the interface.

The clear FET behavior in Fig. 3.8 shows that Co/Al_2O_3 electrodes fabricated by shadow-mask evaporation can be used to inject charge carriers in rubrene single-crystals. However, the influence of a possible Schottky barrier, which can be present when the workfunction at the interface of the electrodes does not align with the Fermi level of rubrene SC, has to be investigated. The contact-dominated behavior and low current as compared to similar devices with different electrodes [16], might indicate that the current was injected through the Al_2O_3 tunnel barrier, desired for efficient spin injection and detection (see chapter 2). However, typical electrode dimensions are in the order of 10–100 μm (see Fig.

3.6). Smaller dimensions are hard to obtain with shadow-mask fabrication due to several reasons, as will be discussed below.

When photolithography is used to fabricate the shadow masks, the limit set by the wavelength of the UV light is in the order of 1–2 μm. Using other techniques (e-beam lithography, deep UV) could solve this problem in principle. However, since the shadow mask is basically only a very thin Si membrane, smaller structures will be extremely vulnerable and difficult to handle.

The shadow masks are clamped above the substrate, leaving a small separation ($\sim$1 mm) between the shadow mask and the substrate. Metal evaporated at a small angle to the substrate normal can therefore be deposited at areas underneath the closed parts of the shadow mask and can make the width of the electrodes larger than the opening in the shadow masks, as is illustrated in Fig. 3.9a. This problem could be solved by clamping the shadow masks directly on the sample. However, in that case it is not possible to slide away the substrate from underneath the shadow mask in the evaporation chamber to completely cover the substrate and electrodes with Al_2O_3. This is important, since especially the edges of the electrodes, where carrier injection into the OSC takes place, should be completely covered with the tunnel barrier.

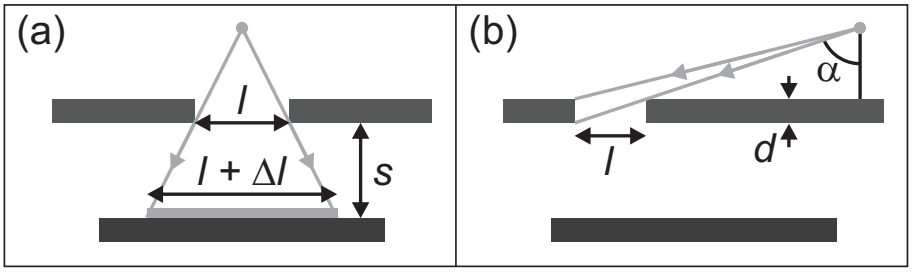

Figure 3.9: Undesired effects during deposition through shadow masks. (a) When metal is evaporated from a source (dot on top) onto a substrate at a small angle to the substrate normal through a shadow mask at a distance s from the substrate, the width of the electrode $l + \Delta l$ is bigger than the opening in the shadow mask l. (b) When the angle of evaporation α is too large with respect to the dimensions of the openings in the shadow masks (thickness d and width l) as drawn here, the metal flux can be blocked.

Another problem occurs when the metal is evaporated at a large angle with respect to the substrate normal, as schematically shown in Fig. 3.9b. When the electrode width is too small compared to the thickness of the shadow mask, a metal flux incident at a large angle is blocked by the shadow mask. Instead of

reaching the sample, the metal flux is deposited on the sidewalls of the etched holes in the shadow mask. The way to solve is by making the Si membrane thinner. However, a silicon membrane of 1–5 μm is probably very fragile and difficult to be handled in the fabrication process. Another solution is to evaporate at a small angle to the substrate normal. However, this is only possible when the layout of the evaporator allows this.

In conclusion, the use of shadow masks for electrode fabrication has the advantage of producing very clean electrodes, since materials like resists and solvents (which are used in the case of lithography) are not in contact with the substrate or electrodes. The absence of organic resists, which are outgassing when introduced in vacuum and could leave resist remnants on sample holders, makes them very compatible with evaporation setups with a UHV evaporation chamber. However, due to the above mentioned problems, obtaining small electrode widths and separations for the realization of spintronic devices with suitable dimensions is still difficult. The spin diffusion length is likely to be below $\sim$1 μm (see chapter 5) and also the width of electrodes, which should be smaller than 10 μm, poses a problem. Despite these problems, fabrication of FET devices with shadow masks is a good test to see if charge carriers can be injected in rubrene SC using the combination of Co and Al_2O_3. The results described in this section give an indication that the combination of these materials is suited for the realization of OSC FETs with FM electrodes. Optimization of the shadow masks using different techniques and/or materials might give the right fabrication tools to realize FET structures with smaller dimensions.

Using a different fabrication scheme, the problems which the small electrode width and separation pose, might be circumvented. Using different FM materials for spin injection and detection avoid the need for small electrode widths, since different switching fields are now achieved by the material properties instead of the shape anisotropy. Different shadow masks can be used to evaporate the different electrodes, but the alignment of the shadow masks on a μm scale in between the clamping plates (see Fig. 3.5), to obtain small electrode spacing is almost impossible. The small separations might be obtained by evaporating through the same shadow mask with different evaporation angles for the different metals, as explained below.

Metals which are evaporated at an angle with respect to the normal of the shadow mask will not be deposited directly underneath the openings in the shadow mask, as is illustrated in Fig. 3.10a. Therefore, evaporating two different materials at different angles will result in two electrodes at different places (see Fig. 3.10b). Since the sample holder can not be tilted with respect to the metal source in the metal evaporator used to fabricate the devices investigated in

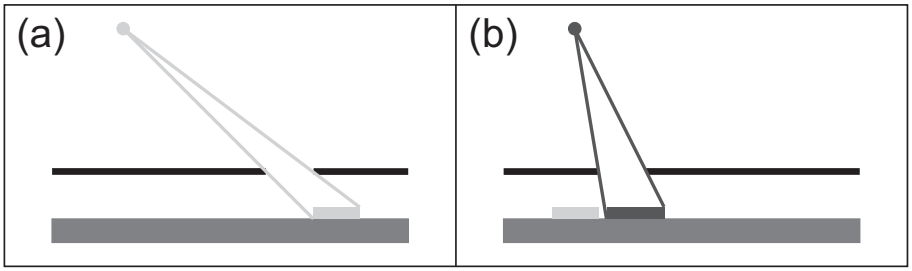

Figure 3.10: Fabrication of electrodes by evaporating two different metals at different angles. (a) A metal is evaporated from a source (dot at the top) at an angle through an opening in the shadow mask. (b) After rotating the sample, a second metal is evaporated, with a metal flux coming at a different angle through the same opening, resulting in an electrode at a different position.

this thesis, a different route has to be followed. The two metals were evaporated from the same source position, and different angles can be obtain by rotating the substrate. The substrate is then at a different position and hence at a different angle with respect to the metal source (see also Fig. 3.10b). After the evaporation of the electrodes, the sample was rotated underneath an opening without a shadow mask. Al was evaporated over the whole sample and plasma-oxidized to obtain Al_2O_3. An example of electrodes evaporated in this way is shown in Fig. 3.11.

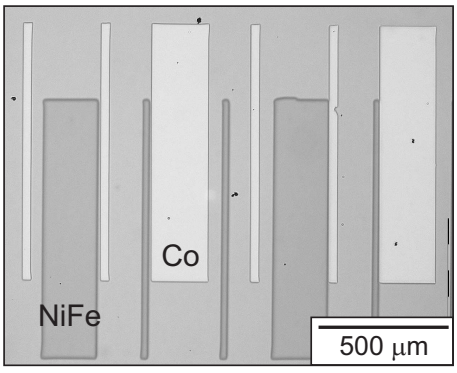

Figure 3.11: Photograph of Co (light rectangles) and NiFe (darker rectangles) electrodes fabricated by evaporating at different angles through a shadow mask.

Electrical measurements on a rubrene SC FET with Co and NiFe electrodes evaporated at different angles are shown in Fig. 3.12. FET behavior was observed,

and although the channel length in this device (80 μm) is probably still larger than the spin relaxation length, it demonstrates that FET structures with FM electrodes can be made using this method. Further research has to show if a sufficiently small electrode separation can be achieved.

The flattening of the I-V curve around $V_{SD} = 0$ V, which could indicate a large charge injection barrier (i.e. tunneling is prevailing), also requires more investigation, since back-to-back Schottky-like transport has been observed in similar devices [16]. The absence of the back-to-back Schottky behavior and the larger source-drain currents as compared to devices with only Co electrodes (see Fig. 3.8), might indicate a smaller Schottky barrier for NiFe/Al_2O_3 electrodes as compared to Co/Al_2O_3 electrodes in organic single-crystal FETs. More research on NiFe/Al_2O_3 can reveal the charge injection properties for these electrodes.

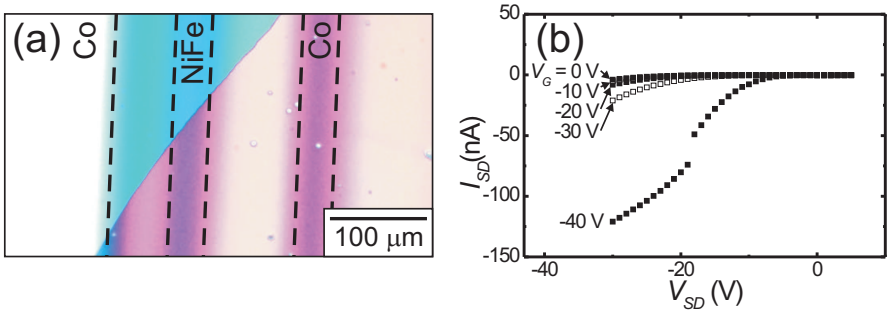

Figure 3.12: FET measurements on a rubrene single-crystal (SC) device with Co(15 nm) and NiFe(15 nm) electrodes evaporated at different angles through a shadow mask and covered with Al_2O_3(1.5 nm). Channel length $L = 80$ μm and channel width $W = 250$ μm (set by the width of the crystal). (a) Picture of the device, showing the electrodes which are (partly) covered by a rubrene SC on the right. (b) Source-drain current I_{SD} vs. source-drain voltage V_{SD} for different values of the gate voltage V_G.

3.3.2 Photo- and e-beam lithography

Although Co/Al_2O_3 electrode fabrication with shadow masks is a very clean method, small electrode separations below 10 μm are not easily obtained, as explained in the previous section. Well established methods to obtain smaller features are photo- and e-beam lithography. However, since photo- or e-beam resist requires the use of organic solvents like acetone and 2-propanol, it is not a priori known if electrodes fabricated in this way can be used for spin injection and detection. Contaminations from the resist and solvents could be detrimental for

the electron spin polarization. Another problem is the impossibility of covering the whole substrate with a layer of Al_2O_3, since the resist can only be removed after the formation of the Al_2O_3 to prevent oxidation of Co. These problems will be intensively discussed in chapter 4. In this section, the process of fabrication with photo- and e-beam lithography will briefly be discussed.

Photolithography

Using photolithography, feature sizes down to 1–2 μm can be obtained. The photoresist process was already schematically shown in chapter 1.

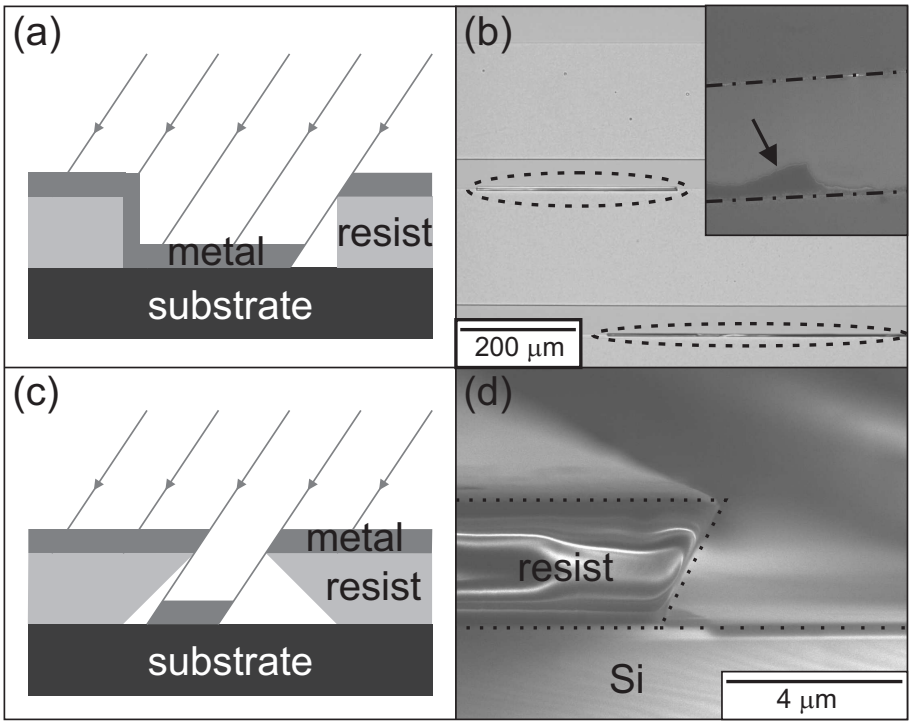

Figure 3.13: Photolithography. (a) Schematic figure of metal deposition at an angle on resist with straight walls and (b) an optical picture of results after lift-off, showing undesired metal parts at the edge of the electrodes, encircled by the dotted lines. The inset shows a SEM picture of two metal electrodes (above and below the dashed-dotted lines) with an unwanted metal part denoted by the arrow. (c) Schematic figure of metal deposition on resist with edges with a negative slope and (d) a SEM picture of this resist on a Si substrate, clearly showing the negative slope.

If Olin 907/17 positive photoresist (i.e. the exposed parts of the resist will be removed) is used, holes with straight walls are obtained in the resist. These

straight walls cause problems when the metals are deposited at an angle to the substrate normal, as is the case for the evaporator used to fabricate devices described in this thesis. In this case, also metal will be deposited on the walls of the resist (see Fig. 3.13a). After lift-off, the metal deposited on the walls gives undesired metal parts on the edges of the electrodes, as can be seen in Fig. 3.13b, which can give problems with OSC lamination. Actually, when the metal is covering the whole wall, lift-off is completely impossible since acetone can not dissolve the resist. This problem is solved by using an image reversal resist TI-35-ES from MicroChemicals, which gives a resist pattern having edges with a negative slope, as schematically drawn in Fig. 3.13c and shown in Fig. 3.13d. This negative slope is formed due to a short over-development of the resist and prevents metal to be deposited on the walls of the resist.

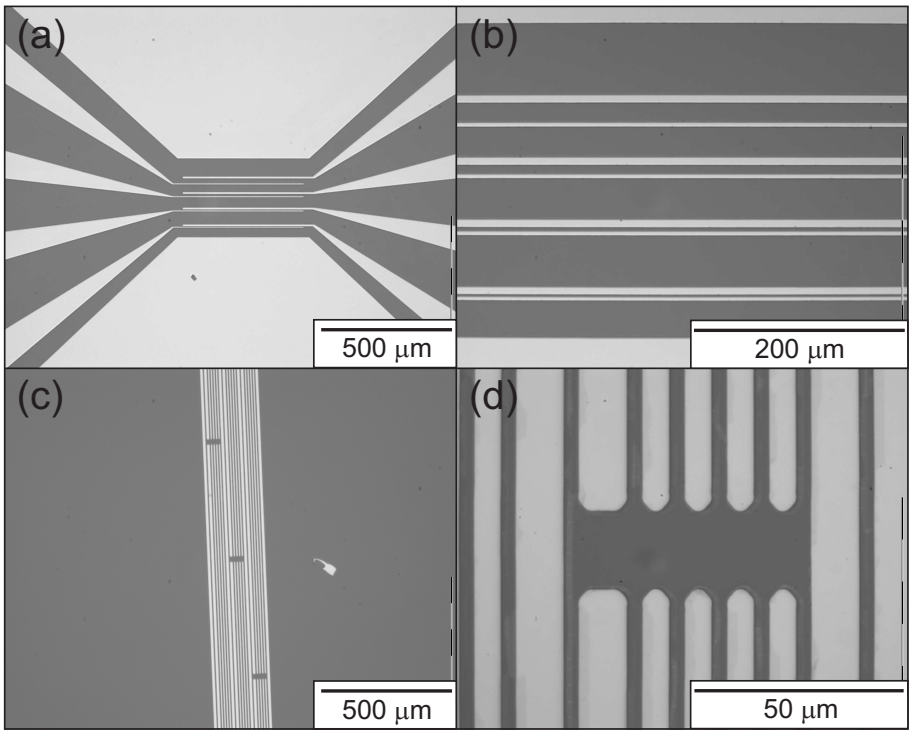

Figure 3.14: Co/Al_2O_3 electrodes (light parts) fabricated with photolithography on Si/SiO_2 substrates. (a) Photograph and (b) a close-up of electrodes suitable for local measurements, and (c) photograph and (d) a close-up of electrodes suitable for non-local measurements.

Several Co/Al_2O_3 electrode layouts using the image reversal resist TI-35-ES are shown in Fig. 3.14. These pictures show layouts suitable for local and non-

local spin-valve measurements (see section 2.2.4), as will be discussed in chapter 5. Electrodes with small widths in the order of μm and smooth edges, without undesired metal parts, were obtained. As will be shown in chapter 4, due to the negative slope in the resist, Al_2O_3 is completely covering the Co electrode.

E-beam lithography

E-beam lithography allows to reach features in the order of several tens of nm. The process was already briefly discussed in chapter 1. To prevent any metal to be deposited on the walls of this resist, a double layer resist is used, as shown in the inset of Fig. 3.15a. Since the bottom resist layer develops faster, an undercut appears in this layer. This gives resist patterns with no danger of depositing metals on the sidewalls. Results of this fabrication method are shown in Fig. 3.15a and b. Electrodes with small widths of 100 nm and 200 nm, and small separations down to 100 nm can be fabricated in this way.

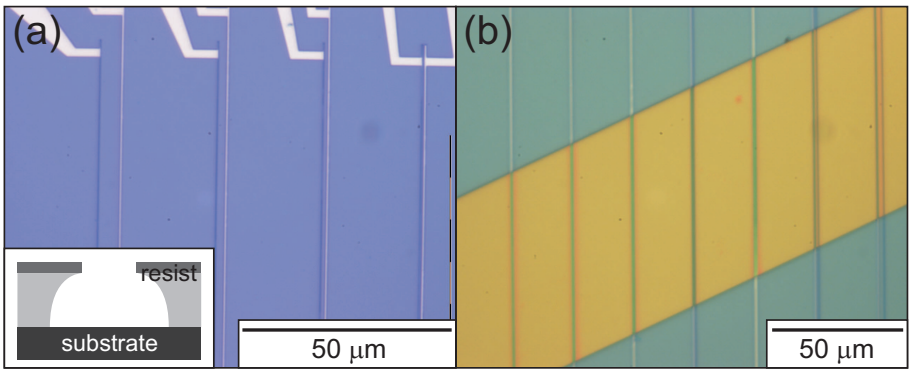

Figure 3.15: E-beam lithography. Co/Al_2O_3 electrodes (light parts) fabricated on a Si/SiO_2 substrate using e-beam lithography with (a) and without (b) a laminated rubrene single-crystal (partly) covering the electrodes. The electrodes are arranged in pairs with widths of 100 and 200 nm. The spacing between these electrodes ranged from 5 μm to 100 nm. The inset in (a) is a schematic picture of the double-layer e-beam resist.

References

[1] R.W.I. de Boer, A.F. Stassen, M.F. Craciun, C.L. Mulder, A.S. Molinari, S. Rogge And A.F. Morpurgo, Appl. Phys. Lett. **86**, 262109 (2005).

[2] V.C. Sundar, J. Zaumseil, V. Podzorov, E. Menard, R.L. Willett, T. Someya, M.E. Gershenson and J.A. Rogers, Science **303**, 1644 (2004).

[3] V. Podzorov, E. Menard, A. Borrisov, V. Kiryukhin, J.A. Rogers and M.E. Gernshenson, Phys. Rev. Lett. **93**, 086602 (2004).

[4] O.D. Jurchescu, J. Baas and T.T.M. Palstra, Appl. Phys. Lett. **84**, 3061 (2004).

[5] R.W.I. de Boer, M.E. Gershenson, A.F. Morpurgo and V. Podzorov, Phys. Stat. Sol. (a) **201** 1302 (2004).

[6] R.W.I. de Boer, T.M. Klapwijk and A.F. Morpurgo, Appl. Phys. Lett. **83**, 4345 (2003).

[7] I.N. Hulea, S. Russo, A. Molinari and A.F. Morpurgo, Appl. Phys. Lett. **88**, 113512 (2006).

[8] A.S. Molinari, I. Gutiérrez, I.N. Hulea, S. Russo and A.F. Morpurgo, Appl. Phys. Lett. **90**, 212103 (2007).

[9] A.F. Stassen, R.W.I. de Boer, N.N. Ioas and A.F. Morpurgo, Appl. Phys. Lett. **85**, 3899 (2004).

[10] J. Takeya, M. Yamagishi, Y. Tominari, R. Hirahara, Y. Nakazawa, T. Nishikawa, T. Kawase, T. Shimoda and S. Ogawa, Appl. Phys. Lett. **90**, 102120 (2007).

[11] G.A. Prinz, Physics Today **48**, 58 (1995); G.A. Prinz, Science **282**, 1660 (1998); S.A. Wolf, D.D. Awschalom, R.A. Buhrman, J.M. Daughton, S. von Molnár, M.L. Roukes, A.Y. Chtchelkanova and D.M. Treger, Science **294**, 1488 (2001).

[12] J.H. Shim, K.V. Raman, Y.J. Park, T.S. Santos, G.X. Miao, B. Satpati and J.S. Moodera, Phys. Rev. Lett. **100**, 226603 (2008).

[13] G. Schmidt, D. Ferrand, L.W. Molenkamp, A.T. Filip and B.J. van Wees, Phys. Rev. B **62**, R4790 (2000).

[14] A. Fert and H. Jaffrès, Phys. Rev. B **64**, 184420 (2002).

[15] R.W.I. de Boer, *PhD Thesis*, Ponsen & Looijen, Delft (2005).

[16] A.S. Molinari, G. Lezama, P. Parisse, T. Takenobu and A.F. Morpurgo, Appl. Phys. Lett. **92**, 133303 (2008).

[17] R. Meservey and P.M. Tedrow, Phys. Rep. **238**, 175 (1994).

[18] R.A. Laudise, C. Kloc, P.G. Simpkins and T. Siegrist, J. Cryst. Growth **187**, 449 (1998).

[19] Klauk H (ed.), *Organic Electronics: Materials, Manufacturing and Applications*, Wiley-VCH, Weinheim (2006).

[20] G. Szulczewski, S. Sanvito and M. Coey, Nature Mat. **8**, 693 (2009).

[21] J.S. Moodera, L.R. Kinder, T.M. Wong and R. Meservey, Phys. Rev. Lett. **74**, 3273 (1995).

[22] T.S. Santos, J.S. Lee, P. Migdal, I.C. Lekshmi, B. Satpati and J.S. Moodera, Phys. Rev. Lett. **98**, 016601 (2007).

[23] N. Tombros, C. Jozsa, M. Popinciuc, H.T. Jonkman and B.J. van Wees, Nature **448**, 571 (2007).

[24] S.M. Sze and K.K. Ng, *Physics of Semiconductor Devices*, Wiley, New Jersey (2007).

Chapter 4

Interfaces between ferromagnetic electrodes and organic materials

In this chapter, the interface between Co/Al_2O_3 electrodes and organic materials is studied. X-ray photoelectron spectroscopy (XPS) and UV photoemission spectroscopy (UPS) showed the existence of a contamination layer on the electrodes, consisting of carbon and oxygen, after they were cleaned with organic solvents. Moreover, measuring the energy level alignment revealed a large hole injection barrier from these contaminated electrodes to organic materials. Magnetic tunnel junctions (MTJs) with this contamination layer have lower MR values than clean ones. The contamination layer was removed by an oxygen plasma cleaning, which led to an increase of the MR value as compared to the contaminated electrode. Transmission electron microscopy (TEM) showed the detailed structure of the Co electrodes, which seemed to be completely covered with a fabricated Al_2O_3 layer.

Parts of this chapter will be published as M. Grobosch, C. Schmidt, W.J.M. Naber, W.G. van der Wiel and M. Knupfer, *accepted for publication in* Synthetic Metals.

4.1 Introduction

The interfaces between the ferromagnetic (FM) electrode and the organic materials in an organic spin valve is of crucial importance. Here, the spin injection in the organic layer takes place and defects or impurities can scatter the spins, leading to spin relaxation. Clean interfaces are therefore necessary for good spin injection properties. Schottky barrier formation is an effect which takes place at the interface of a metal and a semiconductor, when the Fermi energies of the two materials are not aligned. In spin-valve devices, Schottky barriers are in principle undesired, since it is not clear what the influence of the Schottky barrier on spin injection is. Inelastic scattering events inside the Schottky barrier can lead to spin relaxation. Spin injection through Schottky barriers, to solve the conductivity mismatch problem, has been reported, although in these studies very thin Schottky barriers are used [1]. The influence of larger Schottky barriers is not exactly known. However, Schottky barrier formation has been proposed as the explanation of the observed MR in metal/organic devices without tunnel barriers [2]. Anticipating on the conductivity mismatch problem [3, 4], an Al_2O_3 tunnel barrier is fabricated on the Co electrodes for the organic single-crystal field-effect transistors studied in this thesis. In contrast to a Schottky barrier, the Al_2O_3 provides a controlled tunnel barrier for which the resistance can be tuned by varying the thickness.

In this chapter, the interfaces of the proposed spin valve (see chapter 3) are investigated in different ways. X-ray photoelectron spectroscopy (XPS) and UV photoemission spectroscopy (UPS) were performed to study the energy-level alignment of Co and Co/Al_2O_3 electrodes in contact with rubrene and pentacene thin films. Although the use of thin films is very different from the proposed spin valve, in which highly-ordered and very pure organic single crystals are used, it still can give information about the used electrodes. Before the deposition of the organic thin films, the electrodes were cleaned with acetone, mimicking the real fabrication procedure with photo- and e-beam lithography. The measurements reveal a contamination layer. Based on this result, it turned out to be necessary to perform additional cleaning of the electrodes before they can be used for realizing organic spin valves. Plasma oxidation was used for this purpose. To test the influence of this cleaning method on the spin injection properties of the Co/Al_2O_3 electrodes, MTJs have been fabricated for which the fabrication of the bottom electrode is similar to the fabrication of the electrodes used in real organic single-crystal FET devices. A detailed picture of the Co/Al_2O_3 electrode interfaces was obtained using transmission electron microscopy (TEM). This will give a detailed understanding of the structure of the fabricated electrodes.

4.2 Photoemission of organic semiconductors and Co or Co/Al_2O_3

Up to now only a few studies on interfacial properties of spintronic relevant electrode materials (e.g. LSMO and Co) and organic semiconductors using photoemission spectroscopy were published. Zhan *et al.* have published interface studies for the organic semiconductor Alq_3 in contact with the electrode materials LSMO [5] and Co [6]. The interfacial properties between LSMO and two organic semiconductors α-sexithiophene (α-6T) and copper-phthalocyanine (CuPc) were also studied, reflecting the influence of an *in-situ* [7] or *ex-situ* [8] cleaning procedure. The interface properties of the organic semiconductor pentacene in contact with Co were previously published by Tiba *et al.* [9] and Popinciuc *et al.* [10]. The influence of a thin tunnel barrier on the interfacial structure between Co and pentacene was studied by Popinciuc *et al.* [11]. In the past, the interfaces between various metallic electrodes and organic semiconductors have been studied widely [12–17]. Most of these interfaces are characterized by the presence of an interface dipole confined to a thin interfacial layer, whereas the origin of this interface dipole is not fully understood yet [18, 19].

In this section, a detailed analysis of interfaces for two organic semiconductors, pentacene and rubrene thin film, in contact with ex-situ, acetone cleaned Co or Co/Al_2O_3 electrodes is presented. The energy-level alignment was studied using combined XPS and UPS. The results demonstrate that the work function of the electrodes under these conditions was smaller than in the atomically clean case, as reported in literature. Moreover, the acetone cleaned interfaces are characterized by very small, short-range interface dipoles and substantial injection barriers for holes. The core-level photoemission spectroscopy measurements rule out chemical reactions. These results give essential information in view of the use of these electrodes in organic spintronic devices.

4.2.1 Ultraviolet photoemission spectroscopy and X-ray photoelectron spectroscopy

UPS combined with XPS is a powerful method to look at the energy level alignment at the interface of different materials in contact with each other. To explain the principle of UPS and XPS, the energy levels of interest have to be considered [12]. In Fig. 4.1a a schematic picture of the Coulombic potential well of an atomic nucleus is drawn. Different energy levels for electrons, the atomic orbitals, are formed inside this potential well. The vacuum level (VL) is the energy above

which an electron can escape from the atom. A simplified picture of an organic molecule consisting of several atoms is given in Fig. 4.1b. The electrons feel an effective potential which is formed by the potential wells of the nuclei and by the interaction with other electrons. At high energy the atomic orbitals form delocalized energy levels, which are filled with electrons up to the highest occupied molecular orbital (HOMO) level. Deep atomic orbitals (core levels) are still localized. The VL represents the energy of an electron just outside the molecule. The difference between the HOMO and the VL is called the ionization energy I and the difference between the lowest unoccupied molecular orbital (LUMO) and the VL the electron affinity A.

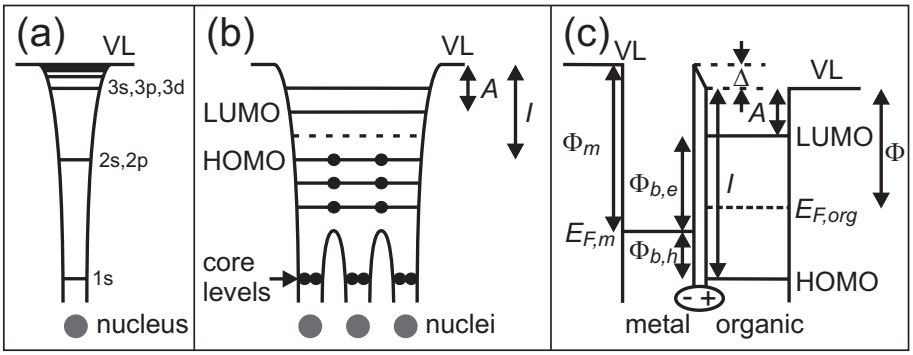

Figure 4.1: (a) Electronic structure inside a potential well for a single atom, showing the atomic orbitals labeled with the orbital names (quantum numbers). (b) Electronic structure of a polyatomic molecule formed by several nuclei, showing the filled (represented by the dots) and empty molecular orbitals, VL, HOMO, LUMO and core levels, ionization energy I and electron affinity A. (c) Representation of the energy levels of a metal and organic material in contact with each other. Shown are the VLs, the Fermi energies of the metal $E_{F,m}$ and the organic material $E_{F,org}$, the workfunction of the metal Φ_m and the organic material Φ, the injection barrier for electrons $\Phi_{b,e}$ and holes $\Phi_{b,h}$, and the shift of the VL at the interface, Δ, due to a dipole, schematically drawn at the bottom.

When an organic semiconductor is brought into contact with a metal (as is the case for an organic FET with metal electrodes), this can be represented by the energy diagram shown in Fig. 4.1c. The two VLs for the metal and organic are shown on the left and right. $\Phi_{b,e}$ and $\Phi_{b,h}$ denote the injection barriers for electrons and holes, respectively. At the interface between the metal and organic material a dipole can be formed, due to charge transfer across the interface, redistribution of the electron cloud, interfacial chemical reactions or an interface layer,

for example. Due to this dipole, there will be an abrupt change in the potential across the interface resulting in a shift of the VL, Δ, across the interface. This is usually denoted as the change in workfunction or surface potential. For UPS, the flat band picture (i.e. band bending, due to, for example, Schottky barrier formation, is not considered) can be considered as a good first-order approximation in the case of thin organic layers, since alignment of the Fermi energies is only possible when there are sufficient mobile charge carriers. For thin layers of non-polar organic materials grown under UHV conditions, this number is expected to be not so large [12].

During UPS, monochromatic light with a high energy (typically 10–45 eV) is radiated on the substrate and the kinetic energy E_k of the emitted electrons (UPS spectrum) is measured. This spectrum can be measured for different thicknesses of the organic layer on a metal surface. First, the bare metal surface is considered, as shown on the left in 4.2a. Electrons in the occupied states below E_F can be excited by the photon energy $h\nu$, where h is the Planck constant and ν the photon frequency, and those with energies above the VL can escape from the metal. The kinetic energy of the electrons is given by

$$E_k = h\nu - E_b, \tag{4.1}$$

where E_b is the binding energy of the electrons before excitation. The electrons with the maximum energy $E_{k,max,m}$ are excited from the Fermi level and the low energy cutoff is set by the VL of the metal $E_{vac,m}$. The work function of the metal can then be calculated by

$$\Phi_m = h\nu - E_{k,max,m}, \tag{4.2}$$

The situation for an organic material in contact with the metal is shown on the right in Fig. 4.2a. The UPS spectrum becomes dominated by electrons originating from the organic material when the thickness of the organic material is increased. The electrons with the maximum kinetic energy $E_{k,max}$ are excited from the HOMO level of the organic material. The ionization energy is given by

$$I = h\nu - E_{k,max}. \tag{4.3}$$

When the spectra of the bare metal and that of the organic material are compared (see also Fig. 4.2b, where they are plotted as a function of E_b according to Eq. 4.1), several quantities can be extracted. A shift in the VL at the interface, Δ, is observed as a shift of the lower cutoff of the UPS spectra. The shift in the upper cutoff of the two spectra $\epsilon_{v,F}$ is given by the energy difference between the HOMO level of the organic material and the Fermi energy of the metal $E_{F,m}$,

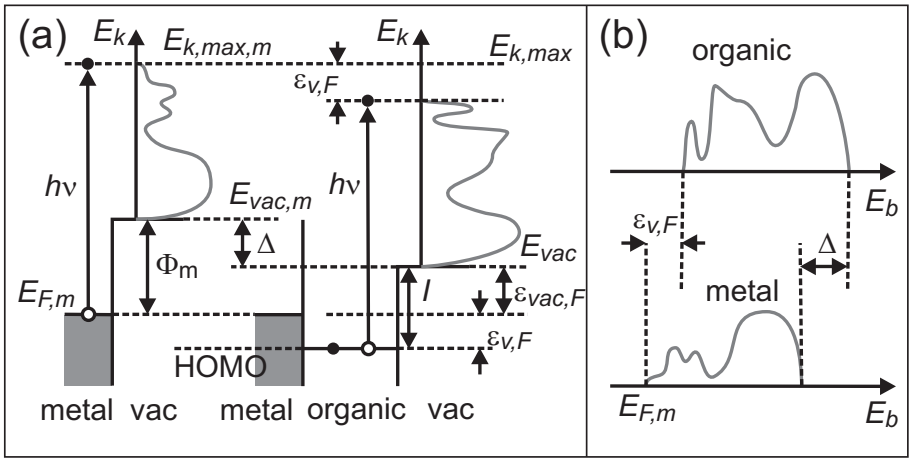

Figure 4.2: (a) Energy levels and UPS spectra (grey lines, intensity vs. kinetic energy E_k) of a metal (left) and a metal/organic interface (right) in vacuum (vac). The UPS spectra result from electrons excited by photons with an energy $h\nu$ as schematically shown by the arrows. Symbols are explained in the text. (b) UPS spectra from the systems in (a) plotted as a function of the binding energy E_b.

which corresponds to the hole injection barrier $\Phi_{b,h}$. The energy of the VL of the organic material relative to the Fermi level of the metal is given by

$$\epsilon_{vac,F} = I - \epsilon_{v,F}. \tag{4.4}$$

This quantity is only equal to the workfunction Φ of the organic material when the Fermi levels of the metal and organic material are aligned, which is not always the case, as explained above.

XPS is based on the same principles as UPS, but the sample is irradiated with photons with a higher energy (typically 200–2000 eV) than during UPS measurements. By tuning the energy of the photons, the core levels (see Fig. 4.1) of the material can be probed, just as the valence levels in the case of UPS. The energy of the core levels is given by

$$E_{core} = E_{k,core} - h\nu, \tag{4.5}$$

where $E_{k,core}$ is the kinetic energy of electrons originating from the core levels by excitation by X-ray radiation. In this way, the chemical composition of the substrate can be determined.

4.2.2 Sample fabrication

As electrodes to the organic layer, ex-situ cleaned polycrystalline Co(40 nm) and Co(40 nm)/Al_2O_3(∼3 nm) films were used. Two pieces of Si wafer with a thermally grown 300 nm thick SiO_2 layer were used as the substrate. The substrates were cleaned in a cleanroom environment with acetone, 2-propanol, and DI-water. In a UHV chamber (base pressure $p_b \leq 10^{-10}$ Torr) Co and Al were deposited via e-beam evaporation, as explained before. The Al coated samples were transferred to a load lock for plasma oxidation without breaking the vacuum. The plasma oxidation was performed with a pressure of 100 mTorr and a voltage of 800 V. The Co/Al samples with a thickness of the Al layer of 2.5 nm were oxidized for 30 minutes resulting in a ∼3 nm thick Al_2O_3 layer. The height of the Al film before the oxidation was determined by a quartz crystal thickness monitor.

The Co and Co/Al_2O_3 substrates were exposed to ambient conditions and subsequently cleaned ex-situ using acetone (2 minute acetone bath and additionally rinsing the sample for 1 minute). In the fabrication of organic electronic devices, e.g. devices which used LSMO as the bottom electrode, such a treatment is also applied [20–23]. By using this kind of ex-situ cleaning it is therefore possible to provide an energy-level alignment that is of relevance for understanding and modeling real devices.

Thin films of rubrene and pentacene were deposited by thermal evaporation on the Co and Co/Al_2O_3 electrodes with a typical evaporation rate of 0.1-0.25 nm/min in a preparation chamber (base pressure $p_b = 2 \cdot 10^{-10}$ mbar), which is directly connected to the analyzer chamber. Subsequently, the films were transferred to the analyzer chamber without breaking the vacuum and characterized taking a full-range XPS spectrum. The number of impurities in the films was very small and below the detection limit of the XPS due to the ultrahigh vacuum conditions during the evaporation of the organic films.

To estimate the thickness of the organic layers the attenuation of the intensity of the Co2p peak was monitored for the Co thin films and the O1s substrate peak for the Co/Al_2O_3 films [24, 25] due to the increasing thickness of the organic film. Following the procedure of Seah and Dench [25], the mean free path of the electrons was calculated to be about 2.27 and 2.11 nm in rubrene and pentacene films, respectively, for the kinetic energy of 955.6 eV for the O1s signal from the contaminated substrates and a density of 1.27 g cm^{-3} for rubrene and 1.32 g cm^{-3} for pentacene [26, 27]. This procedure to determine the thickness of the organic layer is only correct for layer-by-layer growth. If the organic film does not grow uniformly, this method underestimates the film thickness.

4.2.3 Core level spectroscopy

The combined XPS and UPS studies were performed using a commercial PHI 5600 spectrometer, which is equipped with two photon sources. Monochromatized photons with an energy of 1486.6 eV from an Al Kα source for XPS and photons from a He-discharge lamp with an energy of 21.21 eV for UPS were provided. All UPS measurements were done by applying a bias voltage of -9 V to distinguish between the analyzer and sample cutoffs. The spectra were additionally corrected for the contributions of He-satellite radiation. The total energy resolution of the spectrometer was determined by analyzing the width of an Au Fermi edge to be about 350 meV (XPS) and 100 meV (UPS), respectively.

From the core-level photoemission (i.e. XPS) studies before deposition of the organic layer it was concluded that the Co and Co/Al_2O_3 surfaces were covered with a contamination layer consisting of carbon and oxygen. The composition of this contamination layer was determined to be on average 70% carbon and 30% oxygen. The thickness of the contamination layer is about 1 - 2 nm. The thickness of the contamination layer was estimated from photoemission intensities. In previous publications it was already demonstrated that ex-situ cleaning results in a contamination layer independent on the individual details of the applied treatment [8, 28, 29].

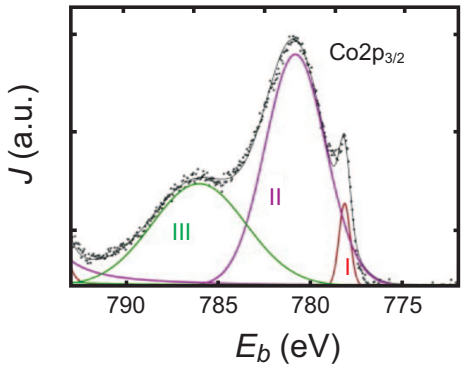

Figure 4.3: XPS spectrum (intensity J vs. binding energy E_b) for the Co2p features of an ex-situ acetone cleaned Co(40 nm) substrate.

To examine the contamination layer in more details the $Co2p_{3/2}$ (in which "2" stands for the shell, "p" for the subshell and the subscript "3/2" for the total angular momentum) core-level emission features is plotted in Fig. 4.3 for a contaminated Co surface after applying an ex-situ cleaning treatment as described above. The Co2p emission shows clearly a three-peak structure (peaks

labeled with I, II, and III). The first peak (I) appears at 778.2 eV for the $Co2p_{3/2}$ component. This binding energy is approximately equal to the binding energy of metallic Co (778.3 eV [30] for Co2p). The two peaks at higher binding energies of 780.8 eV (Peak II) and 786.0 eV (Peak III) match very well the peak structure in the spectrum of native CoO [6, 11, 31]. From the core-level spectroscopy measurements of the Co2p emission it can be concluded that after exposure to air and acetone cleaning, a native cobalt oxide layer results. The separate measurements of the C1s and O1s core-level (spectra not shown) of ex-situ cleaned Co surfaces agree with this result.

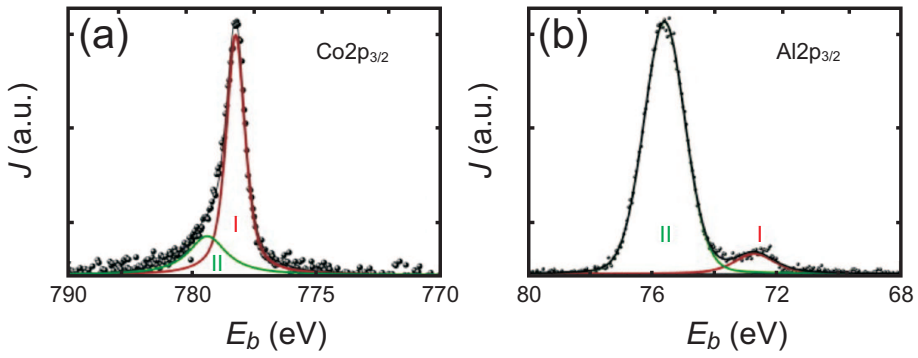

Figure 4.4: XPS spectra (intensity J vs. binding energy E_b) of an ex-situ acetone cleaned Co(40 nm)/Al_2O_3 substrate for the (a) Co2p and (b) Al2p features.

The above described ex-situ cleaning procedure was also applied to the Co/Al_2O_3 electrodes. In Fig. 4.4 the results of the core-level spectroscopy measurements for this electrode are depicted for the $Co2p_{3/2}$ peak (Fig. 4.4a) and the $Al2p_{3/2}$ peak (Fig. 4.4b). The Co2p core-level emission consists of a large peak at a binding energy of 778.3 eV, equal to the binding energy of pure (metallic) Co [30, 31], with a small contribution of CoO (Peak II at 779.4 eV) [6, 11, 31]. As expected from previous publications, the Al_2O_3 layer on top of Co prevents the oxidation of the Co film. The small CoO contribution might be due to a slight over-oxidation of the Al during the fabrication process. The spectrum of the Al2p emission feature shows a two-peak structure indicating the presence of reduced species at the lower binding energy side (Peak I at 72.7 eV). The structure at higher binding energies (Peak II) at 75.6 eV is in good agreement with the energy of the Al2p emission in Al_2O_3.

From the obtained core-level photoemission spectroscopy studies some first information about the interfacial electronic properties can be obtained. The data for the Co2p (Fig. 4.5a) and the Al2p (Fig. 4.5b) core-level emission features

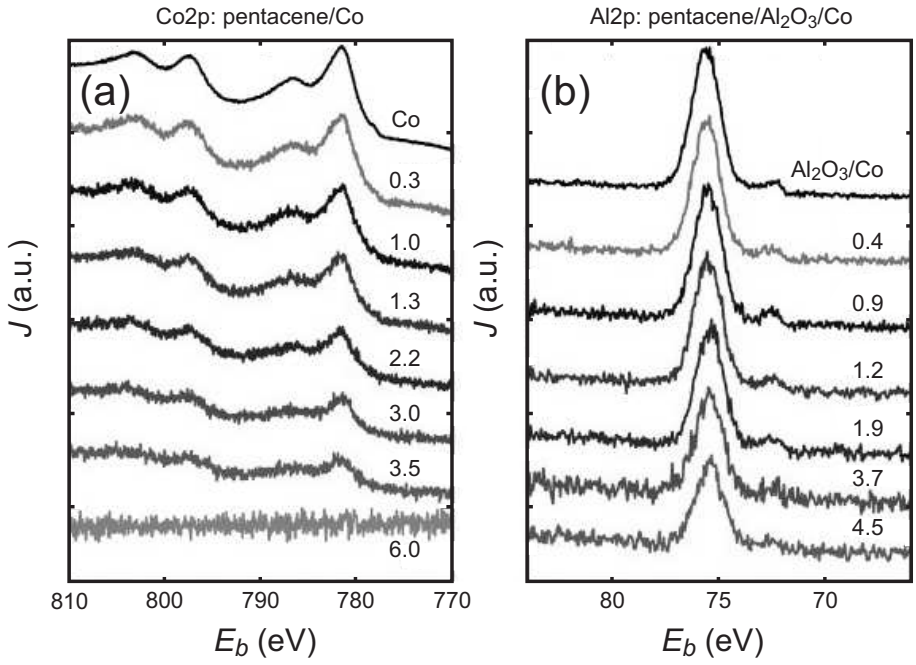

Figure 4.5: XPS spectra (intensity J vs. binding energy E_b) for (a) the Co2p features of an ex-situ acetone cleaned Co(40 nm)/pentacene sample for different pentacene thicknesses and (b) the Al2p features of an ex-situ acetone cleaned Co(40 nm)/Al_2O_3/pentacene sample for different pentacene thicknesses.

for a Co/pentacene and Co/Al_2O_3/pentacene interface is plotted, respectively, depending on the film thickness of pentacene. The spectral shape of the Co2p and Al2p core-level remain unchanged independent of the respective film thickness. The binding energy of the core-level is constant. In the core-level photoemission spectra of the Co2p and Al2p (not shown) emissions for the Co/Al_2O_3/rubrene interface constant binding energies and an unchanged spectral shape for different rubrene film thicknesses are also observed. This shows that the contamination layer is closed and prevents any chemical reactions between the substrates and the organic semiconductors.

4.2.4 Valence level spectroscopy

The UPS data of a Co/Al_2O_3/pentacene and Co/Al_2O_3/rubrene sample are shown in Fig. 4.6a and b, respectively. Different spectra are plotted for different thicknesses of the organic layer. These data give a detailed knowledge of the interface properties of these two different electrode/organic interfaces. In the

top spectra of each panel the valence-band spectra from the ex-situ cleaned Co and Co/Al_2O_3 surfaces are shown. In both cases the characteristic valence-band features of the substrate are suppressed due to the presence of the contamination layer on top of the substrate surface. Consequently, the valence-band region is featureless as expected for such contaminated electrodes.

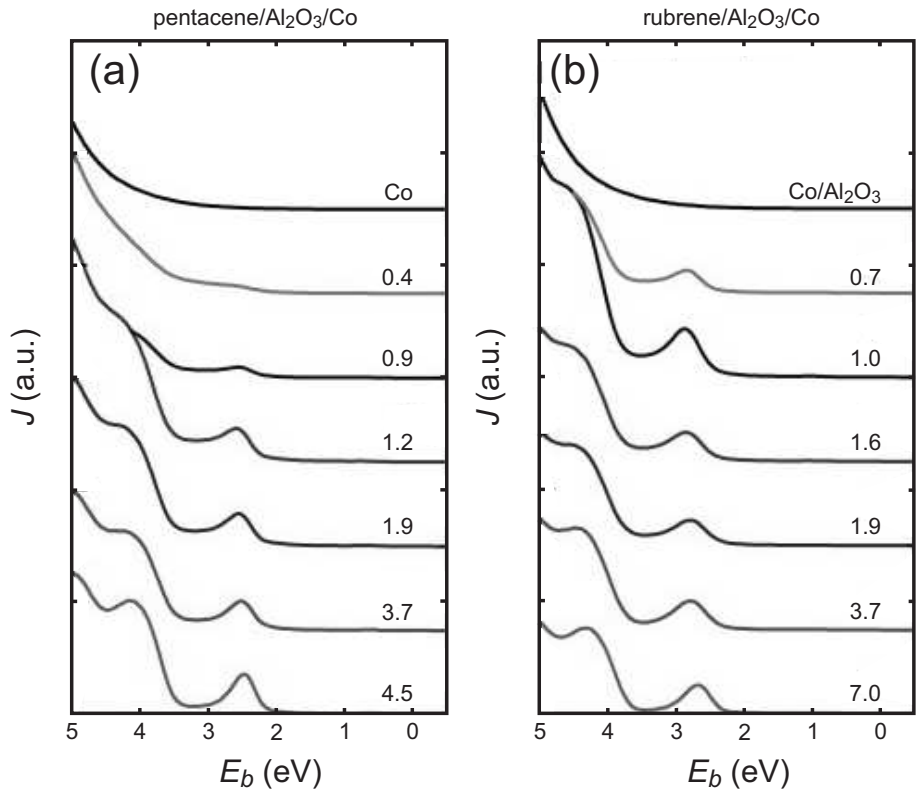

Figure 4.6: UPS spectra (intensity J vs. binding energy E_b) for (a) an ex-situ acetone cleaned Co(40 nm)/Al_2O_3/pentacene sample for different pentacene thicknesses and (b) an ex-situ acetone cleaned Co(40 nm)/Al_2O_3/rubrene sample for different rubrene thicknesses

The work function of the ex-situ cleaned Co surface used in the studies was measured to be 4.3 eV within an experimental error of 0.1 eV. This value is substantially smaller than that of a clean polycrystalline Co surface (5.0-5.1 eV) [6, 9, 10, 32]. The reduced work function due to presence of the contamination layer and the oxidation of Co presents an expected result which is in good agreement to previously published interface studies using ex-situ cleaned electrode materials [8, 28, 29]. In the case of ex-situ cleaned Al_2O_3 surfaces a work function ranging from 3.1 to 3.5 eV was measured, which was very low compared to

the literature value of the workfunction of Co. This reduced workfunction might originate from the contamination layer and the Al_2O_3 tunnel barrier. Further research has to determine the reason for the observed low workfunction and the influence of the tunnel barrier thickness.

The typical valence-band features of the organic semiconductors pentacene and rubrene become more and more visible with an increase in the organic semiconductor film thickness. In the case of contaminated Co/Al_2O_3/pentacene and Co/Al_2O_3/rubrene interfaces (see Fig. 4.6), and for Co/pentacene interfaces (not shown) the energy position of the features is almost independent of the corresponding organic film thickness. Consequently the energy-level alignment can be measured in a thin interfacial region. The individual features of the pentacene valence-band are in good agreement with previous publications [33, 34]. Previously reported valence-band studies [35, 36] on rubrene interfaces show a good agreement with the individual features of the observed rubrene valence-band in this study. The point of interest here is the onset of the spectral feature at the lowest binding energy side, corresponding to excitation from the HOMO level of the organic material, as explained in section 4.2.1. The low binding emission edge of the valence-band onset was determined by linear extrapolation. The uncertainty of this procedure is estimated to be 0.1 eV. The hole injection barrier at both interfaces is 1.0 and 2.2 eV for the Co/pentacene and the Co/Al_2O_3/pentacene interfaces, respectively. For the Co/Al_2O_3/rubrene interface the barrier for hole injection was determined to be 2.3 eV.

4.2.5 Energy level alignment

The results of the energy-level alignment for the three studied interfaces are summarized in Fig. 4.7. The interface between pentacene and CoO is characterized by a very small interface dipole Δ =-0.1 eV (see Fig. 4.7a). The strong change of the interface dipole compared to clean Co electrodes is attributed to the reduced work function of Co due to the contamination layer on top of the acetone cleaned Co surface. The previously reported origin of the interface dipole at clean Co/pentacene interfaces in the form of chemical reactions (hybridization) and formation of interface gap states [9, 10] can be ruled out in case of contaminated Co/pentacene interfaces. The UPS results show no evidence for the formation of interface gap states. Furthermore, the observed thickness-independent and constant binding energy features of the core-level emissions of Co2p and the valence band emission of the HOMO level exclude chemical reactions at the studied Co/pentacene interfaces. The hybridization of the frontier HOMO level of pentacene and the Co3d bands observed in former studies [9, 10], is precluded due to

the fact that the contaminations of carbon and oxygen result in a native Co oxide layer on the ex-situ cleaned Co surfaces. This conclusion was also confirmed by a featureless valence-band of the contaminated Co substrates as discussed before.

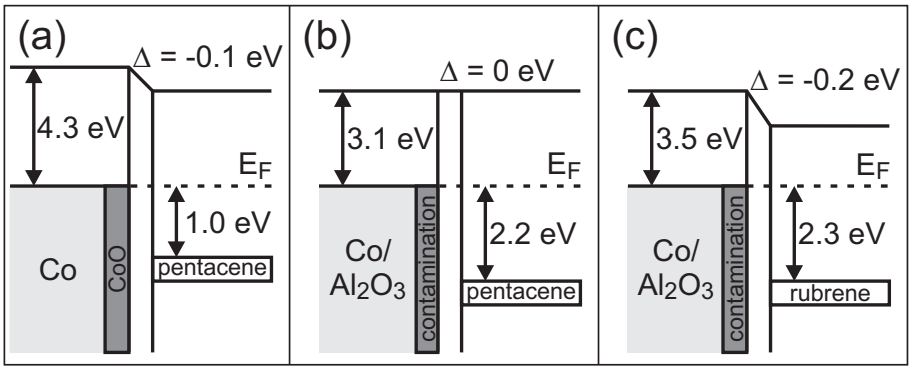

Figure 4.7: Schematic energy level diagrams for ex-situ acetone cleaned (a) Co/pentacene, (b) Co/Al_2O_3/pentacene and (c) Co/Al_2O_3/rubrene samples. The Fermi energy E_F of the electrode, the shift of the VL at the interface, Δ, and the hole injection barrier Φ_b^h are shown.

For the Co/pentacene sample a hole injection barrier of 1.0 eV was observed, equal to the barrier for hole injection at clean Co/pentacene interfaces [9, 10]. In comparison to the results of clean Co/pentacene interfaces a reduction of the interface dipole by 0.9 eV and a comparable reduction of the Co work function by 0.8 eV was measured. Thus, the energy level alignment at contaminated Co/pentacene interfaces is only influenced by the reduction of the Co work function due to the observed contamination layer.

In Fig. 4.7b and c the data of the energy-level alignment for the Co/Al_2O_3/ pentacene and the Co/Al_2O_3/rubrene interfaces are depicted, respectively. For the Co/Al_2O_3/ rubrene sample a very small interface dipole Δ =-0.2 eV could be observed. In the case of the Co/Al_2O_3/pentacene VL alignment is measured. As discussed above, constant binding energy features for the Co2p and Al2p core-level emissions as well as of the frontier orbitals (HOMO) with increasing organic film thickness could be determined. Furthermore, no interface gap states could be observed. Consequently, both interfaces are free from chemical reactions.

For both interfaces a very large hole injection barrier of 2.2 $\pm$ 0.1 eV could be demonstrated. Popinciuc *et al.* [11] demonstrated that the hole injection barrier depends on the thickness of the Al_2O_3 tunnel barrier. They report a hole injection barrier of 0.85 eV for an Al_2O_3 thickness of 1 nm for clean Co/Al_2O_3/pentacene interfaces. For a Al_2O_3 barrier of 0.6 nm the hole injection barrier became 0.60

eV. The difference for the interface measured in this chapter could arise from the thicker tunnel barrier and the presence of a contamination layer.

As compared to the clean (the samples were not taken out of the UHV in between fabrication and measurement) Co and Co/Al_2O_3 cases an increase of the hole injection barrier for acetone cleaned electrodes was observed. The observed small interface dipoles correspond nearly to the Schottky-Mott limit (vacuum level alignment) [37, 38]. The energy-level alignment is therefore not influenced by charge transfer through the tunnel barrier. The large hole injection barriers are expected to hinder the injection of charge carriers in spintronic devices, resulting in an increase of the interface resistance. This might be a problem for spin injection. To stress the relevance of this work done on Co/Al_2O_3/organic semiconductor samples, it can be noted that spin-polarized injection at room temperature using Co/Al_2O_3 electrodes has been demonstrated by Santos *et al.* [39]. In this work the organic semiconductor Alq_3 has been used as spacer material. Spin injection into graphene [40] and silicon [41] has also been demonstrated using Co/Al_2O_3 and FM/Al_2O_3 electrodes.

In summary, the energy-level alignment of ex-situ acetone cleaned Co and Co/Al_2O_3 electrodes in contact with organic semiconductors pentacene and rubrene was determined. The results demonstrate that the work function under these conditions is smaller than the atomically clean case. Moreover, the studied interfaces are characterized by very small interface dipoles (within the experimental error of 0.1 eV) and substantial injection barriers for holes, which could be due to the presence of the tunnel barrier and the contamination layer. Further measurements with different thickness of the tunnel barrier and samples without contamination layers could give more information about the injection barrier. The data of the experiments described above represent essential information in view of their use in organic spintronic devices. The core-level photoemission spectroscopy measurements rule out chemical reactions.

4.3 Cleaning of interfaces by plasma oxidation

The photoemission spectroscopy reveals a contamination layer on the Co/Al_2O_3 electrodes cleaned with acetone and a large hole injection barrier is formed. This could be detrimental for injecting a spin-polarized current, since the spins could be scattered and the polarization lost. It will be showed here that the acetone cleaning is indeed detrimental for spin injection. Cleaning of the electrodes is therefore needed before organic single-crystal (OSC) lamination. Plasma oxidation was tested as a cleaning method and show this method gives electrodes with

good spin injection properties.

4.3.1 Contaminated interfaces

To test the spin injection and detection properties of the Co/Al_2O_3 electrodes, magnetic tunnel junctions (MTJs) consisting of Co as the bottom electrode, Al_2O_3 as the tunnel barrier and NiFe (Py) as the top electrode were fabricated. The MTJs were fabricated by evaporating Co through a shadow mask in an evaporator with base pressure $p_b \leq 10^{-10}$ Torr. Al was evaporated on top of the Co layer through the same mask. Without breaking the vacuum, the sample was transferred to the load lock of the evaporator, where the Al was plasma oxidized to form a layer of Al_2O_3. After that, the sample was transferred back to the UHV chamber to deposit a NiFe layer on top through a different shadowmask. The active tunnel area of this MTJ is 250 x 300 μm^2. MTJs fabricated in this way give a magnetoresistance (*MR*) of around 18% (see Fig. 4.8a), which is in good agreement with values reported in literature [42]. These MTJs with clean interfaces are used as reference samples.

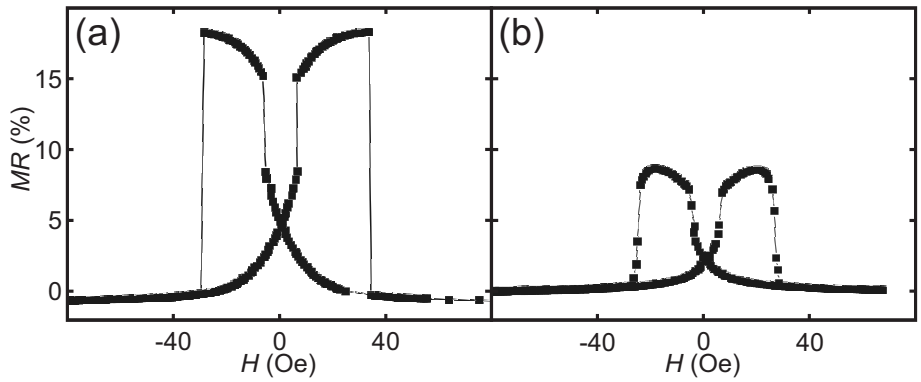

Figure 4.8: *MR* of MTJs consisting of a Co/Al_2O_3/NiFe stack for (a) an MTJ fabricated without breaking the vacuum (Al_2O_3 thickness $d_{Al_2O_3} \sim 3.5$ nm, device resistance $R = 3.6$ kΩ) and (b) an MTJ where the Co/Al_2O_3 layer was treated with acetone and 2-propanol ($d_{Al_2O_3} \sim 3$ nm, $R = 68$ kΩ). The applied voltage V = -10 mV for both devices.

To study the influence of the contamination layer on the electrodes after cleaning with acetone, MTJs in which the Co/Al_2O_3 layer has been exposed to acetone and 2-propanol were fabricated. This is a way to study the effect of fabrication with photo- and e-beam lithography, since in these fabrication methods acetone is used for lift-off (see chapter 1 and Appendix A). In these

samples, the Co/Al_2O_3 was fabricated as described above. After that, the samples were put in acetone for one night, dipped in 2-propanol and dried using a spinner. The sample were put back into the evaporator to deposit the NiFe top electrode. The resulting *MR* of these devices are shown in Fig. 4.8b.

If the two devices are compared, a large drop in *MR* from 18% to 9% is observed in the MTJ for which the Co/Al_2O_3 layer has been exposed to acetone and 2-propanol. Although the value of the *MR* shows that spin injection with the contaminated Co/Al_2O_3 was still possible, it clearly demonstrates the negative effect of acetone and 2-propanol cleaning on the spin injection properties.

4.3.2 Cleaned interfaces

As is clear from the previous sections, a cleaning step after fabrication of the electrodes with photo- or e-beam lithography is desired, since the acetone and 2-propanol form a contamination layer which is hindering the injection of spin polarized currents. Cleaning of the electrodes can be done by an oxygen plasma cleaning step to remove any organic contaminations. During the oxygen plasma cleaning, the Co/Al_2O_3 layer will also be further oxidized. After the complete oxidation of Al, Co will be oxidized and CoO will be formed. If this happens, the spin polarized current will be lower, since CoO possesses anti-ferromagnetic correlations, which cause spin-flip scattering. Therefore, over-oxidation of the Al_2O_3 has to be prevented.

To prevent over-oxidation, but at the same time use plasma oxidation for cleaning, MTJs are fabricated as described below. Co and Al were deposited in the same way as for the reference samples. The plasma oxidation step to form Al_2O_3 was shortened by 10 minutes (see Appendix A for the oxidation times). In this shorter oxidation step, substoichiometric AlO_x is formed [43]. The obtained Co/AlO_x electrodes were then dipped in acetone, covered with a photoresist layer, dipped in a photoresist developer (OPD 4262), put in acetone for one night, dipped in 2-propanol and dried using a spinner, to completely mimic the fabricating method with photolithography. The samples were put back in the loadlock of the evaporator for an additional plasma oxidation of 10 minutes to complete the stoichiometric Al_2O_3 formation *and* clean the electrodes at the same time. After that, NiFe was deposited on top. The resulting MR of devices with two different Al thicknesses, $d_{Al_2O_3} \sim 2.5$ and 3 nm, are shown in Fig. 4.9a and c, respectively. For both thicknesses several MTJs are fabricated.

Cleaning the Co/Al_2O_3 electrodes with an oxygen plasma step before deposition of the NiFe electrode resulted in an increase of the MR values as compared to the uncleaned electrodes. For $d_{Al_2O_3} \sim 2.5$ nm, *MR* values of ∼12–16% are

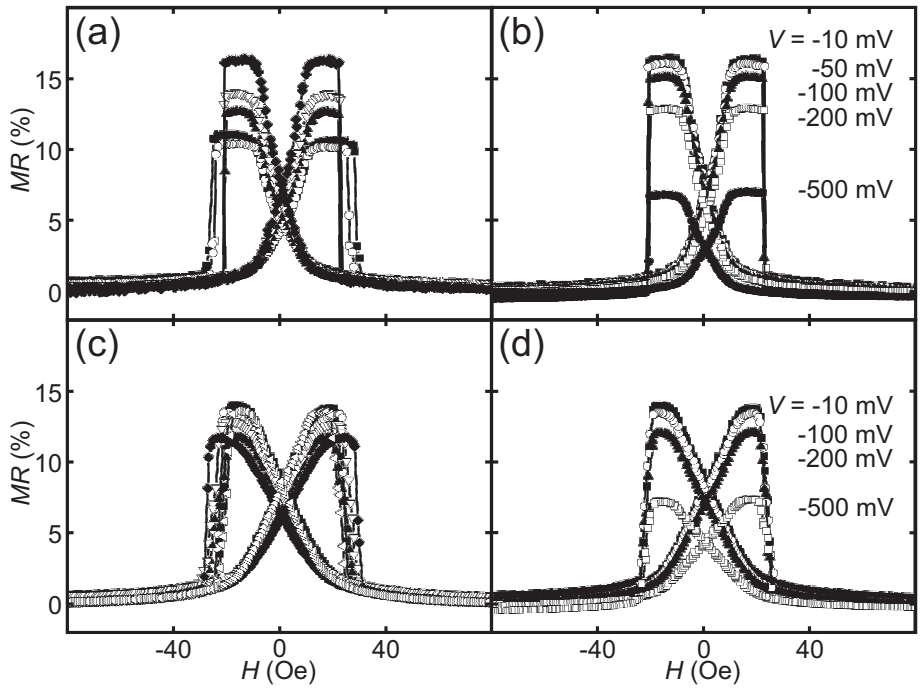

Figure 4.9: *MR* of MTJs consisting of a $Co/Al_2O_3/NiFe$ stack with an oxygen plasma cleaned interface as described in the text for (a) 5 MTJs with $d_{Al_2O_3}$ ∼2.5 nm and R = 110-150 kΩ and (b) the bias dependence of the *MR* for one of these MTJs, and (c) 6 MTJs with $d_{Al_2O_3}$ ∼3 nm and $R \sim 70$ kΩ and (b) the bias dependence of the MR for one of these MTJs. The applied voltage in (a) and (c) V = -10 mV.

obtained, and for $d_{Al_2O_3} \sim 3$ nm, *MR* values of ∼12–14%. These values are substantially larger than in the case of the contaminated bottom electrode. Although the *MR* values are not as high as in the case of the reference MTJ, the oxygen plasma cleaning can increase the *MR* to values close to it. This cleaning step is therefore a good option to obtain clean Co/Al_2O_3 electrodes with good spin injection properties.

MR as a function of the applied voltage was also measured for Al_2O_3 thicknesses of ∼2.5 and 3 nm, as shown in Fig. 4.9b and d, respectively. A drop was observed in the MR as the voltage increased. This is usually observed in spintronic devices, but not yet fully understood. These measurements will give an idea how much current can pass through the electrodes before the spin injection property is lost. Voltages $|V| > 2$ V resulted in break-down of the MTJ.

4.4 Ferromagnetic electrodes

As discussed in the previous section, clean Co/Al_2O_3 electrodes with good spin injection properties can be made using photolithography. Since the proposed FET structure, as discussed in chapter 3 consist of small electrodes, these kind of structures have to be considered for fabrication of organic spin valve FETs. Charge injection in OSC FETs happens in a small region close to the dielectric interface, since only there charges are induced by the gate electrode. This implies that especially the edge of the electrode, close to the SiO_2/organic interface, is important for good charge and spin injection.

To study the FM electrodes used in OSC FETs, a cross section of these electrodes (see Fig. 4.10a), was imaged with transmission electron microscopy (TEM). A TEM picture of a region in the middle (i.e. not on the edges) of one of the electrodes is shown in Fig. 4.10b. Co and Al_2O_3 films on a Si/SiO_2 substrate can be observed. The Al_2O_3 film was covered by a metal capping layer, needed for sample preparation. The smooth Al_2O_3 film completely covers the Co film.

Since the large non-conducting SiO_2 layer is charged during TEM, which makes it more difficult to see small features, also Co/Al_2O_3 electrodes on Si with only a thin native SiO_2 layer are fabricated. A high-resolution TEM picture of the cross section of part of one of these electrodes is shown in Fig. 4.10c. The crystalline Si, amorphous SiO_2, polycrystalline Co and amorphous Al_2O_3 layers can be seen. The Al_2O_3 is covered with glue, which was needed for preparing the sample for TEM measurements. Again, the Al_2O_3 fully covers the Co layer.

In Fig. 4.10d a TEM picture is shown which was taken on the edge of one of the electrodes. Due to the resist with edges with a negative slope (see chapter 3), the edge of the electrode also has a finite slope. The whole (dark) Co electrode is covered with a lighter layer, which is probably the Al_2O_3 layer. However, this has to be stated with care, since CoO can be formed when the Co is uncovered, which will also give a layer with a lighter color.

To investigate the precise composition of the layers, energy filtered (EF) TEM were performed. EFTEM makes it possible to visualize the different elements which are present. In Fig. 4.10e and f, a normal TEM picture and an EFTEM picture of the same area is shown. The elements Co, O and Si are shown, represented by the different colors red, blue and yellow, respectively. In this picture the oxide layers are clearly observed. The sharp interfaces between the Co and the oxide layer makes it very likely that the Co is fully covered by an Al_2O_3 layer. The red an blue parts on the top left of the picture are caused by drift in the measurement, giving distortions in the glue. The red parts on top of the Co/Al_2O_3 electrode therefore do not correspond to Co found outside the electrodes.

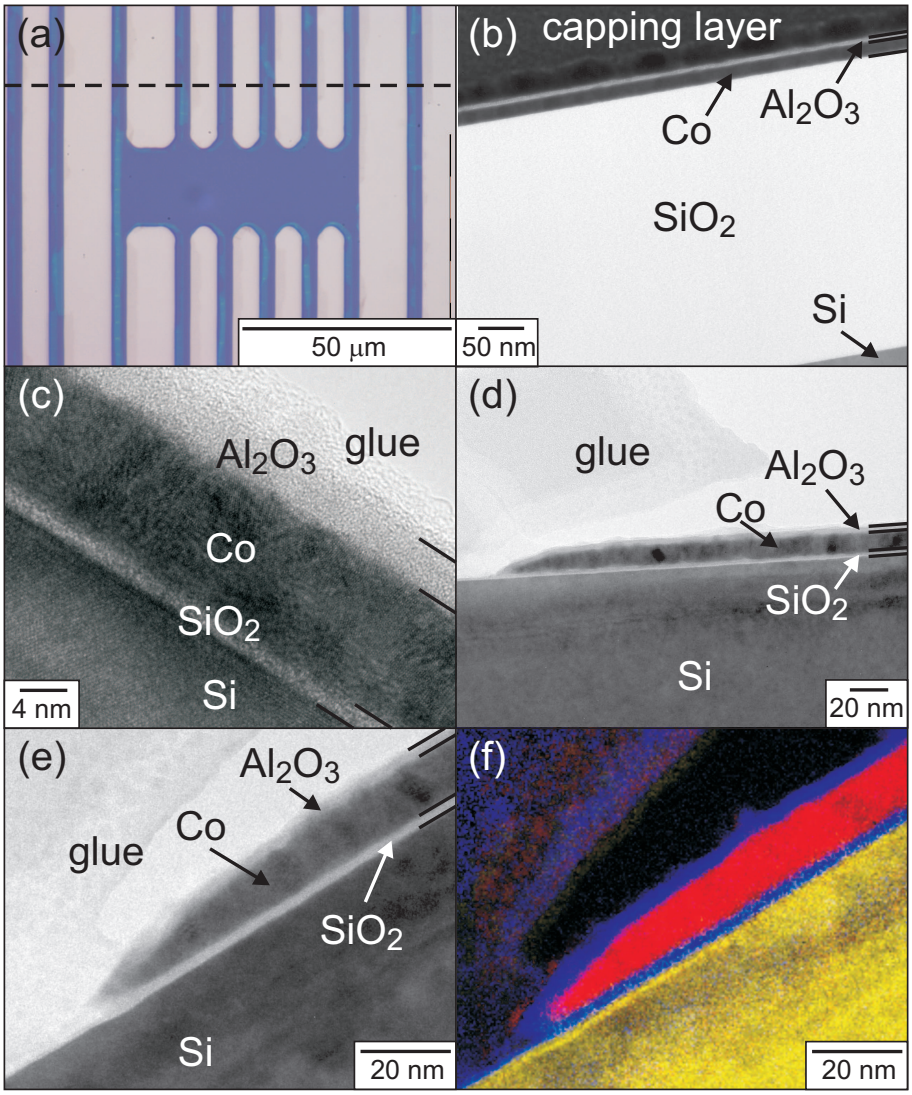

Figure 4.10: TEM measurements. (a) Photograph of Co/Al_2O_3 electrodes, showing the cross section (dashed line) for TEM images. TEM pictures of a cross section of (b) the middle of an electrode on Si/SiO_2(300 nm), (c) the middle of an electrode on Si/native SiO_2, (d) – (f) the edge of an electrode on Si/native SiO_2. The picture in (f) is an image from the same area as in (e), made with energy filtered (EF) TEM, showing the elements Co (red), O (blue) and Si (yellow).

4.5 Conclusions

In the studies presented in this chapter, it was observed that the photolithography process, in which acetone is used, leads to a contamination of the Co/Al_2O_3 electrodes. This contamination layer is accompanied by a large hole injection barrier and a deterioration of the spin injection properties. This problem is solved by adding a cleaning step to the fabrication process. Cleaning of the electrodes by oxygen plasma resulted in an increase of the MR values of contaminated MTJs. This shows that photolithography can be used to fabricate FM electrodes suitable for spin-valve devices.

TEM images show that the Al_2O_3 is covering the Co over the whole electrodes. This is important considering the conductivity mismatch problem. In particular the edge of the electrode is of crucial importance, since there the charge and spin injection takes place. The images seem to reveal that the Co is also on the edges covered with Al_2O_3. This makes these electrode potentially suitable for spin injection and detection in OSC spin valves.

In short, fabrication by photolithography and e-beam lithography, in which organic solvents are used, seems suitable to fabricate clean FM electrodes suitable for spin injection and detection.

References

[1] O.M.J. van 't Erve, G. Kioseoglou, A.T. Hanbicki, C.H. Li and B.T. Jonker, Appl. Phys. Lett. **84**, 4334 (2004).

[2] H.-W. Liu, H.-J. Chang, G.-P. Li and M. Bachman, IEEE Electron Dev. Lett. **30**, 346 (2009).

[3] G. Schmidt, D. Ferrand, L.W. Molenkamp, A.T. Filip and B.J. van Wees, Phys. Rev. B **62**, R4790 (2000).

[4] A. Fert and H. Jaffrès, Phys. Rev. B **64**, 184420 (2002).

[5] Y.Q. Zhan, I. Bergenti, L.E. Hueso, V. Dediu, M.P. de Jong and Z.S. Li, Phys. Rev. B **76**, 045406 (2007).

[6] Y.Q. Zhan, M.P. de Jong, F.H. Li, V. Dediu, M. Fahlman and W.R. Salaneck, Phys. Rev. B **78**, 045208 (2008).

[7] M. Grobosch, K. Dörr, R.G. Gangineni and M. Knupfer, Appl. Phys. A **95**, 95 (2009).

[8] M. Grobosch, K. Dörr, R.G. Gangineni and M. Knupfer, Appl. Phys. Lett. **92**, 023302 (2008).

[9] M.V. Tiba, W.J.M. de Jonge, B. Koopmans and H.T. Jonkman, J. Appl. Phys. **100**, 093707 (2006).

[10] M. Popinciuc, H.T. Jonkman and B.J. van Wees, J. Appl. Phys. **100**, 093714 (2006).

[11] M. Popinciuc, H.T. Jonkman and B.J. van Wees, J. Appl. Phys. **101**, 093701 (2007).

[12] H. Ishii, K. Sugiyama, E. Ito and K. Seki, Adv. Mater. **11**, 605 (1999).

[13] W.R. Salaneck, K. Seki, A. Kahn and J.J. Pireaux, *Conjugated Polymer and Molecular Interfaces: Science and Technology for Photonic and Optoelectronic Applications*, Marcel-Dekker, New York (2002).

[14] A. Kahn, N. Koch and W. Gao, J. Polym. Sci. **41**, 2529 (2003).

[15] M. Knupfer and H. Peisert, Phys. Stat. Sol. (a) **201**, 1055 (2004).

[16] N. Koch, ChemPhysChem **8**, 1438 (2007).

[17] N. Koch, J. Phys.: Cond. Matter **20**, 184008 (2008).

[18] M. Knupfer and G. Paasch, J. Vac. Sci. Technol. A **23**, 1072 (2005).

[19] H. Vazquez, W. Gao, F. Flores and A. Kahn, Phys. Rev. B **71**, 041306(R) (2005).

[20] Z.H. Xiong, D. Wu, Z.V. Vardeny and J. Shi, Nature **427**, 821 (2007).

[21] S. Majumdar, R. Laiho, P. Laukkanen, I.J. Vayrynen, H.S. Majumdar and R. Österbacka, Appl. Phys. Lett. **89**, 122114 (2006).

[22] S. Majumdar, H.S. Majumdar, R. Laiho and R. Österbacka, J. Alloys Compd. **423**, 169 (2006).

[23] Z.Y. Pang, Y.X. Chen, T.T. Liu, Y.P Zhang, S.J. Xie, S.S. Yan, S.H. Han, Chin. Phys. Lett. **23**, 1566 (2003).

[24] H. Peisert, T. Schwieger, M. Knupfer, M.S, Golden and J. Fink, J. Appl. Phys. **88**, 1535 (2000).

[25] M.P. Seah and W.A. Dench, Surf. Interface Anal. **1**, 2 (1979).

[26] R.B. Campbell and J.M. Robertson, Acta Cryst. **15**, 289 (1962).

[27] E.A. Silinsh and V. Capek, *Organic Molecular Crystals: Interaction, Localization and Transport Phenomena*, AIP Press, New York (1994).

[28] A. Wan, J. Hwang, F. Amy and A. Kahn, Organ. Electron. **6**, 47 (2005).

[29] M. Grobosch and M. Knupfer, Adv. Mater. **19**, 754 (2007).

[30] J.F. Moulder, W.F. Stickle, P.E. Sobol and K.D. Bomben, *Handbook of X-ray Photoelectron Spectroscopy*, J. Chastain (ed.), Perkin-Elmer Cooperation, Eden Prairie (1992).

[31] B.V. Christ, *Handbook of monochromatic XPS spectra: The elements of native oxides*, Wiley-VCH, Chichester (2000).

[32] H.B. Michaelson, J. Appl. Phys. **48**, 4729 (1977).

[33] N. Koch, I. Salzmann, R.L. Johnson, J. Pflaum, R. Friedlein and J.P. Rabe, Org. Electron. **7**, 537 (2006).

[34] A. Vollmer, H. Weiss, S. Rentenberger, I. Salzmann, J.P. Rabe and N. Koch, Surf. Sci. **600**, 4004 (2006).

[35] Y. Harada, T. Takahashi, S. Fujisawa and T. Kajiwara, Chem. Phys. Lett. **62**, 283 (1979).

[36] L. Wang, S. Chen, L. Liu, D. Qi, X. Gao and A.T.S. Wee, Appl. Phys. Lett. **90**, 132121 (2007).

[37] W. Schottky, Phys. Z. **41**, 570 (1940).

[38] N.F. Mott, Proc. R. Soc. London **171**, 27 (1939).

[39] T.S. Santos, J.S. Lee, P. Migdal, I.C. Lekshmi, B. Satpati and J.S. Moodera, Phys. Rev. Lett. **98**, 016601 (2007).

[40] N. Tombros, C. Jozsa, M. Popinciuc, H.T. Jonkman and B.J. van Wees, Nature **448**, 571 (2007).

[41] B.T. Jonker, G. Kioseoglou, A.T. Hanbicki, C.H. Li and P.E. Thompson, Nature Phys. **3**, 542 (2007).

[42] J.S. Moodera, L.R. Kinder, T.M. Wong and R. Meservey, Phys. Rev. Lett. **74**, 3273 (1995).

[43] A.E.T. Kuiper, M.F. Gillies, V.Kottler, and G.W. 't Hooft, J.G.M. van Berkum, C. van der Marel, Y. Tamminga and J.H.M. Snijders, J. Appl. Phys. **89**, 1965 (2001).

Chapter 5

Controlled tunnel-coupled ferromagnetic electrodes for spin injection in organic single-crystal transistors

In this chapter, single-crystal rubrene field-effect transistors (FETs) with ferromagnetic Co electrodes, tunnel-coupled to the conduction channel via an Al_2O_3 tunnel barrier, are presented. Magnetic and electronic characterization showed that the Al_2O_3 film not only protected the Co from undesired oxidation, but also provided a highly controlled tunnel barrier for overcoming the conductivity mismatch problem when injecting spins from a ferromagnetic metal into a semiconductor. These FETs provide a significant step towards the realization of a device that integrates FET and spin-valve functionality, one of the major goals of spintronics.

Parts of this chapter will be published as W.J.M. Naber, M.F. Craciun, J.H.J. Lemmens, A.H. Arkenbout, T.T.M. Palstra, A.F. Morpurgo and W.G. van der Wiel, *accepted for publication in* Organic Electronics.

5.1 Introduction

Both spin electronics (spintronics) and organic electronics have made their introduction in science and technology in the last few decades. Spintronics adds new functionality and economy to electronic devices by not only applying the electron's charge, but also its spin [1]. Organic materials particularly provide fabrication advantages, allowing for, e.g., light-weight and flexible electronics [2]. The merging of these two developments into the field of *organic spintronics* [3, 4] not only potentially combines the advantages of both parental fields, but also provides additional value. Organic materials are expected to have long spin lifetimes, due to their low spin-orbit coupling and reduced hyperfine interaction, as compared to their inorganic counterparts [5]. This makes organic materials particularly interesting for application in spintronic devices.

In this chapter, a crucial step towards the application of organic single-crystals [6] for realizing *spin-valve field-effect transistors (spin-valve FETs)* is described. The long-range order of these crystals makes them the organic semiconductors with the highest carrier mobility known at the moment [7]. They are therefore a logical choice for spin-valve FETs, in which both the scattering time and spin lifetime need to be sufficiently long [3]. Recent studies on organic single-crystal FETs have shown that a broad variety of materials can be used as source and drain electrodes with good performance. Since some of those materials are ferromagnetic [8–10], the question naturally arises whether the spin polarization of the electrodes can be used to inject spins into the accumulation layer of an organic FET, to realize an electrically controlled spin-valve, i.e. a spin-valve FET [11]. This is a highly desired – but, to the best of our knowledge, yet to be realized – goal in spintronics.

Unfortunately, the ferromagnetic electrode materials used so far (nickel and cobalt) are not suitable without modifications, since their oxides are antiferromagnetic and would therefore cause spin randomization during the injection of charge carriers from the metal into the organic single-crystal. Moreover, the electrodes should be tunnel-coupled to the conduction channel in the organic single-crystal, to overcome the conductivity mismatch problem of injecting spins from a metallic ferromagnet into a semiconductor [12, 13].

For the first time, FETs of 5,6,11,12-tetraphenylnaphthacene (rubrene, $C_{42}H_{28}$) single-crystals with high-quality, ferromagnetic Co electrodes and Al_2O_3 tunnel barriers are presented, that can be used for carrier injection without spin randomization. Although the device layout, well-controlled interface, and choice of materials seem ideal for realizing the spin-valve effect, it has remained elusive in these devices so far. Possible reasons are discussed near the end of the chapter,

and are expected to evoke both theoretical and experimental follow-up.

5.2 Device characterization

Figure 5.2a is a photograph of one of the devices, showing the Co/Al_2O_3 electrodes (light bars) underneath a piece of rubrene single-crystal. Cobalt electrodes were chosen for two reasons. First, its work function aligns favorably with the HOMO of rubrene [4], which helps in maximizing the amount of carriers injected from the electrodes into the semiconductor via tunneling (rather than thermal activation over the Schottky barrier). Second, technological processes are known, that allow the controlled realization of a very thin Al_2O_3 layer on top of the Co film, acting at the same time as a well-defined tunnel barrier and as a protective layer against oxidation of the ferromagnet (which is crucial, since CoOx is known to possess antiferromagnetic correlations, which would cause spin-flip scattering, randomizing the carrier spin during the injection. The Co electrodes (16 nm thick) were defined by photolithography on a highly doped Si/SiO_2(300 nm) wafer and covered with a 2.5 nm Al_2O_3 tunnel barrier. The high-quality, pin-hole-free Al_2O_3 film was formed by plasma oxidation of Al evaporated on top of Co without breaking the UHV (10^{-10} Torr). This Al_2O_3 tunnel barrier prevents the Co electrodes from oxidation and helps to overcome the conductivity mismatch, as mentioned above. After lift-off with acetone, the electrodes were thoroughly cleaned in an oxygen plasma to ensure no resist was left. This is essential, as demonstrated by independent photon emission spectroscopy measurements (see chapter 4) [14]. Directly after this a rubrene single-crystal was electrostatically laminated on top of the electrodes. The lamination process yields uniform contact without air gaps, bubbles or interference fringes [6]. Similar single-crystal FET geometries were studied before in the case of non-ferromagnetic electrodes [6, 8, 9].

In order to verify the critical features of the device, first the experiments described below are performed. A $Co/Al_2O_3/NiFe$(permalloy) magnetic tunnel junction (MTJ [15], see inset to Fig. 5.1a) was used to check the quality of the Co/Al_2O_3 electrodes after exposure to air, acetone and oxygen plasma cleaning. To mimic the FET device fabrication process, the calibrated 2.0 nm thick Al film on top of the Co film (both grown in UHV) was first plasma oxidized for 10 min., exposed to air, covered with photoresist, cleaned by acetone and isopropanol, and oxidized again for 10 min. to remove photoresist remnants and clean the bottom layer. The MTJ was completed by evaporating the NiFe top electrode in UHV again. The magnetoresistance of a representative MTJ thus fabricated, is

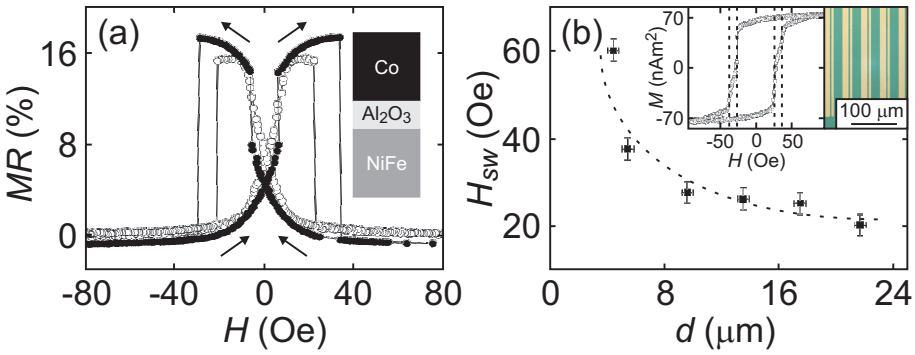

Figure 5.1: Electrode characterization. (a) Magnetoresistance MR vs. magnetic field H for Co/Al_2O_3(∼2.5 nm)/NiFe(15 nm) magnetic tunnel junctions (MTJs, inset). Data shown for a MTJ with 16 nm Co layer treated with photoresist, acetone and IPA (open circles) and an untreated one with a 8 nm Co layer (solid dots). MR is defined as $(R - R_P)/R_P$, with R_P the resistance for parallel magnetization of the Co and NiFe layers at large magnetic fields. Arrows denote the sweep directions. (b) Switching field H_{sw} vs. electrode width d for Co/Al_2O_3 (16 nm/2.5 nm) electrodes. The dotted line is a guide to the eye. Left inset: Magnetization M vs. magnetic field H for electrodes with a width of 5.4 and 13.5 ± 0.4 μm. The switching field H_{sw} for the two widths is denoted by the dashed lines. Right inset: Ensemble of electrodes for H_{sw} measurements.

shown in Fig. 5.1a. A clear hysteresis and a magnetoresistance (MR) of 16% was observed, very close to the value of clean interfaces produced without breaking the vacuum (also shown in Fig. 5.1a), implying the good quality of the Al_2O_3 tunnel barrier (protecting the underlying Co from oxidation) and its robustness under the FET fabrication process. The difference in switching field was attributed to the different thickness of the Co layer in the reference MTJ (8 nm). The realization of air-exposed FM electrodes in an organic spin-valve structure has been demonstrated before [16], but here an additional cleaning step was used to remove any organic contaminations.

The switching fields H_{sw} of the Co/Al_2O_3 electrodes were independently determined as follows. For spin valves, the ability to reverse the magnetization of the injector and detector electrodes independently is essential [1]. Therefore, the switching fields of both electrodes need to be sufficiently different. The magnetization of the 16 nm Co layer was in plane, and its switching field depended on the ratio between length and width. The switching fields for different electrode widths d were determined from test samples with an ensemble of electrodes (see right inset to Fig. 5.1b), using the same fabrication procedure and substrate as

for the FET devices. Hysteresis curves measured in a vibrating sample magnetometer (VSM) clearly revealed sharp switching fields, as shown in the left inset to Fig. 5.1b for the case of a test sample containing an ensemble of electrodes with two different widths (5.4 and 13.5 $\pm$ 0.4 μm). From these VSM measurements the switching field as function of electrode width was derived (see Fig. 5.1b). H_{sw} strongly depended on electrode width for $d < 10$ μm, but saturated for wider electrodes.

5.3 Field-effect transistor measurements

The multi-terminal single-crystal device of Fig. 5.2a was characterized using different measurement configurations, and the main characteristics have been reproduced in multiple devices. The negative Si back gate voltage (used to induce holes) was expected to be screened by the Co/Al_2O_3 electrodes, i.e. the charge accumulation should be much less on top of the electrodes than at the crystal/SiO_2 interface in between the electrodes. To confirm this, a voltage of -10 V was applied between electrode 0 and 7 for a gate voltage of -40 V. No current larger than 10^{-11} A was measured. This meant that, although current between adjacent electrodes could flow over the full crystal width, for non-adjacent electrodes there only was a current path through the non-contacted region (channel width $W = 50$ μm, channel length $L = 60$ μm) denoted by the dashed lines in Fig. 5.2a. Using electrodes 1-12, 2- and 4-terminal measurements were performed. The multi-terminal layout is also suitable for measuring spin accumulation in the so-called non-local geometry [17].

For 2-terminal measurements, the source-drain voltage V_{SD} was applied over electrodes 1 and 7, and the resulting current I_{SD} was measured using the same electrodes. Different electrode combinations will be discussed later on. I_{SD}-V_{SD} curves for different gate voltages V_G are shown in Fig. 5.2b. The typical gate leakage current in these devices was $I_{leak} < 10^{-11}$ A. The threshold voltage V_{th} was -25 V (inset of Fig. 5.2b), obtained from extrapolating the I_{SD}-V_G curves for large V_G (linear regime) to $I_{SD} = 0$. This value is relatively high, and might be related to hole trapping at the SiO_2/single-crystal interface or incomplete lamination of the crystal to the substrate.

The weak gate dependence around $V_{SD} = 0$ V implied that the device resistance was contact dominated [8, 9], as discussed in more detail below. The contact-dominated behavior was expected, since tunnel barrier was on top of the Co electrodes. The good contact quality without a large hole injection barrier was demonstrated by the linearity at $V_{SD} = 0$ V, as can be seen in Fig. 5.2c [18].

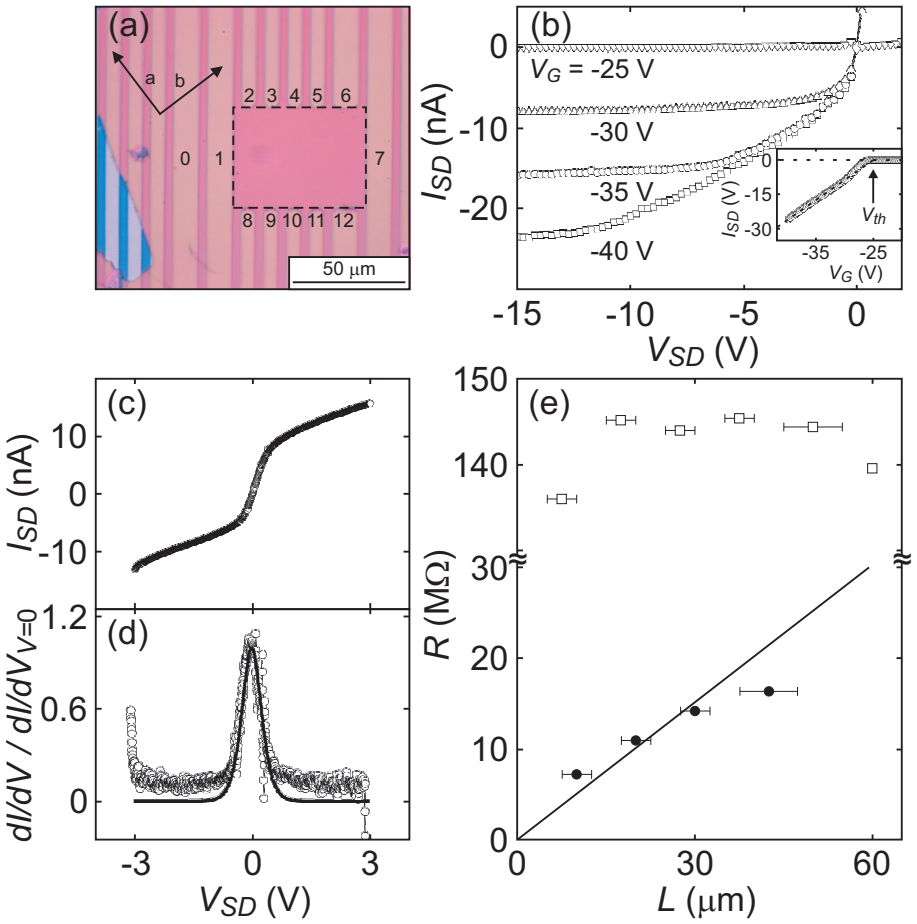

Figure 5.2: Organic single-crystal FET device. (a) Photograph of the rubrene single-crystal (partly) overlapping with Co/Al_2O_3 electrodes (numbered 0 to 12; other electrodes not used). Electrodes 1, 6, 7 and 12 have 12 ± 0.4 μm width, 2–5 and 8–11 6.5 ± 0.4 μm. The doped Si substrate was used as back gate. The active device area is denoted by the dashed rectangle, with channel length L = 60 μm and width W = 50 μm. The crystal axes a and b (the latter corresponding to the highest mobility) are denoted by the arrows. (b) Source-drain current I_{SD} vs. voltage V_{SD} (electrodes 1 and 7) for different gate voltages V_G. Inset: I_{SD} vs. V_G for V_{SD} = -10 V. The threshold voltage V_{th} = -25 V is indicated by the arrow. (c) Zoom-in around V_{SD} = 0 V ($V_G = -40$V) for the measurements in (b). (d) Normalized differential conductance dI/dV / $dI/dV_{V=0}$ vs. V_{SD}. The line is a fit to the derivative of Eq. 5.1. (e) Resistance R vs. channel length L for two-terminal measurements (open squares) for V_{SD} = -1 V and 4-terminal measurements (solid dots) for I_{SD} = -1 nA (linear regime, V_G = -40 V for all measurements). The solid line is a fit to Eq. 5.3.

The overall non-linear shape around $V_{SD} = 0$ (see Fig. 5.2c) could be described by a back-to-back diode model [8]

$$I_{b-b} = I_0 \tanh(\frac{eV_{SD}}{2\eta k_B T}), \tag{5.1}$$

where I_0 is the saturation current, η the diode ideality factor, k_B the Boltzmann constant and T the temperature. The normalized differential conductance, obtained by numerical differentiation of the data, could be fitted by the derivative of Eq. 5.1, as shown in Fig. 5.2d. The small offset is explained by the fact that I_0 is weakly bias dependent, contrary to what was assumed in the derivation of Eq. 5.1. A value $\eta = 7.7 \pm 0.2$ was obtained, as compared to $\eta = 1$ for an ideal Schottky diode. This high value demonstrated that although Schottky barrier formation plays a role in these devices, tunneling was important [19] and holes were indeed injected in the single-crystal through the tunnel barrier. Temperature-dependent measurements should give more insight in the height of the Schottky barriers.

In the linear regime, the usual FET relation applies

$$I_{SD} = \frac{W}{L}\mu C_i (V_G - V_{th}) V'_{SD}, \tag{5.2}$$

where C_i the capacitance of the gate insulator per unit area and μ the carrier mobility. Note that V'_{SD} is the voltage drop over the conducting channel, excluding the voltage drop over the electrodes. The channel resistance R_{ch} was determined from 4-terminal measurements. Current was driven between electrodes 1 and 7, and the voltage drop was measured using the intermediate electrodes, to study the channel resistance as function of length, see Fig. 5.2e (solid dots). Note that the square resistance $R_\square \sim 25$ M$\Omega/\square$ was $\sim 10^3$ times the quantum resistance. By rewriting Eq. 5.2, R_{ch} is given by

$$R_{ch} = \frac{L}{W C_i (V_G - V_{th})} \frac{1}{\mu} \tag{5.3}$$

Fitting to Eq. 5.3, a hole mobility of 0.25 cm^2(Vs)$^{-1}$ was extracted. The relatively low mobility was attributed to contaminations in the starting material (only one purification cycle was used) and the rather long period ($\sim$weeks) between crystal growth and device fabrication. Although the crystals were stored in a nitrogen environment, oxidation could not completely be ruled out [20]. Optimization of these factors has proven to result in typically 1–10 cm^2(Vs)$^{-1}$ mobilities [21].

The 2- and 4-terminal resistance measurements are compared in Fig. 5.2e, where the difference is explained by the contact resistance. The normalized contact resistance R_cW of 0.28 MΩcm (used in 2D devices) dominated the 2-terminal resistance, as concluded before. This was much higher than contact resistances found for nickel oxide electrodes (0.1 to 1 $k\Omega$cm) [10] and cobalt oxide electrodes (10 to 200 $k\Omega$cm) [8]. The high contact resistance in the devices presented in this chapter can be explained by the Al_2O_3 tunnel barrier, and implies that charge was injected through the tunnel barrier, as intended.

In spite of the seemingly ideal choices for the spin injecting and detecting interfaces, a spin-valve effect has not been unambiguously demonstrated in these FETs. This could have several reasons. First of all, the spin relaxation time τ_s may be not as long as expected. Based on EPR studies [22], a lower bound of 1 μs for τ_s is assumed. Using $l_s = \sqrt{D\tau_s}$, where l_s is the spin relaxation length, D the diffusion constant, and the Einstein relation $D = \mu k_B T/e$, gives $l_s > 1\mu$m, comparable to the present device dimensions. Recently, even much larger values ($\sim$mm) were predicted for rubrene single-crystals [23]. However, if τ_s is significantly shorter, the channels should be made shorter and/or crystals with higher mobility should be used. It can not be excluded that τ_s is temperature dependent as well and is longer at lower temperatures. Devices similar to those demonstrated here, with shorter channel length, will provide a well-controlled experimental platform to investigate the conditions for the occurrence of spin injection in organic semiconductors.

5.4 Ferromagnetic electrodes fabricated using e-beam lithography

A picture of a rubrene single-crystal FET with electrodes fabricated with e-beam lithography is given in Fig. 5.3a. A piece of rubrene single-crystal was laminated on several Co(15 nm)/Al_2O_3(3 nm) electrodes. The metal evaporation was done in the same way as described for the photolithography samples, including the oxygen plasma cleaning step. The electrodes are arranged in pairs of electrodes, each pair having two different widths of 100 and 200 nm. The electrode spacing ranged from 5 μm to 100 nm. Although the lamination was incomplete (as can be seen from the dark spots on the rubrene single-crystal next to the pairs of electrodes), FET behavior was measured with two electrodes which were 400 nm apart, as shown in Fig. 5.3b. These measurements showed that FET structures with small electrode width and small electrode spacing could be realized using Co and Al_2O_3.

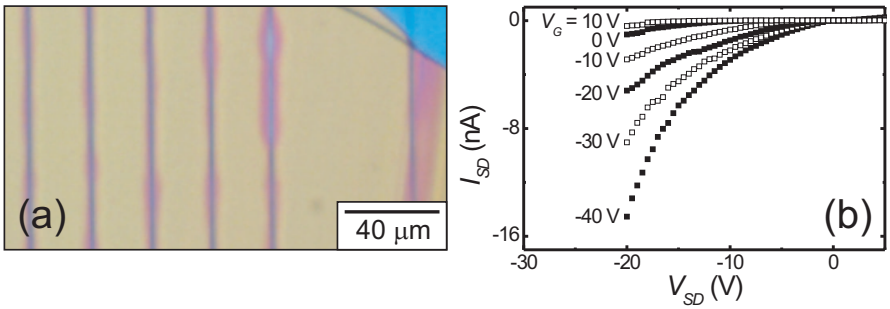

Figure 5.3: Organic single-crystal FET device fabricated with e-beam lithography. (a) Photograph of the rubrene single-crystal (partly) overlapping with Co(15 nm)/Al_2O_3(2.5 nm) electrodes. (b) Source-drain current I_{SD} vs. source-drain voltage V_{SD} for different values of the gate voltage V_G for a channel length L = 400 nm and channel width W = 220 μm (set by the width of the crystal).

The current observed in this device is comparable to the current in Fig. 5.2b, indicating that it is contact dominated. The flattening of the current around V_{SD} = 0 V, in contrast to the data in Fig. 5.2b, could indicate a large charge injection barrier (i.e. tunneling is prevailing). This can probably be ascribed to the incomplete OSC lamination on the electrodes.

5.5 $LaSrMnO_3$ electrodes

A rubrene single-crystal FET device with $LaSrMnO_3$ (LSMO) electrodes is presented in Fig. 5.4. To the best of our knowledge, this device is the first of this kind. LSMO was studied since it is a half-metal (see chapter 2), with workfunction around 5 eV, which has also been used in other organic spintronic devices (see chapter 2). The substrate was a 0.5 mm thick $SrTiO_3$ (STO) substrate of 1 x 1 cm^2, which was also used as the dielectric. A hole was mechanically etched in the STO using dimple-grinding, to reduce the thickness of the dielectric below the actual device. This method is usually applied for the preparation of thin transmission electron microscopy (TEM) samples. A sphere-shaped hole is ground in the substrate using a grinding wheel with a diameter of 7.5 mm and a diamond paste. The thickness of the STO at the thinnest point was $\sim$50 μm (see inset of Fig. 5.4a). This was 2 orders of magnitude larger than the thickness of the SiO_2 dielectric in the previous section, but this is compensated by the relative dielectric constant of STO, which can be as high as 310 at room temperature (as

compared to 3.9 for SiO_2) [24].

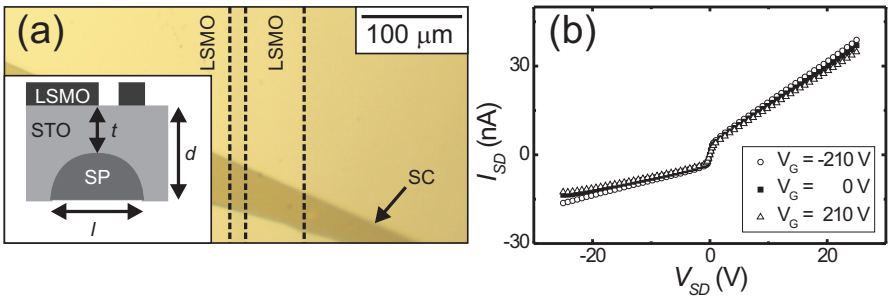

Figure 5.4: (a) Photograph of LSMO electrodes (left of the first dashed line, in between the second and third dashed line) on STO, partly covered by rubrene single-crystal (SC). Inset: schematic cross section of the device with the silver paint (SP) gate electrode, STO gate dielectric and LSMO electrodes, with lengths $t = 50$ μm, $d = 0.5$ mm and $l = 5.2$ mm (drawing not on scale). (b) Source-drain current I_{SD} vs. source-drain voltage V_{SD} for different gate voltages V_G, as denoted in the figure.

On the substrate, 20 nm thick LSMO electrodes were deposited through a shadow mask (see chapter 3) using pulsed laser deposition (PLD). The LSMO electrodes were cleaned by ultrasonication in acetone and 2-propanol. Then, a rubrene single-crystal was laminated onto the electrodes and substrate. The hole in the STO was filled with a conductive silver epoxy paste, which could be used as a back gate (see Fig. 5.4a).

Transport measurements of this device in ambient conditions are shown in Fig. 5.4b. Similar measurements have been reproduced in two devices. No current larger than 10^{-11} A was measured between two LSMO electrodes which were not bridged by rubrene single-crystal. However, when a rubrene single-crystal was lying between two electrodes, clear currents were observed, which seemed to indicate charge injection from the LSMO electrodes into the organic single-crystal. The typical gate leakage current in these devices was $I_{leak} < 10^{-11}$ A. The overall non-linear shape of the I_{SD}-V_{SD} curve might indicate back-to-back Schottky diode behavior, as was also observed for the organic single-crystal devices with Co/Al_2O_3 electrodes presented in this chapter.

The observation of a sizeable source-drain current at $V_G = 0$ V, seems to reveal the presence of a large built-in gate voltage, but this has to be investigated further to determine the precise cause. The small gate dependence of the source-drain current might be caused by the thickness of the gate dielectric. Since the shape of the hole in the dielectric is spherical, the thickness of the dielectric

was not uniform over the sample. The thickness of the dielectric at the position where the rubrene single-crystal was laminated was estimated to be ∼150 μm. Contact-dominated behavior, which could be explained by a substantial hole injection barrier, as was measured before for charge injection from acetone-cleaned LSMO to organic thin films [25], might also be a reason for the small gate effect. Applying larger gate voltages or fabricating devices with a thinner gate dielectric might provide more understanding of the observed electrical transport.

5.6 Conclusion

In conclusion, well-defined tunnel barriers between ferromagnetic electrodes and organic single-crystals are realized. The high-quality tunnel barrier should allow for spin injection without randomization. This, in combination with the observed FET functionality, provide the necessary conditions for demonstrating a spin-valve FET. Similar devices are also expected to shine light on the spin relaxation time in organic semiconductors and the underlying physical mechanisms.

Devices fabricated with e-beam lithography, with small electrodes spacing of a few hundreds of nm are potentially suitable to study spin injection and detection in rubrene single-crystal FET devices.

LSMO, being a half-metal, is also interesting to be used as electrode material. Further research has to demonstrate the potential of these electrodes for being used in organic single-crystal spin valves.

References

[1] G.A. Prinz, Physics Today **48**, 58 (1995); G.A. Prinz, Science **282**, 1660 (1998); S.A. Wolf, D.D. Awschalom, R.A. Buhrman, J.M. Daughton, S. von Molnár, M.L. Roukes, A.Y. Chtchelkanova, and D.M. Treger, Science **294**, 1488 (294).

[2] R. Farchioni and G. Grosso, *Organic Electronic Materials*, Springer-Verlag, Berlin (2001); G. Cuniberti, G. Fagas and K. Richter (eds), *Introducing Molecular Electronics*, Springer-Verlag, Berlin Heidelberg (2005); H. Klauk (ed), *Organic Electronics: Materials, Manufacturing and Applications*, Wiley-VCH, Weinheim (2006).

[3] W.J.M. Naber, S. Faez and W.G. van der Wiel, J. Phys. D: Appl. Phys. **40**, R205 (2007).

[4] V.A. Dediu, L.E. Hueso, I. Bergenti and C. Taliani, Nature Mat. **8**, 707 (2009).

[5] S. Sanvito and A.R. Rocha, J. Comput. Theor. Nanosci. **3**, 624 (2006).

[6] R.W.I. de Boer, M.E. Gershenson, A.F. Morpurgo and V. Podzorov, Phys. Stat. Sol. (a) **201**, 1302 (2004).

[7] V. Podzorov, E. Menard, A. Borissov, V. Kiryukhin, J.A. Rogers and M.E. Gershenson, Phys. Rev. Lett. **93**, 086602 (2004).

[8] A.S. Molinari, I. Gutiérrez, I.N. Hulea, S. Russo and A.F. Morpurgo, Appl. Phys. Lett. **90**, 212103 (2007).

[9] A.S. Molinari, G. Lezama, P. Parisse, T. Takenobu and A.F. Morpurgo, Appl. Phys. Lett. **92**, 133303 (2008).

[10] I.N. Hulea, S. Russo, A. Molinari and A.F. Morpurgo, Appl. Phys. Lett. **88**, 113512 (2006).

[11] C.L. Dennis, C.V. Tiusan, J.F. Gregg, G.J. Ensell and S.M. Thompson, IEE Proc.-Circuits Devices Syst. **152**, 340 (2005); S. Sugahara, IEE Proc.-Circuits Devices Syst. **152**, 355 (2005).

[12] G. Schmidt, D. Ferrand, L.W. Molenkamp, A.T. Filip and B.J. van Wees, Phys. Rev. B **62**, R4790 (2000).

[13] A. Fert and H. Jaffrès, Phys. Rev. B **64**, 184420 (2002).

[14] M. Grobosch, C. Schmidt, W.J.M. Naber, W.G. van der Wiel and M. Knupfer, *Accepted for publication in Synthetic Metals*

[15] J.S. Moodera, L.R. Kinder, T.M. Wong and R. Meservey, Phys. Rev. Lett. **74**, 3273 (1995).

[16] G. Szulczewski, H. Tokuc, K. Oguz and J.M.D. Coey, Appl. Phys. Lett. **95**, 202506 (2009).

[17] M. Johnson and R.H. Silsbee, Phys. Rev. Lett. **55**, 1790 (1985).

[18] N. Kawasaki, Y. Ohta and Y. Kubozono, Appl. Phys. Lett. **91**, 123518 (2007).

[19] S.M. Sze and K.K. Ng, *Physics of Semiconductor Devices*, Wiley, New Jersey (2007).

[20] C. Kloc, K.J. Tan, M.L. Toh, K.K. Zhang and Y.P. Xu, Appl. Phys. A **95**, 219 (2009).

[21] A.F. Stassen, R.W.I. de Boer, N.N. Iosad and A.F. Morpurgo, Appl. Phys. Lett. **85**, 3899 (2004); I.N. Hulea, S. Fratini, H. Xie, C.L. Mulder, N.N. Iossad, G. Rastelli, S. Ciuchi and A.F. Morpurgo, Nat. Mat. **5**, 982 (2006).

[22] V.I Krinichnyi, Synth. Met. **108**, 173 (2000).

[23] J.H. Shim, K.V. Raman, Y.J. Park, T.S. Santos, G.X. Miao, B. Satpati and J.S. Moodera, Phys. Rev. Lett. **100**, 226603 (2008).

[24] K.A. Müller and H. Burkard, Phys. Rev. B **19**, 3593 (1979).

[25] M. Grobosch, K. Dörr, R.B. Gangineni and M. Knupfer, Appl. Phys. Lett. **92**, 023302 (2008).

Chapter 6

Metal transfer printing of electrodes on organic single-crystal

In this chapter, a soft-lithography method to fabricate metal electrodes *on top* of rubrene and pentacene single-crystals is discussed. Metal transfer printing (MTP) was used to transfer a thin Au film from a patterned elastomeric stamp to organic single-crystals. While stamping bare Au is found to be irreproducable, due to the comparable free surface energy of PDMS and organic single-crystals, large ($\sim$100 μm) and small (several μm) Au features were transferred by modifying the Au surface with organic molecules. In some cases, the Au is damaged and the order of the stamped pattern is lost, probably due to molecules penetrating the Au/PDMS interface. Measurements in the space charge limited current regime and on FET devices show contact of the Au film to the organic single-crystal. A large charge injection barrier is observed, which could be due to the organic molecules.

6.1 Introduction

Conventional ways of fabricating top electrodes by depositing metal on top of a conductor, e-beam evaporation or sputtering, seems problematic in the case of organic single-crystals (OSC), since high-energy metal particles can easily damage the soft organic material. Heat generated during evaporation can cause traps at the metal/organic interface or can even lead to sublimation of the OSC, resulting in irreproducable results in organic field-effect transistors (FETs) [1, 2]. Metal contamination in the current channel, which can easily occur due to scattered atoms from residual gas in the evaporation chamber, dramatically effect the performance and mobility of OSC FETs [3]. Top electrodes have been manually applied by using conducting paste [4]. Although this might circumvent the problem of damaging the OSCs, it is difficult to produce small and nicely-shaped electrodes with this method.

Two different electrode configurations, showing a top and bottom electrode configuration, are shown in Fig. 6.1. Due to the above mentioned problems, the bottom electrode configuration is mostly used [5]. In this case, the fabrication relies on the selection of thin OSCs ($< 1\ \mu$m) and the manual lamination of these crystals on pre-fabricated electrodes. The fabrication of electrodes directly on top would ease the fabrication process, since also thick OSCs ($> 1\ \mu$m) can be used, eliminating the need for a selection procedure, and there is no need to handle the fragile OSCs by hand.

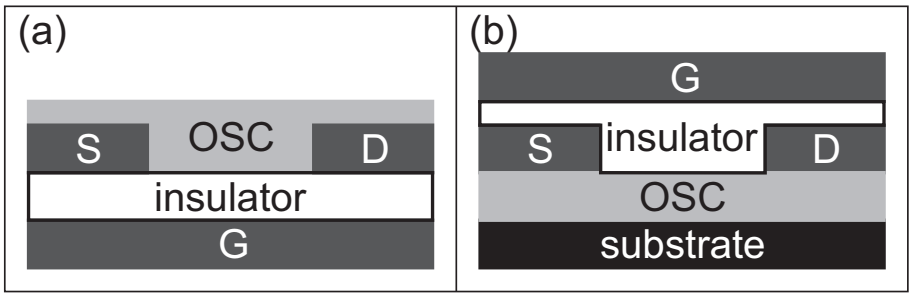

Figure 6.1: Schematic layout of an organic single-crystal (OSC) FET structures for a (a) bottom electrode and (b) top electrode configuration. The gate electrode (G), which induces a conducting channel, is separated from the OSC by an insulator. The current through the OSC is injected and collected by a source (S) and drain (D) electrode.

In this chapter, the first results of the fabrication of Au electrodes on top of OSCs by metal transfer printing (MTP) [6], facilitated by using organic molecules on the transferred Au for enhancing the interaction between the Au film and the

OSCs. Good adhesion of Au to OSCs was obtained. Both measurements in the space charge limited current (SCLC) regime as well as on FET devices were performed. Although MTP has been successfully applied to different organic materials [7], to the best of our knowledge, it has never been done on OSCs, materials with the highest mobility among organic semiconductors [5].

6.2 Conditions for Au transfer to organic single-crystals

Transfer printing is a technique in which a patterned stamp is used to selectively transfer a material to a substrate. The material can for example be a metal film [7, 8], nanoparticles (see chapter 7) [9], or a self-assembled monolayer [10]. The transfer is initialized by placing the stamp in close contact with the substrate and either covalent or non-covalent forces can be used to transfer the pattern to the desired substrate, in this case the OSC.

In order to have good contact with the substrate, elastomeric polydimethylsiloxane (PDMS) stamps are used. This flexible material has the ability to adapt its form to the surface of the substrate, so no large forces, which can possibly damage the underlying material, are needed to initialize the transfer. PDMS has a low surface energy, which is crucial for MTP, as will be explained below. The desired pattern can be achieved by structuring the PDMS in such a way that only the desired pattern is in contact with the substrate, as illustrated in Fig. 6.2. This structure is obtained by fabricating the stamps from a pre-polymer, which can be poured in a mold, in this case an etched silicon wafer. After curing, solid PDMS is obtained, which can be used for MTP.

In case of MTP using non-covalent forces, the transfer is based on a difference in surface energies between the starting situation, where the metal layer is on the stamp, and the final situation, when the metal layer is attached to the substrate [7]. Taking into account all surface energies, the energy difference in this case is given by

$$\Delta E_{stamp} = (\gamma_{PDMS} - \gamma_{OSC}) - (\gamma_{OSC-Au} - \gamma_{PDMS-Au}), \tag{6.1}$$

where γ_{PDMS} is the free surface energy of PDMS, γ_{OSC} the free surface energy of the OSC, γ_{OSC-Au} the interfacial energy between the OSC and Au, and $\gamma_{PDMS-Au}$ the interfacial energy between PDMS and Au.

For transfer of Au to OSCs to be energetically favorable, ΔE_{stamp} has to be negative. When the surface energy of Au (1.5 J/m^2) is much larger than that of PDMS (19.8 mJ/m^2) and the OSC, the second term in equation 6.1 is much

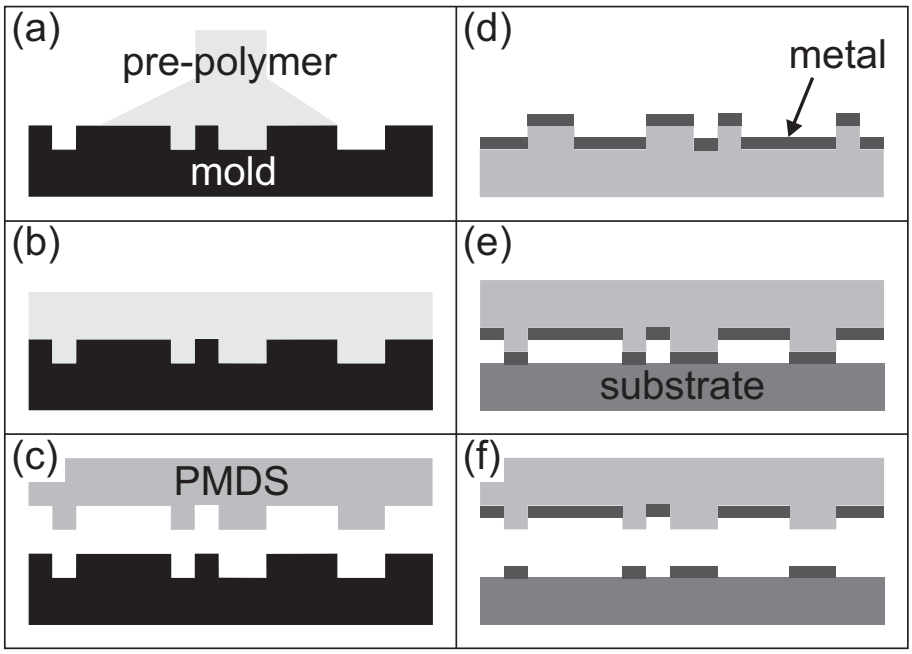

Figure 6.2: PDMS stamp fabrication and metal transfer printing (MTP). (a) Pouring the pre-polymer into a mold. (b) Curing the pre-polymer to PDMS. (c) Retracting the PDMS stamp from the mold. (d) Metal deposition on the stamp. (e) Putting the stamp in contact with the substrate. (f) Retracting the stamp, leaving the stamped features on the substrate.

smaller than the first term. This is the case for several organic materials [7]. Due to the high order, the surface energy of OSCs is expected to be lower than that of organic thin films, making this assumption also valid for the case of MTP on OSCs. In that case, the transfer of Au depends on the difference in free surface energy of the PDMS stamp and the OSC.

To compare the surface free energy of PDMS with rubrene single-crystal (SC), contact angle measurements were performed on both materials using milli-Q water. A drop of water was placed on the surface of PDMS and rubrene SC and the contact angle between the surface of these materials and the surface of the drop was measured. A large contact angle means the substrate is hydrophilic, indicating the surface free energy of the substrate is low, and vice versa for a small contact angle. Measurements showed that the contact angles for the two materials were similar, $103 \pm 7°$ and $103 \pm 5°$ for PDMS and rubrene SC, respectively. This implies that stamping on rubrene SC is very hard, as will also be shown below. When a metal layer is evaporated on the PDMS, the surface

energy of the PDMS can be increased, due to modifications on the surface [7]. This makes the transfer even more difficult. In the attempts discussed below, a high evaporation rate (> 0.6 Å/s, see below) is preferred, since at lower rates the Au atoms may be engulfed by the polymer, leading to strongly attached Au films which are harder to transfer [18, 19].

When organic molecules on the Au film are used to enhance the transfer to the OSC, Eq. 6.1 changes to

$$\Delta E_{stamp} = (\gamma_{PDMS} - \gamma_{OSC}) - (\gamma_{PDMS-Au} - \gamma_{Au}) - (\gamma_{mod} - \gamma_{mod-OSC}), \quad (6.2)$$

where γ_{mod} is the surface energy of the modified Au surface and $\gamma_{mod-OSC}$ is the interfacial energy between the modified Au surface and the OSC. As concluded from the contact angle measurements the first term can be neglected. The second term can also be neglected since $\gamma_{metal} \gg \gamma_{PDMS}$. The transfer is in this case governed by the third term. If the organic molecules have a high affinity for the OSC, it is expected that $\gamma_{mod-OSC} < \gamma_{mod}$ and Eq. 6.2 becomes negative. In this case, transfer of a Au layer to rubrene SC is energetically favorable.

Since rubrene consist of a tetracene backbone with four benzene rings as substituents (see chapter 3), an obvious choice for a molecules with high affinity for rubrene is one ending with a benzene ring. Since the molecules will be between the Au and OSCs after the transfer, current will have to be injected through the molecules. For this reason a short molecule will be preferred. Taking into account these considerations, benzyl mercaptan (phenylmethanethiol, $C_6H_5CH_2SH$, see inset of Fig. 6.4a) seemed to be a good choice, having a sulfur group at one end to attach to the Au film, and a benzene ring on the other side.

To test if the molecules have a high affinity for rubrene, contact angle measurements were performed on Au layers and on Au layers modified with benzyl mercaptan molecules. The Au surface is modified by putting an Au layer on PDMS in a 5 mM benzyl mercaptan solution in ethanol for several hours. The contact angle of the bare Au and the modified Au surface were $70 \pm 10°$ and $90 \pm 10°$, respectively. The increase in surface energy towards the value as measured for rubrene, showed the increase in hydrophobicity and the increased affinity for the rubrene. It is therefore expected benzyl mercaptan molecules can be used to facilitate the transfer of Au to rubrene.

Covering the Au with benzyl mercaptan in solution requires an Au film that is strongly enough attached to the PDMS to undergo the modification by the benzyl mercaptan molecules, but on the other hand is able to detach from the PDMS after stamping. The evaporation rate of Au onto the PDMS seemed to be crucial for the stability of the Au film [18]. However, choosing the rate too low resulted in Au films which could not be transferred to the OSC [19]. Choosing

the rate too high however resulted in very poor adherence of the Au film to the PDMS, due to rapid nucleation and film growth [20], and immediate detachment of the Au when it was dipped in benzyl mercaptan solution. These Au structures could still be transferred, but the process of transfer was by falling off the stamps, rather than by a controlled transfer, resulting in poor control of the Au placement on the OSCs. If the rate was roughly in a window between 0.6 and 1 Å/s, the Au layer in solution was stable enough to be transferred to the OSC, as will be shown below.

Another problem is the damaging of the Au layer. Dipping PDMS stamps with Au in ethanol showed some cracks appear in the gold, due to swelling ($\sim$5%) of the PDMS when ethanol was absorbed, but only at the edges of the Au structures. A more severe problem is that due to their short length ($\sim$5 Å), benzyl mercaptan molecules can be expected to penetrate in between the PDMS and the Au, irrespective of the evaporation rate. This becomes worse if the Au structures become smaller, because when the Au layer is continuous, benzyl mercaptan can only penetrate the Au/PDMS interface at the edges of the Au structures. This penetration might cause the Au to be detached from the PDMS. A solution to this problem could be the modification of the Au surface by molecules in the vapor phase instead of in a solution. By placing a stamp above the benzyl mercaptan solution with Au facing the solution, the benzyl mercaptan molecules are transferred to the Au layer. Because the benzyl mercaptan molecules are less mobile due to the absence of any liquid on the PDMS stamp, penetration underneath the Au layer will be less of a problem.

6.3 Transferred Au electrodes on organic single-crystals

As expected from Eq. 6.1, numerous attempts of transferring Au to OSC were unsuccessful and only a few times the transfer of small Au lines to a piece of rubrene SC was achieved, as shown in the inset of Fig. 6.3a. These successful stamping attempts are probably caused by contamination of the surface of the rubrene SC, which could increases the free surface energy [11].

Results of Au transferred to rubrene SC facilitated by benzyl mercaptan molecules from solution are shown in Fig. 6.4. Evaporation rates $r > 1$ Å/s resulted in uncontrolled transfer (see Fig. 6.4a). Large Au areas (order of several hundreds of μm) and smaller structure in the order of μm were transferred in a controlled way when evaporation rates 0.6 Å/s $< r <$ 1 Å/s were used (see Fig. 6.4b and c).

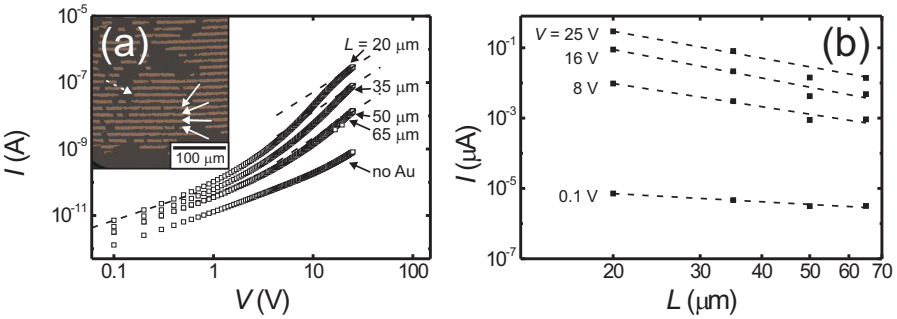

Figure 6.3: (a) Current I vs. voltage V through a rubrene SC with transferred Au electrodes for different electrode separations L and for probes directly placed on the rubrene SC (no Au). Dashed lines are proportional to V (at small voltages) and V^2 (at large voltages). Inset: optical picture of the rubrene SC with transferred Au lines. Dashed arrow denotes the Au electrode to which the first probe is contacted, solid arrows the Au lines for length-dependent measurements. (b) Current I vs. channel length L for different voltage V. Dashed lines are a fit to a power law ($I \propto V^P$) with P = -0.7, -2.2, -2.7 and -2.5 for V = 0.1, 8, 16 and 25 V, respectively.

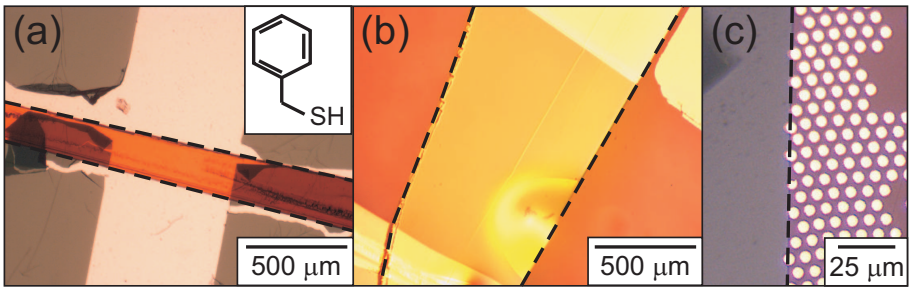

Figure 6.4: MTP results of Au on OSC facilitated by benzyl mercaptan molecules from solution. (a) Transferred Au areas using an evaporation rate r = 1.5 Å/s (rubrene SC in between the dashed lines). Inset: molecular structure of benzyl mercaptan. (b) Transferred Au areas, using an evaporation rate r = 0.9 Å/s (rubrene SC in between the dashed lines). (c) Transferred hexagonal pattern of circular shaped Au structures with a diameter of 5 μm, using an evaporation rate r = 0.8 Å/s (pentacene SC right of the dashed line).

6.4 Electrical characterization

Although the Au lines are not always continuous, I-V measurements on the SC device with transferred Au electrodes as shown in the inset of Fig. 6.3a could be performed by placing two probes of a probe station gently on the Au lines. Measurements in the SCLC regime (without the use of a gate electrode) are shown in 6.3. In this regime, the current is given for the 1D case by [5, 12, 13]

$$I = \frac{9}{8} W h \epsilon_0 \epsilon_r \mu \frac{V}{L^3}, \tag{6.3}$$

and for the 2D case by [13, 14]

$$I = \frac{2}{\pi} W \epsilon_0 \epsilon_r \mu \frac{V}{L^2}, \tag{6.4}$$

where W is the width of the current channel, h the channel height, ϵ_0 the permittivity in free space, ϵ_r the relative dielectric constant of the OSC, μ the charge carrier mobility, V the applied voltage and L the channel length. This equation only holds for the trap-free regime. A trapping factor Θ can be added to account for bulk traps in the SC[13]. A cross-over form the 1D to the 2D case is expected for increasing L/h, determined by the distribution of the electric field in the OSC [13].

The current I as a function of the voltage V for different channel length L are shown in Fig. 6.3a. All measurements were done under ambient conditions. First, the current was measured by applying a voltage between two probes directly on the rubrene SC surface (i.e. not on the stamped Au lines) with a separation of $\sim$20 μm. The current increased by more than an order of magnitude when the probes were placed on the Au lines, showing than indeed current was injected through the Au lines, which were in intimate contact with the OSC. The current was linear around $V = 0$ V, while it seemed to approach a quadratic dependence (according to Eq. 6.3 or 6.4) at higher voltages. Small deviations from the linear and quadratic dependence might be explained by Schottky barrier formation between the Au electrodes and the OSC [13]. The voltage dependence at the intermediate voltages might be explained by surface traps, causing a dependence with powers higher than 2 in the transition from the linear to the SCLC regime [15]. At this stage, also a large injection barrier between the Au electrodes and the OSC can not be excluded. The measured current was much larger than expected [16, 17], which confirmed the idea of surface contamination and doping of the rubrene SC by oxygen.

The length dependence of the current I for different voltages V is plotted in Fig. 6.3b. It is *a priori* not exactly known for which lengths Eq. 6.3 or 6.4 are

valid. Based on the results found for pentacene [13] and the fact that the rubrene SC has a thickness of several μm, it could be expected that this device was in the cross-over regime between the 1D and 2D case. To test this, the data was fitted by a power law ($I \propto V^P$). Since the whole data set can be fitted with P around -2.5 (except for $V = 0.1$ V, since this is the linear regime), it seemed like this device was indeed in the cross-over regime and the transition from the 1D to the 2D case was not going very fast for these length scales. However, it has to be noted that the $I - V$-behavior was measured for only four different lengths and the channel width in this device was not very well defined. Deviations from a clear trend of the length dependence could occur because of this.

Probe station measurements performed on a pentacene SC with stamped Au circular shapes (see Fig. 6.4c) using benzyl mercaptan molecules from solution are shown in Fig. 6.5. These measurements have been reproduced in several devices. I-V measurements were first performed without contacting the Au structures, by placing the probes directly on the SC surface with a separation of $\sim$200 μm. The curves were quadratic at large V, as expected from Eqs. 6.3 and 6.4. When the probes were placed on the Au shapes, the current increased by more than an order of magnitude, demonstrating current injection through the Au structures, which were in intimate contact with the OSC. The current did not depend on the length of the current channel, as can be seen in Fig. 6.5. This indicates the total resistance was contact-dominated, which could be caused by the benzyl mercaptan molecules on the Au. Due to the contact-dominated resistance, it was not possible to fit the curves with Eq. 6.3 or 6.4.

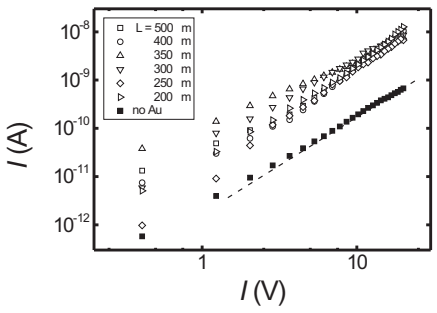

Figure 6.5: Current I vs. voltage V through a rubrene SC with and without contact to stamped circular Au shapes. The length between the Au shapes ranged from 200–500 μm, as denoted in the figure. The dashed line is proportional to V^2.

Au electrodes transferred to the surface of OSCs were used to fabricate FET devices. As dielectric and gate electrode parylene and colloidal graphite paint

was used, respectively. Parylene has been used before as dielectric for OSC FET structures and can easily be deposited without damaging the organic material [21, 22]. In Fig. 6.6, *I-V* curves for both rubrene and pentacene SC FET devices are shown. The electrodes in this case were stamped using benzyl mercaptan molecules from solution (see Fig. 6.5b). As can be seen, clear FET behavior was observed. The curves around $V_{SD} = 0$ V are flattened, indicating a large charge injection barrier, as has also been observed for the measurements in the SCLC regime.

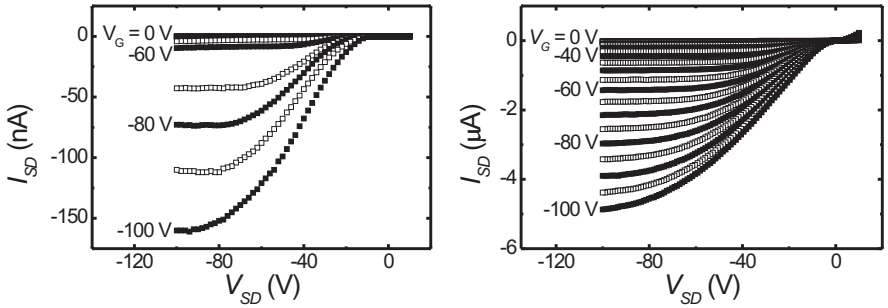

Figure 6.6: Source-drain current I_{SD} vs. voltage V_{SD} for different gate voltages V_G of FET structures fabricated using MTP with (a) rubrene SC (channel width $W = 1$ mm (set by the width of the OSC), channel length $L = 1$ mm and parylene thickness $d = 2$ μm) and (b) pentacene SC (channel width $W = 1.5$ mm (set by the width of the OSC), channel length $L = 1$ mm and parylene thickness $d = 1.7$ μm.)

From the *I-V* curves, the mobility can be calculated using [23]

$$\mu = \frac{L}{WC_iV_D}\frac{\partial I_D}{\partial V_G}, \tag{6.5}$$

where L and W are the length and width of the current channel respectively, and C_i the capacitance of the gate insulator per unit area. Estimates for the mobility $\mu = 2 \cdot 10^{-4}$ cm^2(Vs)$^{-1}$ and $\mu = 0.6$ cm^2(Vs)$^{-1}$ are obtained for rubrene and pentacene SC, respectively. This is probably an underestimate, because the large charge injection barrier at the Au/SC interface is not taken into account. The variation of the exact composition of the charge injection barrier can be a cause for the very different observed mobilities in the OSC devices. The long time ($\sim$ days – weeks) between crystal growth and device fabrication can also be a cause of the observed low mobility and the difference of the mobilities [11]. At this stage it is also difficult to fully exclude any damage due to stamping.

6.5 Conclusions

In this chapter, the first preliminary results of MTP on OSC are described. Some first results have been obtained, although due to the low free surface energy of the SC, MTP of bare Au layers is difficult and found to be irreproducible. Transfer is probably caused by contamination of the surface of the OSC, resulting in an increase of the free surface energy.

Increasing the surface energy of the stamped electrode by modifying the Au by benzyl mercaptan molecules resulted in transfer of both large areas (several hundreds of μm) and small (several μm) features. The small features were in some cases damaged and order was not always maintained in the stamped patterns, which might be due to benzyl mercaptan penetrating the interface between Au and PDMS. As a solution for the penetration of the benzyl mercaptan molecules, MTP could be done by modifying the Au surface by benzyl mercapatan molecules from the vapor phase.

Transferred Au electrodes have been used to perform measurements in the SCLC regime. Clear FET behavior is observed in 3-terminal devices. The I-V characteristics reveal the presence of a large charge injection barrier, probably caused by the benzyl mercaptan molecules on the Au. The contact-dominated behavior of the current injected through the Au dots requires further research, to determine its exact origin.

Further research has to demonstrate if Au patterns can be transferred reproducible to the surface of OSCs. Different molecules can be used to facilitate the metal transfer, to study the influence on the I-V characteristics. The molecules can even be used to modify the workfunction of the metal electrode, as has been reported before [24, 25]. This can help to fabricate FET structures with small Schottky barriers.

Monolayers have been formed on the surface of OSCs [26]. By choosing the right monolayer which is also able to bond to Au, this might be an interesting option for MTP that relies on covalent forces.

6.5.1 Metal transfer printing with FM materials

As shown above, Au features can be stamped to OSCs by using organic molecules to modify the Au surface. For spin-valve structures however, FM materials should be transferred onto the surface of OSCs. Using a bare FM material, like Co, Ni or Fe, would not be compatible with the method described in this chapter, since these materials would easily oxidize. Covering the FM material with an Al_2O_3 tunnel barrier, as used for the pre-fabricated electrodes as described in chapter

3, would prevent oxidation and would at the same time be a way to overcome the conductivity mismatch. Based on the experiments described in this chapter, stamping in this case will probably be difficult and the modification of the Al_2O_3 surface by molecules might be needed.

The molecule used in the experiment described in this chapter easily attaches to the Au surface, but using an oxide surface requires different molecules. Monolayer formation on oxide layers has been reported [27], showing monolayer formation is an option. All the ingredients to use the same method as described above for the transfer of FM electrodes seem to be available. However, the influence of these molecules on spin injection has to be tested and more research will be needed to see if it is possible to fabricate spin-valve structures with this method.

References

[1] C. Shen and A. Kahn, J. Appl. Phys. **90**, 4549 (2001).

[2] D.B.A. Rep, A.F. Morpurgo and T.M. Klapwijk, Org. Electron. **4**, 201 (2003).

[3] V. Podzorov, S.E. Sysoev, E. Loginova, V.M. Pudalov and M.E. Gershenson, Appl. Phys. Lett. **83**, 3504 (2003).

[4] R.W.I. de Boer, M. Jochemsen, T.M. Klapwijk, A.F. Morpurgo, J. Niemax, A.K. Tripathi, and J. Pflaum, J. Appl. Phys. **95**, 1196 (2004).

[5] R.W.I. de Boer, M.E. Gershenson, A.F. Morpurgo and V. Podzorov, Phys. Stat. Sol. (a) **201** 1302 (2004).

[6] H. Schmid, H. Wolf, R. Allenspach, H. Riel, S. Karg, B. Michel and E. Delamarche, Adv. Funct. Mat. **13**, 145 (2003).

[7] S.-H. Hur, D.-Y. Khang, C. Kocabas and J.A. Rogers, Appl. Phys. Lett. **85**, 5730 (2004).

[8] C. Kim, M. Shtein and R. Forrest, Appl. Phys. Lett. **80**, 4051 (2002).

[9] S. Kinge, T. Gang, W.J.M. Naber, H. Boschker, G. Rijnders, D.N. Reinhoudt and W.G. van der Wiel, Nano Letters **9**, 3220 (2009).

[10] A. Kumar and G.M. Whitesides, Appl. Phys. Lett. **63**, 2002 (1993).

[11] C. Kloc, K.J. Tan, M.L. Toh, K.K. Zhang and Y.P. Xu, Appl. Phys. A **95**, 219 (2009)

[12] M. A. Lampert and P. Mark, *Current Injection in Solids*, Academic Press Inc., New York (1970).

[13] O.D. Jurchescu and T.T.M. Palstra, Appl. Phys. Lett. **88**, 122101 (2006).

[14] R. Zuleeg and P. Knoll, Appl. Phys. Lett. **11**, 183 (1967).

[15] R.W.I. de Boer and A.F. Morpurgo, Phys. Rev. B **72**, 073207 (2005).

[16] A.F. Morpurgo, *private communication*

[17] O. Mitrofanov, D.V. Lang, C. Kloc, J.M. Wikberg, T. Siegrist, W.-Y. So, M.A. Sergent and A.P. Ramirez, Phys. Rev. Lett. **97**, 166601 (2006).

[18] C.A. Nijhuis, *PhD Thesis*, Wöhrmann Print Service, Zutphen (2006).

[19] V. Zaporojtchenko, T. Strunskus, K. Behnke, C. von Bechtolsheim, M. Kiene and F. Faubel, J. Adhesion Sci. Technol. **14**, 467 (2000).

[20] G.C. Martin, T.T. Su, I.H. Loh, E. Balizer, S.T. Kowel and P. Kornreich, J. Appl. Phys. **53**, 797 (1982).

[21] V. Podzorov, V.M. Pudalov and M.E. Gershenson, Appl. Phys. Lett. **82**, 1739 (2003).

[22] A.F. Stassen, R.W.I. de Boer, N.N. Iosad and A.F. Morpurgo, Appl. Phys. Lett. **85**, 3899 (2004).

[23] S.M. Sze and K.K. Ng, *Physics of Semiconductor Devices*, Wiley, New Jersey (2007).

[24] B. de Boer, A. Hadipour, M. Magdalena Mandoc, T. van Woudenbergh and P.W.M. Blom, Adv. Mat. **17**, 621 (2005).

[25] B.H. Hamadani, D.A. Corley, J.W. Ciszek, J.M. Tour and D. Natelson, Nano Letters **6**, 1303 (2006).

[26] M.F. Calhoun, J. Sanchez, D. Olaya, M.E. Gershenson and V. Podzorov, Nature Materials **7**, 84 (2007).

[27] N.L. Jeon, K. Finnie, K. Branshaw and R.G. Nuzzo, Langmuir **13**, 3382 (1997).

Chapter 7

Low-temperature solution synthesis of chemically functional ferromagnetic FePtAu nanoparticles

Magnetic nanoparticles are of great scientific and technological interest. The application of ferromagnetic nanoparticles for high-density data storage has great potential, but energy efficient synthesis of uniform, isolated, and patternable nanoparticles that remain ferromagnetic at room temperature is not trivial. In this chapter, a low-temperature solution synthesis method for FePtAu nanoparticles is presented that addresses all those issues and therefore can be regarded as an important step toward applications. The onset of the chemically ordered face-centered tetragonal ($L1_0$) phase was obtained for thermal annealing temperatures as low as 150 °C. Large uniaxial magnetic anisotropy (10^6 Jm^{-3}) and a high long-range order parameter have been obtained. The low-temperature solution annealing left the organic ligands intact, so that the possibility for post-anneal monolayer formation and chemically assisted patterning on a surface was maintained.

This chapter has been published as S. Kinge, T. Gang, W.J.M. Naber, H. Boschker, G. Rijnders, D.N. Reinhoudt and W.G. van der Wiel, Nano Letters **9**, 3220 (2009)

7.1 Introduction

The continuously increasing demand for data storage capacity has very much stimulated research on magnetic recording media [1, 2]. In modern hard disk drives, the magnetic medium layer is usually a CoCr-based alloy, containing magnetic regions smaller than 100 nm representing the bits of information. Every single magnetic region consists of ∼100 magnetic grains, which are the basic elements to be magnetized. One of the main challenges in increasing the data storage capacity by reducing the magnetic grain size is maintaining its magnetization despite the superparamagnetic limit [3–6]. Current hard disk technology has an estimated limit of 100–1000 gigabit per square inch due to this superparamagnetic limit [1, 2].

It has been argued [1, 2] that thin layers (ideally monolayers) of ferromagnetic FePt nanoparticles (NPs) enable recording densities ∼10 times larger than those achievable with CoCr based media. Due to their very high magnetocrystalline anisotropy ($K_u = 10^6$ Jm^{-3}), FePt NPs remain ferromagnetic up to room temperature, even for few nanometer particle sizes. Furthermore, in traditional magnetic media, grain sizes show a wide distribution in size and shape, reducing the signal-to-noise ratio. In contrast, FePt NPs can be chemically synthesized with a highly uniform shape and narrow size distribution [1, 2]. This ultimately allows for 1 bit per nanometer-sized grain storage capacity [7].

One of the major issues in FePt NP growth, however, is the need for a high-temperature annealing treatment (∼700 °C and above) to obtain the desired high magnetocrystalline anisotropy [8]. The as-synthesized FePt NPs are namely in the chemically disordered face-centered-cubic (fcc) phase, which has low magnetic anisotropy. High-temperature annealing converts the NPs into the chemically ordered face-centered tetragonal (fct) phase, referred to as the $L1_0$ phase, where Fe and Pt planes alternate along the c-axis. High-temperature annealing, however, has a couple of severe disadvantages.

Annealing is usually performed on dried nanopowders, which often results in particle agglomeration and, consequently, a reduction of the particle uniformity and magnetic anisotropy. High-temperature annealing also destroys the organic ligands of the NPs, which takes away the advantage of the specific chemical functionality of the end groups, useful for chemical recognition and self-assembly in monolayers. A couple of methods have been developed to avoid agglomeration upon annealing, including a thick (10 nm) SiO_2 coating [9], salt matrix annealing [10], zeolite matrix annealing [11], and quite recently MgO coating [12, 13]. Although these methods reduce agglomeration and result in ferromagnetic NPs at room temperature, still high temperatures are required and consequently the

organic ligands are destroyed, losing all chemical functionality.

Given the above problems, a reduced annealing temperature is strongly favored. Doping the FePt lattice with specific transition metals turns out to be advantageous for the $L1_0$ phase transformation [1, 2, 14]. Au (or Ag) doping in small amounts leads to significant lowering of the annealing temperature for transforming the face-centered cubic (fcc) phase to the fct $L1_0$ phase. This is suggested to be related to defects and strain introduced by Au (or Ag) atoms. Upon annealing, Au (or Ag) atoms leave the FePt lattice at low temperature, leaving lattice vacancies that increase the mobility of Fe and Pt atoms to rearrange [3–6, 14]. Dry annealing studies of FePtAu NPs show a lowering of the annealing temperature with at least 100 °C compared to FePt NPs [3–6, 14]. Although dry annealing at reduced annealing temperatures results in (partly) transformation into the $L1_0$ phase, still large-scale NP agglomeration occurs [15–17]. A way to avoid this is to anneal the NPs in a liquid. Harrell *et al.* investigated postsynthesis, high-pressure annealing of FePtAu NPs in diphenyl ether solvent, and in silicone oil at atmospheric pressure [14]. However, these methods result in significant increase in particle size. Alternatively, one can already perform the NP synthesis at elevated temperature in a high-boiling point solution. This was done by Jia *et al.*, improving somewhat the dispersity [18].

7.2 FePtAu nanoparticle synthesis

A comprehensive and systematic study of low-temperature, solution synthesis that results in highly uniform ferromagnetic and chemically patternable FePtAu NPs is presented. Magnetic analysis indicated a large $L1_0$ phase fraction and that NPs of few nanometer size remained ferromagnetic up to room temperature. The onset for the $L1_0$ phase occured for annealing temperatures as low as 150 °C, where the long-range order parameter S [16] increased monotonically with annealing temperature. Importantly, the procedure left the organic ligands intact and demonstrated post-anneal chemically assisted monolayer patterning. Inorganic (magnetic) and organic materials, as well as bottom-up (self-assembly) and top-down fabrication methods were synergistically combined, being main motivations for organic spintronics [19].

The FePtAu NP synthesis was partly based on that of Jia *et al.* [18]. To synthesize FePtAu NPs, a combination of oleic acid and oleyl amine was used as stabilizing agent. The preparation is based on the reduction of platinum acetylacetonate and gold acetate by a diol and the decomposition of iron pentacarbonyl in high-temperature solutions. The octyl ether and hexadecylamine were used

as solvents. Importantly, the addition of octyl ether as a solvent was different from the original method described by Jia *et al.* and is considered essential in this case. Hexadecylamine is solid, whereas octyl ether is liquid at room temperature. This allowed the metal precursors already to dissolve at low temperature in the octyl ether before the hexadecylamine became liquid. It was expected that the improved mixing conditions were responsible for the small size dispersity for the NPs.

7.3 Chemical characterization of FePtAu nanoparticles

Figure 7.1 shows transmission electron microscope (TEM) images of $(FePt)_{85}Au_{15}$ NPs synthesized at standard conditions (30 min at 150 °C, Fig. 7.1a), and for 3 h at 150–350 °C (Fig. 7.1, panels b – e, respectively). The TEM analysis indicated regular NP assembly and small size dispersion, in particular for the lowest synthesis temperatures (Fig. 7.1f). The particle diameters for different synthesis temperatures, derived from TEM analysis, and the elementary composition of the particles obtained from energy dispersive X-ray diffraction (EDX) are given in table 7.1. At 250 and 350 °C, the NPs had a broader size distribution. For synthesis at 150 and 200 °C, the average NP composition was uniform and close to the metal precursor ratio. At 250 and 350 °C, a relative large distribution of Au contents was observed. NPs with Au content as high as $Fe_{16}Pt_{22}Au_{62}$ and as low as $Fe_{47}Pt_{45}Au_8$ were observed for 250 °C. For 350 °C, the highest Au content was $Fe_{21}Pt_{24}Au_{55}$ and lowest $Fe_{41}Pt_{47}Au_{12}$. This suggests the segregation of Au atoms from the FePt bulk at higher temperatures. This is in agreement with the mechanism suggested above that Au creates empty sites, which can subsequently be occupied by randomly distributed Fe and Pt atoms, thereby transferring the fcc disordered phase into the ordered fct ($L1_0$) phase [3–6, 14].

Figure 7.2 shows the XRD analysis, indicating the evolution of the $L1_0$ phase with increasing synthesis temperature. The evolution of the superlattice peaks, (001) and (110), as well as the fundamental peak (002), was clearly observed. The development of the Au(111) peak indicates the segregation of Au atoms from the FePt fcc lattice thereby transforming the lattice to fct ($L1_0$).

The lattice constant determined from the Pt(111) peak indicated a gradual decrease from 2.262 Å (150 °C, 3 h) to 2.211 Å (350 °C, 3 h), see Table 7.1, slowly approaching the ideal value of 2.197 Å for a FePt fct lattice. The as synthesized particles (150 °C, 30 min.) showed a lattice constant of 2.294 Å, indicating a fcc lattice. This clearly demonstrated the phase transformation from fcc to fct NPs.

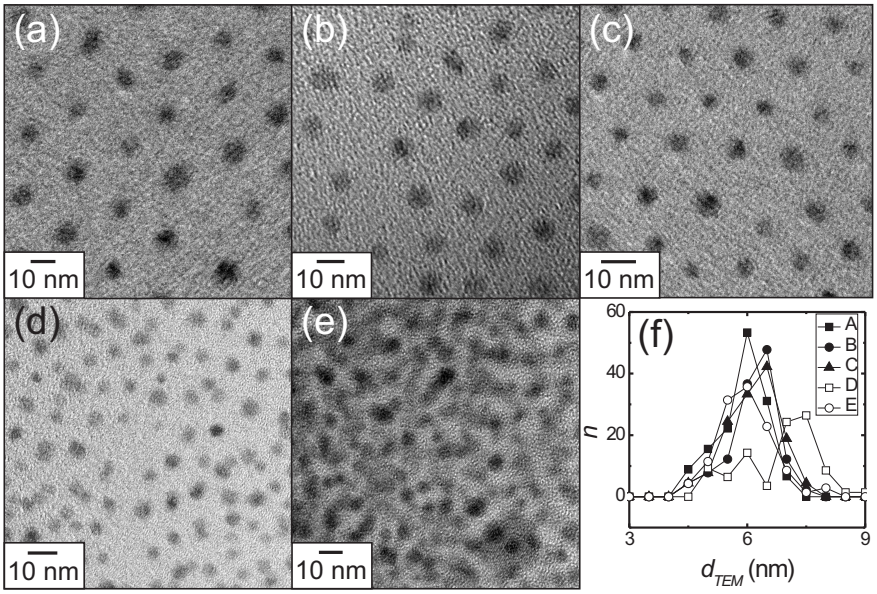

Figure 7.1: TEM images of $(FePt)_{85}Au_{15}$ NPs synthesized under different conditions: (a) 150 °, 30 min, (b) 150 °, 3 h, (c) 200 °, 3 h, (d) 250 °, 3 h, (e) 350 °, 3 h. (f) Particle size distribution (counts n vs. particle diameter d_{TEM}) determined from TEM imagines. Curves A – E correspond to panels a – e.

Table 7.1: Summary of FePtAu nanoparticle diameter d_{TEM} obtained by TEM, particle composition C_{EDX} obtained by EDX and lattice constant c_{XRD} calculated from XRD analysis for different synthesis temperature T_{synth} and time t_{synth}. For samples D and E, C_{EDX} was distributed.

sample	T_{synth} (°C)	t_{synth} (h)	d_{TEM} (nm)	C_{EDX}	c_{XRD} (Å)
A	150	0.5	5.5 ± 0.3	$Fe_{42}Pt_{41}Au_{17}$	2.294
B	150	3	6.2 ± 0.3	$Fe_{42}Pt_{44}Au_{14}$	2.262
C	200	3	6.4 ± 0.3	$Fe_{42}Pt_{40}Au_{18}$	2.241
D	250	3	7.2 ± 0.3	–	2.234
E	350	3	5.8 ± 2.3	–	2.211

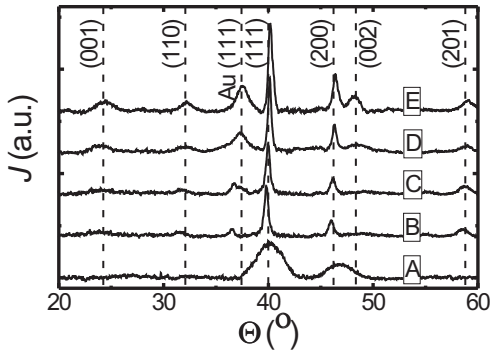

Figure 7.2: XRD spectra (intensity J vs. angle Θ) of $(FePt)_{85}Au_{15}$ NPs synthesized under different conditions: 150 °C, 30 min (A); 150 °C, 3 h (B); 200 °C, 3 h (C); 250 °C, 3 h (D); 350 °C, 3 h (E). The position of the superlattice peaks are denoted by the dashed lines.

To quantify the chemical ordering in the $L1_0$ phase, one often uses the long-range ordering parameter S, defined as [20]

$$S \simeq 0.85 \left(\frac{I_{(001)}}{I_{(002)}} \right)^{1/2}, \tag{7.1}$$

where $I_{(001)}$ and $I_{(002)}$ are the integrated intensities of the superlattice (001) and fundamental (002) peaks in the XRD spectrum. S is unity for perfectly ordered films and is zero for a chemically disordered film [21]. The long-range order parameter S for different synthesis temperatures extracted from the XRD data is plotted in Fig. 7.3d (open symbols). The ordering parameter linearly increased with synthesis temperature, reaching $S = 0.68$ for 350 °C. For comparison, Sun *et al.* have achieved an ordering parameter of $S = 0.98$ for dry annealing at 725 °C for 2 h in He [1, 2]. Significant ordering was achieved without much agglomeration at temperatures not more than 350 °C, maintaining the end group functionality (see below). The ordering process starts already from 150 °C onward for longer synthesis times. This is very remarkable as previous reports for annealed NP powders showed the onset of ordering around 350 °C (30 min) [3–6, 14].

As suggested by Chepulskii *et al.*, the ordering process is kinetically regulated [17, 22]. As a consequence, it was expected that approaching the equilibrium ordered state at low temperature will take longer. Therefore kinetic acceleration methods such as irradiation and or addition of other types of atoms are potentially effective in accelerating the formation of long-range order. To the best of our knowledge, all the previous studies report the synthesis of NPs by refluxing the

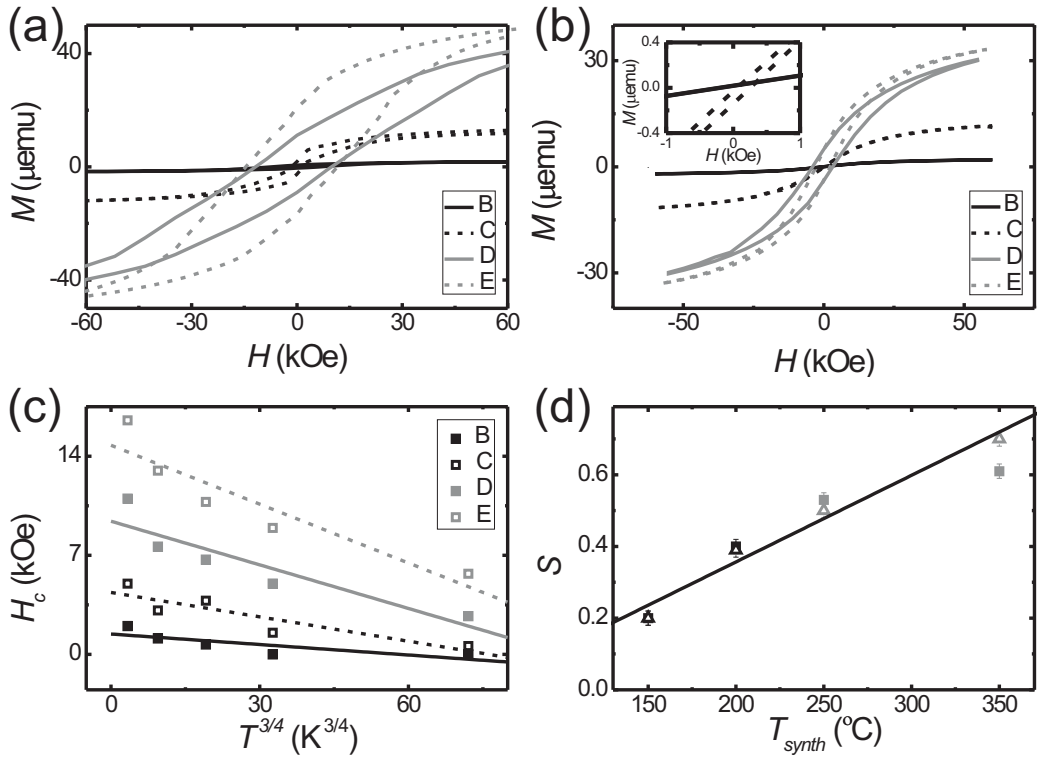

Figure 7.3: NP magnetization M vs. magnetic field H for different synthesis conditions at (a) 5 K and (b) room temperature. The inset in (b) is a zoom-in around zero field. (c) Coercive field H_c vs. temperature $T^{3/4}$ for different synthesis conditions. The lines are a fit to the Garcia-Otero model. (d) Ordering parameter S vs. synthesis temperature T_{synth} extracted from XRD data (open triangles) and from the Garcia-Otero model (solid dots). The line is a guide to the eye. Different lines and symbols correspond to the different synthesis conditions: 150 °, 3 h (B); 200 °, 3 h (C); 250 °, 3 h (D); 350 °, 3 h (E).

precursors solution only for 30 min. The duration of gentle refluxing is increased to 3 h. Increasing the refluxing time gave the NPs more time to organize in the desired crystal phase (kinetic control). This resulted in significantly higher chemical ordering of the NPs in the fct phase.

X-ray photoelectron spectroscopy (XPS) is performed to analyze the elemental states of Fe, Pt, and Au in the NPs. The NP surface composition indicates the presence of Fe_2O_3, while removal of the outer 1 nm shell by sputtering results in a composition of elements near to the expected value. This suggests that the surface is partially covered with Fe_2O_3.

7.4 Magnetic characterization of FePtAu nanoparticles

Single monolayers of FePtAu NPs for magnetic characterization [2, 21] were prepared. A silicon/silicon oxide substrate was functionalized with a very thin polyethylenimine (PEI) layer. When the polymer-derivative substrate was dipped into the particle dispersion, pendant functional groups of the polymer replaced the particle stabilizers and a strong monolayer particle assembly was formed. The substrate was then rinsed with solvent to remove physisorpted NPs and dried. This process resulted in one single FePtAu NP monolayer, as was confirmed by atomic force microscopy (AFM) and scanning electron microscopy (SEM).

The magnetic properties of NP monolayers were characterized by a vibrating sample magnetometer (VSM) with variable temperature (5–300 K). The magnetization curves at 5 and 300 K for NPs synthesized at different temperatures are shown in of Fig. 7.3a and b, respectively. The coercive field (H_c) clearly increased with synthesis temperature. At 5 K, magnetic hysteresis was observed for all synthesis temperatures, whereas at 300 K hysteresis was observed for synthesis temperatures 200 °C (H_c = 600 Oe), 250 °C (H_c = 2700 Oe), and 350 °C (H_c = 4800 Oe). This demonstrated room-temperature ferromagnetism from synthesis temperatures starting from 200 °C only.

The saturation magnetic moment of the monolayers was ∼35–40 μemu, both at room temperature and low temperature. This value for 350 °C synthesis temperature was compared with the momentum density of bulk FePt (1140 emu cm^{-3}) [23], assuming the ratio of FePt in the FePtAu NPs to be 0.85, 2.9 nm NP radius, and 1 nm ligand length. On the basis of those parameters, a saturation magnetic moment of 47 μemu was found. The experimentally observed value was slightly lower, as expected when taking into account the not fully developed $L1_0$ phase and lower effective packing density.

The observed temperature dependence of the magnetic hysteresis loops could be understood by realizing that the NP coercive fields decrease due to thermal fluctuations as the temperature increases. In this regard, Sharrocks formula [24] is the most widely used thermal relaxation model. However, it is valid for 2D systems rather than 3D systems like these NPs. Therefore, the model proposed by Garcia-Otero *et al.* was applied here to study the magnetic properties of NPs. This model applies to magnetically isolated and 3D random particle systems [20]. It can be described as

$$\frac{H_c}{H_k} = 0.479 - 0.81 \left(\frac{k_B T}{2 K_u V} (\ln \tau_m + 20.7) \right)^{3/4}, \tag{7.2}$$

where H_k is the critical field in Oe, defined as the field at which the NPs undergo an irreversible jump in their magnetization direction when decreasing the magnetic field, k_B the Boltzmann constant, K_u is the uniaxial anisotropy energy density, V is the particle volume, and τ_m is the measurement time. Using this model, the magnetic properties of the magnetic NPs can be evaluated. H_c vs $T^{3/4}$ is plotted in Fig. 7.3c. According to Eq. 7.2, from the intercept of the H_c versus $T^{3/4}$ curves, H_k could be derived. From the slopes of the curves K_uV was derived.

Table 7.2: Anisotropy constant K_u derived from the Garcia-Otero model and corresponding ordering parameter S for different synthesis temperature T_{synth} and time t_{synth}

sample	T_{synth} (°C)	t_{synth} (h)	K_u (10^6 Jm^{-3})	S
B	150	3	1.2	0.2
C	200	3	2.0	0.4
D	250	3	2.3	0.5
E	350	3	2.7	0.6

The anisotropy constants derived from the fits with Eq. 7.2 in Fig. 7.3c are given in Table 7.2. The long-range ordering parameter S for different annealing temperatures obtained based on a measured relationship between anisotropy constants K_u and ordering parameter S, is given in Table 7.2 as well, and plotted in Fig. 7.3d (solid symbols) [25]. The obtained ordering parameter is in good agreement with the ordering parameter determined by XRD (open symbols in Fig. 7.3d). A large anisotropy constant underlines the potential of these NPs for high-density data storage.

7.5 Patterning of FePtAu nanoparticles

Solution annealed FePtAu NPs dispersed very well, indicating that the ligands were still intact. In order to demonstrate that post-anneal patterning based on ligand exchange is still possible with our NPs, the NP patterns of Fig. 7.4 were fabricated. The used NPs were annealed at 350 °C for 3 h (according to sample E). The Si/SiO_2 substrate was covered with a thin (0.62 ± 0.04 nm) layer of hexamethyldisilazane (HMDS). Subsequently a pattern was defined by standard photolithography for selective self-assembly of the FePtAu NPs. When the substrate was dipped in the particle dispersion, pendant functional groups -NH- of the HMDS replaced the particle stabilizers and a strong NP monolayer was formed

in the exposed regions. Physisorbed NPs and resist were easily removed afterward. The successful patterning of the FePtAu NPs based on ligand exchange indicated that the ligands were intact after the solution annealing procedure.

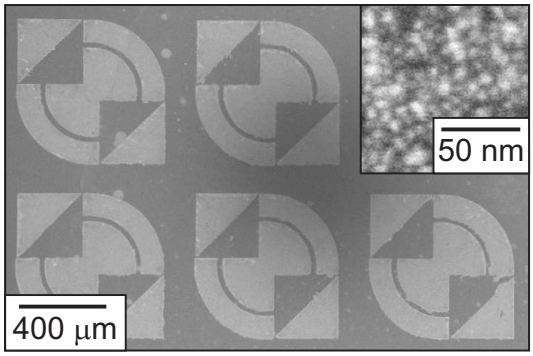

Figure 7.4: SEM image of a FePtAu NP monolayer pattern. The inset shows a zoom-in of a patterned area.

7.6 Conclusions

In conclusion, a low-temperature solution synthesis method for fabricating FePtAu NPs was demonstrated, for which the NPs remained ferromagnetic up to room temperature. This method strongly reduced NP agglomeration associated with high annealing temperatures and left the organic ligands intact. As a result, the post-annealed NPs still left the flexibility for further processing, patterning for instance. Low-temperature bottom-up synthesis of ferromagnetic, patternable NPs is considered to be an important step toward application of ferromagnetic NPs in high-density data storage and spintronics.

References

[1] S.H. Sun, Adv. Mater. **18**, 393 (2006).

[2] S.H. Sun, C.B. Murray, D. Weller, L. Folks and A. Moser, Science **287**, 1989 (2000).

[3] S.S. Kang, Z.Y. Jia, D.E. Nikles and J.W. Harrell, IEEE Trans. Magn. **39**, 2753 (2003).

[4] S.H. Kang, Z.Y. Jia, D.E. Nikles and J.W. Harrell, IEEE Trans. Magn. **40**, 513 (2004).

[5] S. Wang, S.S. Kang, D.E. Nikles, J.W. Harrell and X.W.J. Wu, Magn. Magn. Mater. **266**, 49 (2003).

[6] C.H. Yu, N. Caiulo, C.C.H. Lo, K. Tam, S.C. Tsang, Adv. Mater. **18**, 2312 (2006).

[7] T. Schrefl, G. Hrkac, D. Suess, W. Scholz and J.J. Fidler, Appl. Phys. **93**, 7041 (2003).

[8] I. Zafiropoulou, V. Tzitzios, D. Petridis, E. Devlin, J. Fidler, S. Hoefinger, D. Niarchos, Nanotechnology **16**, 1603 (2005).

[9] S. Yamamoto, Y. Morimoto, T. Ono and M. Takano, Appl. Phys. Lett. **87**, 032503 (2005).

[10] B.A. Jones, J.D. Dutson, K. OGrady, B.J. Hickey, D.R. Li, N. Poudyal and J.P. Liu, IEEE Trans. Magn. **42**, 3066 (2006).

[11] S. Momose, H. Kodama, W. Yamagishi and T. Uzumaki, Jpn. J. Appl. Phys. **46**, L1105 (2007).

[12] J. Kim, C.B. Rong, Y. Lee, J.P. Liu and S.H. Sun, Chem. Mater. **20**, 7242 (2008).

[13] J.M. Kim, C.B. Rong, J.P. Liu and S.H. Sun, Adv. Mater. **21**, 906 (2009).

[14] J.W. Harrell, D.E. Nikles, S.S. Kang, X.C. Sun, Z. Jia, S. Shi, J. Lawson, G.B. Thompson, C. Srivastava, and N.V. Seetala, Scr. Mater. **53**, 411 (2005).

[15] H. Borchert, E.V. Shevehenko, A. Robert, I. Mekis, A. Kornowski, G. Grubel and H. Weller, Langmuir **21**, 1931 (2005).

[16] B.E. Warren, *X-Ray Diffraction* Addison-Wesley Publishing Company, Reading (1969).

[17] R.V. Chepulskii, J. Velev and W.H.J. Butler, Appl. Phys. **97**, 10J311 (2005).

[18] Z.Y. Jia, S.S. Kang, D.E. Nikles and J.W. Harrell, IEEE Trans. Magn. **41**, 3385 (2005).

[19] W.J.M. Naber, S. Faez and W.G. van der Wiel, J. Phys. D: Appl. Phys. **40**, R205 (2007).

[20] J. Garcia-Otero, A.J. Garcia-Bastida and J.J. Rivas, Magn. Magn. Mater. **189**, 377 (1998).

[21] S.H. Sun, S. Anders, T. Thomson, J.E.E. Baglin, M.F. Toney, H.F. Hamann, C.B. Murray and B.D.J. Terris, Phys. Chem. B **107**, 5419 (2003).

[22] R.V. Chepulskii and W.H. Butler, Phys. Rev. B **72**, 134205 (2005).

[23] T. Klemmer, D. Hoydick, H. Okumura, B. Zhang and W.A. Soffa, Scr. Metall. Mater. **33**, 1793 (1995).

[24] D. Weller and A. Moser, IEEE Trans. Magn. **35**, 4423 (1999).

[25] T. Shima, T. Moriguchi, S. Mitani and K. Takanashi, Appl. Phys. Lett. **80**, 288 (2002).

Chapter 8

Two-dimensional organic spin systems and their interaction with electrons

In this chapter, monolayers of organic complexes with an unpaired spin on a thin Au film were investigated. XPS and EPR measurements showed the existence of an unpaired spin in $[Co(tpy\text{-}SH)_2]^{2+}$ complexes. In a number of systems with diluted monolayers, electrical transport measurements showed an increase of the Au film sheet resistance for temperatures below $\sim$20 K, possibly implying Kondo physics. A negative magnetoresistance was observed, which was larger for lower temperatures.

8.1 Introduction

The electronic interaction of magnetic impurities with their environment can lead to different spin phenomena, like the Kondo effect [1–6], RKKY interaction [7–9] and spin glasses [10] (see also chapter 1). These spin phenomena are very interesting from a fundamental point of view, since they lie at the very heart of solid-state physics. In this chapter, a 2D spin system, consisting of a monolayer of organic molecules with an unpaired spin is proposed, and its interaction with an underlying metal substrate was investigated. Using bottom-up fabrication techniques, this system potentially offers a large set of parameters which can be tuned, including the nature of the molecules, the density and ordering of the localized spins, and the coupling between the localized spins and the conduction electrons, to study their effect on the different spin interactions.

A schematic picture of the investigated 2D spin system is given in Fig. 8.1. It consists of a thin Au film (typically 10 nm) covered with a monolayer of chemisorbed organic molecules, of which some have an unpaired spin. Several ways to vary the properties of this system are schematically shown in the figure. The interaction between the isolated spin and the conduction electrons in the Au substrate can be tuned by changing the nature of the organic molecule. For example, a larger molecule can be synthesized to change the distance between the localized spin and the substrate, which will change the interaction between the localized spins and the electrons in the substrate. The interaction between the localized spins themselves, via the RKKY interaction (see chapter 1), can be changed by varying the distance between them. This can be achieved by changing the concentration of paramagnetic molecules in the monolayer. In this 2D spin system, it is thus potentially possible to study the competition between a pure Kondo system (i.e. without interaction between the localized spins), and the RKKY interaction.

By changing the thickness of the Au, this system could also offer the possibility to investigate the extent of the Kondo cloud [11, 12]. This idea is illustrated in Fig. 8.1. Conduction electrons which are interacting with the unpaired spin of the molecules over a distance ξ_K, the Kondo screening length, contribute to the Kondo effect, while the electrons further away do not. By varying the thickness d of the metal layer, this ratio will be different and a change in the Kondo effect might be observed. This change is therefore related to the Kondo screening length ξ_K.

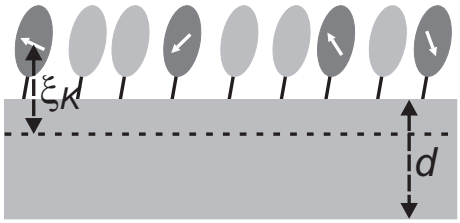

Figure 8.1: Schematic picture of a 2D spin system consisting of a monolayer of molecules with (dark grey) and without (light grey) an unpaired spin, on top of a conducting substrate with thickness d. The localized spins, denoted by the arrows, interact with the conduction electrons over a distance ξ_K.

8.2 Monolayer fabrication and characterization

For an interaction between the localized spins of the organic molecules with the underlying substrate, electrons must be able to tunnel back and forth to these magnetic impurities. The molecule $[Co(tpy\text{-}SH)_2]^{2+}$, where (tpy-SH) is the thiol-modified terpyridine ligand 4'-(5-mercaptopentyl)-2,2':6',2"-terpyridinyl (see Fig. 8.4a), seems suitable for this purpose. According to literature [13], this complex is mostly in the low-spin state in the temperature range of the measurements (0.25–80 K, as shown later on), so the ground state of the Co^{2+} has spin $s = \frac{1}{2}$ (see chapter 1). It is known from electrochemical studies that the charge state of the Co can change from Co^{2+} to Co^{3+} at low voltages ($\sim$0.25 V) [14], which is essential for screening of the spin since an electron has to be able to tunnel from the spin impurity for a short time. Furthermore, Park *et al.* [15] have observed the Kondo effect in the case of transport through this Co-complex. Their experiment shows that electrons can indeed tunnel to and from the molecule in a sufficient rate to screen the magnetic impurity.

To confirm the oxidation state of the Co-complex in the monolayer, XPS measurements were performed on Au substrates with a monolayer formed in solution. A Si/SiO_2($\sim$1 nm) substrate covered with 10 nm Au (purchased from Ssens, Hengelo, The Netherlands) was put in a 0.5 mM Co-complex in acetonitrile solution (with PF_6^- as the counterion). After a couple of hours (typically overnight), the substrate was taken out of the solution and rinsed with acetonitrile, to remove any physisorbed molecules. XPS measurements, shown in Fig. 8.2a, identified the ion inside as Co^{2+}. The two main peaks at 781.3 and 796.3 eV, corresponding to the $Co2p_{3/2}$ and $Co2p_{1/2}$ state, respectively, are representative for a system with a Co^{2+}-ion in an octahedral structure [16]. The satellite peaks are associated with

outer-shell excitations parallel to the photoionization of an inner-shell electron, which disturbs the central potential [17, 18].

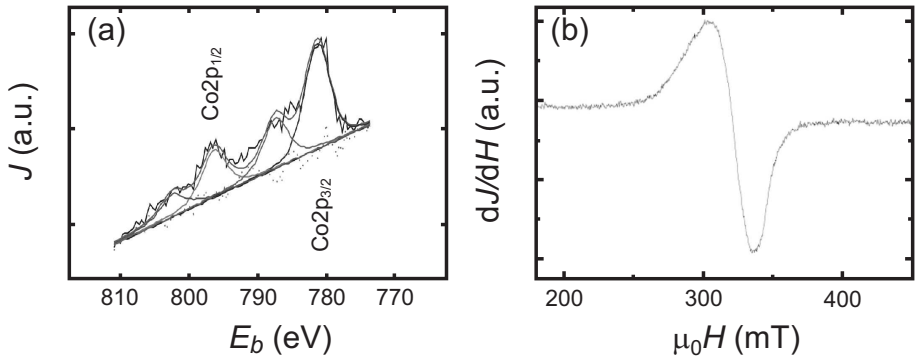

Figure 8.2: (a) XPS spectrum (intensity J vs. binding energy E_b) of the Co-complex. The two peaks at 781.3 and 796.3 eV correspond to the $Co2p_{3/2}$ and $Co2p_{1/2}$ state. (b) EPR measurements (the derivative of the intensity dJ/dH vs. magnetic field H) on powder of the Co-complex at 165 K, showing a resonance at $\mu_0 H = 320$ mT.

To confirm the existence of an unpaired spin, the molecule was also characterized by electron paramagnetic resonance (EPR) measurements. The measurements on powder of the Co-complex clearly showed a resonance at $\mu_0 H = 320$ mT, indicating the presence of an unpaired spin with a g-factor $g = 2.09$ (see Fig. 8.2b).

To determine the coverage of the monolayer on the Au surface, cyclic voltammetry measurements were performed, which are shown in Fig. 8.3a. Measurements were done with an Au electrode covered with a monolayer of Co-complexes in a 0.1 M tetra-n-butylammonium hexafluorophosphate acetonitrile solution. A peak was observed around 0.375 V, which was attributed to the redox process of the Co^{2+}-ion. Integration of the I-V curves give the total charge Q, from which the surface coverage of the monolayer can be determined by

$$\Gamma = \frac{Q}{nFA}, \tag{8.1}$$

where n is the number of electrons per mol of reaction, F the Faraday constant and A the surface area. By taking I-V curves for different scan rates, Q could be determined as a function of the scan rate, as shown in Fig. 8.3b. The independence of Q on the scan rate shows that it is a surface-confined process, as is expected for a monolayer [19]. By using Eq. 8.1, $\Gamma = 5.4{\cdot}10^{-11}$ mol cm^{-2} was found, which corresponds to one molecule per 3.1 nm^2. Assuming a diameter of

11 Å, leading to an area of 98 Å^2 per molecule, this corresponds to a surface coverage of ∼30%. This result may be important for determining the RKKY interaction in this particular system, although the exact strength is not known. At this moment, it is not clear why the redox potential is different from that reported by other groups [14], but it might be due to the different surface coverage in the experiments, causing a different interaction between the Co-complexes in the monolayer.

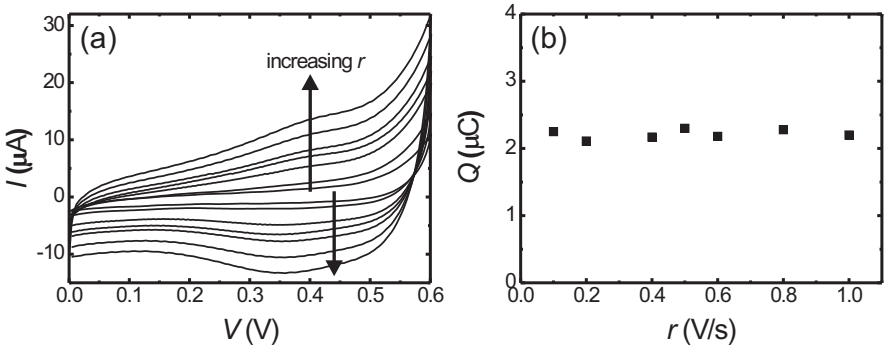

Figure 8.3: Cyclic voltammetry measurements on a Co-complex ($[Co(tpy\text{-}SH)_2]^{2+}$) monolayer. (a) Current I vs. voltage V for different scan rates r (the direction of the arrows denote increasing r) and (b) charge Q vs. scan rate, obtained from the curves in (a).

To vary the concentration of the Co-complexes on the Au film, different solutions were used to form the monolayer. To lower the concentration, molecules, which were similar to the Co-complex, but in which the Co^{2+}-ion is replaced by a Zn^{2+}-ion, were added to the solution. Zn has the electron configuration [Ar] $3d^{10}$ $4s^2$, so a Zn^{2+}-ion has 10 electrons in the 3d-shell and no unpaired spin. Since this molecule has the same structure, the same chemisorption process as that of the Co-complex was expected. The ratio of the Co- and Zn-complexes in solution will therefore be reflected in the ratio of Co- and Zn-complexes in the monolayer. However, if the chemisorption process will be different due to, for example, magnetic or electric interactions between the molecules, at least a smaller concentration of the Co-complex in the diluted monolayer is expected as compared to the monolayer formed with only Co-complexes in the solution. A good control over the precise concentration of the Co-complex in the monolayer will however be difficult in that case. By using a diluted Co-complex monolayer, the magnetic ions are placed further apart, and this can change the strength of the coupling between the localized spins.

8.3 Temperature dependent resistivity measurements

A Van der Pauw measurement technique was used to electrical characterize the Au substrates covered with a monolayer of molecules with an unpaired spin by measuring the sheet resistance R_s of the Au film as a function of temperature. After monolayer formation, the substrate was wire-bonded at the four corners and measured with a Physical Properties Measurements System (PMMS) of Quantum Design (see chapter 1). With these four contacts, Hall measurements could also be performed, to determine the charge carrier density in the sample. Hall measurements in all samples gave a carrier density in the Au film of $\sim 5.2 \cdot 10^{28}$ m^{-3}, close to the value of bulk Au ($\sim 5.9 \cdot 10^{28}$ m^{-3}), showing the good quality of the Au layers and the fact the Au is unaffected by the monolayer formation.

For the $[Co(tpy\text{-}SH)_2]^{2+}$ complex (see Fig. 8.4a), different samples with different ratios of Co-complexes and Zn-complexes were measured. Samples were fabricated with only Co-complexes, only Zn-complexes, and both Co-complexes and Zn-complexes in the ratios 1:1, 1:100 and 1:1000 on Au films cleaned with acetone and 2-propanol. The given ratios are the ratios as used in the solutions prior to the monolayer formation. Temperature dependent measurements of the sheet resistance R_s with a current of 100 μA, are shown in Fig. 8.4b – f. These measurements are typical for our samples and have been reproduced in a lot of devices. When lowering the temperature starting at 40 K, the same behavior was observed in the range 40– $\sim$20 K. R_s dropped, as is expected for a metal as phonon scattering is reduced. Lowering the temperature further however, resulted in different behavior for different samples.

The samples with only Zn-complexes showed a saturation of the resistance around 10 K (see Fig. 8.4b), as expected for a metal without any magnetic impurities. The same behavior was observed for the samples with only Co-complexes (Fig. 8.4c), and for the ratio 1:1000 (Fig. 8.4f).

The temperature dependence was different for the other measured samples. For the ratio 1:1 (Fig. 8.4d) a small increase in the resistance was observed when the temperature decreased below 10K. A large increase in the resistance when the temperature is lowered was seen in the sample with the ratio 1:100 (Fig. 8.4f, filled squares). This increase was as high as several percent as compared to the minimum value at $\sim$20 K. This behavior was observed in 40% of the samples with this ratio. An absence of the local resistance minimum in the other samples with ratio 1:100 might originate from impurities, clustering of the Co-complexes (resulting in a large spin interaction) or the formation of a disordered monolayer.

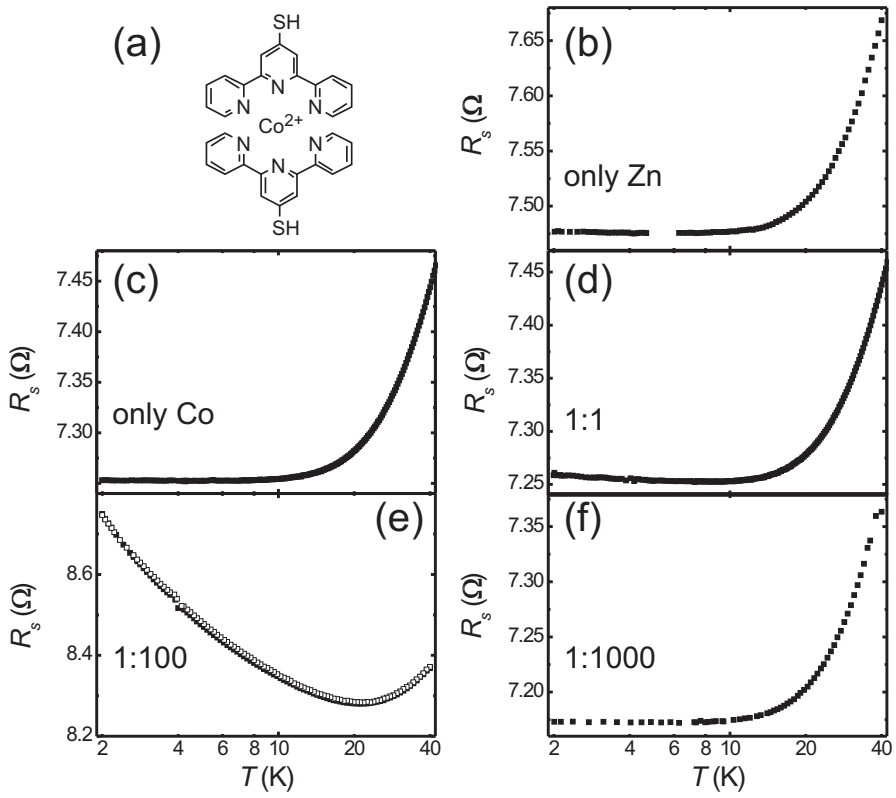

Figure 8.4: (a) Molecular structure of the Co-complex used in measurements of the sheet resistance R_s vs. temperature T for samples with a 10 nm Au layer covered with a monolayer consisting of (b) Zn-complexes, (c) Co-complexes, and Co- and Zn-complexes in the ratio (d) 1:1, (e) 1:100 and (f) 1:1000. In (e) measurements are shown without (filled squares) and with (open squares) a magnetic field of 8 T. Error bars are smaller than the used symbols.

Another option might be the formation of polymers by the Co- and Zn-complexes, because of the two functional SH-groups. This might result in a different number of Co-complexes directly attached to the surface as what might be expected from the used solution for monolayer formation.

While the local resistance minimum was sometimes absent samples with the ratio 1:100, this effect was never measured in one of the other samples with ratios 1:1000 and 1:10 000. More importantly, this local resistance minimum was never measured in samples with only Zn-complexes (i.e. without any magnetic impurities). This makes the assumption that the effect originated from magnetic impurities (Co-complexes), and not from e.g. heating effects, very likely.

To exclude impurities and polymer formation in the samples, samples were fabricated with molecules with only one thiol-group, $[Co(tpy)(tpy\text{-}SH)]^{2+}$ (see Fig. 8.5a), on thoroughly cleaned Au films using piranha solution.

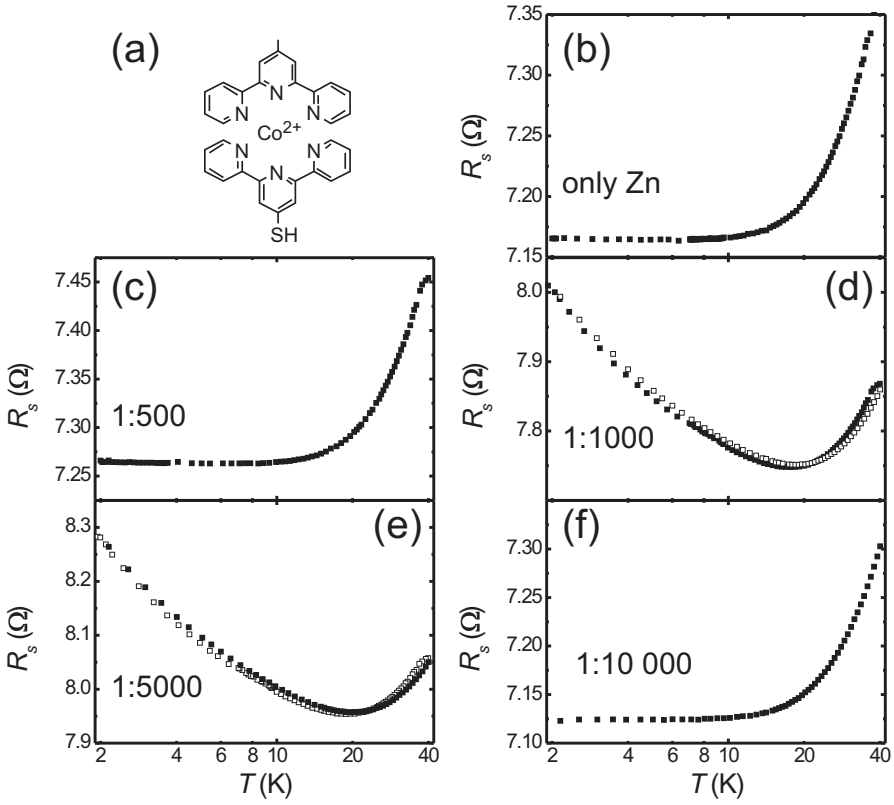

Figure 8.5: (a) Molecular structure of the Co-complex used in measurements of the sheet resistance R_s vs. temperature T for samples with a 10 nm Au layer covered with a monolayer consisting of (b) Zn-complexes, and of Co- and Zn-complexes in the ratio (c) 1:500, (d) 1:1000, (e) 1:5000 and (f) 1:10 000. In (d) and (e) measurements are shown without (filled squares) and with (open squares) a magnetic field of 8 T. Error bars are smaller than the used symbols.

Measurements of the sheet resistance R_s of these samples as a function of the temperature are shown in Fig. 8.5. All measurements have been reproduced with several samples. In the sample with only Zn-complexes a decrease in the sheet resistance R_s was observed when the temperature was lowered, and the resistance saturated at low temperatures below 10 K. This behavior was also observed for samples with a ratio of 1:500 and 1:10 000.

Different behavior was observed for the ratios 1:1000 and 1:5000. In approx-

imately 40% of the measured samples an increase in the sheet resistance of a few percent (as compared to the lowest sheet resistance) was observed when the temperature was decreased below ∼20 K (Fig. 8.5d and e).

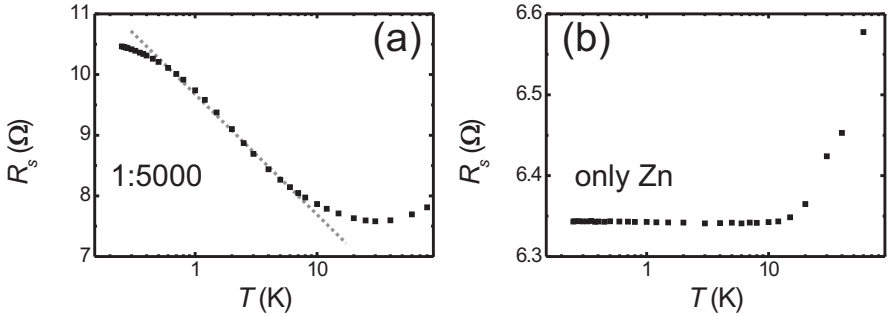

Figure 8.6: Sheet resistance R_s vs. temperature T of a 10 nm Au layer covered with a monolayer of (a) Co- and Zn-complexes in the ratio 1:5000 and (b) only Zn complexes. Error bars are smaller than the used symbols.

One of the samples with a ratio of 1:5000 was also measured at lower temperatures, down to 0.27 K, in a Heliox VL system (see chapter 1). An increase in the sheet resistance when the temperature was decreased below ∼20 K down to 0.270 K was observed (Fig. 8.6a). This increase was found to be logarithmic over one decade (∼0.5–5 K, see Fig. 8.6a). This local resistance minimum was absent in a sample with only Zn-complexes (see Fig. 8.6b), which was consistent with the measurements down to 2 K shown above.

8.4 Magnetic field dependent resistivity measurements

A local resistance minimum in samples with magnetic impurities is the signature of the Kondo effect. To make this more plausible, the temperature-dependent resistivity measurements were performed in the presence of a magnetic field of 8 T. The Kondo effect was expected to be absent when the energy of the magnetic field becomes larger than the energy associated with the Kondo effect, due to the Zeeman splitting of the spin-up and spin-down energy states

$$g\mu_B H > k_B T_K, \tag{8.2}$$

where g is the g-factor of the material ($g \sim 2$ for free electrons), μ_B the Bohr magneton, H the magnetic field, k_B the Boltzmann constant and T_K the Kondo

temperature. In this case, a spin-flip process is energetically unfavorable and the Kondo effect will be suppressed [20]. If T_K is taken as the temperature at the local resistance minimum, from Eq. 8.2 the energy associated with the magnetic field is estimated to be larger than the energy associated with the Kondo effect in the samples at 2 K, and an effect of the magnetic field should be seen.

The measurement at $\mu_0 H = 8$ T are shown in Fig. 8.4e for $[Co(tpy\text{-}SH)_2]^{2+}$, and in Fig. 8.5d and e for $[Co(tpy)(tpy\text{-}SH)]^{2+}$ (open squares). Almost no change is observed as compared to the measurement at $\mu_0 H = 0$ T. To investigate the magnetic field dependence in more detail, the temperature was fixed at 2 K and the magnetic field was swept from -8 T to 8 T (Fig. 8.7 and Fig. 8.8a and b). A small decrease in resistance was observed, which was two orders of magnitude lower than the observed resistance increase as compared to the lowest resistance value. This magnetic field dependence was seen in all samples that showed a local resistance minimum. To exclude that this behavior was due to any heating effect or influence on the temperature sensor by the sweeping magnetic field, different sweep rates were used, but no change in the magnetic field dependent behavior was observed. In addition, no temperature change was seen on the temperature sensor close to the sample during the sweep, making a temperature effect not likely. Even if a local temperature change in the Au layer was responsible for the effect, some temperature relaxation would be expected during the slowest sweep rate, which was not observed. This change in sheet resistance with magnetic field has never been observed in any sample without magnetic molecules and did not depend on the direction of the magnetic field, which seems to exclude interference effects like weak localization [21]. A superimposed increase in the resistance at magnetic fields larger than 6 T was observed. This resistance increase is measured in all samples, with and without paramagnetic molecules, and was associated with Lorentz magnetoresistance.

If the resistance lowering is due to the a weakening of the Kondo effect, it is much smaller than expected [20]. This can imply several things. One is that the thermal energy has to be considered, which is given by $3.5 k_B T$. If this value is larger than the splitting of the spin states caused by the magnetic field, electrons are still able to flip their spin, since the required energy can come from thermal fluctuations. For free electrons, the spin-splitting in a field of 8 T is, according to the first part of Eq. 8.2, $\sim$900 μeV. The thermal energy at 2 K is $\sim$600 μeV. These values are comparable, so the splitting could be less effective in suppressing the Kondo effect, which might explain the small influence of the magnetic field. Another explanation is that the g-factor in the system is not the same as for free electrons. However, it is unclear why it would deviate significantly from 2 and Park *et al.* [15] have measured the g-factor in the Co-complex to be close to 2.

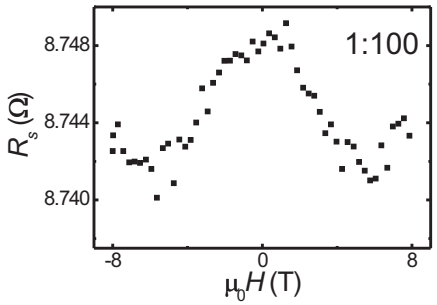

Figure 8.7: Sheet resistance R_s vs. magnetic field H for the sample with ratio 1:100 in Fig. 8.4.

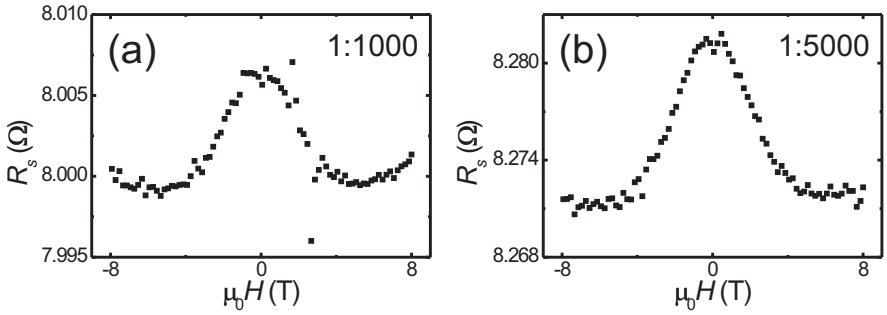

Figure 8.8: Sheet resistance R_s vs. magnetic field H for the samples with ratio (a) 1:1000 and (b) 1:5000 in Fig. 8.5.

Moreover, the EPR measurements on the Co-complexes (see Fig. 8.2) showed a g-factor only slightly larger than 2. A different explanation may lie in the fact that there may be another mechanism involved in this effect, like coupling between the magnetic moments due to the RKKY interaction. It also has to be considered that this behavior is not due to the Kondo effect, and another explanation has to be found. At the moment however, to the best of our knowledge, no other effect is known that shows a local resistance minimum in the presence of localized spins.

To investigate the influence of a magnetic field for different temperatures, the sheet resistance of the sample in Fig. 8.6 was measured while sweeping a magnetic field from -1 T to 8 T at 0.27 K, 0.5 K and 1 K (see Fig. 8.9a). For all temperatures, a drop in R_s was seen for increasing fields. This magnetic field effect is independent of the field direction and has not been observed in samples

without paramagnetic molecules, excluding orbital effects like weak localization. The magnetoresistance MR in this sample is defined as $MR(H) = [R_s(H) - R_s(0)]/R_s(0)$. The MR for different temperatures, including the MR at 2 K extracted from Fig. 8.8, is given in Fig. 8.9b. The negative MR increased for decreasing temperature. This could be due to the lower thermal energy and might be a further explanation for the small magnetic field dependence observed at 2 K. This is consistent with literature, in which it has been theoretically shown that the splitting of the energy levels becomes less pronounced at higher temperatures [20]. However, the decrease of the resistance was lower than what might be expected from Eq. 8.2.

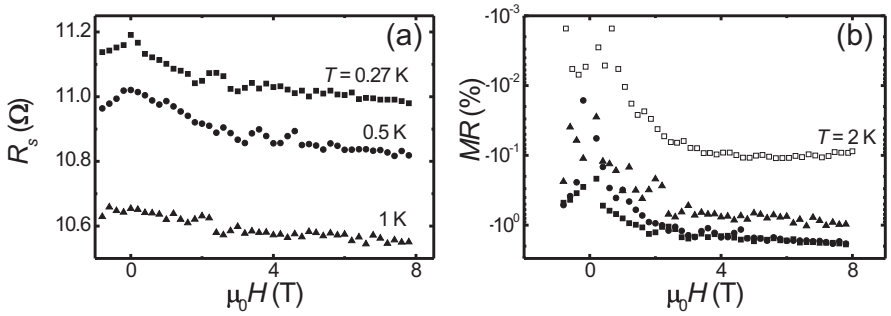

Figure 8.9: Magnetic field dependence for the sample of Fig. 8.6. (a) Sheet resistance R_s vs. magnetic field H for different temperatures, as denoted in the figure, and (b) magnetoresistance $MR(H) = [R_s(H) - R_s(0)]/R_s(0)$ vs. H for different temperatures, as denoted in the figure for $T = 2$ K. Other symbols corresponds to the temperatures in (a).

8.5 Conclusions and outlook

Electrical measurements on 10 nm thick Au films covered with a monolayer of organic molecules with an unpaired spin showed a local resistance minimum for specific concentrations of the paramagnetic molecule. This effect has been observed in ∼40% of the samples with that specific concentration and has been reproduced in several samples and in different measurement setups. Importantly, it has never been observed in samples without paramagnetic molecules, making it very likely to originate from the interaction of the conduction electrons with the localized spins of the monolayer.

Two slightly different molecules gave similar result, with the only difference

being the concentration of paramagnetic molecules for which the local resistance is observed. The difference might be attributed to polymer formation or impurities on the Au film before monolayer formation.

The existence of a local resistance minimum is the signature of the Kondo effect. The suppression of this effect at high magnetic fields, due to the splitting of the spin-up and spin-down energy states was expected. A small *MR* effect which depends on the temperature was observed, but this effect was smaller than what might be expected from literature.

Interestingly, the local resistance minimum was absent for high and low concentrations of the paramagnetic molecule. Although still speculating at this moment, it can be explained in terms of Kondo physics. Lowering the concentrations reduces the magnetic scattering sites, which will lead to a less pronounced Kondo effect. At high concentrations, the magnetic impurities might start to couple to each other via the RKKY interaction, thereby suppressing the Kondo effect.

The absence of the local resistance minimum in 60% of the samples for which it was observed in the other 40%, indicated the lack of control over the monolayer formation. This might be due to disorder in the monolayer, making it impossible to reproduce the exact same monolayer in different samples. For long alkanethiols, it is known that they can form highly ordered SAMs due to the interaction between these molecules [22]. Increasing the length of the "tail" of the molecule which is used to attach it to the Au film might therefore increase the order, leading to a controlled system in which different ratios can systematically be investigated. Care has to be taken though, since a longer tail could also effect the Kondo parameters.

As mentioned before, the system proposed in this chapter offers a lot of parameters that can be varied to study the interaction of the 2D spin system with its environment. As already described above, the concentration of the paramagnetic molecule can be varied over orders of magnitude, to change the interaction between the localized spin on the organic molecules. The interaction of the localized spin with the conduction electrons can be changed by chemically engineering the distance between the localized spin and the Au film on the Å-scale. Further influence on the Kondo physics can be achieved by using a semiconducting substrate, whereof the Fermi energy can be changed by a nearby gate electrode. Another interesting idea would be to place a gate electrode close to the paramagnetic monolayer. In this way, the spin state can be electrically tuned, potentially leading to an electrically controlled Kondo effect.

Monolayers could also be patterned on the nm scale, using well-developed patterning techniques like transfer printing, possibly leading to the fabrication

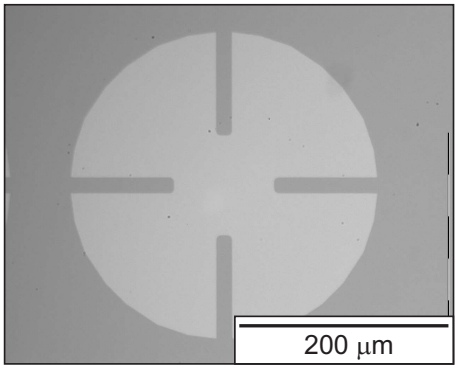

Figure 8.10: Picture of a patterned 10 nm thick Au structure (light area) in the shape of a clover leaf, suitable for Van der Pauw measurements. The central square area is 100 x 100 μm^2.

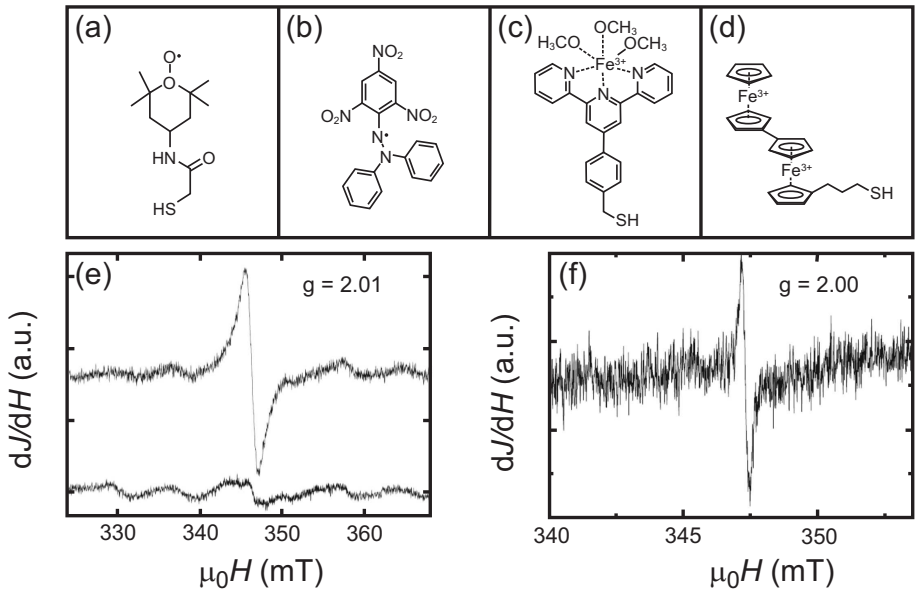

Figure 8.11: Structures of organic molecules with an unpaired spin. (a) A 2,2,6,6-tetramethyl-1-piperidinyloxy (TEMPO) derivative, (b) 2,2-diphenyl-1-picrylhydrazyl (DPPH), (c) a Fe-complex and (d) biferrocene. The unpaired spin is denoted by the dot in (a) and (b) or the charge on Fe in (c) and (d). EPR spectra (derivative of the intensity dJ/dH vs. magnetic field H) is given in (e) and (f) for the molecules drawn in (a) (monolayer on Au, top spectrum) and (b) (physisorbed layer on Au). For comparison, the bottom EPR spectrum in (e) shows the data for a bare Au substrate.

of artificial spin superlattices. Alternatively, the Au film can be patterned, to achieve small areas in which a highly-ordered monolayer might be achieved. An example of a patterned 10 nm thick Au film is shown in Fig. 8.10.

Many different paramagnetic molecules can easily be tested. Examples of several synthesized molecules are given in Fig. 8.11a – d. Some of these molecules have been characterized by EPR (see Fig. 8.11e and f), which demonstrates the presence of an unpaired spin in a monolayer of these molecules on Au films. A clear resonance is observed with g-factors close to 2, as given in the figure. These molecules have not yet been thoroughly electrically investigated.

References

[1] W.J. de Haas, J.H. de Boer and G.J. van den Berg, Physica **1**, 1115 (1934).

[2] J. Kondo, Prog. Theor. Phys. **32**, 37 (1964).

[3] L.P. Kouwenhoven and L.I. Glazman, Physics World **14**, 33 (2001).

[4] D. Goldhaber-Gordon, H. Shtrikman, D. Mahalu, D. Abusch-Magder, U. Meirav and M.A. Kastner, Nature **391**, 156 (1998).

[5] S. Sasaki, S. De Franceschi, J.M. Elzerman, W.G. van der Wiel, M. Eto, S. Tarucha and L.P. Kouwenhoven Nature **405**, 764 (2000).

[6] W.G. van der Wiel, S. De Franceschi, T. Fujisawa, J.M. Elzerman, S. Tarucha and L.P. Kouwenhoven Science **289**, 2105 (2000).

[7] M.A. Ruderman and C. Kittel, Phys. Rev. **96**, 99 (1954).

[8] T. Kasuya, Prog. Theor. Phys. **16**, 45 (1956).

[9] K. Yosida, Phys. Rev. **106**, 893 (1957).

[10] A.C. Hewson, *The Kondo problem to Heavy Fermions*, Cambridge University Press, Cambridge (1997).

[11] I. Affleck and P. Simon, Phys. Rev. Lett. **86**, 2854 (20011).

[12] G. Bergmann, Phys. Rev. B **77**, 104401 (2008).

[13] S. Kremer, W. Henke and D. Reinen, Inorg. Chem. **21**, 3013 (1982).

[14] M. Maskus and H.D. Abruña, Langmuir **12**, 4455 (1996).

[15] J. Park, A.N. Pasupathy, J.I. Goldsmith, C. Chang, Y. Yaish, J.R. Petta, M. Rinkoski, J.P. Sethna, H.D. Abruña, P.L. McEuen and D.C. Ralph, Nature **417**, 722 (2002).

[16] M. Oku and K. Hirokawa, Journal of Electron Spectroscopy and Related phenomena **8**, 475 (1976).

[17] T. Novakov, Phys. Rev. B **3**, 2693 (1971).

[18] A. Rosenewaig, C.K. Wertheim and H J. Guggenheim, Phys. Rev. Lett. **27**, 479 (1971).

[19] C.A. Nijhuis, *PhD Thesis*, Wöhrmann Print Service, Zutphen (2006).

[20] T.A. Costi, Phys. Rev. Lett. **85**, 1504 (2000).

[21] G. Bergmann, Phys. Rev. B **25**, 2937 (1981).

[22] M.D. Porter, T.B. Bright, D.L. Allara and C.E.D. Chidsey, J. Am. Chem. Soc. **109**, 3559 (1987).

Appendix A

Fabrication recipes

In this appendix, the recipe for fabrication of the shadow mask as discussed in Chapter 3, the recipe for the electrode fabrication with shadow masks and the recipes for electrode fabrication with photo- and e-beam resist are given.

A.1 Shadow mask fabrication

- Double-side wafer cleaning in HNO_3
- Resist spinning front and backside, OLIN 907/17, 5" 500 rpm and 20" 4000 rpm
- Pre-exposure bake 1' at 90°C
- Exposure front side 7"
- After-exposure bake 1' at 120 °C
- Develop 40" in OPD 4262
- Dry etching 15-20', Adixen SE, recipe B.HARS: C_4F_8 200 sccm 1", SF_6 250 sccm 3", 1500 W 10°C
- Resist removal with HNO_3, wafer cleaning in HNO_3, HF dip
- LPCVD 300 nm SiRN
- Resist spinning front and backside, OLIN 907-17, 5" 500 rpm and 20" 4000 rpm
- Pre-exposure bake 1' at 90°C
- Exposure back side 7"
- After-exposure bake 30' at 120°C
- Develop 40" in OPD 4262
- Dry etching 20', PlasmaTherm 790, recipe ETCH: CHF_3 25 sccm, O_2 5 sccm, 1500 W, 10°C
- Resist removal with HNO_3, wafer cleaning in HNO_3
- Wet etch in KOH:DI 1:3, ∼500 min

- RCA clean in HCL:H_2O_2:H_2O 1:1:5
- Waterinse, 2-propanol dip, dry in air
- Wafer breaking
- SiRN removal in HF 50%, 75'
- Waterinse, 2-propanol dip, dry in air

The process flow for the fabrication of shadow masks is given in Fig. A.1.

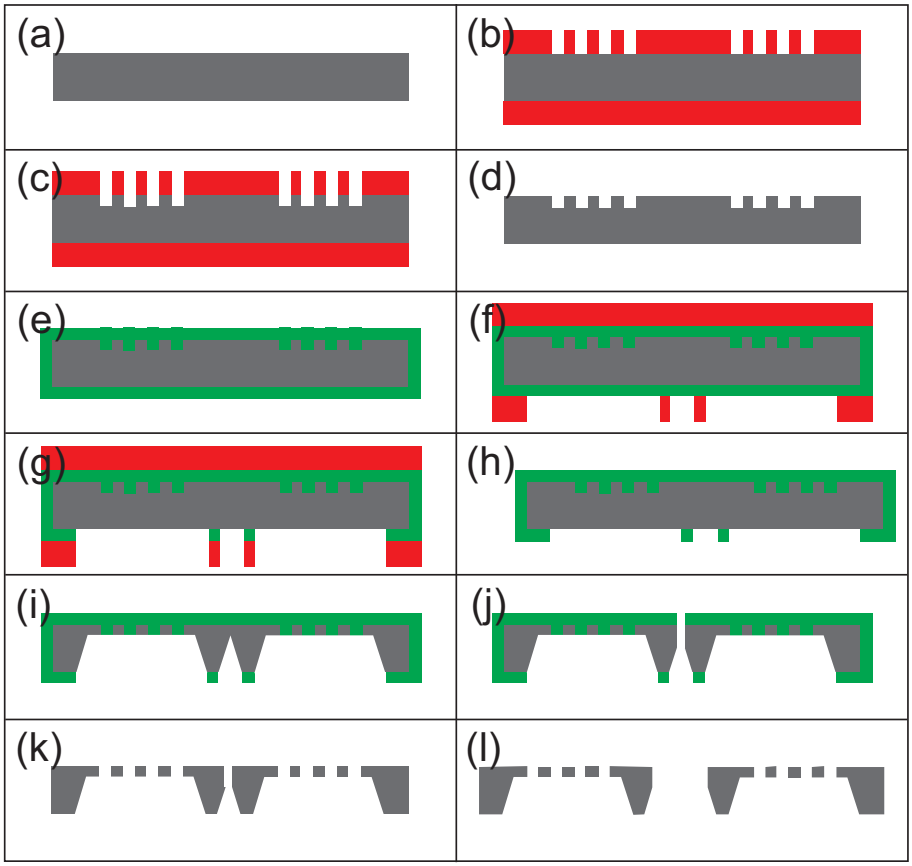

Figure A.1: Shadow mask fabrication process flow. (a) Starting with double sided polished Si wafer. (b) Resist spinning and developing. (c) Etching small features. (d) Resist removal. (e) SiRN deposition. (f) Resist spinning and developing. (g) SiRN etching. (h) Resist removal. (i) Backside KOH etching. (j) Wafer breaking. (k) Removing SiRN. (l) Finished shadow masks.

A.2 Electrode fabrication with shadow mask

- Sample cleaning:
  10' ultrasonicate in acetone
  10' ultrasonicate in 2-propanol
  waterrinse, spindry
- Bake 5' at 120°C
- Co evaporation through shadow mask, 8–16 nm, 1 Å/s, $1{\cdot}10^{-10}$ Torr
- Al evaporation over whole wafer, 1–3 nm, 1 Å/s, $1{\cdot}10^{-10}$ Torr
- Oxidation in load lock 8–30', 100 mTorr O_2, 800 V (see table A.1)

A.3 Electrode fabrication with photoresist

- Sample cleaning:
  10' ultrasonicate in acetone
  10' ultrasonicate in 2-propanol
  waterrinse, spindry
- Bake 5' at 120°C
- Resist spinning, TI35ES, 5" 500 rpm and 20" 4000 rpm
- Pre-exposure bake 2' at 90°C
- Exposure 20"
- Delay 30'
- After-exposure bake 2' at 120°C
- Flood exposure 60"
- Develop 50" in OPD 4262
- Co evaporation, 8–16 nm, 1 Å/s, $1{\cdot}10^{-10}$ Torr
- Al evaporation, 1–3 nm, 1 Å/s, $1{\cdot}10^{-10}$ Torr
- Plasma oxidation in load lock 8–30', 100 mTorr, 800 V
  (see table A.1, shorten oxidation time with 5 or 10'
- Lift-off with acetone, ultrasonicate 20", 2-propanol dip, spindry
- Plasma oxidation in load lock 5 or 10', 100 mTorr, 800 V
  (if no contact pads are fabricated)

A.4 Electrode fabrication with e-beam resist

- Resist spinning, 3% 495K PMMA in anisol, 6000rpm ($\sim$73 nm)
- Pre-exposure bake 60' at 175 °C
- Deep UV exposure to shorten molecules, 6–8', $\lambda \sim 220$ nm
  $P = \sim 42\ \mu\mathrm{W/cm^2}$

- Resist spinning, 1.5% 950K PMMA in MIBK, 1500rpm (∼62)
- Pre-exposure bake 60' at 175 °C
- Exposure
  fine structure: beam size ∼14 nm, dose 1200 or 2000 μC/cm^2
  course structure: beam size ∼136 nm, dose 1200 μC/cm^2
- Develop 60" in MIBK:IPA 1:3
- 2-propanol rinse, spindry
- Co evaporation, 8–16 nm, 1 Å/s, $1{\cdot}10^{-10}$ Torr
- Al evaporation, 1–3 nm, 1 Å/s, $1{\cdot}10^{-10}$ Torr
- Plasma oxidation in load lock 8–30', 100 mTorr, 800 V
  (see table A.1, shorten oxidation time with 5 or 10'
- Lift-off, see A.5
- Plasma oxidation in load lock 5 or 10', 100 mTorr, 800 V
  (if no contact pads are fabricated)

A.5 Lift-off

- Submersion in acetone, one night
- Ultrasonicate in acetone, 30–45"
- Acetone spray
- 2-propanol dip
- Spindry

A.6 Contact pad fabrication with photoresist

- Resist spinning, Olin 907/17, 5" 500 rpm and 20" 4000 rpm
- Pre-exposure bake 1' at 90°C
- Exposure 6"
- After-exposure bake 1' at 120 °C
- Develop 40" in OPD 4262
- Ti evaporation, 50 nm, 2 Å/s, $1{\cdot}10^{-7}$ Torr
- Au evaporation, 250 nm, 2 Å/s, $1{\cdot}10^{-7}$ Torr
- Lift-off, see A.5
- Plasma oxidation in load lock 5 or 10', 100 mTorr, 800 V

A.7 Plasma oxidation times

In table A.1, the different plasma oxidation times for different Al film thicknesses are given, in order to obtain an Al_2O_3 film.

Table A.1: Plasma oxidation times t_{ox} for different Al film thicknesses d_{Al}.

d_{Al} (nm)	t_{ox} (min)
1	8
1.1–1.6	10
1.7–2.0	15
2.1–2.4	20
2.5–2.9	30

Summary

Electron transport and spin phenomena in hybrid organic/inorganic systems

This thesis describes a series of electron transport experiments that all focus on systems consisting of both organic and inorganic materials. The combination of these two classes of materials offer the possibility to exploit the huge potential of organic chemistry, making hybrid organic/inorganic systems both interesting from a fundamental point of view as well as of technological relevance. Organic chemistry allows for engineering structures at the atomic level, with a large choice of building blocks, bottom-up fabrication and self-assembly, thereby opening up ways to experimentally study key problems in solid-state physics, like magnetic interactions and the control of nanosystems, as has been done in this thesis.

Organic spintronics combines the advantages of spintronics (non-volatility, potentially faster and cheaper electronic devices in which logic operations, storage and communication can be integrated) with the advantages of organic materials, which include cheap, light-weight and mechanically flexible electronics. Besides the advantages of the aforementioned fields, the spin relaxation time is predicted to be potentially very long in organic materials, making these devices very promising for spintronic applications. Most organic materials have low mobilities ($\ll$ 1 $cm^2(Vs)^{-1}$), due to impurities, grain boundaries, and the lack in long-range order. As a solution to this problem, highly ordered and very pure organic single crystals (with reported mobilities up to 40 $cm^2(Vs)^{-1}$) in field-effect transistor layouts with ferromagnetic electrodes are studied in this thesis.

The fabrication of ferromagnetic/tunnel barrier Co/Al_2O_3 electrodes is discussed, for the purpose of both injecting charge and spin into rubrene single-crystals. The tunnel barrier is added to protect the Co from oxidation and as a way to overcome the conductivity mismatch, a problem when injecting a spin-polarized current from a highly conductive metal electrode into a less conductive semiconductor. Several methods, including shadow mask fabrication, photo- and e-beam lithography are investigated. Electrodes fabricated with shadow masks

can be used to realize field-effect transistors with organic single-crystals, but smaller features than 10 μm have not been obtained, which is probably needed for spin-valve devices. Photo- and e-beam lithography allowed to obtain smaller features, down to $\sim$2 μ and 100 nm, respectively.

Using X-ray photoelectron spectroscopy and UV photoemission spectroscopy, the interfaces of Co/Al_2O_3 are investigated. These measurements show that after contact with acetone and 2-propanol, as used in photo- and e-beam lithography processes, a contamination layer is present on the Co/Al_2O_3 electrodes. This contamination layer results in a large hole injection barrier, which could be detrimental for spin injection. It is shown in reference magnetic tunnel junctions that the contamination layer decreases the spin-polarized signal. This signal can be restored by cleaning the electrodes by plasma oxidation to remove the organic contamination.

Photolithography has been used to fabricate single-crystal field-effect transistors with Co/Al_2O_3 electrodes. The electrodes have different widths, with switch their magnetization at different magnetic fields, which makes it possible to achieve parallel and anti-parallel magnetization, needed for spin-valve devices. This device shows clear field-effect transistor behavior and the current is contact dominated, as expected for electrodes with a tunnel barrier. The mobility in this device is measured to be 0.25 $cm^2(Vs)^{-1}$. The current can be fitted with a back-to-back Schottky model, which shows that although Schottky barrier formation plays a role in these devices, tunneling is important. Spin-valve behavior is not observed in these devices, which might indicate the need for smaller electrode separations or organic single-crystals with higher mobility. Field-effect transistors with electrodes fabricated with e-beam lithography and with LSMO electrodes have also been realized.

Top electrodes are hard to realize on organic materials, because material deposited using e-beam evaporation or sputtering can cause damage, leading to surface traps and irreproducible results. However, top electrode fabrication would ease the fabrication process by eliminating the need to select thin organic single-crystals, which can be laminated on pre-fabricated bottom electrodes, and the need to handle the fragile organic single-crystal. Top electrodes have been realized by transferring Au from a soft elastomeric stamp to the surface of an organic single-crystal. This process is however irreproducible. Better results are obtained when the transfer is facilitated by an organic molecule, benzyl mercaptan, which are attached to Au in solution. Electrodes have been realized in this way, and current is injected in these organic single-crystals in the space-charge-limited current regime and in field-effect transistors.

Ferromagnetic nanoparticles capped with organic ligands are an interesting option to increase magnetic storage densities. FePt nanoparticles remain ferromagnetic at room temperature, even for nanometer particle size, due to their high magnetocrystalline anisotropy. The high annealing temperature (around 700 °C), needed to obtain a face-centered tetragonal ($L1_0$) phase with a high anisotropy, can lead to agglomeration of the nanoparticles and the destruction of the organic ligands. Adding a small fraction of Au decreases the annealing temperature. The annealing temperature can also be lowered if the particles are annealed for a longer time. Nanoparticles annealed in solution at temperatures as low as 150°C show the onset of the $L1_0$ phase. The low-temperature annealing leaves the organic ligands intact, which can be used for patterning the nanoparticles.

Spin interactions between magnetic impurities and their solid-state environment can give rise to different spin phenomena, like the Kondo effect and Ruderman-Kittel-Kasuya-Yosida (RKKY) interaction. The Kondo effect is a many-body phenomenon, arising from the interaction of the spin of a magnetic impurity with the spins of conduction electrons. The Kondo effect is suppressed by the RKKY interaction, an interaction between impurity spins via the conduction electrons. A new system for investigating spin interactions between magnetic impurities and their environment, consisting of a metal layer with paramagnetic organic molecules on top, acting as the magnetic impurities, is proposed and investigated. A monolayer of cobalt complexes on an Au layer can be realized in which the organic molecules have an unpaired spin, as confirmed by X-ray photoelectron spectroscopy and electron paramagnetic resonance measurements. In a number of systems with diluted monolayers, a local resistance minimum is observed, possibly implying Kondo physics. A negative magnetoresistance is observed, which is larger for lower temperatures.

Wouter J.M. Naber
January 2010

Samenvatting

Elektrontransport en spinverschijnselen in hybride organische/anorganische systemen

Dit proefschrift beschrijft een serie elektrontransport experimenten die zich focussen op systemen bestaande uit zowel organische als anorganische materialen. De combinatie van deze twee klassen van materialen biedt de mogelijkheid om de enorme potentie van organische chemie te benutten, wat hybride organische/anorganische interessant maakt vanuit zowel een fundamenteel oogpunt als voor technologisch relevante toepassingen. Organische chemie biedt de mogelijkheid om functionele structuren te ontwerpen op atomair niveau, met een grote keuze aan bouwstenen, *van-onderaf* fabricage en zelfopbouw, waarbij mogelijkheden gecreëerd worden om experimenteel sleutelproblemen in de vastestoffysica te bestuderen, zoals magnetische interacties en het beheersen van nanosystemen, zoals gedaan is in dit proefschrift.

Organische spintronica combineert de voordelen van spintronica (niet-vluchtigheid van data, potentieel snellere en goedkoper elektronische apparaten waarin logische operaties, opslag en communicatie kunnen worden geïntegreerd), met de voordelen van organische materialen, waaronder goedkope, lichtgewicht en flexibele elektronica. Naast de voordelen van de bovengenoemde gebieden, is voorspeld dat de spinrelaxatietijd mogelijk erg lang is in organische materialen, waardoor deze structuren veelbelovend zijn voor spintronische toepassingen. De meeste organische materialen hebben een lage mobiliteit ($\ll 1$ cm^2(Vs)$^{-1}$), door onzuiverheden, structuurgrenzen en het ontbreken van een uitgestrekte orde. Als oplossing voor dit probleem zijn in dit proefschrift zeer goed geordende en zeer zuivere organische één-kristallen bestudeerd.

De fabricage van ferromagnetische/tunnelbarrière Co/Al_2O_3 elektroden wordt beschreven, met het doel zowel lading als spin in rubreen één-kristallen te injecteren. De tunnelbarrière is toegevoegd om kobalt te beschermen tegen oxidatie en om de geleidingsongelijkheid op te lossen, een probleem wanneer er een gepolariseerde stroom vanuit een goed geleidend metaal in een minder goed geleidende

halfgeleider wordt geïnjecteerd. Enkele methodes, waaronder schaduwmasker fabricage, foto- en elektronenstraal lithografie, zijn onderzocht. Elektroden gefabriceerd met schaduwmaskers kunnen worden gebruikt om veldeffecttransistoren met organische één-kristallen te realiseren, maar kleinere afmetingen dan 10 μm, die waarschijnlijk nodig zijn voor spintronische structuren, zijn niet behaald. Foto- en elektronenbundel lithografie bieden de mogelijkheid tot kleinere afmetingen, tot respectievelijk $\sim$2 μ en 100 nm,

Met röntgenstraling foto-elektronspectroscopie en ultraviolet foto-emissie-spectroscopie is het oppervlak van Co/Al_2O_3 bestudeerd. Deze metingen tonen aan dat na contact met aceton, zoals gebruikt wordt in foto- en elektronenstraal lithografie, een verontreinigingslaag op de Co/Al_2O_3 elektroden aanwezig is. Deze verontreinigingslaag leidt tot een grote injectiebarrère voor gaten, die nadelig kan zijn voor het injecteren van spin. Het is aangetoond in referentie magnetische tunnel structuren dat de verontreinigingslaag het spingepolariseerde signaal doet afnemen. Dit signaal kan worden hersteld door de elektroden schoon te maken met plasma oxidatie om organische verontreinigingen weg te halen.

Fotolithografie is gebruikt om organische één-kristal veld-effect transistoren te fabriceren met Co/Al_2O_3 elektroden. De elektroden hebben verschillende breedtes, zodat hun magnetisatie omdraait bij verschillende magneetvelden. Dit maakt het mogelijk om parallelle en antiparallelle magnetisatie te bereiken, wat nodig is voor spintronische structuren. Deze transistor vertoont een duidelijk veld-effect gedrag en de stroom wordt gedomineerd door de elektroden, zoals verwacht wordt voor elektroden met een tunnelbarrière. De mobiliteit in deze transistor is 0.25 $cm^2(Vs)^{-1}$. De stroom kan worden gefit aan een ruggelings Schottky model, wat aantoont dat er ondanks dat het ontstaan van een Schottky barrière een rol speelt, tunnelen belangrijk is. "Spin-valve" gedrag is niet gezien in deze transistoren, wat de noodzaak voor kleinere elektrodeafstand of organische één-kristallen met een hogere mobiliteit kan betekenen.

Topelektroden zijn moeilijk te vervaardigen op organische materialen, omdat materialen die gedeponeerd zijn met elektronenstraal verdamping of sputteren schade kunnen toebrengen, wat leidt tot oppervlaktevallen en onreproduceerbare resultaten. Topelektroden zouden echter wel het fabricage proces vergemakkelijken omdat ze de noodzaak wegnemen om dunne organische één-kristallen, die kunnen worden gelamineerd op vooraf gefabriceerde elektroden, te selecteren, en om de fragiele één-kristallen te hanteren. Topelektroden zijn gefabriceerd door goud over te brengen van een zachte elastomeer stempel naar het oppervlak van een organisch één-kristal. Dit proces is echter moeilijk reproduceerbaar. Betere resultaten zijn behaald als de overdracht gestimuleerd wordt door een laag van organische molekulen, benzyl mercaptan, die wordt vastgezet aan het goud in een

oplossing. Elektroden zijn met deze methode gerealiseerd en stroom is genjecteerd in de organische één-kristallen in het ruimtelading-gelimiteerde-stroom-regime en in veldeffecttransistoren.

Ferromagnetische nanodeeltjes, ingesloten met organische molekulen zijn een interessante optie om de dataopslag dichtheid te verhogen. FePt nanodeeltjes blijven ferromagnetisch bij kamertemperatuur, zelfs deeltjes zo groot als enkele nanometers, door hun grote magnetokristallijne anisotropie. Het is nodig de nanodeeltjes tot hoge temperaturen (rond 700 °C) te verhitten om de face-centered tetragonal ($L1_0$) fase met een hoge anisotropie te verkrijgen. Dit kan leiden tot het samenklonteren van de nanodeeltjes en het verwoesten van de organische molekulen. Het toevoegen van een kleine hoeveelheid goud verlaagt de temperatuur. De temperatuur kan ook verlaagd worden als de deeltjes gedurende een langere tijd op deze temperatuur worden gehouden. In nanodeeltjes die zijn verhit in oplossing tot een temperatuur zo laag als 150°C is het begin van de $L1_0$ fase te zien. De verhitting tot lage temperatuur laat de organische moleculen intact, zodat ze kunnen worden gebruikt voor het patroneren van de nanodeeltjes.

Spininteracties tussen magnetische onzuiverheden en hun vaste-stof omgeving kunnen aanleiding geven tot verschillende spinverschijnselen, zoals het Kondo effect en de Ruderman-Kittel-Kasuya-Yosida (RKKY) interactie. Het Kondo effect is een veel-deeltjes verschijnsel, dat ontstaat door de wisselwerking van de spin van een magnetische onzuiverheid en de spin van geleidingselektronen. Het Kondo effect is in competitie met de RKKY interactie, een wisselwerking tussen de magnetische onzuiverheden via de geleidingselektronen. Een nieuw systeem om de spin wisselwerking tussen magnetische onzuiverheden en hun omgeving te bestuderen, dat bestaat uit een metaallaag met er bovenop paramagnetische moleculen, die zich gedragen als de magnetische onzuiverheden, is voorgesteld en onderzocht. Een monolaag van kobaltcomplexen, waarin de moleculen een ongepaarde spin hebben, kan worden gevormd op een goudlaag. Dit is bevestigd door röntgen foto-elektron spectroscopie en elektron paramagnetische spectroscopie. In enkele systemen met een verdunde monolaag is een lokaal weerstandsminimum gemeten, dat mogelijk Kondo fysica kan betekenen. Een negatieve magnetoweerstand is gezien, die groter is bij lagere temperaturen.

Wouter J.M. Naber
January 2010

Curriculum Vitae

Wouter Johannes Marinus Naber

30-06-1981	Born in Leiderdorp, the Netherlands.
1993–1999	Grammar school, Bonaventura College, Leiden
1999–2005	M.Sc. Applied Physics, Delft University of Technology Graduate research in the Quantum Transport group of prof. dr. ir. L.P. Kouwenhoven Subject: Spin-dependent transport in few-electron laterally coupled double quantum dots
2005	Internship, NTT Basic Research Laboratories, Japan Subject: Surface acoustic wave induced transport in a double quantum dot
2005–2010	Ph.D, University of Twente Ph.D research in the Group NanoElectronics under supervision of prof. dr. ir. W.G. van der Wiel Subject: Electron transport and spin phenomena in organic/inorganic systems

List of publications

8. *Controlled tunnel-coupled ferromagnetic electrodes for spin injection in organic single-crystal transistors*
W.J.M. Naber, M.F. Craciun, J.H.J. Lemmens, A.H. Arkenbout, T.T.M. Palstra, A.F. Morpurgo and W.G. van der Wiel, Organic Electronics – accepted for publication

7. *A photoemission study of interfaces between organic semiconductors and Co as well as Al_2O_3/Co contacts*
M. Grobosch, C. Schmidt, W.J.M. Naber, W.G. van der Wiel and M. Knupfer, Synthethic Metals – accepted for publication

6. *Low-temperature solution synthesis of chemically functional ferromagnetic FePtAu nanoparticles*
S. Kinge, T. Gang, W.J.M. Naber, H. Boschker, G. Rijnders, D.N. Reinhoudt and W.G. van der Wiel, Nano Letters **9**, 3220 (2009).

5. *The formation of large-area conducting graphene-like platelets*
R. Salvio, S. Krabbenborg, W.J.M. Naber, A.H. Velders, D.N. Reinhoudt and W.G. van der Wiel, Chemistry - A European Journal **15**, 8235 (2009).

4. *Interaction of a 2-level system with 2D phonons*
W.J.M. Naber, T. Fujisawa, H.W. Liu and W.G. van der Wiel, AIP Conference Proceedings (peer-reviewed), Vol. **893**, 755, W. Jantsch and F. Schffler (Eds.), Melville, New York (2007).

3. *Organic Spintronics - Topical Review*
W.J.M. Naber, S. Faez and W.G. van der Wiel, Journal of Physics D: Applied Physics **40**, R205 (2007).

2. *Surface Acoustic Wave Induced Current in a Double Quantum Dot*
W.J.M. Naber, T. Fujisawa, P.V. Santos, H.W. Liu and W.G. van der Wiel, Physical Review Letters **96**, 136807 (2006).

1. *Single-Shot Readout of Electron Spin States in a Quantum Dot Using Spin-Dependent Tunnel Rates*
   R. Hanson, L.H. Willems van Beveren, I.T. Vink, J.M. Elzerman, W.J.M. Naber, F.H.L. Koppens, L.P. Kouwenhoven and L.M.K. Vandersypen, Physical Review Letters **94**, 196802 (2005).

Propositions

belonging to the thesis

Electron transport and spin phenomena in hybrid organic/inorganic systems

Wouter J.M. Naber

1. Organic single-crystal field-effect transistors can be fabricated with controlled tunnel-coupled ferromagnetic electrodes, which makes them promising for spintronic applications.
   Chapter 5 and 6 of this thesis

2. Monolayers of superparamagnetic molecules on conducting substrates are ideal test beds for studying 2D spin systems and their interaction with conduction electrons.
   Chapter 8 of this thesis

3. For the technological applications of nanoparticles, understanding their risks is at least as important as establishing their physical and chemical functionality.

4. Given the fact that nature uses self-assembly processes that result in complex systems like the human body, it is surprising these processes are not widely implemented in electronics.

5. It is better to have ten reasonable samples, than one perfect sample.

6. Anonymous paper submission is beneficial for the scientific community.

7. Environmental-friendly thinking is strongly inhibited by the fact the polluter rarely has to pay for this.

8. The phrase "Great power comes with great responsibility" does not only hold for Spiderman.

9. It is more logical to open shops outside office hours than during office hours.

10. The best propositions are the ones your promotor approves, but does not agree with.

These propositions are considered opposable and defendable and as such have been approved by the promotors, prof. dr. ir. D.N. Reinhoudt and prof. dr. ir. W.G. van der Wiel.

Enschede, January 2010

Stellingen

behorende bij het proefschrift

Elektrontransport en spinverschijnselen in hybride organische/anorganische systemen

Wouter J.M. Naber

1. Organische één-kristal veld-effect transistoren kunnen worden gefabriceerd met gecontroleerde tunnel-gekoppelde ferromagnetische elektroden, wat ze veelbelovend maakt voor spintronische toepassingen.
   Hoofdstuk 5 van 6 van dit proefschrift

2. Monolagen van superparamagnetische moleculen op geleidende substraten zijn ideale teststructuren voor het bestuderen van 2-dimensionale spinsystemen en hun interactie met geleidingselektronen.
   Hoofdstuk 8 van dit proefschrift

3. Voor technologische toepassingen van nanodeeltjes is het minstens zo belangrijk hun risico's te begrijpen, als hun fysische en chemische functionaliteiten vast te stellen.

4. Gegeven het feit dat de natuur zelfopbouwprocessen gebruikt die resulteren in complexe systemen zoals het menselijk lichaam, is het opmerkelijk dat deze processen niet breed geïmplementeerd zijn in de elektronica.

5. Het is beter om tien redelijke teststructuren te hebben, dan één perfecte.

6. Het anoniem insturen van artikelen is voordelig voor de wetenschappelijke gemeenschap.

7. Milieuvriendelijk denken wordt zwaar belemmerd door het feit dat de vervuiler zelden betaalt.

8. De uitspraak "Grote macht vraagt een grote verantwoordelijkheid" is niet alleen geldig voor Spiderman.

9. Het is logischer dat winkels buiten kantooruren open zijn, dan tijdens kantooruren.

10. De beste stellingen zijn diegene die je promotor goedkeurt, maar waar hij het niet mee eens is.

Deze stellingen worden opponeerbaar en verdedigbaar geacht en zijn als zodanig goedgekeurd door de promotoren, prof. dr. ir. D.N. Reinhoudt en prof. dr. ir. W.G. van der Wiel.

Enschede, januari 2010